THÈSE

En vue de l'obtention du

DOCTORAT DE L'UNIVERSITÉ DE TOULOUSE

Délivré par :

Institut National Polytechnique de Toulouse (Toulouse INP)

Discipline ou spécialité :

Génie des Procédés et de l'Environnement

Présentée et soutenue par :

M. ALEXIS TOURBIER

le mercredi 6 décembre 2023

Titre :

Simulation numérique des écoulements de Taylor réactifs

Ecole doctorale :

Mécanique, Energétique, Génie civil, Procédés (MEGeP)

Unité de recherche :

Laboratoire de Génie Chimique (LGC)

Directeur(s) de Thèse :

MME JOELLE AUBIN

Rapporteurs :

M. ARNAUD ANTKOWIAK, UNIVERSITE SORBONNE

M. DIETER BOTHE, TECHNISCHE UNIVERSITAT DARMSTADT

Membre(s) du jury :

M. STÉPHANE ZALESKI, UNIVERSITE SORBONNE, Président

M. CHIARA GALLETTI, UNIVERSITA DI PISA, Membre

M. HRVOJE JASAK, UNIVERSITE DE CAMBRIDGE, Membre

M. LIONEL GAMET, IFPEN, Membre

MME JOELLE AUBIN, TOULOUSE INP, Membre

MME PANAGIOTA ANGELI, UNIVERSITY OF LONDON, Membre

MME TYPHENE MICHEL, IFPEN, Invitée

M. PHILIPPE BEARD, IFPEN, Invité

Abstract:
Microfluidics has been of significant interest in recent years. Indeed, the high surface to volume ratio, combined with small reagent volumes make micro-devices an outstanding tool for process intensification. The continual increase in computational power also allows more complex engineering problems to be solved through computational fluid dynamics. However, there is still a lack in trustworthy tools to predict the most difficult multi-physics problems. Among these, micro-scale two-phase flows involving coupled mass and heat transfer still present several issues, the major one being the prediction of the surface tension force. This study investigates the numerical simulation of reactive Taylor flows. A new solver based on the Volume of Fluid framework to account for mass transfer between gas and liquid has been developed. A new methodology to implement the transport of concentration is proposed to avoid numerical diffusion and artificial mass transfer. Test-cases were used to demonstrate the performances of the new solver and the tool was used to study Taylor flows in T-junctions.

Résumé :
La microfluidique bénéficie d'un intérêt considérable du fait des nombreux avantages qu'elle présente. Les importants rapports surface-volume ainsi que les faibles volumes de réactifs impliqués rendent les microsystèmes très attractifs pour l'intensification des procédés. L'augmentation des ressources numériques a aussi permis la résolution de simulations de plus en plus réalistes. Il manque cependant encore d'outils rigoureusement validés pour résoudre les problèmes multiphysiques les plus compliqués, notamment les écoulement diphasiques à l'échelle microscopique impliquant le transfert de matière et de chaleur. Cette étude porte sur la résolution numérique des écoulements de Taylor réactifs. Un nouveau solveur utilisant la méthode Volume of Fluid a été développé pour prédire le transfert de matière entre un gaz et un liquide. Afin d'éviter le transfert de matière artificiel au niveau de l'interface, une nouvelle stratégie pour la discrétisation de l'équation de transport de la concentration a été mise en place avec succès. Différents cas tests ont démontré les performances du solveur, en particulier pour la résolution d'écoulements de Taylor dans des injecteurs en T.

Acknowledgements

I would like to express my sincere gratitude to my supervisors Lionel Gamet, Philippe Béard, Typhène Michel, Hrvoje Jasak and Joelle Aubin for their help and availability thoughout this project. Lionel in particular, thank you for your time and the discussion we had.

I am also indebted to the members of my thesis committee, Arnaud Antkowiak, Dieter Bothe, Panagiota Angeli, Chiara Galletti and Stéphane Zaleski for their insightful feedback and critical evaluation of this research. Your expertise has enriched the quality of this thesis.

I am of course grateful to all my friends and fellow PhD students at IFP Énergies Nouvelles with whom I shared countless working hours and coffee breaks. Many thanks also to Annie Borg who helped a lot with the administrative work.

Special thanks to all my familly, especially my parents Sandrine and Yves and my brother Nicolas, who always believed in my success and allow me to get to this stage. Finally, I could not have undertaken this journey without my wife Camille, who has always been supportive during these three years.

Contents

List of Figures **VIII**

List of Tables **XI**

Symbols **XIII**

Introduction **1**

1 An overview of gas-liquid two-phase flows simulations in microchannels **4**
1.1 Introduction . . . 4
1.2 Generalities on Taylor flows . . . 4
1.2.1 Description of the flow regime . . . 4
1.2.2 Main dimensionless numbers . . . 5
1.2.2.1 Reynolds number . . . 5
1.2.2.2 Weber number . . . 6
1.2.2.3 Capillary number . . . 6
1.2.2.4 Bond number . . . 6
1.2.2.5 Sherwood number . . . 7
1.2.2.6 Schmidt number . . . 7
1.2.2.7 Péclet number . . . 7
1.2.2.8 Hatta number . . . 8
1.2.3 Hydrodynamics of Taylor flows . . . 8
1.2.3.1 Liquid film . . . 8
1.2.3.2 Bubble formation . . . 9
1.2.3.3 Bubble length . . . 10
1.2.4 Mass transfer estimation for Taylor flows . . . 11
1.3 Governing equations . . . 15
1.4 Modeling approaches . . . 17
1.4.1 The Finite Volume Method . . . 17
1.4.2 Solving the Navier-Stokes equations . . . 21
1.4.3 The Volume of Fluid method . . . 21
1.4.4 Piecewise Linear Interface Construction . . . 23
1.4.5 The Continuum Surface Force . . . 23
1.5 The open-source CFD code OpenFOAM® . . . 25
1.5.1 OpenFOAM® general description . . . 25
1.5.2 Presentation of multiphase solvers . . . 25
1.5.3 The geometric Volume of Fluid method `isoAdvector` . . . 26

1.6 Phase change in the Volume of Fluid framework . . . 29
1.6.1 The single-field and CST approach . . . 29
1.6.2 The two-field approach . . . 30
1.7 Chemical reaction . . . 32
1.8 Limits and difficulties . . . 32
1.8.1 Mesh size in the liquid film surrounding Taylor bubbles . . . 32
1.8.2 Spurious currents . . . 33
1.9 Summary and objectives of current work . . . 33
1.9.1 Gaps identified . . . 33
1.9.2 Objectives of this work . . . 35

2 Concentration transport without phase change, implementation and validation 37
2.1 Introduction . . . 37
2.2 Description of the boundary conditions . . . 38
2.2.1 Velocity . . . 38
2.2.2 Pressure . . . 38
2.2.3 Volume fraction . . . 39
2.2.4 Concentration . . . 39
2.2.5 Summary . . . 40
2.3 Performance assessment of existing VOF solvers . . . 40
2.3.1 Developed Taylor flows in a tube . . . 40
2.3.1.1 Geometry and initialization . . . 40
2.3.1.2 Meshing . . . 42
2.3.1.3 Boundary conditions . . . 42
2.3.1.4 Results . . . 43
2.3.2 Taylor bubble generation in a coaxial injector . . . 46
2.3.2.1 Geometry . . . 46
2.3.2.2 Meshing . . . 46
2.3.2.3 Boundary conditions . . . 46
2.3.2.4 Results . . . 47
2.3.3 Taylor bubble generation in a T-junction . . . 51
2.3.3.1 Geometry . . . 51
2.3.3.2 Meshing and initialization . . . 51
2.3.3.3 Boundary conditions . . . 52
2.3.3.4 Mesh sensitivity . . . 52
2.3.3.5 Results . . . 53
2.3.4 Conclusion . . . 56
2.4 Advecting a concentration field: issues and solutions . . . 57
2.4.1 Consistency with the advection of a free surface . . . 59
2.4.2 Implicit formulation attempt . . . 61
2.4.3 Description of a geometric methodology . . . 62
2.4.4 Parallelization of the algorithm . . . 63
2.5 Diffusing a species without phase change . . . 65
2.5.1 Correction of the diffusion coefficient . . . 65
2.5.2 Correction of the diffusion fluxes . . . 66
2.5.3 The deferred correction: an attempt to improve stability . . . 70

2.5.4 Implementation of the transport equation . . . 71
2.6 Validation of concentration transport without phase change . . . 74
2.6.1 Generic test cases . . . 74
2.6.1.1 Mesh sensitivity analysis . . . 76
2.6.1.2 3D simulations . . . 77
2.6.1.3 Impact of `isoAdvector` tolerances . . . 79
2.6.1.4 Conclusions on the generic test cases . . . 79
2.6.2 Simulation of Taylor flow without phase change-limits and difficulties 80
2.6.2.1 Results without face limited concentration . . . 81
2.6.2.2 2D T-junction . . . 83
2.6.2.3 Capillary number sensibility . . . 85
2.6.2.4 3D T-junction . . . 86
2.6.2.5 Conclusions on the specific tests in T-junctions . . . 87
2.7 Conclusion . . . 88

3 Mass transfer at a gas-liquid interface in the Volume of Fluid framework 90
3.1 Introduction . . . 90
3.2 Implementing concentration driven phase change with a volumetric source term 90
3.2.1 Computation of the advective part of the source term . . . 94
3.2.2 Computation of the diffusive part of the source term . . . 95
3.2.3 Updating the concentration field . . . 98
3.2.4 Introducing volume change in the volume fraction equation . . . 99
3.2.5 Numerical implementation . . . 100
3.3 The Stefan problem in 1D . . . 101
3.3.1 Test case setup . . . 101
3.3.2 Analytical solution . . . 101
3.3.3 Results and discussion . . . 102
3.3.4 Subgrid scale model . . . 104
3.4 Other validation test cases . . . 106
3.5 Mass transfer around a Taylor bubble in a T-junction . . . 107
3.6 Conclusion . . . 110

4 Towards the simulation of reactive Taylor flows 113
4.1 Introduction . . . 113
4.2 Oligomerization of ethylene . . . 113
4.2.1 Prediction of the physical properties . . . 114
4.2.1.1 Compressibility and density prediction . . . 114
4.2.1.2 Solubility . . . 116
4.2.1.3 Diffusivity . . . 117
4.2.1.4 Viscosity . . . 123
4.2.1.5 Thermal conductivity . . . 124
4.2.1.6 Surface tension . . . 126
4.2.2 Description of the chemical reaction . . . 126
4.3 Implementing a chemical reaction through a volumetric source term . . . 130
4.4 Preliminary test cases . . . 135
4.4.1 Motivation for additional test cases . . . 135
4.4.2 Reactors description . . . 135

4.4.3 The catalyst inlet is on the side of the gas inlet 138
4.4.4 The catalyst inlet is on the opposite side of the gas inlet 139
4.4.5 The catalyst is injected in a mixing cross after the gas inlet 140
4.5 Conclusion 141

Conclusions **142**

Perspectives **144**

A Hydrodynamics study **145**

B Fluid properties **146**
B.1 Compressibility and density prediction 146
B.1.1 Soave-Redlich-Kwong 146
B.1.2 Peng-Robinson 147
B.1.3 Compressibility factor prediction 148

Bibliography **150**

List of Figures

1.1 Simple 1D uniform structured stencil for the integration of the diffusion equation 19
1.2 Two-dimensional example of the reconstructed interface with PLIC 23
1.3 Advection of a free surface with `isoAdvector` during a time step Δt 27
1.4 Liquid immersed part of the top face (A_{im}) during a time step Δt 27
1.5 Illustration for the computation of the liquid immersed area 28
1.6 `isoAdvector` where the volume fraction field is updated 28

2.1 3D tube with the angular sector used for 2D axisymmetrical simulations in blue and the initialization of the bubble in red 41
2.2 Geometry of a 3D tube with the bubble intialised in red dashed lines 41
2.3 Comparison between a single H block grid and the O-H butterfly topology . 42
2.4 Bubble of gas in a 2D axisymmetrical simulation 43
2.5 Comparison of the magnitude of the velocity ($\mathrm{m\,s^{-1}}$) at time 0.1s for the three solvers, in a 2D axisymmetric wedge simulation 44
2.6 Bubble of gas in a sliced 3D channel 44
2.7 Comparison of the magnitude of the velocity ($\mathrm{m\,s^{-1}}$) at 0.1s for the three solvers in a 3D simulation 45
2.8 Comparison of the magnitude of the velocity ($\mathrm{m\,s^{-1}}$) at 0.5s for the three solvers in a 3D simulation 45
2.9 3D coaxial injector with the symmetry axis represented as a black dashed line and the wedge used for 2D axisymmetrical simulation as a blue dashed line . 46
2.10 Comparison between `interFoam` and `interFlow` on the coaxial injector at 0.037s 47
2.11 Comparison between `interFoam` and `interFlow` on the coaxial injector at 0.235s 48
2.12 Comparison between `interFoam` and `interFlow` on the coaxial injector at 0.324s 48
2.13 Comparison between the `Gauss linear` and `pointCellsLeastSquares` gradient schemes, and with the snap tolerance for `interFlow` at 0.040s 49
2.14 Comparison between the `Gauss linear` and `pointCellsLeastSquares` gradient schemes for `interFlow` at 0.040s, after changing the boundary condition of the gas side wall for a constant contact angle of 180°. 50
2.15 Cutting plane in $z = 0$ of a three-dimensional coaxial injector using `interFoam` 50
2.16 3D T-junction with the cross-section used for 2D simulation in blue 51
2.17 Simulation of a T-junction with a highly refined 2D mesh of 140 cells per diameter 52
2.18 Simulation of a T-junction with a highly refined 2D mesh of 140 cells per diameter and buffer at the gas inlet 53
2.19 Volume fraction field and bubbles simulated with `interFlow` after 0.018 s in 2D 54

2.20 Volume fraction field and bubbles simulated with `interFlow` after 0.018 s in 3D 55
2.21 Bubble length. Orange: experimental work from Guo et al., Grey: numerical work from Guo et al., Blue: numerical work with `interFlow` (2D) 56
2.22 Bubble length. Orange: experimental work from Guo et al., Blue: numerical work with `interFlow` (3D) 56
2.23 Schematic of a two-dimensional stencil with the upwind differencing scheme for the interpolation of C_k 58
2.24 Schematic diagram of a two-dimensional stencil with the central differencing scheme for the interpolation of $C_{k,f}$ 59
2.25 Schematic of a one-dimensional channel used to test the advection performances of interpolation schemes 60
2.26 Comparison of the volume fraction field α and the liquid phase concentration $C_{k,1}$ obtained using different interpolation schemes 60
2.27 Schematic of two cells cut by the interface with a volume fraction of 0.5 . . . 61
2.28 Function computing the face concentration 63
2.29 Representation of two neighbouring cells on two processors with the patch face in blue 64
2.30 Representation of two neighbouring cells on two processors with the patch face in blue 64
2.31 Simple 1D uniform structured stencil for the integration of the diffusion equation 66
2.32 Schematic of the test case for the diffusion equation 68
2.33 Non-dimensional volume average concentration profiles at $0.5s$ 69
2.34 Non-dimensional phase average concentration profiles at $0.5s$ 70
2.35 Flowchart of the global algorithm for the transport of concentration 72
2.36 Flowchart for the correction of the advection process 73
2.37 Liquid concentration field obtained with three different interpolation schemes for the face values 75
2.38 Comparison of the mean error value for three levels of refinement 76
2.39 Comparison between 2D and 3D simulations of the mean error value 77
2.40 Comparison between 2D and 3D simulations of the maximum error value . . 78
2.41 Comparison of the 3D (top) and the 2D (bottom) error distributions in a straight channel 78
2.42 Mean error variations with time according to `surfCellTol` and `isoFaceTol` values 80
2.43 Schematic of an interface crossing a 2D cell diagonally 81
2.44 Time variation of the surface fraction on a face for a 2D T-junction 82
2.45 Visualization of the error "explosion" in the bubble growing in a T-junction . 83
2.46 Mean error comparison between two refinement levels for a 2D T-junction . . 84
2.47 Maximum error comparison between two refinement levels for a 2D T-junction 85
2.48 Comparison of the mean error values obtained for three different Ca numbers in a T-junction 86
2.49 Time evolution of the mean error in a 3D T-junction 87
2.50 Gas bubble on the outer wall of the gas inlet of a 3D T-junction 88

3.1 Stencil for the computation of an interfacial concentration gradient 96

3.2 1D mesh with the concentration variations in ordinate . . . 97
3.3 Two cells with a different interface position and the corresponding interface normal . . . 97
3.4 Parallel implementation of the mass source term . . . 100
3.5 Phase average concentration field update . . . 100
3.6 Volume fraction field update after mass transfer . . . 100
3.7 Numerical set up for Stefan's sucking interface test case . . . 101
3.8 Time evolution of the interface position for different mesh refinements . . . 103
3.9 Comparison between the analytical concentration and its numerical counterpart with a diffusivity of $1 \times 10^{-9}\,\mathrm{m^2\,s^{-1}}$ . . . 104
3.10 Mass source term for the subgrid-scale model . . . 105
3.11 Comparison between the analytical solution of the interface displacement and its numerically predicted counterpart with a diffusivity of $1 \times 10^{-9}\,\mathrm{m^2\,s^{-1}}$ . . . 105
3.12 Comparison between the analytical concentration and its numerical counterpart with a diffusivity of $1 \times 10^{-9}\,\mathrm{m^2\,s^{-1}}$ . . . 106
3.13 Liquid concentration "C" around a rising bubble in a quiescent liquid with a modified gravity acceleration . . . 107
3.14 Liquid phase concentration field of ethyene close to the interface of a growing bubble in the gas injector of a T-junction . . . 108
3.15 Mass transfer around a bubble growing downward in the gas injector of a 2D T-junction . . . 109
3.16 Mass transfer around a developped Taylor bubble flowing from left to right in the channel of a 2D T-junction . . . 110
3.17 Liquid phase ethylene concentration comparison between 2D (top) and 3D (bottom) T-junctions . . . 111

4.1 Isotherms of solubility of ethylene in cyclohexane with pressure from the work of Zhuze and Zhurba [1] . . . 117
4.2 Takahashi's correction factor at reduced pressure and temperature for gaseous diffusion coefficient . . . 120
4.3 Definition of the species Ethylene inside the `constant/transportProperties` dictionary . . . 131
4.4 Source code of the chemical reaction source term and equation solving . . . 132
4.5 Flowchart of the algorithm sequence for one species . . . 134
4.6 T-junction where the catalyst inlet is on the side of the gas inlet . . . 136
4.7 T-junction where the catalyst inlet is on the opposite side of the gas inlet . . . 137
4.8 T-junction where the catalyst is injected in a mixing cross after the gas inlet 137
4.9 Catalyst (top) and ethylene (bottom) fields in a 2D T-junction with injectors at 0.005 s . . . 138
4.10 Catalyst (top) and ethylene (bottom) fields in a 2D T-junction with injectors at 0.05 s . . . 139
4.11 Catalyst (top) and ethylene (bottom) fields in a 2D T-junction with injectors at 0.1 s . . . 140
4.12 Catalyst (top) and ethylene (bottom) fields in a 2D T-junction with injectors after 0.02 s . . . 141

List of Tables

1.1 Film thickness variations with temperature for the highest two-phase velocity $U_{TP} = U_G + U_L = 0.0231 \times 10^{-3}\,\mathrm{m\,s^{-1}}$. Ca is defined by equation 1.5 33

2.1 Types of boundary conditions used in the simulations 40

4.1 Critical properties of ethylene (database DIPPR) 114
4.2 Prediction of ethylene density ($\mathrm{kg\,m^{-3}}$) under operating temperature and pressure. Results obtained with SRK (left) and PR (right) 115
4.3 Prediction of ethylene density ($\mathrm{kg\,m^{-3}}$) under operating temperature and pressure. Results obtained with an ideal gas assumption 115
4.4 Density prediction from the NIST database for ethylene (left) and cyclohexane (right) 116
4.5 Values of the molar fraction of ethylene under pressure and temperature from [1] 117
4.6 Atomic diffusion volumes from [2] 119
4.7 Values of ethylene diffusivity in the gas phase ($\mathrm{cm^2\,s^{-1}}$) computed from relationship 4.5 at low pressures 119
4.8 Values of ethylene diffusivity in the gas phase ($\mathrm{cm^2\,s^{-1}}$) computed from the relationship of Takahashi [3] at operating pressures 120
4.9 Impact of temperature on the diffusivity coefficient of ethylene in cyclohexane 121
4.10 Infinite dilute diffusivity of ethylene in cyclohexane calculated with the Wilke-Chang relationship $\times 10^{-5}\,\mathrm{cm^2\,s^{-1}}$ 122
4.11 Values of self-diffusion of cyclohexane ($\times 10^{-5}\,\mathrm{cm^2\,s^{-1}}$) under pressure and temperature from Jonas [4] 123
4.12 Values of dynamic viscosity ($\times 10^{-5}\,\mathrm{Pa\,s}$) under pressure and temperature for ethylene from NIST 124
4.13 Values of dynamic viscosity ($\mathrm{mPa\,s}$) under pressure and temperature for cyclohexane from NIST 124
4.14 Values of thermal conductivity ($\mathrm{W\,m^{-1}\,K^{-1}}$) versus pressure and temperature for ethylene from NIST 125
4.15 Values of thermal conductivity ($\mathrm{W\,m^{-1}\,K^{-1}}$) versus pressure and temperature for cyclohexane from NIST 125
4.16 Values of surface tension coefficients for cyclohexane from NIST 126
4.17 Products distribution (w%) reported by Mahmoud Kamaleddine 127
4.18 Values of the dimensionless numbers for the minimum and maximum superficial velocities 135

A.1 Operating conditions and results from the work of Guo et al. [5] 145

B.1 Values of the compressibility factor Z for different temperatures and pressure using the SRK equation 149
B.2 Values of the compressibility factor Z for different temperatures and pressure using the PR equation 149

Symbols

α	Liquid volume fraction	
δ	Liquid film thickness	m
κ	Interface curvature	m^{-1}
μ	Dynamic viscosity	$\mathrm{Pa\,s}$
ρ	Density	$\mathrm{kg\,m}^{-3}$
σ	Surface tension coefficient	$\mathrm{N\,m}^{-1}$
Φ_i	CST flux of species i	$\mathrm{mol\,m}^{-2}\,\mathrm{s}^{-1}$
C	Concentration	$\mathrm{kg\,m}^{-3}$
C_p	Specific heat (isobaric)	$\mathrm{J\,kg}^{-1}\,\mathrm{K}^{-1}$
CFL	Courant number	
D	Molecular diffusivity	$\mathrm{m}^2\,\mathrm{s}^{-1}$
Δx	Mesh cell size	m
Δt	Time space	s
d_h	Hydraulic diameter	m
d_t	Channel diameter	m
F_σ	Surface tension force	$\mathrm{N\,m}^{-3}$
f_k	Fugacity of species k	Pa
g	Gravity acceleration	$\mathrm{m\,s}^{-2}$
H	Henry constant	
k	Thermal conductivity	$\mathrm{W\,m}^{-1}\,\mathrm{K}^{-1}$
M	Molar mass	$\mathrm{kg\,mol}^{-1}$
P	Pressure	Pa
R	Universal gas constant	$\mathrm{J\,mol}^{-1}\,\mathrm{K}^{-1}$

T	Temperature	K
U	Velocity field	$\mathrm{m\,s^{-1}}$
U_c	Compressive velocity (MULES)	$\mathrm{m\,s^{-1}}$
U	Velocity	$\mathrm{m\,s^{-1}}$
U_r	Relative velocity between the liquid and the gas	$\mathrm{m\,s^{-1}}$
U_G	Superficial velocity of the gas	$\mathrm{m\,s^{-1}}$
U_L	Superficial velocity of the liquid	$\mathrm{m\,s^{-1}}$
U_Σ	Gas-liquid interface velocity	$\mathrm{m\,s^{-1}}$
x_i	Liquid molar fraction of species i	
y_i	Gas molar fraction of species i	
Bo	Bond number	
Ca	Capillary number	
Ha	Hatta number	
Pe	Péclet number	
Re	Reynolds number	
Sc	Schmidt number	
Sh	Sherwood number	
We	Weber number	

Introduction

Background

Despite the growing demand for a plastic-free world, the production of commodity resins has experienced an exceptional growth over the last 50 years [6]. Among these plastics, polyethylene (PE) is widely used due to its broad range of applications. The change in density of PE is tuned by the amount of short chained alpha-olefins, especially 1-butene, in the resin. These olefins are mainly produced through ethylene oligomerization. A selective oligomerization is necessary to reach an industrial profitable process meeting productions objectives. As a result, a lot of effort has been made to develop efficient catalytic processes for the production of polymers.

Process design and the elaboration of catalysts represents one of the biggest share of IFP Énergies Nouvelles activities. In the case of the oligomerization of olefins, the choice of a homogeneous reaction was made based on the advantages and disadvantages for reaction performance. The suitable catalysts are tested in pilot plants before scaling-up the process. At this stage we need to evaluate the selectivity, the conversion and other parameters expected from the catalyst in order to choose the best one.

Most of the time, the catalytic tests are conducted in a stirred tank reactor. Where a large volume of reagents and a lot of energy are required to ensure effective mixing. Whilst these vessels are easy to design and a lot of correlations are already available for the temperature control for example, they have several drawbacks. The volume of reagents is large, usually of the order of several liters, which is a problem since catalysts are expensive. Effective temperature control and mixing are also difficult due to the large reactor volume. Also, the reactors are often operated in batch mode and at high pressure, which requires a further depressurization step. This step might be harmful for the products in case of secondary reactions.

One alternative to batch reactors for catalytic screening tests is the choice of a continuous flow capillary reactor. Microfuidics, as a viable option to conventional reactors for screening

tests, has attracted considerable attention over the last years. To ensure micro capillaries can perform at least as well as the agitated reactors, proof is required to demonstrate adequate reaction performance. Several parameters can be evaluated to assess the performances, reaction selectivity, reagents conversion or even local concentration fields for example. Experimental and numerical have their own pros and cons, experimental measurement could be sometimes difficult to conduct, on the other hand, numerical tools must be rigorously validated.

In this work, the oligomerization of ethylene will be used as a case study. The reaction is conducted in a microreactor to produce butene from ethylene. Ethylene is the gas phase. The liquid phase is composed of a solvent, cyclohexane, and the catalyst. It is a homogeneous catalysis, which means that the catalyst is miscible in the liquid phase where the reaction takes place. The mass transfer step should be given special attention as it may be a limiting step if the rate of transfer is low. The interest of the micro capillary reactor over a conventional stirred tank reactor is the ease of temperature control. The diameter of the channel is smaller than one millimeter and the surface to volume ratio is high. It is therefore possible to dissipate a lot of heat with a thermostatic bath for example. The oligomerization reaction is exothermic, so the control of the temperature is an important parameter to avoid catalyst deactivation. An other interesting aspect of microchannels is the ease of use and the reduced operating time. These reactors are operated in continuous mode, so the depressurization step is not needed.

The gas-liquid flow regime targeted is Taylor flow. This regime, also known as segmented or slug flow, is characterized by a train of bubbles filling almost entirely the diameter of the channel, separated by slugs of liquid. It is a two-phase flow displaying very attractive features to conduct chemical reactions. The large surface to volume ratio is very suitable for both mass and heat transfer. The screening test aims at finding the best catalyst for given conditions. And it is important to avoid any mass transfer limitations that could interfere with the measurement of the rate of the reaction.

The purpose of this thesis is to create a multiphysics solver that will account for all the transport phenomena occurring in Taylor flow. Once the solver is validated, it will be tested on ethylene oligomerization to reproduce experimental work previously conducted at IFP Énergies Nouvelles. With an aim of process intensification, the transition from classical stirred tank reactors towards microchannel reactors follows an objective of reducing resources and operational times as well as risk control. Computational fluid dynamics (CFD) is now being considered as a design tool and used as such. It is therefore the logical path to offer a new means for catalyst testing via numerical simulation. CFD is a tool that is not only powerful but also complementary to experimental work. Indeed, it gives access to data such as local

velocity fields that would otherwise require special techniques.

Thesis outline

The thesis aims to provide a comprehensive understanding of microchannel two-phase flows through detailed simulations, validation, and analysis. It is organized into several chapters. Chapter 1 delves into the background of gas-liquid two-phase flows, particularly Taylor flows, discussing relevant dimensionless numbers and hydrodynamics. It then introduces the governing equations, modeling approaches, and the `OpenFOAM` software used for simulations. Chapter 2 focuses on concentration transport without phase change, discussing implementation details, validation, and challenges. Chapter 3 addresses mass transfer at a gas-liquid interface in the Volume of Fluid framework, including implementation of concentration-driven phase change and validation tests. Chapter 4 shifts the focus to simulating reactive Taylor flows, discussing chemical reactions, algorithm sequence, and case studies.

Chapter 1

An overview of gas-liquid two-phase flows simulations in microchannels

1.1 Introduction

In this first chapter, the theoretical background of reactive Taylor flows and the existing literature are presented. The physics behind Taylor flows are described and an in-depth review of the numerical methods used in the work is discussed. As the main purpose of this work is the numerical simulation of such flows, a comprehensive description of the algorithms is an essential primary step to understand the numerical developments made.

1.2 Generalities on Taylor flows

1.2.1 Description of the flow regime

Taylor flow is a two-phase flow regime that is composed of a segmented flow of uniformly sized bubbles separated by liquid slugs. The bubbles fill almost the entire cross-section of the channel, with only a thin liquid film between the channel wall and the bubbles. The length of bubbles is usually larger than the diameter of the channel. The Taylor flow regime is typically established for a wide range of liquid and gas superficial velocities spanning from $1 \times 10^{-4}\,\mathrm{m\,s^{-1}}$ up to several $\mathrm{m\,s^{-1}}$, depending on the velocity ratio between the gas and the liquid. Gas and liquid velocities are not the only parameters influencing the flow regime. Surface tension and viscosity might also become dominant under specific conditions. To

compare which forces are dominant, the capillary number (Ca), which compares viscous to superficial forces, can be used. More details about this number are given in section 1.2.2.3. For small capillary numbers, typically $Ca < 1e-04$, the bubble has two hemispherical caps and the surface tension force is dominant. When it increases, $Ca \approx 5e-03$, a *bullet* shape appears because due to viscous effects.
Taylor flows are used for process intensification as their features permit to tackle some limitations of stirred reactors. Firstly, they offer a large surface to volume ratio, which allows an effective temperature control and a high mass transfer rate [7]. The works on Taylor flow from Gunther et al. [8, 9] highlight a recirculation pattern in the liquid slugs. This mixing is important to ensure renewal of the gas-liquid interface and to guarantee satisfactory mixing between the reagents and the catalyst, both of which enhance the mass transfer [10]. A thin liquid film appears between the bubble and the walls of the channel. The drainage of this film is small in comparison to the rate of flow and ensures low axial dispersion between the slugs [10], which is an important feature for a catalytic reactor.

1.2.2 Main dimensionless numbers

1.2.2.1 Reynolds number

The Reynolds number Re represents the ratio of inertial to viscous forces. Different definitions of Re exist, depending on the velocity used. The most common definition uses the velocity of the two phases $U_{TP} = U_L + U_G$. Here, however, a Re number is defined for each phase, based on the superficial velocity of the phase and the hydraulic diameter of the channel. The reason why a separate Re number is used for each phase comes from the large velocity ratios can exist between the gas and liquid. The definitions are given below:

$$Re_L = \frac{\rho_L \, U_L \, d_h}{\mu_L} \qquad Re_G = \frac{\rho_G \, U_G \, d_h}{\mu_G} \tag{1.1}$$

ρ is the density of the phase ($\mathrm{kg\,m^{-3}}$), μ its dynamic viscosity ($\mathrm{Pa\,s}$), U its superficial velocity ($\mathrm{m\,s^{-1}}$) and d_h the hydraulic diameter (m) of the channel.
The superficial velocity is given by the volumetric flowrate, for example:

$$U_{G,L} = \frac{Q_{G,L}}{A} \tag{1.2}$$

where $Q_{G,L}$ is the volumetric flowrate ($\mathrm{m^3\,s^{-1}}$) of the gas or liquid, and A is the cross-section of the channel ($\mathrm{m^2}$).

The hydraulic diameter is given by the wetted perimeter and the section of the channel:

$$d_h = \frac{4A}{Per_{\text{wetted}}} \tag{1.3}$$

The wetted perimeter Per is the perimeter where the fluid is in contact with the wall.
The Taylor flow regime is established for specific values of superficial velocities corresponding to low Reynolds numbers. When Re increases, the flow is evolving from Taylor to slug-annular, churn or bubble flow, depending on which superficial velocity is increased.

1.2.2.2 Weber number

The Weber number We represents the ratio of inertial to surface tension forces. It is calculated for both phases:

$$We_L = \frac{\rho_L U_L^2 d_h}{\sigma} \qquad We_G = \frac{\rho_G U_G^2 d_h}{\sigma} \tag{1.4}$$

Where σ is the surface tension coefficient ($\mathrm{N\,m^{-1}}$).

1.2.2.3 Capillary number

The capillary number represents the ratio of the viscous to surface tension forces. It can also be viewed as the ratio We/Re. Usually, Ca is defined for each phase as follows:

$$Ca_{G,L} = \frac{\mu_{G,L} U_{G,L}}{\sigma} \tag{1.5}$$

At low capillary number, $Ca \approx 1e-02$, the capillary effects become dominant. The flow is then surface tension dominated.
A bubble capillary number is usually defined considering the bubble velocity U_B and the liquid viscosity:

$$Ca_B = \frac{\mu_L U_B}{\sigma} \tag{1.6}$$

1.2.2.4 Bond number

The Bond number, also called Eötvös number, represents the ratio of the gravitational to surface tension forces. It is an important ratio in microchannel flows because it shows the relative impact of the gravity.

$$Bo = \frac{\Delta\rho\, d_h^2\, g}{\sigma} \tag{1.7}$$

In the conditions of the study, the gravitational forces are negligible in comparison to the capillary forces. Besides, due to a small hydraulic diameter, the Bo is much smaller than unity. Negligible gravitational forces mean that their contribution can be neglected in the simulations.

1.2.2.5 Sherwood number

The Sherwood number Sh is the ratio of mass transfer from advection over mass transfer from diffusion. Correlations giving Sh allow the calculation of the mass transfer coefficient through:

$$Sh = \frac{K_L\, L}{D} \tag{1.8}$$

K_L is the global mass transfer coefficient on the liquid side expressed in $\mathrm{m\,s^{-1}}$, L is a characteristic length, and D is the diffusion coefficient ($\mathrm{m^2\,s^{-1}}$). Different approaches exist. Equation 1.8 defines a global Sh number, which corresponds to a global mass transfer coefficient. One can also calculate a local Sh that will give a local k_L. The result is local or global depending on the quantities used in the Sh definition. Numerical simulations provide local quantities, such as the velocity field, and these can be used to compute a local Sh field, which gives an idea on where and how the mass transfer takes place.

1.2.2.6 Schmidt number

The Schmidt number Sc is the ratio of the kinematic viscosity to the mass diffusivity. By analogy to transport phenomena, the kinematic viscosity can be seen as a diffusivity coefficient for momentum [11]. It is defined as:

$$Sc = \frac{\nu}{D} \tag{1.9}$$

ν is the kinematic viscosity ($\mathrm{m^2\,s^{-1}}$). This number is often used in combination with the Re in correlations calculating Sh.

1.2.2.7 Péclet number

The Péclet number is the ratio of advective to diffusive transfer. It can be written for both mass or heat transfer using a length scale L and a velocity scale U. For mass transfer it is

expressed as:

$$Pe = \frac{L\,U}{D} = Re \cdot Sc \tag{1.10}$$

A large Péclet ($Pe \gg 1$) indicates a diffusion dominated transfer. The ranges of Pe can differ a lot depending on the system. In liquids, diffusion coefficients tend to be several orders of magnitude smaller.

1.2.2.8 Hatta number

The Hatta number is the ratio of mass transfer through an interface to the rate of reaction consuming the reagent. It is based on power law kinectics:

$$Ha = \delta \sqrt{\frac{k\,C^{n-1}}{D}} \tag{1.11}$$

C is the concentration of the reagent, n is the order of the reaction, k is the rate constant and δ the interface thickness. If Ha is small ($Ha < 1e-03$), the reaction is slow and the reagent will have time to cross the interface and migrate to the bulk. On the other hand if Ha is large ($Ha > 3$), the reaction is so fast that the reagent is consumed as soon as it crosses the interface. This number is widely used in chemical engineering to determine which of mass transfer or chemical reaction is the rate determining step.

1.2.3 Hydrodynamics of Taylor flows

1.2.3.1 Liquid film

One of the most studied aspects of Taylor flows is the liquid film between the wall and the bubbles. The study of this kind of flow started in the 20th century when Fairbrother et al. [12] wanted to determine whether it was possible to measure the velocity of a flow in a capillary by measuring the velocity of a bubble carried by this flow. However, the authors found that there is a difference between the bubble velocity and the liquid velocity. This difference is linked to the wetting film surrounding the bubble. As the bubble moves, the film is drained to the end of the bubble and joins the rear. Finally, a part of the liquid is not moving forward but backward and this results in a mean velocity of the liquid that is smaller than that of the bubble. The difference between the apparent velocity of the liquid, which is hypothetically that of the bubble, and the real velocity depends on the film thickness. However, the experiments of Fairbrother et al. [12] were limited to cases where

this difference in velocities was small. The authors proposed a relationship based on the relative difference in velocities:

$$m = \frac{U_{\text{bubble}} - U_{\text{liquid}}}{U_{\text{bubble}}} \tag{1.12}$$

The relationship states that m is proportional to the square root of the capillary number:

$$m = 1.0 \sqrt{\frac{\mu\, U_{\text{liquid}}}{\sigma}} = 1.0 \sqrt{Ca} \tag{1.13}$$

Where μ is the viscosity (Pa s), U_{liq} the velocity of the surrounding liquid (m s^{-1}) and σ the surface tension coefficient (N m^{-1}). We kept the formulation of the authors writting the 1.0 constant in front of the square root [12]. Unfortunately, this relationship is only valid for values of $Ca < 0.015$. Taylor [13] validated this experimental correlation, and extended it to a wider range of velocity differences, up to $m = 0.09$ and for values of $0.015 < Ca < 2$. Taylor also studied the motion of the liquid in the slugs between the bubbles. Bretherthon [14] then refined the relationship as:

$$m \approx 1.29\,(3\mu\, U/\sigma)^{\frac{2}{3}} \tag{1.14}$$

This relationship is accurate within 5% if $Ca < 0.003$. More recently, Aussilous and Quéré [15] extended Bretherton's law. They established that $\delta/d_c = 1.34\,Ca^{2/3}$, with δ the film thickness and d_c the channel diameter. Bretherthon's law is only valid for film thicknesses negligible compared with the channel diameter, i.e for small m values. The improved relationship has been obtained by fitting experimental data:

$$\frac{\delta}{d_c} = \frac{1.34\ Ca^{2/3}}{1 + 1.34 \times 2.5\ Ca^{2/3}} \tag{1.15}$$

In our case, $Ca \sim 10^{-4}$, leading to a film thickness of a few microns.

1.2.3.2 Bubble formation

There are three main formation regimes: dripping, jetting and squeezing. In the case of Taylor flow, it is the squeezing regime involved because of the typically low values of capillary numbers involved ($Ca < 10^{-2}$). According to Garstecki and coworkers [16], there are four main stages during the squeezing. First, the tip of the forming bubble enters the main channel, then the bubble growths until the bubble completely blocks the main channel. Afterwards, the bubble elongates in the downstream direction until the final stage, when the neck of the bubble that connects it to the inlet finally thins and breaks. In the last step of the formation, the neck is constrained faster than in the second step, leading to its thinning.

Van Steijn et al. [17] used μ-PIV to study the formation of segmented flow in T-junction. The authors used a square microchannel to estimate the leakage flow and the stages of the bubble formation. Kolb et al. [18] compared capillaries of square and circular cross-sections. They concluded the difference between square and circular microchannels was increasingly important as Ca decreases. The authors explained that the surface tension force becomes even more dominant at low Ca, leading to an increasing contribution of flow at the corners of the channel. The leakage flowrate is therefore increasing, leading to a change in the final shape of the bubble. Yao et al. [19] studied the effect of the pressure on hydrodynamics. They found a decrease in the bubble generation frequency when the pressure increases. The formation phase has an important role in the mass transfer. In recent studies, the authors have reported the contribution of the bubble formation stage to the total mass transfer. Using a colorimetric method, Yang et al. [20] observed that up to 64% of the mass transfer contribution was due to the formation. The same trend was found by Deleau et al. [21], where 20% of the equilibrium concentration was reached during the formation stage.

1.2.3.3 Bubble length

Garstecki et al. [16] developed a scaling relationship giving the length of the slug for the squeezing regime. They used a side-junction device described in [22] to derive the relationship:

$$\frac{L_B}{W} = c_1 + c_2 \frac{Q_G}{Q_L} \tag{1.16}$$

Where L_B is the length of the bubble (m), W is the width of the channel (m), and Q is the volumetric flowrate of the gas or the liquid ($\mathrm{m^3\,s^{-1}}$). The two constants c_i are of the order of unity and are dependent on the shape of the T-junction. The derivation of this scaling law comes from the analysis of characteristic times. It is based on the time required for the continuous phase to compress the bubble until it breaks. During this compression stage, the amount of dispersed phase flowing in the main channel can be estimated from the dispersed phase flow-rate (gas here) Q_G. From this amount of dispersed phase and the T-junction geometry, the length of the bubble can be deduced.
In their study, van Steijn et al. [17] used the relationship from Garstecki et al. to predict the length of the bubble. They derived the two constants for a square microchannel of 800 µm as $c_1 = 1.5$ and $c_2 = 1.5$. The main difference introduced by van Steijn and coworkers is the notion of leakage flowrate. In a square cross-section T-junction, a part of the liquid flows in the corners of the channel, and does not contribute to the bubble compression and squeezing. The new scaling law includes this partially compressed bubble and adjusts the characteristic

time of the bubble growth. Later, Völkel [23] proposed a scaling law predicting the length of the liquid slug:

$$\frac{L_S}{W} = c_2 + c_1 \frac{Q_L}{Q_G} \tag{1.17}$$

However, the coefficients where found to be different from the ones of the bubble length scaling law. Abadie [24] proposed a different scaling law based on the unit cell length (length of the bubble plus the liquid slug):

$$\frac{L_B}{L_B + L_S} = \frac{\frac{U_G}{U_L}}{\beta + \frac{U_G}{U_L}} \tag{1.18}$$

The value of β was found to be dependent on the shape of the microchannel. In his study, Abadie [24] has reported a value of 0.6 for β. However, the ranges of Ca and Re used for the experiments was wide, with $10^{-4} < Ca < 10^{-1}$ and $0.1 < Re < 231$. Martin et al. [25] and Kamaleddine et al. [26] have reported higher values of β, 0.83 and 0.84 respectively. It is most likely due to the narrower range of Ca and Re used in their study $1.6.10^{-2} < Ca < 4.5.10^{-2}$ and $29 < Re < 61$. Both studies [25, 26] worked on T-junctions under pressure.
Another phenomenon could affect the length of the bubble: the pressure drop. Assuming an ideal gas at constant temperature, the product of the volume by the pressure is constant. Hence, if the pressure drops, the volume increases. As the bubble fills almost entirely the channel, the bubble will elongate. However, Yao et al. [27] showed the impact of the pressure drop on the length was negligible.

1.2.4 Mass transfer estimation for Taylor flows

Since the beginning of the study of Taylor flows, a lot of work has been devoted to the development of empirical relations between the mass transfer coefficient $k_L a$ and the film thickness, the superficial velocities, or other flow parameters. Irandoust and Anderson [28] studied on the hydrogenation of 2-ethyl-hexanal in a monolithic catalyst reactor. They studied how mass transfer influenced the reaction. They concluded that the Taylor flow enhances the mass transfer due to its high interfacial area.
In a more recent study, the same authors have proposed a relationship for $k_L a$ [10]. They assumed a cylindrical gas bubble with hemispherical caps. The mass transfer was separated into two contributions, (i.e. the transfer from the liquid film and from the hemispherical caps) and was calculated both experimentally and theoretically. Irandoust et al. used the

formulation for the film thickness given by Irandoust and Anderson [29]:

$$\delta = 0.18\, d_t \left[1 - \exp\left[-3.1 \left(\frac{\mu\, U}{\sigma}\right)^{0.54}\right]\right] \tag{1.19}$$

Where d_t is the cylindrical tube diameter, in that case equal to the hydraulic diameter. The numerical constants where obtained by least-squares fitting. The velocity used in this correlation should be the same as that used to calculate the Ca number, to keep the same reference velocity. To obtain the mass transfer through the liquid film, these authors derived a mass balance over the dissolved species. A coordinate system is defined such that the bubble is fixed, and the wall is moving. After resolution, Irandoust and Anderson [29] give the following relationship for the concentration in the liquid film:

$$\frac{C_m - C_0}{C^* - C_0} = \left[\int_0^\delta \left(\frac{2(R - \delta + x)}{2R - \delta}\right)\left(\frac{C(z = L_c, x) - C_0}{C^* - C_0}\right) dx\right] / \delta = y_m \tag{1.20}$$

Where R is the tube radius (m), C is the dissolved concentration of the species considered ($\mathrm{mol\,m^{-3}}$), C^* is the equilibrium concentration ($\mathrm{mol\,m^{-3}}$), C_0 is the initial concentration of the species ($\mathrm{mol\,m^{-3}}$), L_c is the length of the gas bubble (m), finally x is the distance in the film between the interface and the wall (m).
The molar flux is then expressed:

$$N_{film} = \Big(\pi\ \delta(d_t - \delta) U_{av}\ y_m\Big)\,(C^* - C_0) \tag{1.21}$$

Where U_{av} is the average velocity in the liquid film ($\mathrm{m\,s^{-1}}$).
The caps were treated as rigid hemispheres by Irandoust and Anderson [29]. For these spheres, it is possible to define a Sherwood number to express the mass transfer:

$$\text{If} \quad 1 \leq Re \leq\ 400: \quad (Sh - 1)Sc^{1/3} = (1 + 1/(Re\, Sc))^{1/3} + Re^{0.41} \tag{1.22}$$

$$\text{If } 100 \leq Re \leq 2000: \qquad Sh = 1 + 0.724 Re^{0.48} Sc^{1/3} \tag{1.23}$$

The definition of the mass transfer flux through the caps is then:

$$N_{caps} = (\pi\ D\ Sh\ d_B)(C^* - C_0) \tag{1.24}$$

The total mass transfer flux is the sum of the two contributions:

$$N_{tot} = N_{film} + N_{caps} = \pi \Big(\delta(d_t - \delta) U_{av}\, y_m + D\ Sh\ d_B\Big)\,(C^* - C_0) \tag{1.25}$$

Finally, the relationship for k_La reads:

$$k_La = 4\ \frac{\delta(d_t - \delta)U_{av}\, y_m + D\ Sh\ d_B}{d_t^2(L_l + L_g)} \tag{1.26}$$

where L_l and L_g are the lengths of the slug and bubble (m).
Berčič and Pintar [30] developed an empirical relationship between the superficial velocity of both phases, the gas hold-up and the length of a unit cell. The resulting global volumetric mass transfer coefficient was expressed as:

$$K_La = \frac{(U_G + U_L)^{1.19}}{((1 - \epsilon_G)L_{UC})^{0.57}} \tag{1.27}$$

The powers indicies were determined by fitting experimental data, and therefore hide the physical phenomena. Nevertheless, their results indicate that mass transfer mainly depends on the liquid slug length and the velocity. They also found that the liquid film contribution to overall mass transfer is not dominant. More recent studies focus on techniques that enable quantification of local fields at the unit cell scale. Among these techniques, we can cite photographic measurement of bubble volume change, planar laser induced fluorescence with inhibition (PLIF-I) or particle image velocimetry (PIV) described by Santiago et al. [31]. Imaging of the flow, inlcuding X-ray imaging, gives the time varying volume of the bubble, which can then be linked to the mass transfer by deriving a mass balance over the unit cell at constant pressure. In their work, Haghnegahdar et al. [32] used this technique to obtain the time variations of the volume, the interfacial area and the bubble length. The authors provided a new correlation for the calculation of the Sherwood number that is more suitable for small pipes.
The PLIF technique measures the local concentration of a dissolved species. The fluorescence of a dye is induced by a laser, the dissolved species resonates and its concentration can be monitored. PLIF-I works on the inhibition of the dye by a dissolved species. Numerous authors have applied this technique to monitor mass transfer in gas-liquid systems. We can cite Dani et al. [33] , Valiorgue et al. [34], Jimenez et al. [35] and Häber et al. [36] who worked with the PLIF technique in different configurations. Butler et al. [37] used this technique to follow mass transfer in Taylor flow in a millimetric channel. They compared their experimental volumetric mass transfer coefficient k_La to that from correlations found in the literature. Butler et al. found the relationship proposed by Van Baten and Krishna [38] was unable to predict the coefficient in case of small liquid slugs. The authors concluded that numerical simulations will be used in future work to predict the film contribution more accurately. Indeed, the local velocity in the liquid film can be resolved with a fine mesh, giving

access to a better prediction according to [37]. Recent advances in numerical simulation have opened a new opportunity for the elaboration and testing of experimental correlations. Van Baten and Krishna [38] decided to reproduce the results of Berčič and Pintar [30] with CFD simulations. They started with a simple model by dividing the mass transfer into two parts as was done by [10]. The contribution of the film on the one side and the contribution of the hemispherical caps on the other side. The main difference with the work of Irandoust et al. lies in the coefficients preceding the square roots. The mass transfer coefficient for the hemispherical caps is based on Higbie's penetration model [39] while the coefficient for the film is calculated through the falling film model. The global mass transfer coefficient is described as the sum of these two contributions. They numerically investigated the values of $K_L a$ and found a good agreement with experiments for small channel diameters (1.5mm). The equations used in their work are given below. The contribution relative to the two hemispherical caps being:

$$K_{Lcap} = 2\sqrt{\frac{2\,D_{diff}\,U_b}{\pi^2\,d_t}} \tag{1.28}$$

And the contribution relative to the liquid film:

$$K_{LF} = \sqrt{\frac{D_{diff}\,U_b}{\pi\,t_F}} \tag{1.29}$$

Where D_{diff} is the diffusivity of ethylene in cyclohexane, d_t is the tube diameter, U_b is the bubble velocity, and t_F is the contact time at the liquid film.

Nevertheless, capillaries with larger diameters diverge from the correlation in case of high bubble velocities. Yue et al. [40] have reported volumetric mass transfer coefficients that are much lower than the ones given by van Baten and Krishna [38]. Yue et al. have explained the poor agreement by the difference in short film contact time. The resulting mixing between the liquid film and liquid slug was not sufficient to comply with the assumptions of the model of van Baten and Krishna.

Kamaleddine [41] presented a mass transfer study in gas-liquid Taylor flow. After a hydrodynamics study, the same operating conditions were used to determine the mass transfer coefficient k_L and the volumetric mass transfer coefficient $k_L a$. The objective of this study was to determine whether the microchannel reactor was suitable for an oligomerization reaction. To be so, the mass transfer coefficient had to be comparable or higher than that determined in a stirred tank reactor. If the mass transfer coefficient is too small, then the reaction is limited by mass transfer and the reactor is not operated in "chemical regime". The study reports mass transfer coefficients in the range of 0.1 to 0.6 s^{-1}, which are of the same order of magnitude than what was found by [42] in their study of mass transfer coefficients in

stirred tank reactors. Based on these results, it can be considered that the reaction was not limited by mass transfer and the Taylor fow microreactor should be suitable to conduct the reaction. Kamaleddine compared the volumetric mass transfer coefficient predicted with the correlations from [38] and [40] and reported a better prediction of experimental data using the relationship from Yue et al. [40].

1.3 Governing equations

The Navier-Stokes equations, namely the mass conservation and the momentum conservation are used to solve the flow and determine the fluid velocity and pressure for each time and each position. The momentum conservation, which is the relationship between the pressure and the velocity of the fluid, is essentially a force balance and can be represented by Newton's second law. On the other hand, the mass conservation for an incompressible flow reduces to a restriction of the fluid velocity. The equations for an incompressible, isothermal, Newtonian fluid are given below:
The mass conservation:

$$\nabla \cdot U = 0 \tag{1.30}$$

The momentum conservation:

$$\frac{\partial U}{\partial t} + \nabla \cdot (UU) = \nabla \cdot (\nu \nabla U) - \nabla P + g + F_\sigma \tag{1.31}$$

ν is the kinematic viscosity, g is the gravitational acceleration. P is indeed p/ρ, where p is the pressure expressed in Pa. In case of multiphase flow, an interface between the phases appears and is characterized by the surface tension force. It may not be represented in the general form of the Navier-Stokes equations but it can be included as a source term in the equation for two-phase flows. The surface tension force F_σ is expressed as a source term per unit of volume in the momentum equation [43]:

$$F_\sigma = \sigma \kappa \nabla \alpha$$

with σ ($\mathrm{N\,m^{-1}}$) the surface tension coefficient, κ the interface curvature ($\mathrm{m^{-1}}$) and α the volume fraction of the liquid phase.
In most cases, an isothermal hypothesis is no longer valid in case of chemical reaction. An exothermic reaction will release heat in the system. Whilst, an endothermic reaction needs energy and it will operate as a heat sink. However, depending on the size of the system,

the temperature can be controlled and isothermal conditions may be justified. Including the energy equation in the simulation can be done at several levels. Regarding the variation of the fluid properties with temperature, one can decide not to predict their change and use constant values for the operating conditions. This choice is justified if the change of temperature in the system is moderate or if the fluid properties do not change much over the range of temperature studied. In this case, the energy equation can be solved as a simple passive scalar transport after the pressure-velocity coupling. On the other hand, if the fluid properties are strongly dependent on temperature, their run time prediction using the local temperature field might become compulsory. The energy conservation in terms of temperature for a pure Newtonian incompressible fluid with constant density can be written as:

$$\rho C_p \frac{\partial T}{\partial t} + \rho C_p U \cdot \nabla(T) = \nabla \cdot (k \nabla T) + S_V \tag{1.32}$$

Where C_p is the calorific capacity per unit mass at constant pressure ($\mathrm{J\,K^{-1}\,kg^{-1}}$), k is the thermal conductivity ($\mathrm{W\,m^{-1}\,K^{-1}}$) and S_V represents a volumetric source term ($\mathrm{W\,m^{-3}}$). A model for each temperature dependent variable is needed to solve the energy equation with varying fluid properties. In most cases, there is no theoretical derivation of the temperature model for these properties. The choice is then made between empirical relations based on experiments or semi-empirical models based on motion theories for example. The models available for the fluid properties will be described in section 4.2.1 and their implementation in OpenFOAM® will be addressed separately. Finally, the last equation presented here is the transport of a chemical species. In two-phase flows, mass transfer usually occurs between the two phases, particularly when they are not in equilibrium. The difference of chemical potential of a species will act as a driving force, leading to phase change whilst the equilibrium is not reached. In dilute conditions, Fick's law is used to express the motion of species i based on the concentration gradient:

$$\frac{\partial C_k}{\partial t} + \nabla \cdot (\mathbf{U} C_k) = \nabla \cdot (D_k \nabla C_k) + R_k \tag{1.33}$$

Where C_k is the concentration per unit mass ($\mathrm{kg\,m^{-3}}$) or mole ($\mathrm{mol\,m^{-3}}$), D_k is the diffusion coefficient ($\mathrm{m^2\,s^{-1}}$) and R_k is a volumetric rate of production or decay ($\mathrm{kg\,m^{-3}\,s^{-1}}$ or $\mathrm{mol\,m^{-3}\,s^{-1}}$). The equation 1.33 expresses the motion of the species transported and diffused by the flow, with a production or consumption source term. It can be applied to both phases but, unfortunately, it does not include the thermodynamic constraint on the species concentration. The concentration jump of a species at the interface is directly linked to its saturation in the accepting phase. Most of the time, there is a discontinuity of concentration at the interface and only the chemical potentials are equal on both sides of the interface at

equilibrium. Usually, the fugacity f_k is defined from the chemical potential μ_k for species k as follows:

$$\mathrm{d}\mu_k = RT \ \mathrm{d}\ln f_k \tag{1.34}$$

Where μ_k is the chemical potential of species k, T is the temperature and R is the ideal gas constant. For a species k at equilibrium between the gas and the liquid, there is equality of fugacities:

$$f_k^L = f_k^G \tag{1.35}$$

Using equation 1.35, and replacing the expression of the fugacities in each phase, we can express the equilibrium:

$$y_k \phi_k P = x_k \gamma_k f_k^{L,*} \tag{1.36}$$

Where y_k is the gas molar fraction of the species, x_k its liquid molar fraction, P the pressure of the gas phase (Pa) and γ_k is an activity coefficient of the solute k in the solvent. γ_k is used to correct the pure component fugacity $f_k^{L,*}$ whilst ϕ_k corrects the deviation from the ideal gas law. Some assumptions are often made to simplify the resolution. The activity coefficient is either predicted (with Margules's law for example) or taken to be unity. Similarly, at low pressures, the deviation from ideality of the gas phase is often neglected. The final law is then rewritten:

$$y_k P = x_k H_{k,S} \tag{1.37}$$

$H_{k,s}$ the Henry's law constant for the solute k in the solvent s (Pa). The full derivation for a binary system is available in Landau & Lifshniz [44]. For the application studied here, the simplified form 1.37 will be considered and used to determine the saturation concentration of a species of the gas phase in the liquid. Note that the base assumption of Henry's law is the dilution of the species. For the level of precision required here and for the sake of ease of implementation, the ultimate expression of the partition coefficient is as follows:

$$H_{k,S} = \frac{C_{k,G}}{C_{k,L}} \tag{1.38}$$

1.4 Modeling approaches

1.4.1 The Finite Volume Method

Different concepts, namely the Finite Difference Method (FDM), Finite Volume Method (FVM) and Finite Element Method (FEM) offer a framework for the numerical resolution of

the Navier-Stokes equations. The main idea behind all these approaches is the same. Firstly, one needs to discretize the spatial domain. The space is divided in subparts: nodes for the FD method, cells for the FV. This step is necessary to convert the continuous space into a storable and computable geometry. The partial differential equations are then discretized, to be able to express the conservation laws in a way the computer can iterate and solve the equations. It is the way of describing the conservation that changes from one method to another.

The majority of CFD software are FVM based codes, including OpenFOAM®, and we will only focus on this method here. The discretization of the domain consists of a grid of a finite number of control volumes (CV). Usually, the centre of this CV is set to be the computational node, i.e. where the computed values are stored. OpenFOAM® relies on this choice, so called a cell-centered formulation. On each CV, the conservation equation of a quantity is applied. Summing all the volumes leads to the global form of the conservation equation: the closed integrals over the boundaries of each CV cancel out [45].

Let's consider the general equation for the transport of a scalar ϕ:

$$\frac{\partial \rho\phi}{\partial t} + \nabla \cdot (\rho U\phi) = \nabla \cdot (\rho\Gamma\nabla\phi) + S(\phi) \tag{1.39}$$

Where Γ is a diffusion coefficient related to the quantity ϕ and $S(\phi)$ is a volumetric source term. The equation is then integrated over a control volume and over time:

$$\int_{CV}\left(\int_{t}^{t+\Delta t}\frac{\partial \rho\phi}{\partial t}dt\right)dV + \int_{t}^{t+\Delta t}\left(\int_{A} n\cdot(\rho U\phi)dA\right)dt = \int_{t}^{t+\Delta t}\left(\int_{A} n\cdot(\rho\Gamma\nabla\phi)dA\right)dt + \int_{t}^{t+\Delta t}\int_{CV} S(\phi)dV\,dt \tag{1.40}$$

For this, integrals of the transient term are inverted and Green-Gauss theorem is used to transform the volume integral of the divergence into the surface integral of the flux. The approximation of the surface integral is of major importance for the overall precision. Usually, the midpoint rule stating that the integral is equivalent to the mean value of the face variable multiplied by the surface of the face is used. We can approximate this product by the value at the centre of the face f multiplied by the face area:

$$\int_{A} \phi\ dA \approx \phi_f A_f \tag{1.41}$$

Unfortunately, the value of ϕ at the face centre f is not known. Thus, face value ϕ_f must be obtained from interpolation of the cell-centered value. A high order interpolation must be used to preserve the accuracy. In most numerical codes, a weight w is computed on each face depending on the selected scheme. This weight is then used to compute the face value

ϕ_f with respect to the two cell centered values ϕ_P and ϕ_N:

$$\phi_f = \phi_N + w(\phi_P - \phi_N) \tag{1.42}$$

We will now consider the steady state diffusion of a property ϕ in a one-dimensional domain. The motion of ϕ can be described with the diffusion coefficient and a source term as follows:

$$\frac{d}{dx}\left(\Gamma\frac{d\phi}{dx}\right) + S = 0 \tag{1.43}$$

Consider a node P with neighbours E and W, sharing respectively the faces e and w:

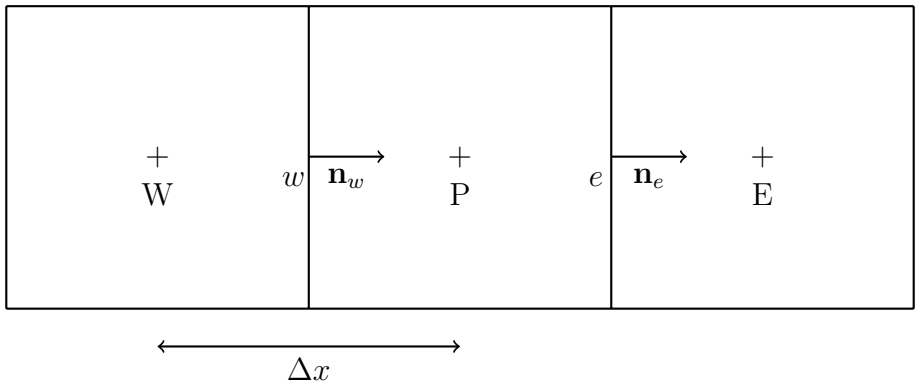

FIGURE 1.1: Simple 1D uniform structured stencil for the integration of the diffusion equation

The volume (in one dimension) will be set to Δx. Integrating equation 1.43 over the control volume yields:

$$\int_{CV} \frac{d}{dx}\left(\Gamma\frac{d\phi}{dx}\right) dV + \int_{CV} S dV = \left(\Gamma A\frac{d\phi}{dx}\right)_e - \left(\Gamma A\frac{d\phi}{dx}\right)_w + \overline{S}\Delta V = 0 \tag{1.44}$$

with A the cross-sectional area of the control volume face (considered constant in the whole domain for this example), ΔV its volume (here Δx, also constant) and $\overline{S}$ the volume averaged value of S on the control volume. To move forward in the resolution, the diffusive flux at the control volume faces must be evaluated. The diffusion coefficient Γ is often calculated as the mean value between the two nodes, for example at face w:

$$\Gamma_w = \frac{\Gamma_W + \Gamma_P}{2} \tag{1.45}$$

The gradient of ϕ on the face is also required. Using a linear approximation the diffusive flux on faces e and w can be expressed as follows:

$$\left(\Gamma A \frac{d\phi}{dx}\right)_e = \Gamma_e A_e \left(\frac{\phi_E - \phi_P}{\Delta x}\right) \tag{1.46}$$

$$\left(\Gamma A \frac{d\phi}{dx}\right)_w = \Gamma_w A_w \left(\frac{\phi_P - \phi_W}{\Delta x}\right) \tag{1.47}$$

The last term remaining is the source term. Since it may depend on the variable ϕ, it is expressed as a linear relationship:

$$\overline{S}\Delta V = (S_u + S_p \phi_P)\Delta x \tag{1.48}$$

After manipulation of equation 1.44, it can be written as:

$$\left(\frac{\Gamma_e + \Gamma_w}{\Delta x} A - S_p\right) \phi_P = \left(\frac{\Gamma_w}{\Delta x} A\right) \phi_W + \left(\frac{\Gamma_e}{\Delta x} A\right) \phi_E + S_u \tag{1.49}$$

Usually, the coefficients are gathered is a simplified form such as:

$$a_P \phi_P = a_W \phi_W + a_E \phi_E + S_u \tag{1.50}$$

This new formulation is interesting because it gives the variation of the quantity ϕ in a cell with respect to its neighbours. The variations of ϕ in the whole domain can be seen as a linear system and can be represented as follows:

$$Ax = b \tag{1.51}$$

If n is the size of the computational grid, $A = [a_{ij}]$ is an $n \times n$ matrix. It contains the coefficients a_P for each cell on the diagonal. The first and last terms of the diagonal have to consider the boundary conditions. For a structured one-dimensional domain, only the upper and lower diagonals have non-zero elements. For a structured two-dimensional domain, each cell has four neighbours. Therefore, there are non-zero terms not only on the lower and upper diagonals. For a structured three-dimensional domain there are six non-zero terms on a row, outside the diagonal. Of course, depending on the scheme used for the discretization, this number can be higher. A scheme with a wider stencil could use the values not only from the neighbouring cells but also one cell further. Given the matrix and the method used to solve the system, pre-conditioning might be necessary. Finally, the vector of unknowns x is of dimensions $n \times 1$. It contains the values of ϕ in each cell of the mesh. Finally, the second member b, on the right-hand side, contains the source term S_u. Solving the system will give

the solution vector x. To do so, a linear solver has to be chosen, which will depend on the matrix and its sparsity [46]. The system can be solved either with an iterative procedure or a direct method. For direct methods, the matrix is factorized into easily invertible matrices. Direct methods are very interesting when robustness is of concern. However, they do not scale up very well with an increasing number of equations and unknowns. For this reason, iterative methods are now widely used to solve partial differential equations. Iterative procedures gather very different methods under the same designation. We can cite the Jacobi, Gauss-Seidel or Krylov subspace methods for example, see [47].

1.4.2 Solving the Navier-Stokes equations

Once the FVM has been described, one may wonder how it can be applied to solve the incompressible flow Navier-Stokes (NS) equations in OpenFOAM® . As there are two coupled equations (momentum and continuity), we need a way to consider their interactions to solve the system. This results in coupled variables, namely pressure and velocity, that need to be solved simultaneously in a so called pressure-velocity coupling algorithm. The coupling is either done through the SIMPLE algorithm for steady problems or PISO algorithm for transient ones. The SIMPLE algorithm stands for Semi-Implicit Method for Pressure Linked Equations and was described by Spalding and Patankar. An overview is given in the work of Patankar [48]. For transient problems, one can use the PISO algorithm, standing for Pressure Implicit with Splitting of Operators, initially described by Issa [49]. These two algorithms are formulated implicitly. Implicit methods have a less strict restriction on the time step and are therefore preferred in most CFD codes. The coupling between pressure and velocity is done iteratively for both methods, which is why iterative methods for the linear solvers presented in section 1.4.1 are more straightforward. In OpenFOAM® , the PISO and SIMPLE algorithms have been combined in an algorithm called PIMPLE.

1.4.3 The Volume of Fluid method

This part aims at presenting the Volume-of-Fluid (VOF) formulation, which will be used to solve the transport of the interface between the phases. To solve a multiphase flow, one must choose between different approaches regarding its needs, the nature of the problem and depending on the scale of the fluid domain. Numerous procedures were detailed to solve two-phase flows with interface capturing, namely, Front Tracking methods [50–54], arbitrary Lagrangian-Eulerian (ALE) [55–57], Level-Set (LS) [58, 59], phase field [60, 61] and also

Volume of Fluid (VOF) [62–68]. Their usage depends on the nature of the problem. In the current simulations we will only be dealing with VOF. This method was developed by Hirt and Nichols [69] and has been designed to study free surface flows that undergo large discontinuities at their interfaces. The method uses an Eulerian description for each phase and a phase indicator function. This means that both phases share a common field of velocity and pressure. The challenges of VOF methods are to avoid smearing of the discontinuity of the interface and to accurately model the surface tension force. The common way to express the surface tension force is the formulation of Brackbill et al. [43] where the surface tension force is converted from a surface force to a volumetric contribution added in the Navier-Stokes equations. The idea of the formulation, called CSF for continuum surface force, is to introduce the curvature of the interface into the force density. A region of finite width is used as a transition zone where the fluid properties will vary continuously from one fluid to the other [43]. This model will be discussed in the next section 1.4.5. Two different classes of VOF methods exist. They differ in the advection of the phase indicator: the algebraic methods use an additional advection equation while the geometric methods reconstruct the interface based on the volume fraction field. More recently, geometric methods have attracted more attention and multiple methods have been released [70–73]. For a while, the CPU time consumption of these methods was a major drawback. However, the new method proposed by Roenby et al. [72] changes the evaluation of the face fluxes, which improves performances. The fundamental benefit of geometric methods over classical algebraic methods is the sharp interface. In the algebraic method of MULES [74], a compression term is added to the advection of the phase indicator to reduce artificially the thickness of the interface. The phase indicator function is defined as:

$$H(\mathbf{x},t) = \begin{cases} 0 & \text{in the gaseous phase} \\ 1 & \text{in the liquid phase} \\ ]0;1[& \text{at the interface} \end{cases}$$

The volume fraction α of the continuous phase for a cell can be derived as follows:

$$\alpha(\mathbf{x},t) = \frac{1}{V_i} \int_{\Omega_i} H(\mathbf{x},t)\,\mathrm{d}V \tag{1.52}$$

where Ω_i represents the cell i and $V_i = \int_{\Omega_i} \mathrm{d}V$ its volume. The volume fraction of the gaseous phase is implicitly defined as $1-\alpha$. The resulting local VOF equation reads:

$$\frac{\partial \alpha}{\partial t} + \nabla \cdot (U\alpha) = 0 \tag{1.53}$$

The issue with algebraic VOF methods and the smearing of the interface have already been widely addressed. Geometric methods, used in combination with a reconstruction algorithm, offer better performances [75]. The Piecewise Linear Interface Construction method will be presented in the following section.

1.4.4 Piecewise Linear Interface Construction

The advection of the interface performed by the VOF algorithm requires a divergence-free velocity field and the volume fraction field at the previous time step. The first step consists in the reconstruction of the interface from the previous time step volume fraction field. This reconstruction will allow the interpolation of the flow variables (mainly the velocity) at the exact position of the interface in geometric methods. The Piecewise Linear Interface Construction (PLIC) methods are known to be the among the most accurate techniques [76–81]. The important feature of PLIC is the absence of connectivity between the interface.

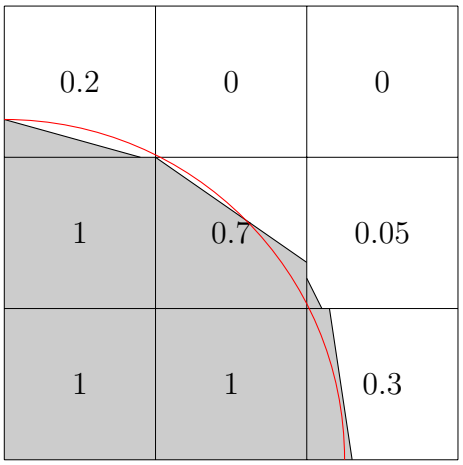

FIGURE 1.2: Two-dimensional example of the reconstructed interface with PLIC

Figure 1.2 shows a theoretical interface in red and the reconstructed PLIC interface in each cell. The volume fractions are only indicative and given to illustrate that the interface does not need to be continuous between cells. PLIC is second order accurate for the reconstruction of the interface [75].

1.4.5 The Continuum Surface Force

At an interface, a difference of pressure exists between the two phases present. This pressure drop, also known as Laplace pressure, is related to the curvature of the interface. When the

interface is not a plane (or a straight line in 2D), a capillary force arises from the curvature and produces this difference of pressure. Numerically, the prediction of the curvature is a difficult task. It is quite straightforward in the case of a circle, as the curvature is equal to the inverse of the radius. On the other hand, for random surfaces (or lines in 2D), an implicit determination is needed. A common way to express the surface force is the formulation proposed by Brackbill et al. [43]. The authors proposed a formulation based on a colour function. Instead of having an infinitely thin interface with a step-wise change of the volume fraction, the colour function is defined to vary smoothly over a region of finite thickness. This formulation allows the conversion of the usual capillary surface force to a volume force. This volume force can then be introduced into the momentum balance as a source term. A natural choice for the colour function is the use of the volume fraction α, especially for VOF simulations where the volume fraction already varies through the interface thickness.
The first step is the expression of the curvature, κ:

$$\kappa = -\nabla \cdot \mathbf{n} \tag{1.54}$$

where $\mathbf{n}$ is the unit normal vector to the surface.
This normal vector can be derived from the volume fraction field as follows:

$$\mathbf{n} = \frac{\nabla(\alpha)}{|\nabla(\alpha)|} \tag{1.55}$$

As mentioned before, the surface tension force is then calculated as the product:

$$F_\sigma = \sigma\kappa\nabla\alpha = -\sigma\nabla \cdot \left(\frac{\nabla\alpha}{|\nabla\alpha|}\right)\nabla\alpha \tag{1.56}$$

One of the main drawbacks of this formulation is the need of the gradient at the interface position. Usually, the gradient of a variable is stored at a cell centre. An interpolation is then required to calculate the gradient at any other location. When dealing with the volume fraction, the exact position of the interface in the cell is generally not computed. The algebraic VOF methods do not explicitly reconstruct the interface from the volume fraction field. The use of the cell centered value instead of the one at the interface induces an error when the force is computed.

1.5 The open-source CFD code OpenFOAM®

1.5.1 OpenFOAM® general description

OpenFOAM® is an open source multi-purpose collection of C++ libraries used for the resolution of partial differential equations involved in very different fields of science. The versatility of an object-oriented language such as C++ allows the user to develop and implement any kind of feature with the help of the already available solvers, function objects or classes. Access to the whole code and the right to create or modify it under the GNU General Public License offers an opportunity to implement and test new ideas. Thus, it is the perfect choice for experimental research work such as the development of a multi-physics solver aiming at resolving complex multiphase reacting flows.

1.5.2 Presentation of multiphase solvers

In OpenFOAM® , the algebraic VOF solver is called `interFoam`. It uses the Multidimensional Universal Limiter for Explicit Solution (MULES). In the case of `interFoam`, the VOF-equation integrates an additional term used to reduce the numerical diffusion by artificially compressing the interface:

$$\frac{\partial \alpha}{\partial t} + \nabla \cdot (U\alpha) + \nabla \cdot [\, U_r \alpha (1-\alpha) \,] = 0 \tag{1.57}$$

Where U_r is the relative or compressive velocity of the interface. The compressive velocity is given by:

$$U_r = \mathbf{n} \left[\min \left(c_\alpha \frac{|\phi_f|}{A_f}, \max_{\Omega} \left(\frac{|\phi_f|}{A_f} \right) \right) \right] \tag{1.58}$$

with ϕ_f the flux on the face ($\mathrm{m^3\,s^{-1}}$), A_f is the surface of the face ($\mathrm{m^2}$) and $\mathbf{n}$ the normal to a face. c_α is a user-specified numerical parameter used to control the compression. A c_α of unity is recommended to avoid numerical smearing of the interface. An in-depth description of `interFoam` can be found in [74].

Recently, a geometric VOF solver has been added to the OpenFOAM® framework, namely `interIsoFoam`. It has been developed by Roenby et al. [72, 73]. The term "Iso" has been added to differentiate this solver from `interFoam`; recall the geometric way of reconstructing the interface as will be presented in section 1.5.3. The last VOF solver available is called `interFlow`. It is an evolution of the `isoAdvector` geometric method and uses the same algorithm for the advection, but the interface reconstruction is different. The solver has

been developed by Scheufler et al. [82]. The authors have made a significant improvement in comparison to `interIsoFoam` in the way of computing the curvature of the interface and the gravity term. Several models have been developed, such as parabolic or height function models. The `interFlow` solver tends to drastically reduce the spurious currents in a solution, which are a known issue when using the volume fraction gradient in the curvature computation. `interFlow` uses the PLIC method to reconstruct the interface, which makes it very reliable on the curvature prediction and thereby generates less spurious currents [83].

1.5.3 The geometric Volume of Fluid method `isoAdvector`

`isoAdvector` is a numerical method developed for the advection of a passive surface. It was implemented in OpenFOAM® to be used in multiphase solvers to advect the interface between two incompressible fluids. Full details on the algorithm are available in [72]. The present section will be used to give some details on the method that will be useful to explain the developments made in this study.
`isoAdvector` introduces two novel features. Firstly, the concept of isosurface is utilized in the reconstruction step. The intersection between the interface and the face (the face-interface intersection line, FIIL) is then updated with time to allow the computation of the face fluxes. The phase indicator function is computed in each cell as:

$$H(\mathbf{x},t) = \frac{\rho(\mathbf{x},t) - \rho_B}{\rho_A - \rho_B} \tag{1.59}$$

The volume fraction is defined exactly as equation 1.52. After some manipulation and integration in time, the new time step volume fraction of cell i is given by:

$$\alpha_i(t+\Delta t) = \alpha_i(t) - \frac{1}{V_f}\sum_f s_{if}\Delta V_f(t,\Delta t) \tag{1.60}$$

In equation 1.60, s_{if} equals $+1$ or -1 depending on the orientation of the face normal $d\mathbf{S}$ appearing in equation 1.61 and ΔV_f is the volume of fluid transported across face f during a time step. It is computed as:

$$\Delta V_f(t,\Delta t) = \int_t^{t+\Delta t}\int_{A_f} H(\mathbf{x},\tau)\mathbf{U}(\mathbf{x},\tau)\ \cdot\ d\mathbf{S}\ d\tau \tag{1.61}$$

To guarantee mass conservation, this "volumetric face flux" is used to update both cells sharing face f.

`isoAdvector` is originally distributed with a reconstruction algorithm called `isoAlpha` [72]. This algorithm is based on the idea of "isosurfaces" i.e. surfaces of the same volume fraction, in the meaning of distribution. The isosurface 0.5 is often used to visualize the concept of interface between to phases. It is the surface that cuts a given cell into two subsets of equal volumes, thus, a volume fraction of 0.5. `isoAlpha` uses the volume fraction field information to find the isovalue that best represents the liquid distribution in each cell. The end of this section will be used to explain how the fluxes are computed. All the details are inspired from the papers of the authors [72, 73].

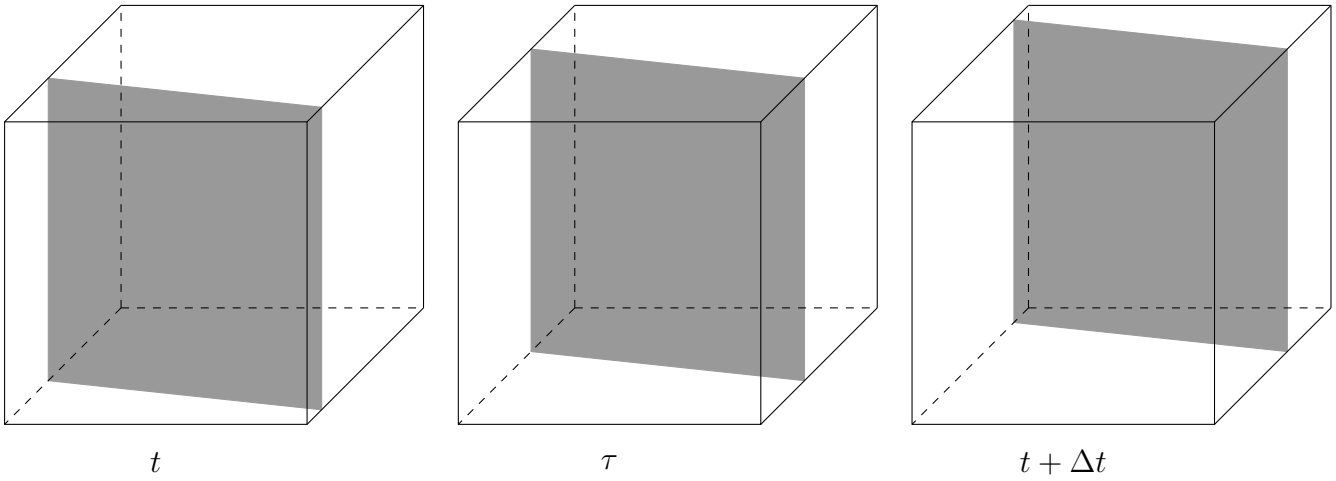

FIGURE 1.3: Advection of a free surface with `isoAdvector` during a time step Δt

Figure 1.3 illustrates a simple case where an interface is moved in a cubic cell. We will now have a look at the top face to describe how the algorithm performs the flux computation.

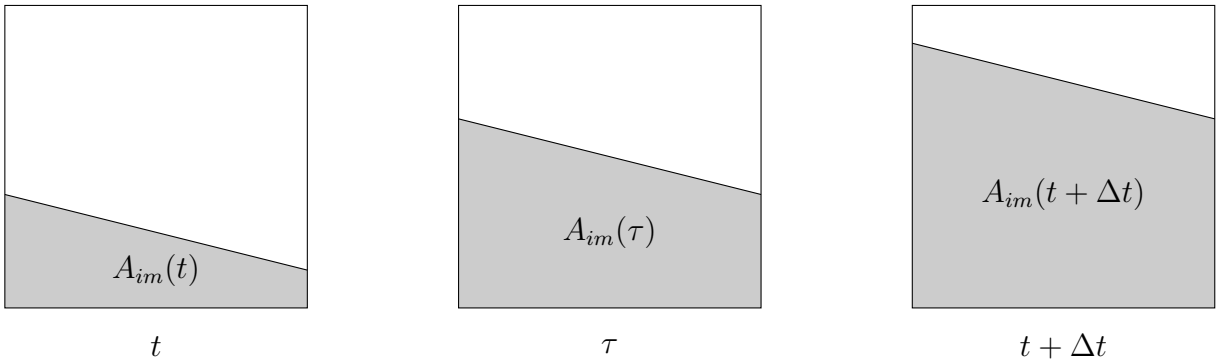

FIGURE 1.4: Liquid immersed part of the top face (A_{im}) during a time step Δt

Figure 1.5 illustrates the time evolution of the interface. The initial area immersed in the liquid phase is given on figure 1.4 by $A_{im}(t)$. During a time step, the area that will be swept by the interface is given by the area of the polygonal $A_{im}(\tau) - A_{im}(t)$. From figure 1.5, we

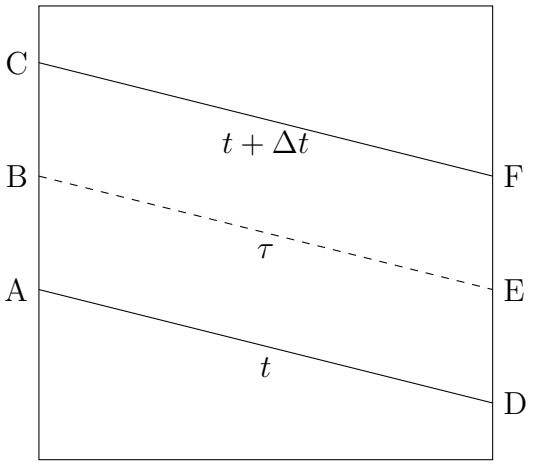

FIGURE 1.5: Illustration for the computation of the liquid immersed area

```
alpha1_.primitiveFieldRef() =
(
        alpha1_.oldTime().primitiveField()*rDeltaT
    + Su.field()
    - fvc::surfaceIntegrate(dVf_)().primitiveField()*rDeltaT
)/(rDeltaT - Sp.field());
```

FIGURE 1.6: `isoAdvector` where the volume fraction field is updated

get:

$$B = A + (C - A)\frac{\tau - t}{(t + \Delta t) - t} \qquad E = D + (F - D)\frac{\tau - t}{(t + \Delta t) - t} \tag{1.62}$$

It is possible to get the area from figure 1.5 with the relationship:

$$A_{im}(\tau) - A_{im}(t) = \frac{1}{2}|AE \times DB| \tag{1.63}$$

After some manipulation, it appears that the time dependent immersed area is a second-order polynomial:

$$A_{im}(\tau) - A_{im}(t) = at^2 + bt + c \tag{1.64}$$

When this second-degree polynomial is integrated over time, it gives a third-degree polynomial, which is quite easy to fit. This volumetric face flux $\Delta V(t, \Delta t)$ is then used to define α_f, which is part of a face that is immersed in the liquid. Considering the divergence free flux from the velocity-pressure solver of face f, F_f, the definition of this liquid immersed part of the face is:

$$\alpha_f = \frac{\Delta V_f}{F_f \Delta t} \tag{1.65}$$

This face value α_f will be used in the future developments.

1.6 Phase change in the Volume of Fluid framework

Recent advances in numerical simulations allow the resolution of more complex multiphysics problems. The numerical simulation of phase change is a very challenging process. However, it allows the simulation of more realistic systems of industrial interest. Multiple articles have dealt with the numerical simulation of mass transfer, using various methods to solve the hydrodynamics. We can cite for example the following works [38, 51, 57, 62, 63, 65, 66, 68, 84–89].

In the context of the current work, the volume of fluid method will be the focus. One of the difficulties of simulating mass transfer is species transport. Since this is performed in a two-phase context, it must be consistent with the method used to advect the free surface. If the transport equation is not consistent with the free surface advection, artificial mass transfer will occur. Artificial mass transfer can be defined as a species transfer occurring because of numerical issues, an incorrect interpolation or any other discrepancy from the free surface advection [66, 86]. Artificial mass transfer is very damaging for the final results. Species flux at the interface depends on the species concentration in the accepting phase and if artificial mass transfer occurs, the final prediction of the species flux will not be exact.

This work focuses on the development and implementation of a consistent transport equation for species concentrations. The VOF method chosen to advect the free surface is `isoAdvector`. The resulting approach to ensure consistency is therefore different from what is required for an algebraic VOF method. The two methods used, depending on the algebraic or geometric nature of the solver, will be introduced in the following.

1.6.1 The single-field and CST approach

We will start with the presentation of the approach adapted to an algebraic VOF method. The first work dealing with such a method dates back to the initial article of Haroun et al.[64]. The main idea in this work was to represent the concentration field in the whole domain with only one field. This approach is known as the single field approach. The discontinuity at the interface was accounted for by an additional diffusion flux which is responsible for mass transfer. Later, the method was extended by Marschall et al. [65] and called Continuous Species Transfer (CST). The main idea was the same as before; the difference was the procedure used to determine the diffusion coefficient in the cells containing the interface. More recently, Maes & Soulaine [86] worked on the integration of volume change. They proposed a different calculation of the diffusion coefficient, as did Deising et

al. [67]. The transport equation is modified to include the additional diffusion flux Φ_k of species k:

$$\frac{\partial C_k}{\partial t} + \nabla \cdot (\mathbf{U} C_k) = \nabla \cdot (D_k \nabla C_k + \Phi_k) + R_k \tag{1.66}$$

This new diffusion flux accounts for the mass transfer at the interface. However, with algebraic VOF methods, the interface is usually spread over a few cells, therefore, the flux will be non-zero only in the cells where $\alpha \in]0;1[$. The expression of this flux was proposed by Haroun et al. [64]:

$$\Phi_k = -D_k \frac{C_k(1 - H_k)}{\alpha + H_k(1 - \alpha)} \nabla \alpha \tag{1.67}$$

1.6.2 The two-field approach

In chemical engineering, concentration or mass fractions are often used to describe chemical species. Concentration is useful when dealing with multiple reactions and to obtain reaction rates or yields. To represent the distribution of species in the domain, a transport equation that will enable the species concentrations to be followed in every control volume is required. There are two choices: the single-field approach, or the two-field approach. In the single-field approach, only one concentration field describes a species throughout the whole domain. This concentration field will not necessarily be continuous through the interface and indeed, most of the time it will not. The two-field approach uses two separate fields, one for each phase ,to describe the species concentration. The interest of a two-field approach is that it facilitates the description of the phase limits and it also avoids the complicated computation of the phase properties in the cells where both phases exist. The single-phase approach has been used by Haroun and coworkers [64] to study chemical mass transfer at a gas-liquid interface. Marschall et al. [65] then developed the Continuous Species Transfer using a different computation for the diffusion coefficient in the interface region. Maes and Soulaine [86] have also succesfully included volume change and derived the Compressive-CST (C-CST), which improves consistency with MULES of `interFoam`. In the two-field approach, the interface concentration is directly accessible through the linear extrapolation of the phase concentration to the interface. The two-field approach is also more consistent with a geometric VOF method, see [86]. Bothe and Fleckenstein [66] applied the two-field approach to the transport of concentration and later included volume change to the multi-component mass transfer previously cited [90]. Both approaches can yield good results, however, the most important thing to keep in mind is artificial mass transfer. Artifical mass transfer occurs when the concentration of a given species becomes non-physical in a phase. It is artificial because the fluxes responsible for the non-significant value come from the discretisation of

the transport equation. The difficulty with two-phase flows is the interface and the transport equation for species must take into account the position of the interface resulting from the VOF solver. Consider a simple case of a gas bubble containing a dilute species advected in a channel filled with liquid. The dilute species in the gas is not soluble in the liquid and therefore its concentration should remain zero everywhere in the liquid phase. If somehow the concentration of the species becomes non-zero in the liquid phase, then there is a flux of species entering a cell filled with liquid. This simple example is useful to describe what is called consistency and this notion will be described in the next section.

The present averaging tools needed to derive a transport equation consistently with a geometric VOF method such as `isoAdvector` will consider a gas-liquid two-phase flow for a two-field approach, the concentration of a species C_k is split into a liquid concentration field and its gaseous counterpart:

$$C_{k,1}(\mathbf{x},t) = \begin{cases} C_k(\mathbf{x},t) & \text{in phase 1} \\ 0 & \text{in phase 2} \end{cases} \tag{1.68}$$

$$C_{k,2}(\mathbf{x},t) = \begin{cases} 0 & \text{in phase 1} \\ C_k(\mathbf{x},t) & \text{in phase 2} \end{cases} \tag{1.69}$$

Two averaged quantities, namely the volume average and the phase average, can be defined. The volume average is the quantity that is transported on the compuational grid in a Finite Volume Method (FVM) framework. It is the concentration averaged over the volume V of a cell:

$$\langle C_{k,1} \rangle_V = \frac{1}{V} \int_{V_1} C_{k,1} \, dV \tag{1.70}$$

Note that as $C_{k,1}$ must be zero in the gas phase, integrating over V_1, which is the volume of liquid inside the cell, or over V which is the total volume of the cell, are equivalent. The same definition holds for phase 2. We can also define the phase average:

$$\langle C_{k,1} \rangle_{V_1} = \frac{1}{V_1} \int_{V_1} C_{k,1} \, dV \tag{1.71}$$

The phase average represents how the concentration is distributed in the phase. The two averages can be linked by the volume fraction:

$$\langle C_{k,1} \rangle_V = \frac{1}{V} \int_{V_1} C_{k,1} \, dV = \frac{V_1}{V} \frac{1}{V_1} \int_{V_1} C_{k,1} \, dV = \alpha \langle C_{k,1} \rangle_{V_1} \tag{1.72}$$

Equation 1.72 will be very important in the following, and both averages will be used depending on the situation because they are very complementary.

1.7 Chemical reaction

The comprehensive numerical simulation of reactive two-phase flows is an exceptionally demanding task, with relatively few studies specifically addressing VOF simulations coupled with chemical reactions and even less dedicated to homogeneous catalysis. Duran and coworkers [91] studied hydrogenation reactions in monolith reactors and particularly mass transfer around Taylor bubbles. However, they did not study the interface advection and used a converged velocity field together with a steady state concentration transport equation. More recently, Woo and coworkers [92] presented some results on the catalytic hydrogenation of nitrobenzene. The flow regime was again a Taylor flow, however, the authors did not solve for the hydrodynamics and used a converged velocity field. There is a major difference with our targeted chemical reaction. Furthermore, the authors used a surface reaction at the wall and a power law expression for the reaction rate, which was integrated over time with an external differential algebraic solver. The authors dedicated substantial effort to acquire experimental data and forecast various fluid properties, which is essential to determine whether each hypothesis is valid or not.

1.8 Limits and difficulties

1.8.1 Mesh size in the liquid film surrounding Taylor bubbles

Numerically, the simulation of thin liquid films is challenging. As explained in section 1.2.4, a well-resolved simulation of the film is important for the prediction of the overall mass transfer. The liquid film plays a role in the absorption of the compounds. A very fine grid is compulsory in order to resolve the film, otherwise a dry wall could result from the simulation [93]. These authors recommend that there are at least five cells in the thickness of the film to correctly capture the interface. They also stated that a cell aspect ratio close to one is better and therefore using square or cubic cells is recommended [38]. The variations of film thickness for the different operating conditions are given in the table below. In order to compute the gradients and capture every feature of the flow, the grid should be fine enough near the walls. If a liquid film of around 5 µm requires at least five cells, it means that

TABLE 1.1: Film thickness variations with temperature for the highest two-phase velocity $U_{TP} = U_G + U_L = 0.0231 \times 10^{-3}\,\mathrm{m\,s^{-1}}$. Ca is defined by equation 1.5

Temperature ($°C$)	$10^4\times$ Capillary number	Film thickness (µm)
30	8.1	5.8
40	7.3	5.4
50	6.7	5.1

the size of the cells in the radial direction at the wall should be around 1 µm. For VOF simulations, it is recommended to use an hexahedral grid so as to reduce numerical errors. A low aspect ratio, ideally near 1 is also recommended. In other words, the size of the cells should be equal in all three directions. This means the hexahedral cells should approach cubic cells and avoid having a long edge in a given direction (e.g. axial or azimuthal) and a short one in the orthogonal direction (e.g. radial). Nevertheless, the size of the mesh will be a limiting point if a high resolution is required. Several options would allow high resolution while limiting the total size of the mesh. One solution is to compute an axially periodic mesh to reduce its size.

1.8.2 Spurious currents

So-called spurious currents are artificial velocities arising from the discretization of the surface tension force [94] in VOF methods. They appear after inconsistencies in the modeling, usually in the computation of curvature. As the surface tension force is a source term in the momentum conservation equation, non-physical velocities arise in order to balance the inconsistencies of modeling procedure. The solvers available in OpenFOAM® have been compared by Gamet et al. [83] and it was concluded that the geometric VOF method `isoAdvector` with PLIC-RDF reconstruction enables greater reduction of the spurious velocities compared with the historical algebraic VOF solver or to the geometric `isoAdvector isoAlpha` formulation.

1.9 Summary and objectives of current work

1.9.1 Gaps identified

Even though the increase in computer resources today allows more complex simulations, the complete multiphysics simulation of a chemical reactor remains challenging. To reduce the

computational cost, some authors [38], [92] are still separating the hydrodynamics from the rest of the simulation and mass transfer is calculated on a "frozen" velocity field. However, this method is only valid in the case of very dilute conditions, where mass transfer will not have a coupled impact on the hydrodynamics. This is not always the case and is particularly true for the transport of ethylene into cyclohexane, which is the case studied here.
Another way of reducing the computational cost is the use of a fixed frame of reference, using periodic boundary conditions. Here, the bubble is kept static at the centre of the unit cell and the fluid around flows at the bubble velocity. This kind of set-up is interesting for the control of the size of the mesh. However, this method requires the shape of the bubble to be fixed at the beginning of the simulation. Furthermore, it is not possible to simulate the formation of the bubble this way and the importance of the bubble formation process on the mass transfer has been shown in recent literature. Tan et al. [95] announced up to 30-40% of the overall mass transfer occurred during bubble formation. Yang et al. [20] found that up to 90% of mass transfer occurred during the bubble formation stage. However, the two present groups of authors used a square microchannel of 0.5 mm. The difference between a circular and a square cross-section might have an impact on the duration of bubble formation, and thus on the overall mass transferred during this step. Nevertheless, the comparison between the two configurations is only possible in a 3D simulation. Butler et al. [37] concluded their work indicating that CFD simulations could be an interesting tool to determine the contribution of the liquid film and the hemispherical caps in the model of [38]. In a more recent work, Butler et al. [87] successfully used the Level-Set method to simulate the mass transfer with a Reynolds bubble number of over 200. Unfortunately, they used a unit cell periodic approach with an axisymmetrical geometry and this configuration did not allow them to simulate the bubble formation process. Recently, Deleau et al. [21] studied the impact of pressure on the mass transfer in Taylor flows and showed that more than 20% of the mass transfer occurred during bubble formation stage. Even if there is not a scientific consensus on the explanation of the phenomenon, a detailed CFD study on the mass transfer occuring during the bubble formation stage compared with that in developed Taylor flows would fill in this gap.
Finally, of the few studies implementing mass transfer in their simulations, even fewer have implemented chemical reaction. One recent study by Woo et al. [92], presented results of mass transfer, but only on a "frozen" velocity field with no coupling between hydrodynamics and mass tranfer. Uncoupling mass transfer and hydrodynamics does not allow to compute the bubble formation stage, furthermore, it is not possible to compute volume change induced by mass transfer.

1.9.2 Objectives of this work

This work aims at simulating fully coupled multiphase flow and chemical reaction in a microchannel. The first set of objectives is necessary to understand the physical phenomena involved and prepare the future simulations:

1. Review the state of the art on Taylor flows
2. Select the most suitable VOF solver present in OpenFOAM® to solve Taylor flows based on parameters identified during the state of the art review
3. Obtain fluid properties from either experimental data or empirical relations to have the most realistic simulations as possible

Once the state of the art is described, the second part of the project is dedicated to mass transfer:

1. Implement the advective transport of concentration consistently with `isoAdvector` to avoid artificial mass transfer
2. Validate the transport of concentration without mass transfer from simple test cases
3. Implement the diffusive transport of concentration on top of the advective transport
4. Validate the full concentration transport with simple test cases and more realistic ones such as Taylor flows in T-junctions
5. Implement a mass source term that uses the interface concentration to compute the interface concentration gradient
6. Validate the mass transfer with test cases such as the Stefan case

At this point, the solver can be used to determine the contribution of the bubble formation to the overall mass transfer. The relative contribution of the liquid film and the bubble caps to the overall mass transfer is also elucidated.
Finally, the solver includes another source term for the chemical reaction. When the solver is thoroughly validated, it is used to solve reactive Taylor flows with a homogeneous catalytic reaction in microchannels. To do so we must cover the following points:

1. Implement a source term for the chemical reaction with a power law expression for the reaction rate

2. Simulate T-junctions with the bubble generation and the chemical reaction to obtain quantitative data such as conversion or selectivity

3. Determine the contribution of the bubble formation and the liquid film to the overall mass transfer

Chapter 2

Concentration transport without phase change, implementation and validation

2.1 Introduction

After dealing with some background information, we step into the core of this work. Implementing an accurate transport equation is in itself a challenging task. Doing it for two-phase flow is even more demanding. To this end, we must compare the three VOF solvers available in OpenFOAM®, namely `interFoam`, `interIsoFoam` and `interFlow`. This comparison will help us choose the most suitable solvers of these three based on our needs, the simulation of Taylor flows in microchannels. The cases for the comparison are gradually increasing in complexity towards Taylor flows in T-junctions. The first cases studied are steady state cases in 2D and 3D were the bubbke is not generated. Then, we study the bubble generation in a coaxial injector with 2D axisymmetric and 3D geometries. Finally, the bubble generation in 2D and 3D T-junctions will be discussed. The second part of the chapter will focus on the implementation of the transport equation. Relevant numerical tests and their results will be presented. At the end of the chapter, an innovative formulation for concentration transport without phase-change is derived.

2.2 Description of the boundary conditions

We open this section with a description of the boundary conditions used for the simulations conducted. The choice of a wise set of boundary conditions is of major importance, as a simulation can converge towards a non-physical solution if the input parameters are not suitable. For the following simulations, the same set of boundary conditions are used. There are only three variables in the incompressible VOF solvers of OpenFOAM® requiring initial and boundary conditions. The pressure, the velocity and the volume fraction fields need to be specified in the `0/` directory. We usually use the same kind of conditions, although there are some specificities depending on the variable.

2.2.1 Velocity

The velocity at a wall is set to zero through a `noSlip` condition to respect the fluid adhesion. At the inlets, we use a `fixedValue` with a uniform value. A constant velocity is set on every face of the inlet patch. We could also have imposed a Poiseuille profile at the inlet. However, the distance for the profile to be established was found to be comparable to the tube diameter, which is short compared with the length of the computational domain. At the outlet patch, an `inletOutletVelocity` condition is used. In the usual case of fluid exiting the domain, this boundary condition is equivalent to a `zeroGradient` condition (Neumann condition). In case of re-entry of fluid at outlet, the `inletOutletVelocity` condition will turn into an imposed velocity, that is set to zero through the `inletValue` input. In this way, we prevent fluid re-entering at the exit, which can occur during transient phases and can conduct to computation blow out. The other option could be to use a `zeroGradient` condition on the outlet. However, the `zeroGradient` does not prevent back-flow, nor the computation to blow out. If the solution has a velocity coming in, there will be some issues with the tracking of the interface near the outlet.

2.2.2 Pressure

The incompressible solver needs a reference pressure in order to start the first iteration and solve the pressure equation. This reference can be either imposed on a patch (eg. on outlet) or through a reference cell in the `PIMPLE` parameters of the `fvSolution` dictionnary. In our cases, we use a `fixedValue` equal to 0 for the pressure at outlet. The multiphase solvers of OpenFOAM® use a reduced pressure, which is the pressure minus the hydrostatic pressure

(ρgh). This is done for computational purposes. However, for incompressible simulations, it is not the absolute pressure that matters. Indeed, only the pressure gradient is needed.

2.2.3 Volume fraction

At inlets, a uniform `inletOutlet` is imposed, either 1 for the liquid or 0 for the gas. Only the `inletValue` keyword is specified. At the outlet, a `zeroGradient` is used.
The walls need a specific formulation. When the gas-liquid interface is in contact with solid walls, the interface intersects the solid surface at a so-called *contact line*, defining a contact angle. This angle depends on many parameters, such as pressure and temperature conditions, wettability and roughness of the solid surface, physical properties of the fluids, etc... In VOF simulations, a paradox appears at walls where a null velocity for both phases should occur, while permitting an advancing interface. In practice, this behaviour is allowed thanks to appropriate contact angle boundary conditions in the volume fraction equation. In our computations, we used a constant contact angle. The corresponding type of condition is `constantAlphaContactAngle`. This boundary condition is the most commonly used boundary conditions in the literature.
Some better formulations, such as dynamic contact angle boundary conditions, can be proposed. In OpenFOAM®, a tanh-based model is currently implemented as:

$$\theta_{\text{dyn}} = \theta_0 + (\theta_A - \theta_R) \tanh\left(\frac{U_{\text{wall}}}{U_\theta}\right) \tag{2.1}$$

Where U_{wall} is the fluid velocity in the wall cell, θ_0, θ_A, θ_R are equilibrium, advancing and receding contact angles. U_θ is a user specified velocity scale that requires experimental data. In this case, the type of boundary condition must be set to `dynamicAlphaContactAngle`. Cox [96] and Kistler [97] have proposed more advanced dynamic contact angle models based on local values of capillary number and contact line velocity. However, these formulations will not be studied here because that is not the topic of this work.

2.2.4 Concentration

No specific boundary conditions for concentration have been implemented. On walls and the outlet, a `zeroGradient` was applied whilst at inlet, we set a `fixedValue`. It is not clear how to correctly model the concentration profile near the boundary of the domain and therefore, the same scaling methodology based on the volume fraction field was applied to the concentration profile. This scaling will be presented in section 2.4.3.

2.2.5 Summary

The table 2.1 summarizes the main types of boundary conditions used in our simulations.

TABLE 2.1: Types of boundary conditions used in the simulations

	U	P	α
gas inlet	`fixedValue`	`zeroGradient`	`inletOutlet`
liquid inlet	`fixedValue`	`zeroGradient`	`inletOutlet`
outlet	`inletOutletVelocity`	`fixedValue`	`zeroGradient`
walls	`noSlip`	`fixedFluxPressure`	`constantAlphaContactAngle`
front and back (2D planar)	`empty`	`empty`	`empty`
front and back (2D axisym.)	`wedge`	`wedge`	`wedge`

2.3 Performance assessment of existing VOF solvers

The section is dedicated to a comprehensive comparison of the three VOF solvers provided by OpenFOAM®: `interFoam`, `interIsoFoam` and `interFlow`. In order to determine the most appropriate solver for constructing the subsequent components, it is essential to start with the most optimal choice currently available. To simulate capillary flows, the prediction of surface tension forces can potentially be considered as the most critical source of error. Therefore, the best option for us is to use a solver that can perform optimally at low capillary number. Several factors will be quantified, such as the velocity field, parameters of the global bubble shape and the volume fraction field and the performance of each solver is assessed.

2.3.1 Developed Taylor flows in a tube

2.3.1.1 Geometry and initialization

For this case, the bubble formation process is not simulated. Instead, a Taylor bubble is initialized as a simple cylinder of gas (corresponding to a rectangle in a 2D axisymmetric simulation). The length of the rectangle (cylinder) is determined through an estimation of the length of the bubble for a given ratio of gas to liquid superficial velocities. The rectangle

(cylinder) volume can be set equal to the desired bubble volume. The total length of the domain is equal to the length of a unit cell. A unit cell is defined as a bubble plus the slug of liquid separating two consecutive bubbles, supposedly of the same size. After some transient time steps, the surface tension force shapes the interface into a realistic bubble shape. The advantage of this method is the reduced mesh size. To evaluate how the solvers deal with microfluidic dimensions, we have started with a static bubble at the centre of the reactor.
For the two-dimensional simulations, we use a wedge of 5°. The bubble is initialized at the center of the channel as illustrated on figure 2.1. The symmetry axis is shown on figure 2.1

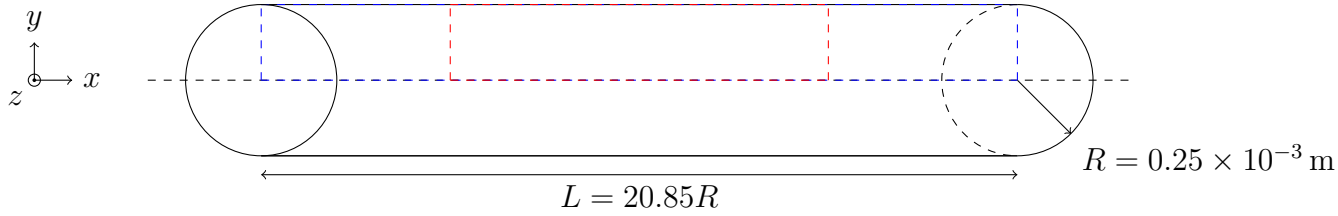

FIGURE 2.1: 3D tube with the angular sector used for 2D axisymmetrical simulations in blue and the initialization of the bubble in red

as a black dashed line. When discussing results, only the cutting plan $z = 0$ is shown.
For 3D cases, we use a cylinder as displayed on figure 2.2. The bubble is initialized as a

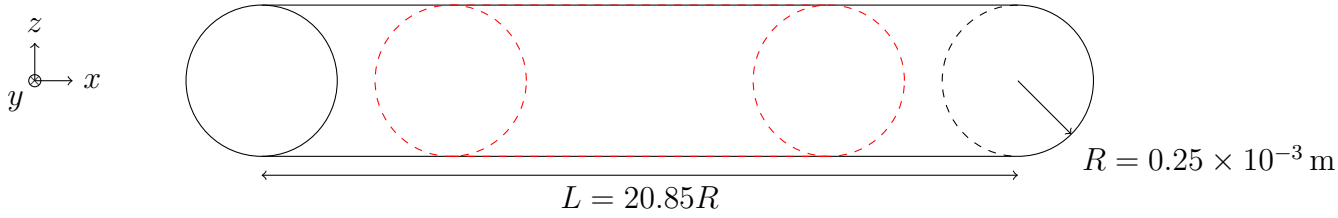

FIGURE 2.2: Geometry of a 3D tube with the bubble intialised in red dashed lines

cylinder. For both 2D and 3D, the length to initalize the bubble is computed based on the superficial velocities using Garstecki model 1.16. When discussing results, only the cross-section $y = 0$ is shown.
No velocity is initialized in the whole domain. As the bubble is static, it is supposed to stay at the center of the channel after the surface tension force has curved the interface. The pressure drop imposed with the cylic boundary conditions allows the fluid to move at the desired velocity.

2.3.1.2 Meshing

For the 2D axisymmetrical case, the mesh is obtained from figure 2.1 putting only one cell in the non-significant direction (the cells get wider in the radial direction). The cells are approximately square cells with 20 cells per radius and 300 cells in the length of the mesh. The 3D simulations were conducted with a O-H or "butterfly" grid topology. This topology allows the mesh to be fully hexahedral while limiting the skewness of the cells. The figure 2.3 below compares a non-optimized single H block grid to the butterfly topology. Meshing a disk with a single H block topology conducts to "flat" cells in the corners of the H block, since two consecutive faces of the corner cells are aligned. The butterfly topology gives more orthogonal hexahedra and thus less skewed cells. Special attention needs to be given to

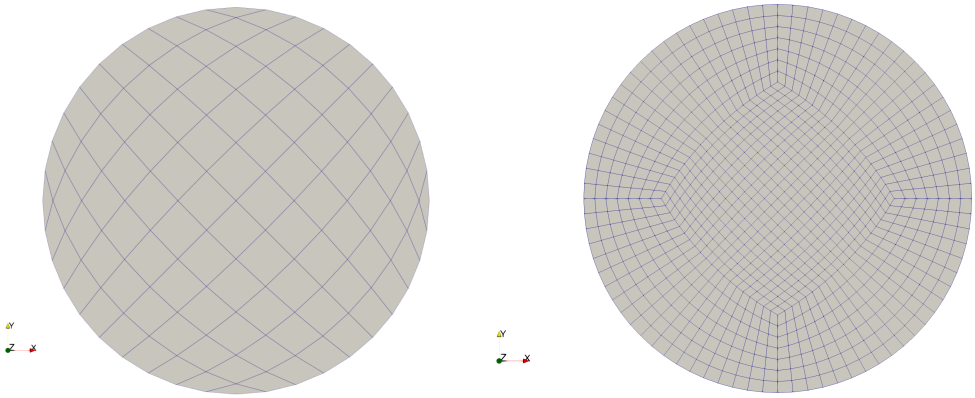

FIGURE 2.3: Comparison between a single H block grid and the O-H butterfly topology

the grid. A single bad cell in a grid can negatively influence the results in all the domain, particularly when solving the Poisson-like equation for the pressure. We have chosen to work with hexahedral grids as they give more precise results during the simulation. Furthermore, the VOF method tends to work better on hexahedral meshes. With a uniform hexahedral grid like the one shown in the right-hand side of figure 2.3, non-orthogonal correctors are not needed. This yields more precise results and the simulation runs faster. The 3D mesh is created to be as similar to the 2D mesh as possible. The dimensions and the refinement are therefore the same.

2.3.1.3 Boundary conditions

In the 2D axisymmetric periodic bubble configuration, left and right boundary conditions are set to `cyclic`. Left and right patches can be viewed as "inlet" and "outlet" boundaries. This cyclic representation is equivalent to compute the bubble inside a traveling window of length

unit cell moving at the same mean speed as the bubble. As the left and right boundary conditions are cyclic, what comes out of the reactor through the right comes back in through the left. In order to compensate the pressure loss in the cyclic pipe, to maintain a constant mean velocity flow, a pressure jump must be artificially imposed between the two left and right patches. At the wall which is the top blue edge on figure 2.1, a no slip condition is imposed on velocity and a contact angle of 0° for the volume fraction field. The axis is given an `empty` boundary condition and in the z direction, a `wedge` boundary condition is imposed. For the 3D case, left and right boundary conditions are cyclic as well. The outter wall of the domain is set to "wall" with a no slip condition on velocity and the same contact angle as the 2D axisymmetrical simulation.

2.3.1.4 Results

We begin the presentation of the results with the 2D axisymmetrical case. Figure 2.4 shows the bubble in grey surrounded by liquid in pink. The symmetry axis is the bottom edge of the rectangle, the top edge is the wall. Looking only at the interface, the issue might not

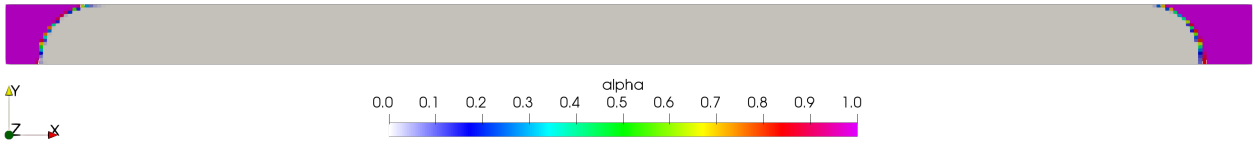

FIGURE 2.4: Bubble of gas in a 2D axisymmetrical simulation

appear clearly. That is why the magnitude of the velocity is represented on figure 2.5. That is a VOF simulation therefore, there is only one velocity field for both liquid and gas.
The initialization of the interface creates velocities arising from the establishment of the bubble caps. As soon as the simulation starts, the velocity of cells located in the gas bubble starts to increase. The largest velocities are located in the caps of the bubble. If we compare figures 2.4 and 2.5, we realize that the large velocities are mostly localised in the gas bubble or near the interface.
For the `interFoam` simulation, we can see the bubble moving through time in the x direction. For `interIsoFoam`, the bubble does not move in the channel. However, high velocities appear at the axis, as soon as the bubble is formed. The fact that these velocities are symmetric is surprising. The bubble does not move because the global balance of mass is respected, even though some cells have a high velocity, particularly near the axis (see figure 2.5). The gas moves at the axis and then recirculates in the caps of the bubble. `interFlow` gives a more satisfactory solution. There are no longer very high velocities at the axis. The bubble

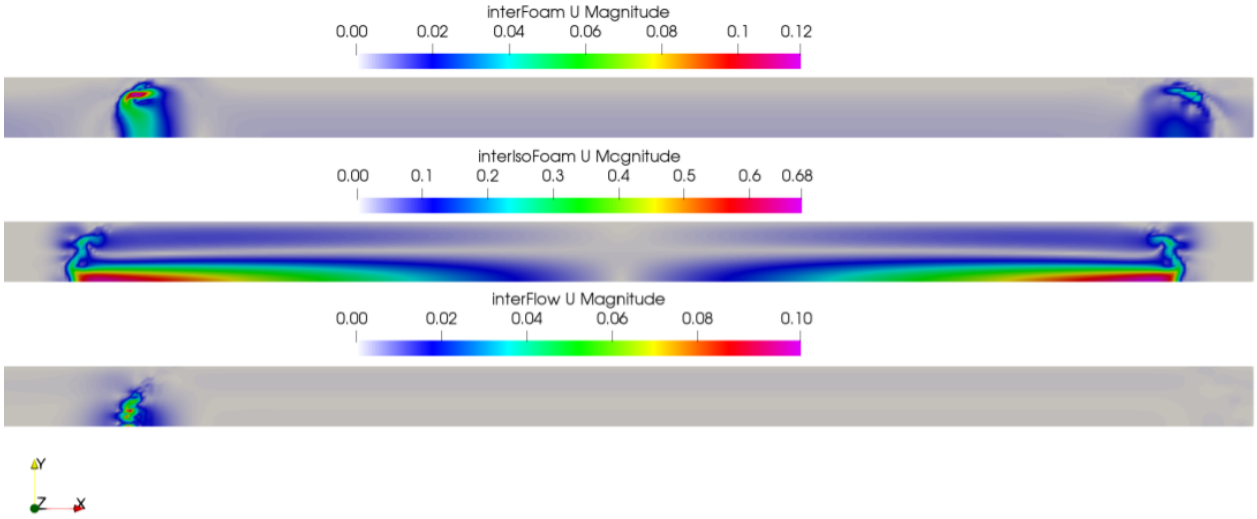

FIGURE 2.5: Comparison of the magnitude of the velocity ($\mathrm{m\,s^{-1}}$) at time 0.1s for the three solvers, in a 2D axisymmetric wedge simulation

starts moving towards the right but stops. As we are not sure the cyclic condition is correctly implemented in `interFlow`, the bubble might stop because of the inconsistency of the boundary condition.

Figure 2.6 shows a cross-section $y = 0$ of the channel 2.2. As for 2D axisymmetrical sim-

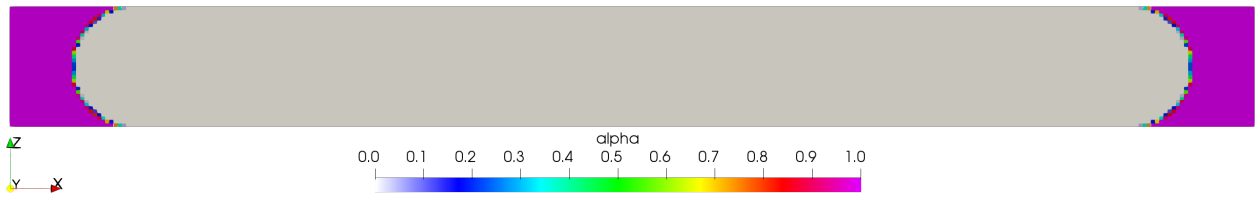

FIGURE 2.6: Bubble of gas in a sliced 3D channel

ulations, it is important checking the velocity field to understand if the `cyclic` boundary condition is correctly accounted for.

Figures 2.7 and 2.8 show the cross-section $y = 0$ of the 3D simulation as displayed on 2.2. `interFoam` gives similar results than the 2D simulations. However, this time, the bubble moves towards the inlet. Also, the maximum of the velocity is located on the axis, which was not the case in 2D. For `interIsoFoam`, high velocities are still located at the axis of the channel. `interFlow` does not have a moving bubble, but the results are still questionable as `interFlow` has some troubles dealing with `cyclic` boundary conditions. The figure 2.8 shows the results after 0.5s. No steady state is achieved for either `interFoam` nor `interIsoFoam` solvers. The coloured dots on `interFoam` velocity magnitude fields are in fact small droplets appearing inside the bubble. These dots may appear when the pressure equation is not well converged. This then, creates a source term in the momentum equation that produces spurious velocities. These velocities will then introduce inconsistencies in the VOF equation.

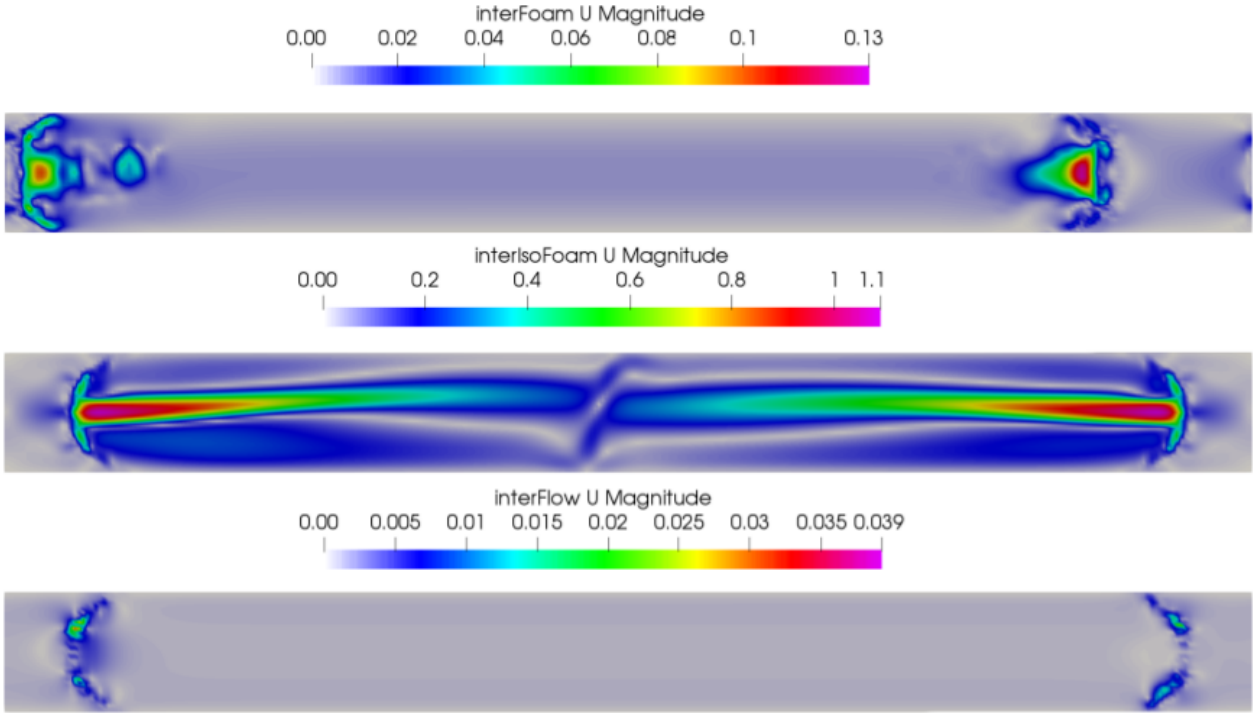

FIGURE 2.7: Comparison of the magnitude of the velocity ($\mathrm{m\,s^{-1}}$) at 0.1s for the three solvers in a 3D simulation

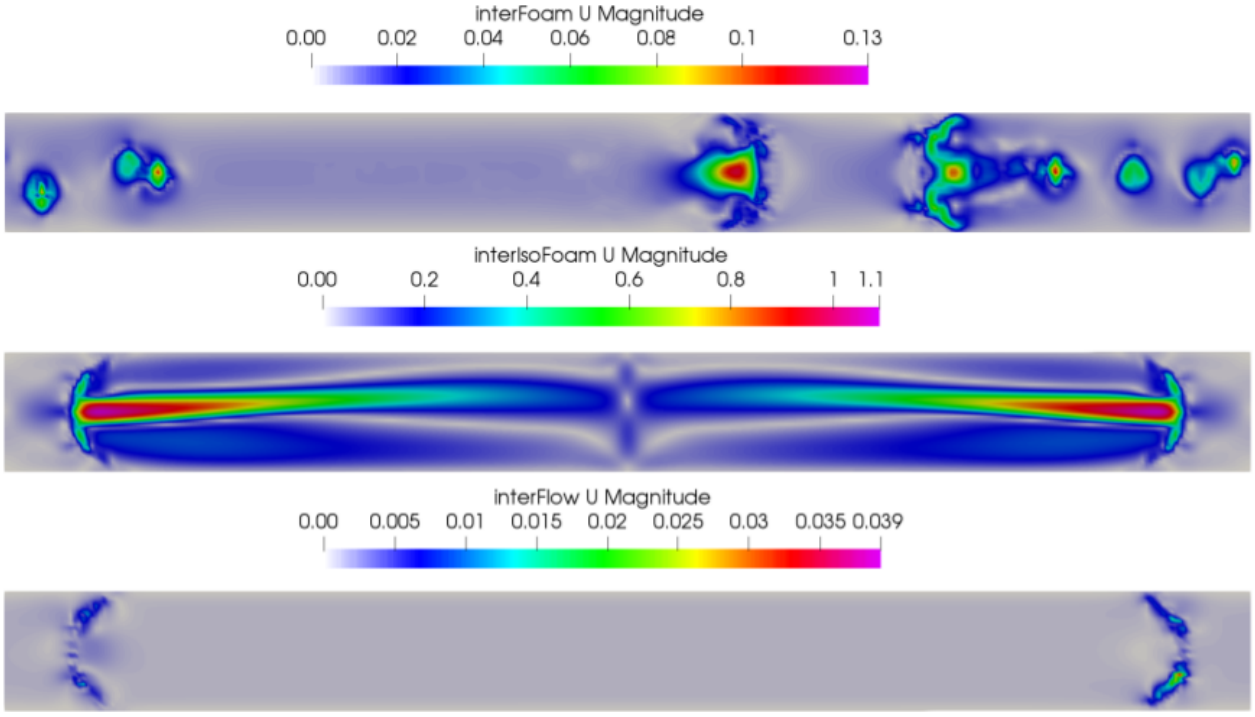

FIGURE 2.8: Comparison of the magnitude of the velocity ($\mathrm{m\,s^{-1}}$) at 0.5s for the three solvers in a 3D simulation

In order to prevent this problem, we have reduced the absolute tolerance on the pressure equation from 1e-07 to 1e-08.

2.3.2 Taylor bubble generation in a coaxial injector

2.3.2.1 Geometry

Figure 2.9 shows the 3D coaxial injector with the wedge used to simulate 2D axisymmetrical cases in OpenFOAM® .

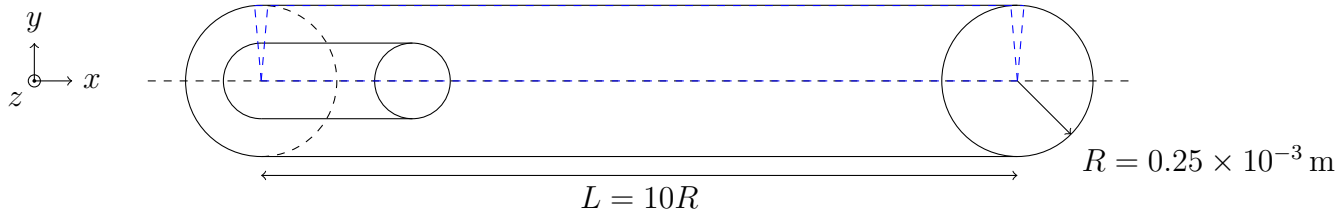

FIGURE 2.9: 3D coaxial injector with the symmetry axis represented as a black dashed line and the wedge used for 2D axisymmetrical simulation as a blue dashed line

For both 2D and 3D, the gas is injected through the inner tube at $6.9\,\mathrm{mm\,s^{-1}}$ and the liquid from the outer tube at $1.3\,\mathrm{mm\,s^{-1}}$. The liquid is cyclohexane and the gas ethylene. Main dimensionless numbers are $Re_L = 0.34$, $Re_G = 3.66$ and the bubble capillary number $Ca_B =$. All the simulations were run using the properties of fluids at 30 °C and 10 bar.

2.3.2.2 Meshing

The mesh of the 2D axisymmetrical simulation is quite similar to the steady case presented on figure 2.1, however, it was heavily refined with 100 cells in a radius. The mesh is uniform, there are 5000 cells in the length of the injector, creating squared cells.
For the 3D mesh, we use the same O-H topology introduced in figure 2.3. Again, the mesh is uniform with 5000 cells in the flow direction.

2.3.2.3 Boundary conditions

The set of boundary conditions used in these simulations were similar to the ones from section 2.3.1.3. For 2D axisymmetrical simulations, we use `wedge` conditions for the non-significant direction and an `empty` condition at the axis. At the inlet, the velocity has a `fixedValue` and the pressure `zeroGradient`. At the outlet, the pressure is set to 0 and the velocity to `inletOutletVelocity` to avoid backflow. At the walls, we use the classical `noSlip` condition for velocity and we impose the flux of pressure. For the volume fraction

field, we impose the values at the inlet depending on the gas or liquid inflow, and we use a constant contact angle at the walls.

2.3.2.4 Results

We compared the solvers `interFoam` and `interFlow` and several issues appeared. The geometric VOF solver `interFlow` shows a lot of oscillations in time at the expansion of the bubble. This issue was corrected by changing the gradient discretisation scheme from Gauss linear to least-squares. The two solvers yield very different results. The curvature of the interface is not the same; `interFoam` has a more circular shape than `interFlow`. The interface is thicker for `interFoam`, which is inherent to the `MULES` algebraic method. We also see the difficulties `interFoam` has with the boundedness of the volume fraction. Figure 2.10 shows some droplets of liquid appearing in the gas phase along the axis of the tube. There are also bubbles appearing inside the liquid phase. In figure 2.11 and 2.12, another difference between the two solvers can be seen. The bubble is formed earlier in the simulation with `interFoam` than with `interFlow`. The two solvers use the model proposed by Brackbill et al. [43] to calculate the surface tension force, however, `interFlow` has an additional step of interface reconstruction, which calculates the exact position of the interface. Every variable can then be interpolated to the exact position of the interface, which allows a better prediction.

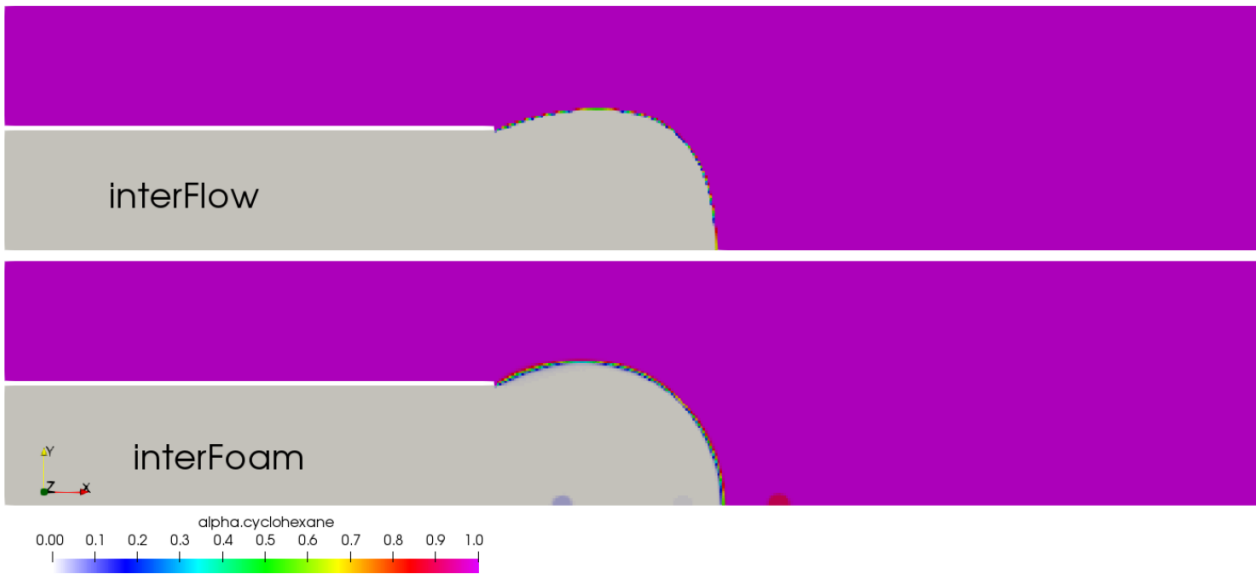

FIGURE 2.10: Comparison between `interFoam` and `interFlow` on the coaxial injector at 0.037s

After the 2D axisymmetrical simulations, we were wondering if the numerical errors appearing at the axis of figures 2.10 2.11 and 2.12 with `interFoam` could be the consequence of the

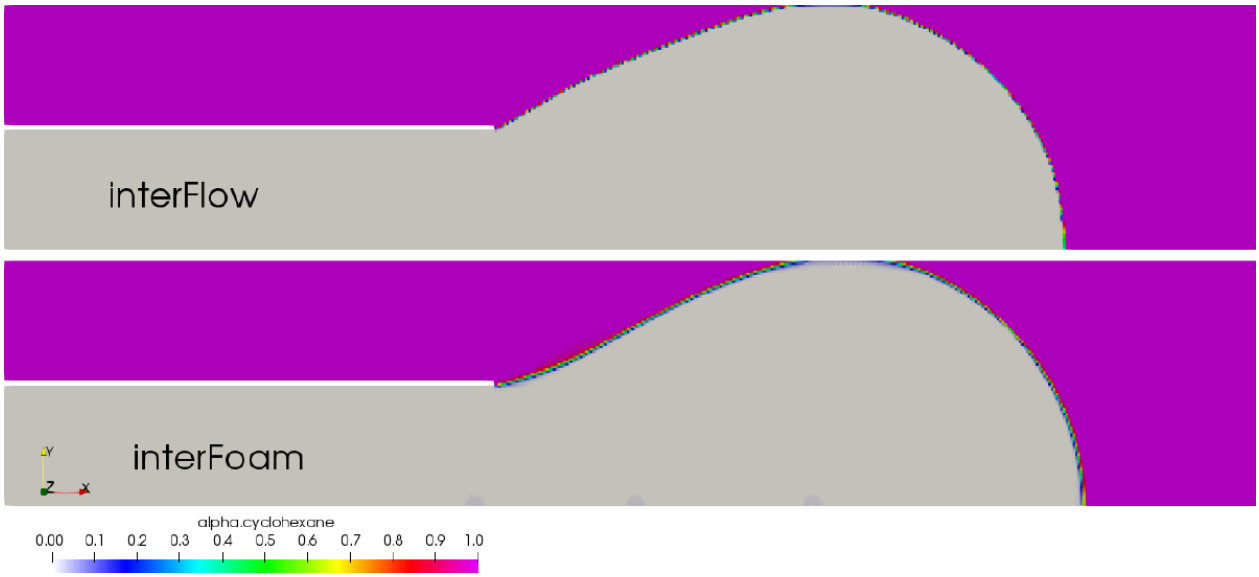

FIGURE 2.11: Comparison between `interFoam` and `interFlow` on the coaxial injector at 0.235s

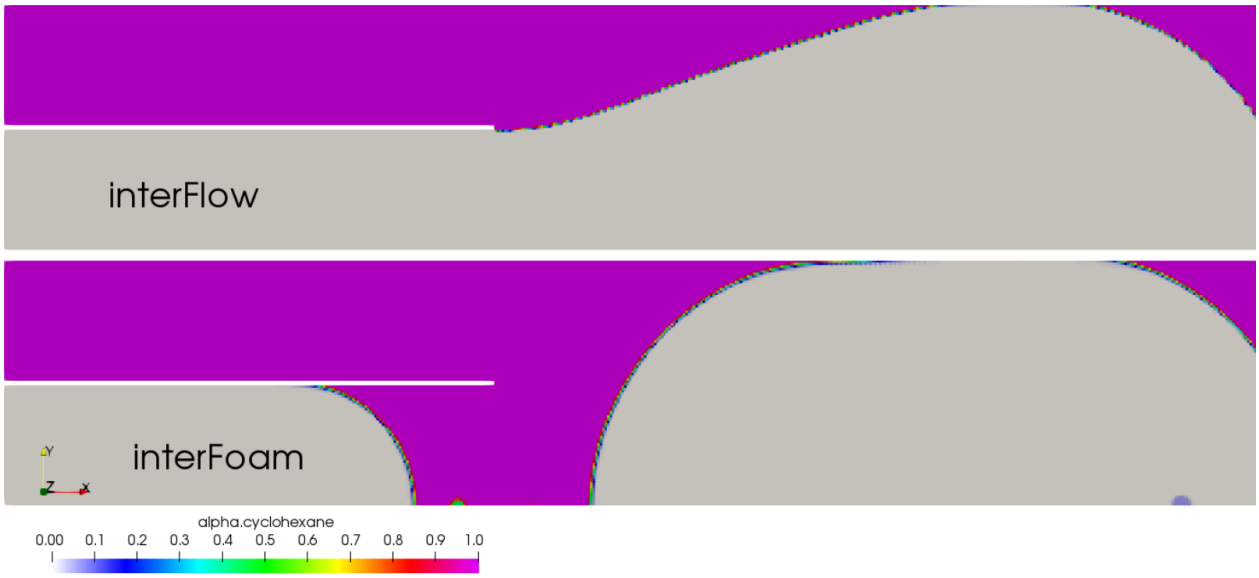

FIGURE 2.12: Comparison between `interFoam` and `interFlow` on the coaxial injector at 0.324s

wedge cells of the axisymmetric mesh. We could not find a method to overcome the issue of droplets inside the gas phase with `interFoam`. 3D simulations will be needed to determine the implication of the wedge topology in this issue. These numerical errors even appeared with a tighter tolerance on the pressure equation. In an attempt to limit the oscillations of the bubbles, the default discretisation scheme to compute all the gradients was changed from Gauss linear, which uses the Green-Gauss theorem, to a Least-Squares approach. The snap tolerance `snapTol`, used to clip unboundednesses of the volume fraction, was also adjsuted from 1e-12 to 1e-8. Lowering the snap tolerance may have a minor impact on the

conservation of volume fraction, while speeding up the calculation. Three cases were set-up:

- One with the `Gauss linear` scheme for the gradient and a snap tolerance of 1e-12, called `pointCellsLeastSquares` on figure 2.13
- A second with the `pointCellsLeastSquares` scheme for the gradient, and a snap tolerance of 1e-12, called `Gauss linear` on figure 2.13
- A final one with the `Gauss linear` scheme and a snap tolerance of 1e-8, called `snapTol 1e-08` on figure 2.13

The results are interesting. It does suppress the non-physical oscillations of the bubbles. On the other hand, the liquid "leaks" into the gas side of the injector as we can see at the top of figure 2.13. The reduction of the snap tolerance speeds up the simulation, but it

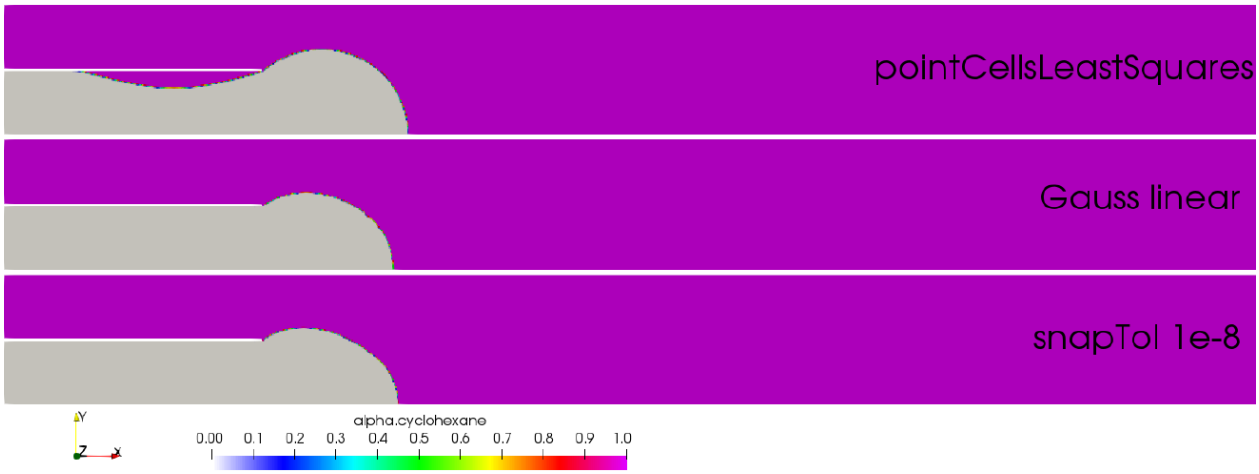

FIGURE 2.13: Comparison between the `Gauss linear` and `pointCellsLeastSquares` gradient schemes, and with the snap tolerance for `interFlow` at 0.040s

has almost no impact on the oscillations of the bubble. On the other hand, switching to a least-squares gradient scheme really improves the stability of the bubble and suppresses the kind of "heartbeat" oscillations that were observed with the Gauss linear scheme. The middle and bottom rows on figure 2.13 have the same scheme, namely `Gauss linear`, while only the snap tolerance changes. On the top row, the injector with the least-squares scheme is shown. To prevent the liquid from flowing into the gas channel, we had to change the volume fraction wall boundary condition of the gas-side of the injector. We also used a constant contact angle of 180°, which means the liquid has no affinity with the wall. This prevents the liquid from flowing into the gas side as it acts as if the wall was repellent. The result is shown on 2.14.

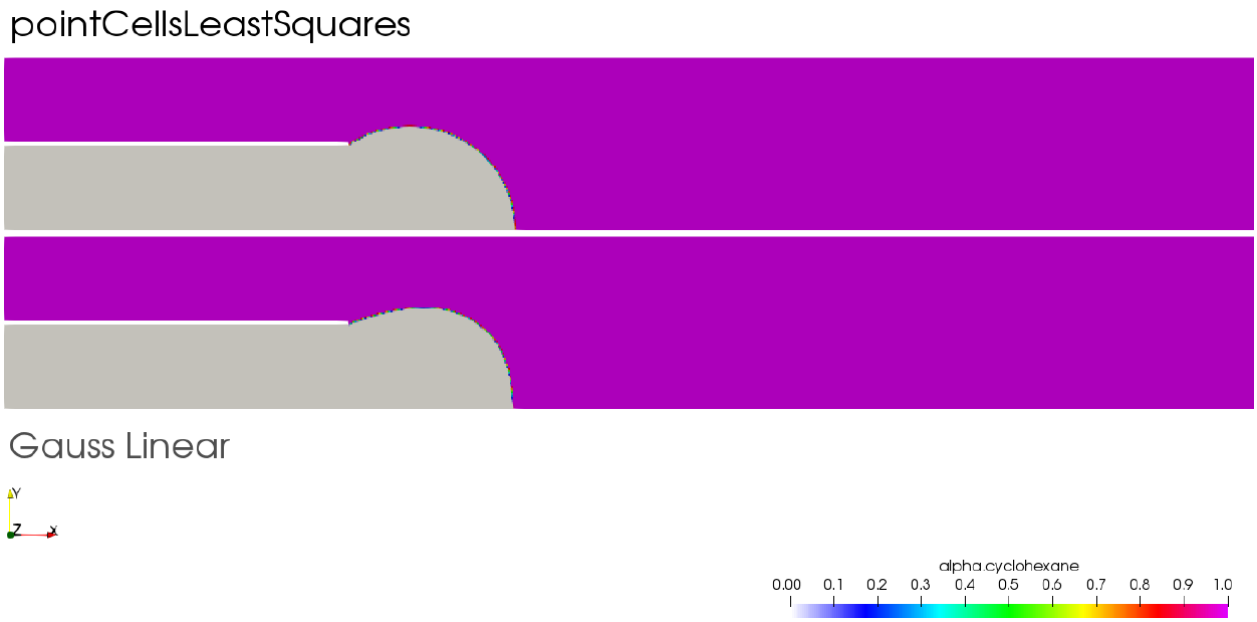

FIGURE 2.14: Comparison between the `Gauss linear` and `pointCellsLeastSquares` gradient schemes for `interFlow` at 0.040s, after changing the boundary condition of the gas side wall for a constant contact angle of 180°.

On figure 2.14 the differences in the bubble shape are explained by the oscillations cause by the Gauss linear scheme for the gradient.

In order to understand whether the wedge cells of the 2D axisymmetrical mesh are the cause of the generation of bubbles and droplets along the centerline of the tube, full 3D simulations were run. Again, some small droplets appear in the gas bubble forming and a bubble also

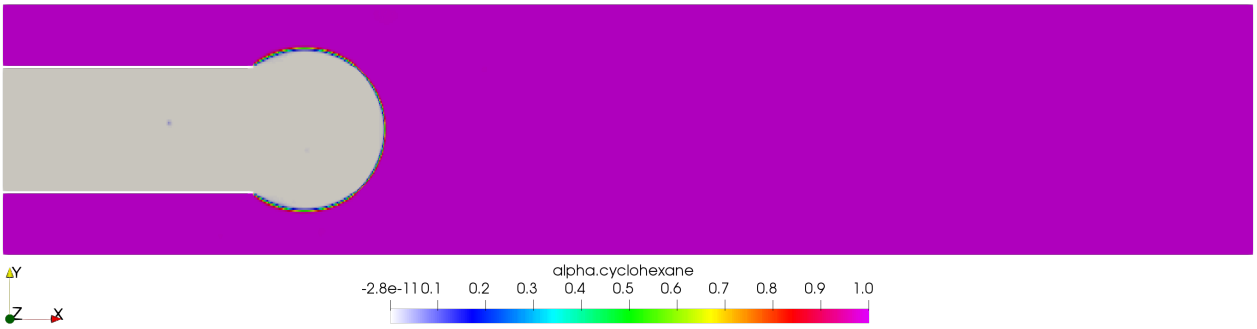

FIGURE 2.15: Cutting plane in $z = 0$ of a three-dimensional coaxial injector using `interFoam`

appears in the liquid bulk. Hence, it is concluded that these results are not due to the nature of the mesh cells and are most likely imputable to the high surface tension force. The Ca numbers in most of our simulations is around 1e-03 or even below, which can be the source f

surface tension force misprediction. The same case does not show small droplets when using `interFlow`.

2.3.3 Taylor bubble generation in a T-junction

This part will be dedicated to the validation of a square T-junction, using the solver `interFlow` to evaluate its performances. In the following, we have decided not to compare with the solver `interFoam` because of the lack of confidence we had with highly capillary flows.

2.3.3.1 Geometry

Figure 2.16 shows a T-junction of square cross-section.

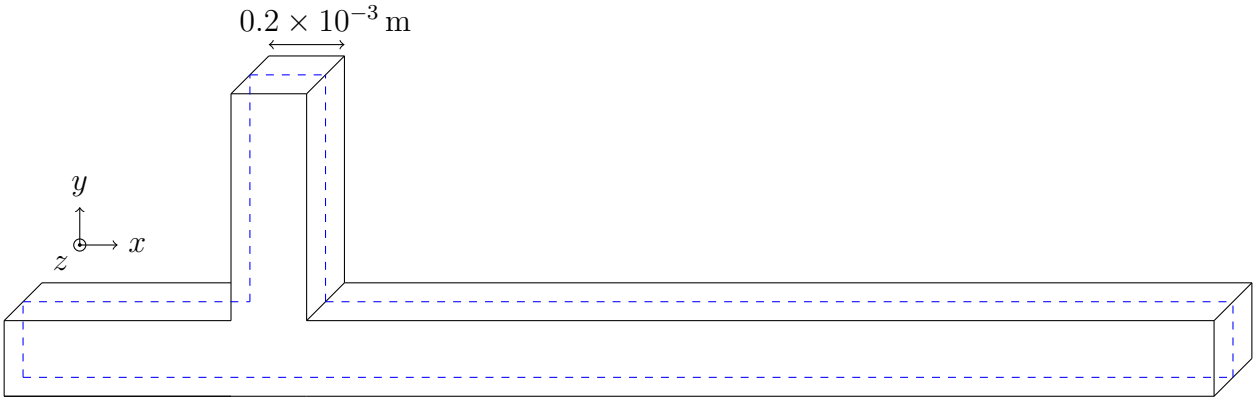

FIGURE 2.16: 3D T-junction with the cross-section used for 2D simulation in blue

For two-dimensional simulations, we use the cutting plane illustrated in blue on figure 2.16. It has a square cross-section of 200 µm.

2.3.3.2 Meshing and initialization

A structured uniform mesh is used, the base mesh has 50 cells per diameter in 2D for a total of 142,500 cells in 2D. For the 3D simulations, the diameter is made of 50x50 cells, the base mesh is therefore 7,125,000 cells. Higher levels of refinement will be indicated, otherwise the mesh is always 50 cells per diameter. The number of cells in the stream wise direction is adapted depending on the length of the T-junction simulated. The liquid is injected on the left and gas comes from the top injector, the stream wise direction of the channel is also initially filled with liquid.

2.3.3.3 Boundary conditions

The set of boundary conditions are similar to the one used for the simulation of the coaxial injector.

2.3.3.4 Mesh sensitivity

Before reproducing experimental results from the literature, a mesh sensitivity analysis was performed. We have started with the uniform mesh with 50 cells per diameter and compared the length of the bubble variations with superficial velocities from relation 1.16.
The results were rather surprising. After a given refinement threshold, the bubbles did not detach anymore. Figure 2.17 shows a refined mesh of 140 cells per diameter.

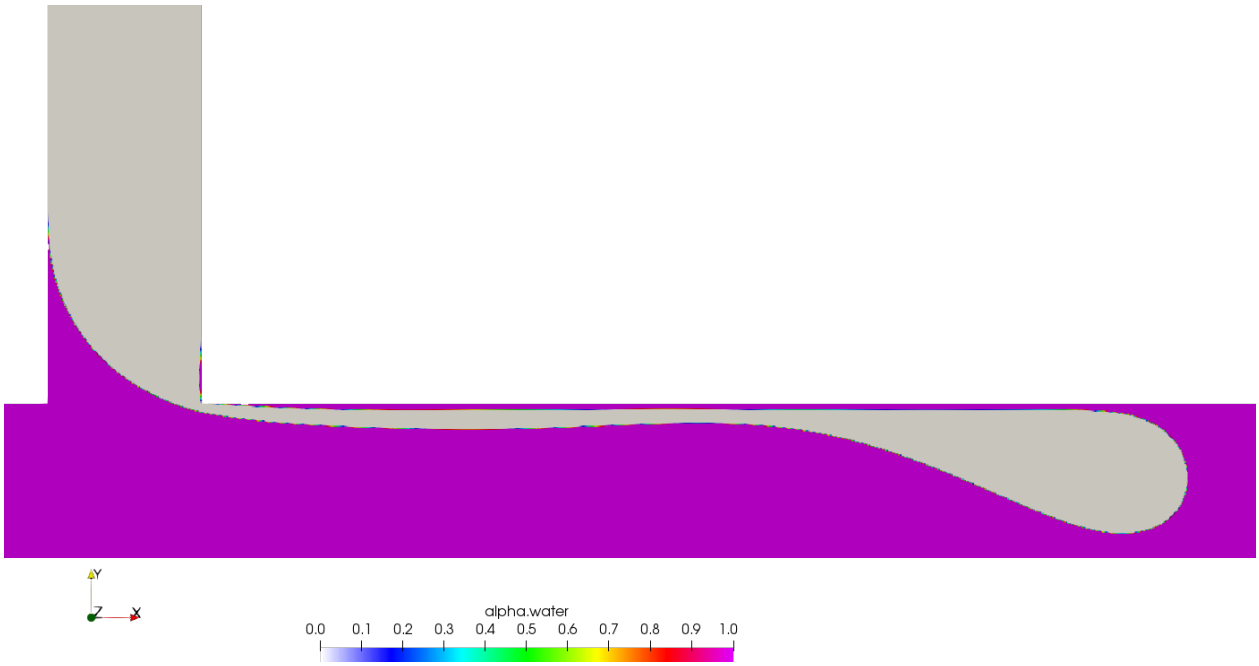

FIGURE 2.17: Simulation of a T-junction with a highly refined 2D mesh of 140 cells per diameter

The total number of cells for the refined mesh is approximately eight times more refined than the base mesh. We have chosen this specific case to illustrate the issue: the bubble does not detach anymore. Instead, a thin neck of gas elongates and the bubble is never released.
We think that the incompressible nature of the solver could make it impossible for the gas bubble to retract when the interface breaks up. Another possible explanation might be the sensitivity of the surface tension force calculation to local grid sizes, particularly at the singularity point at the T-junction where the detachment occurs. In future work, this could be

assessed by conserving the grid size at the corner, while changing the grid refinement level elsewhere. Nevertheless, this method is not very predictable because we are not sure whether the flow parameters are converged on the coarse mesh. Another option adds a kind of buffer at the gas inlet. This zone will allow a recirculation of the gas and give more freedom to the interface in the mixing region. The result is shown at time 0.007s on figure 2.18.

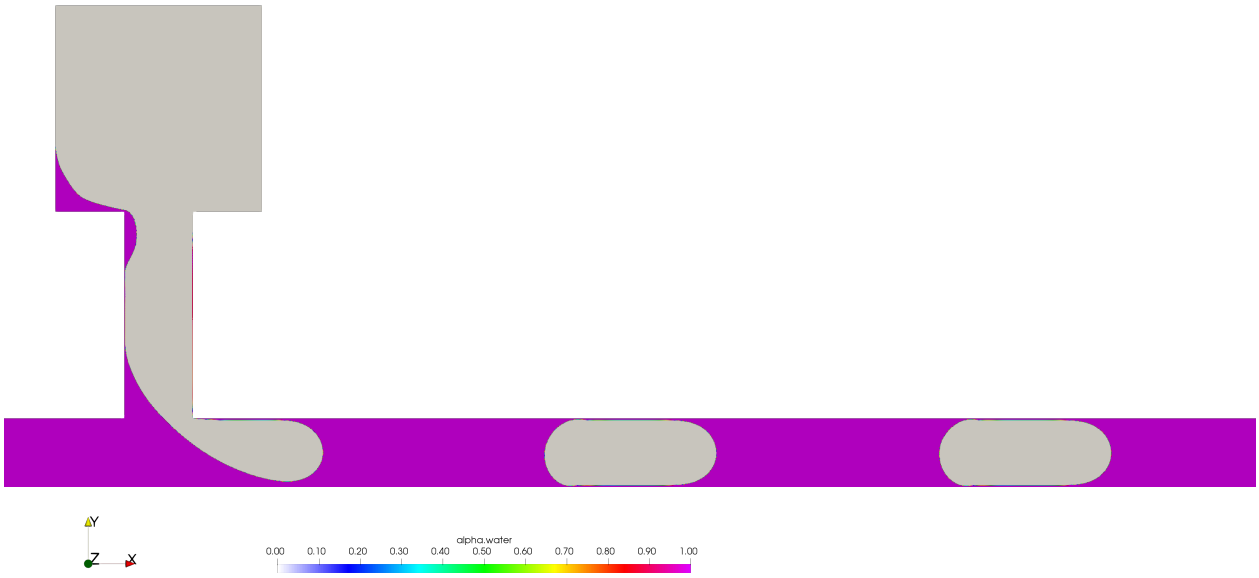

FIGURE 2.18: Simulation of a T-junction with a highly refined 2D mesh of 140 cells per diameter and buffer at the gas inlet

The bubbles generated by this T-junction are no longer symmetrical which is not surprising considering the liquid retention happening on the left-hand side of the buffer. This simulation illustrates how important the question of contact angle is for such microfluidic devices. A 3D simulation with an equivalent level of refinement is required to assess how the result is influenced by the non-significant dimension. Unfortunately, the 2D mesh of figure 2.17 is already more than 1.25 million cells. An equivalent level of refinement on a 3D mesh would mean more than 100 million cells.

2.3.3.5 Results

After the issues presented with mesh refinement, we could not evaluate the dependency of the bubble length on the mesh. However, we still needed some literature data to assess the VOF

solvers performances. To validate the bubbles generated in a T-junction with OpenFOAM®, we compare our results with literature data. Guo et al. [5] worked on a T-junction with a water/air flow at room pressure and temperature. Guo et al. [5] have done both numerical and experimental work. Two gas flow rates and five liquid flow rates were tested, the values of superficial velocities and typical dimensionless numbers are indicated in appendixA. The dimensionless bubble length is plotted against the ratio of gas to liquid superficial velocities in figure 2.21. We obtain a linear relationship as was predicted by Garstecki et al. [22]. Guo et al. [5] have only simulated a two-dimensional plane corresponding to the middle of the channel and no 3D simulation of the T-junction was conducted in this study. According to Guo et al. [5], this difference in flow rates may explain the small difference in bubble lengths.

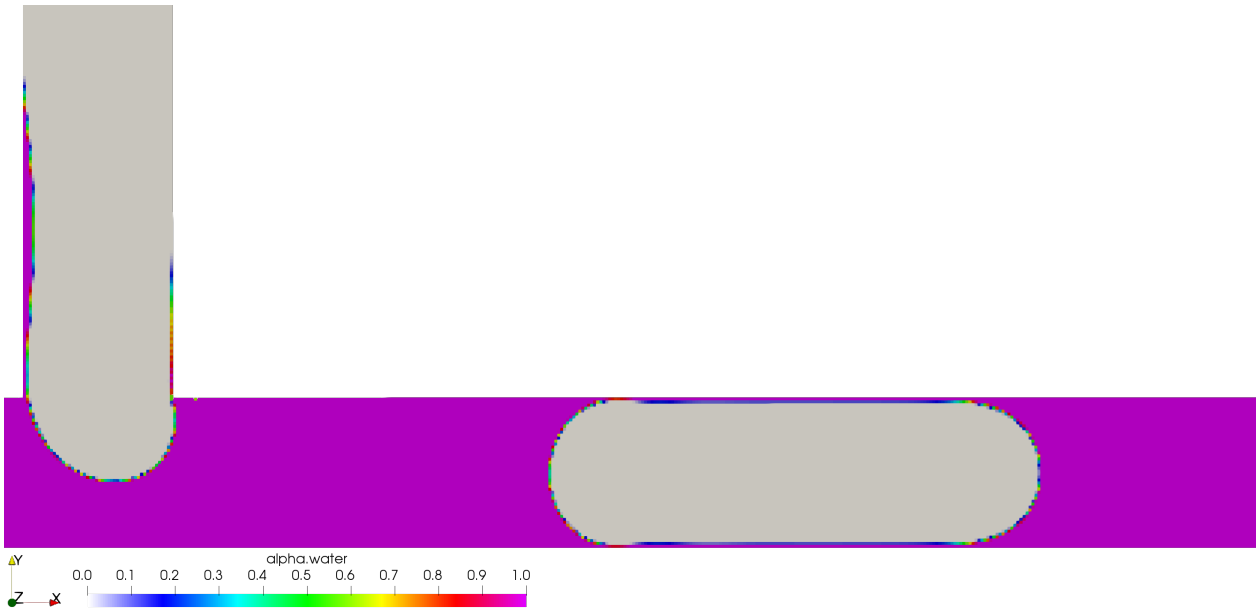

FIGURE 2.19: Volume fraction field and bubbles simulated with `interFlow` after 0.018 s in 2D

Figure 2.19 shows the qualitative shape of bubbles obtained in a two-dimensional simulation. The liquid film can be seen around the bubble on the right, yet, further refinement of the mesh would be required to have at least five cells in the film. Keeping the current level of refinement would most likely lead to relatively large errors in the mass transfer, at least for the contribution of the film. Another strange feature of the bubbles appear in this simulation. After the first bubble is released, the interface is disconnected from the wall in the gas inlet channel. We think this behaviour can be explained by the 2D approximation.
Figure 2.20 shows a plane centered in the middle of the 3D channel. Even though we cannot see the liquid film because the mesh is not refined enough, the result looks more physical than

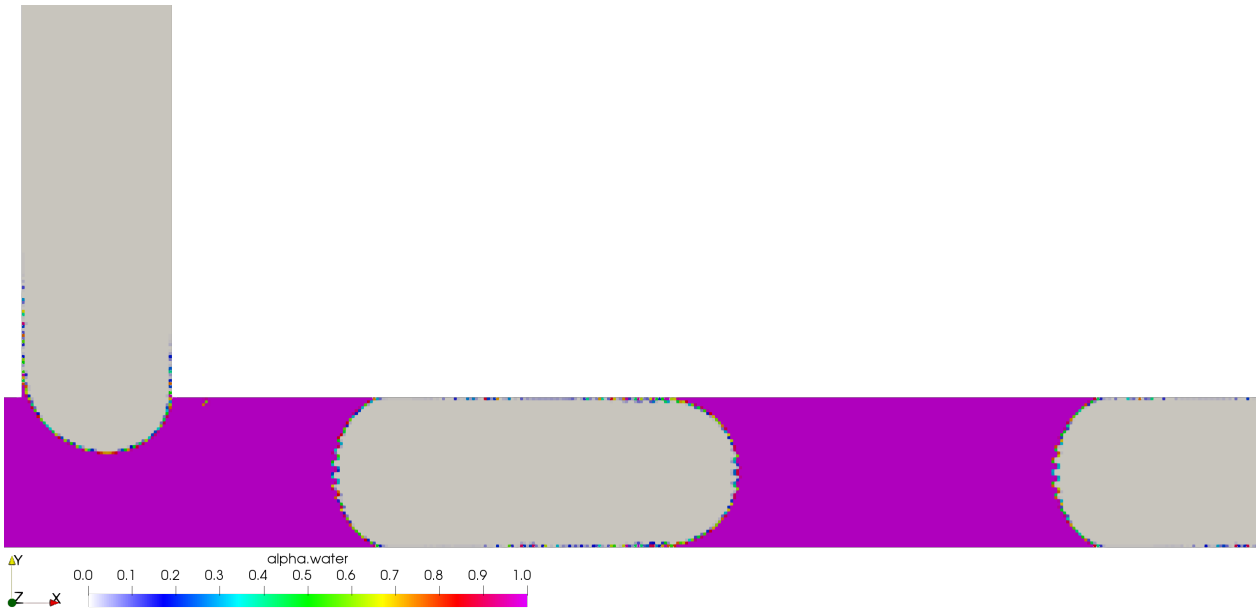

FIGURE 2.20: Volume fraction field and bubbles simulated with `interFlow` after 0.018 s in 3D

in the 2D simulation. The weird liquid film inside the gas channel is no longer present in the 3D simulation. In 2D simulations, we think the interface detaches from the wall because of the lack of surface tension force in the third direction. In the 3D channel, the surface tension force bends the interface to form a cylindrical shape. This shape is more likely to stabilize the bubble and since it touches all four walls, it cannot move anymore. For 2D simulations, the only "connection" between the two sides of the bubble is the cap. That is why an oscillation is more likely to propagate when the interface is disrupted. For each set of superficial velocities, the length of the bubble was measured. The results for the 2D and 3D models are gathered in the graphs 2.21 and 2.22 respectively. Our results are in good agreement with those of Guo et al. However, the bubbles are shorter when performing a 3D simulation. The authors have explained the difference in length between their simulations and their experiments by the difficulty to specify the experimental flowrate. The relationship provided by Garstecki et al. [22] seems to match our results well. The bubble length is globally smaller in 3D than in 2D. This result is noticeable when comparing figures 2.21 and 2.22. Between 2D and 3D, we can also see that there is less disance between the forming bubble and the detached one. Therefore, the bubble release frequency is larger for the 2D simulations than for the 3D. A possible explanation could come from the boundary conditions. In 3D, the square channel offers the possibility to liquid to flow in the corners while the bubble is still growing.

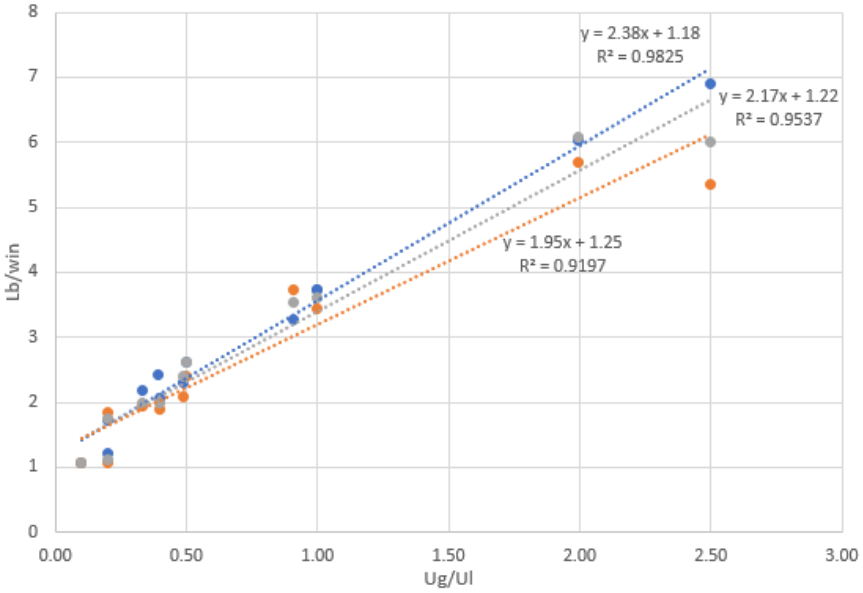

FIGURE 2.21: Bubble length. Orange: experimental work from Guo et al., Grey: numerical work from Guo et al., Blue: numerical work with `interFlow` (2D)

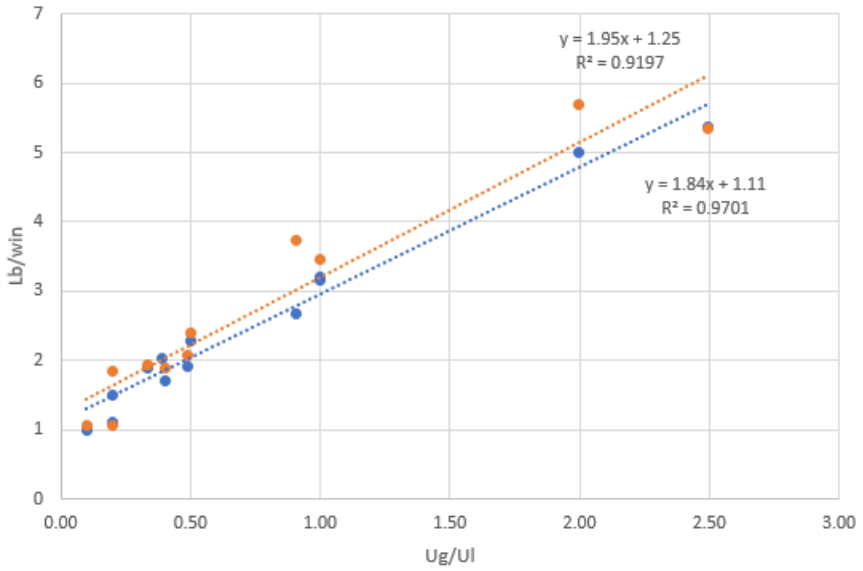

FIGURE 2.22: Bubble length. Orange: experimental work from Guo et al., Blue: numerical work with `interFlow` (3D)

2.3.4 Conclusion

`interFoam` has presented some issues that will most likely impact further developments. The satisfactory results of Taylor bubbles lengths displayed by `interFlow` justify the use of this solver to build the concentration transport on top of it. The question of 2D axisymmetrical

and cyclic simulations has not totally been answered. Some doubts still exist concerning the hability of `interFlow` to be used for these geometries.

2.4 Advecting a concentration field: issues and solutions

This section will present how the major issues of the advection of the concentration field were dealt with. If this task is not done properly, it can become a major source of inconsistencies. As was mentioned in section 1.6.2, the concentration field will be split for each species into two parts, one for each phase. The first part of this work only deals with pure advection. Therefore, the two concentration fields that define a species will not interact with each other. The advection equation of species k is given for phase 1 (for phase 2, the same equations holds by replacing with the adequate subscript):

$$\frac{\partial C_{k,1}}{\partial t} + \nabla \cdot (\mathbf{U} C_{k,1}) = 0 \tag{2.2}$$

In the FVM framework, this equation is integrated over a control volume, typically called cell P of volume V:

$$\int_V \int_{\Delta t} \frac{\partial C_{k,1}}{\partial t} \, dt \, dV + \int_V \int_{\Delta t} \nabla \cdot (\mathbf{U} C_{k,1}) \, dt \, dV = 0 \tag{2.3}$$

After integration over the volume V_i of cell i and a time step Δt, we obtain:

$$\langle C_{k,1} \rangle_{V_i}^{n+1} = \langle C_{k,1} \rangle_{V_i}^{n} - \frac{\Delta t}{V_i} \times \sum_f (\mathbf{n} \cdot \mathbf{U} C_{k,1}^n A)_f \tag{2.4}$$

The main difficulty lies in the sum on the right-hand side: the surface integral is approximated by the face centre value and this approximation is second order accurate. However, we do not have direct access to the face centered value. Thus, the values at the cell centers must be interpolated onto the cell faces to provide the values $\mathbf{U}_f$ or $C_{k,f}$. Different interpolation schemes are available to provide the face centered values from the cell centered values. We will present a few of them that will be used in the following text. All the different schemes presented are used for the interpolation of the passive scalar C_k. There are other schemes for bounded scalars or for vector variables that will not be covered here.

Upwind differencing

Upwind differencing (UD) is perhaps the most simple scheme to interpolate variables. The

idea is to look at the direction of the flow and to directly use the information from the cell located upwind. The notation used here defines the cell centre as P and the neighbour cell centre as N. The value of the variable on the face is then:

$$C_{k,f} = \begin{cases} C_{k,P} & if\ F_f > 0 \\ C_{k,N} & if\ F_f < 0 \end{cases} \tag{2.5}$$

$F_f = \mathbf{n}_f \cdot \mathbf{U}_f$ is the face flux. Considering a simple face f shared by an owner cell P and a neighbour cell N, a schematic of upwind differencing is shown in figure 2.23. The interest of this interpolation scheme is its boundedness: no over or under-shoots occur when advecting a passive scalar. On the other hand, it only offers a spatial first order accuracy and this poor accuracy leads to numerical diffusion when one wants to advect a sharp profile. For this reason, a second order accurate scheme is often preferred.

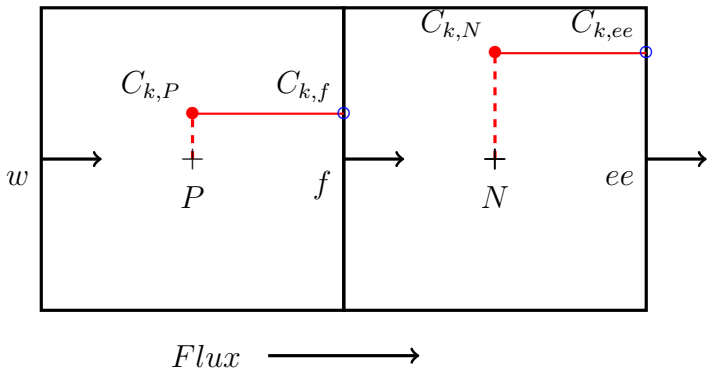

FIGURE 2.23: Schematic of a two-dimensional stencil with the upwind differencing scheme for the interpolation of C_k

Central differencing

Central differencing (CD), also known as linear differencing, uses a distance-based weight to provide second order accuracy for the prediction of the face value. The face value is computed as:

$$C_{k,f} = wC_{k,N} + (1-w)C_{k,P} \tag{2.6}$$

With the weight computed using the distances of the centroids of the cells from the centroid of the face.

$$w = \frac{|\mathbf{x}_f - \mathbf{x}_P|}{|\mathbf{x}_N - \mathbf{x}_P|} \tag{2.7}$$

The weight w is therefore bounded between 0 and 1. The schematic diagram in figure 2.24 illustrates how the face value is obtained in a simple two-dimensional configuration.

This scheme provides a better accuracy than upwind differencing. However, the issue is its

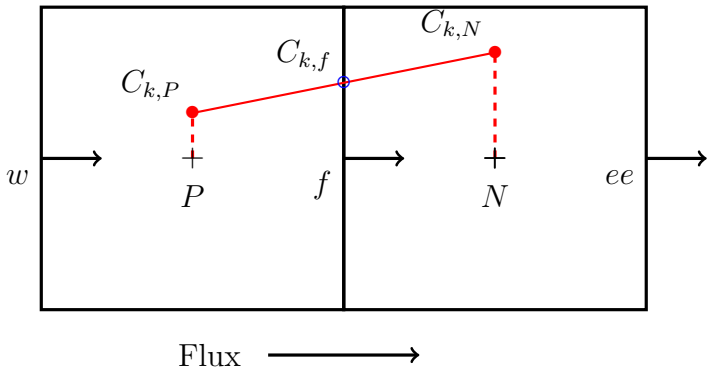

FIGURE 2.24: Schematic diagram of a two-dimensional stencil with the central differencing scheme for the interpolation of $C_{k,f}$

boundedness: schemes with high order of accuracy tend to be oscillatory.

MUSCL

The MUSCL scheme (Monotonic Upstream-centered Scheme for Conservation laws) was developed by van Leer [98–102] in order to provide a second order accurate scheme that offers conditions such as the Total Variation Diminishing (TVD) schemes (see [103]) to limit the over and under shoots. In the next part of the text, we will try to use these interpolation schemes to advect the concentration field, and we will discuss the issues and the need of a new development.

2.4.1 Consistency with the advection of a free surface

Numerical diffusion is a well-known issue when trying to advect a sharp profile. This issue has motivated a lot of numerical developments, including the VOF method. When transporting a concentration field in a two-phase flow, the same issue occurs for the concentration field. Indeed, the preservation of the discontinuity of the interface imposed by thermodynamics, requires the same kind of treatment as free surface flows. There exists an interface where the fluid properties and concentrations will undergo a jump. This interface must coincide with the hydrodynamic interface resulting from the VOF solver, i.e. the interface between the two phases as solved through the liquid volume fraction equation(1.53). If the interfaces do not coincide, it means that artificial mass transfer has occurred because the concentration value is not consistent with the volume fraction. This issue can be seen on a simple test case of a bubble of gas flowing in a liquid channel illustrated on the schematic 2.25.

We consider a dilute species in the liquid phase that does not transfer through the interface and its concentration is homogeneous. Since there is no concentration gradient in the liquid

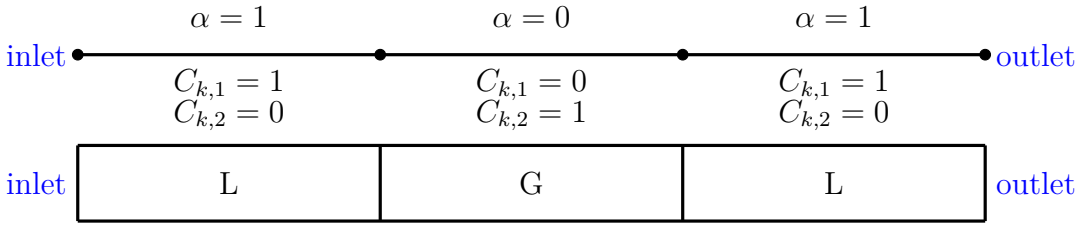

FIGURE 2.25: Schematic of a one-dimensional channel used to test the advection performances of interpolation schemes

phase, it is a purely advective case and therefore, the concentration should follow the shape of the interface. However, the use of an UD scheme to interpolate the concentration onto the cell faces leads to an overdiffused concentration profile. This numerical diffusion spreads the initially sharp concentration profile, making it become non-zero in the gas phase, as shown in figure 2.26.

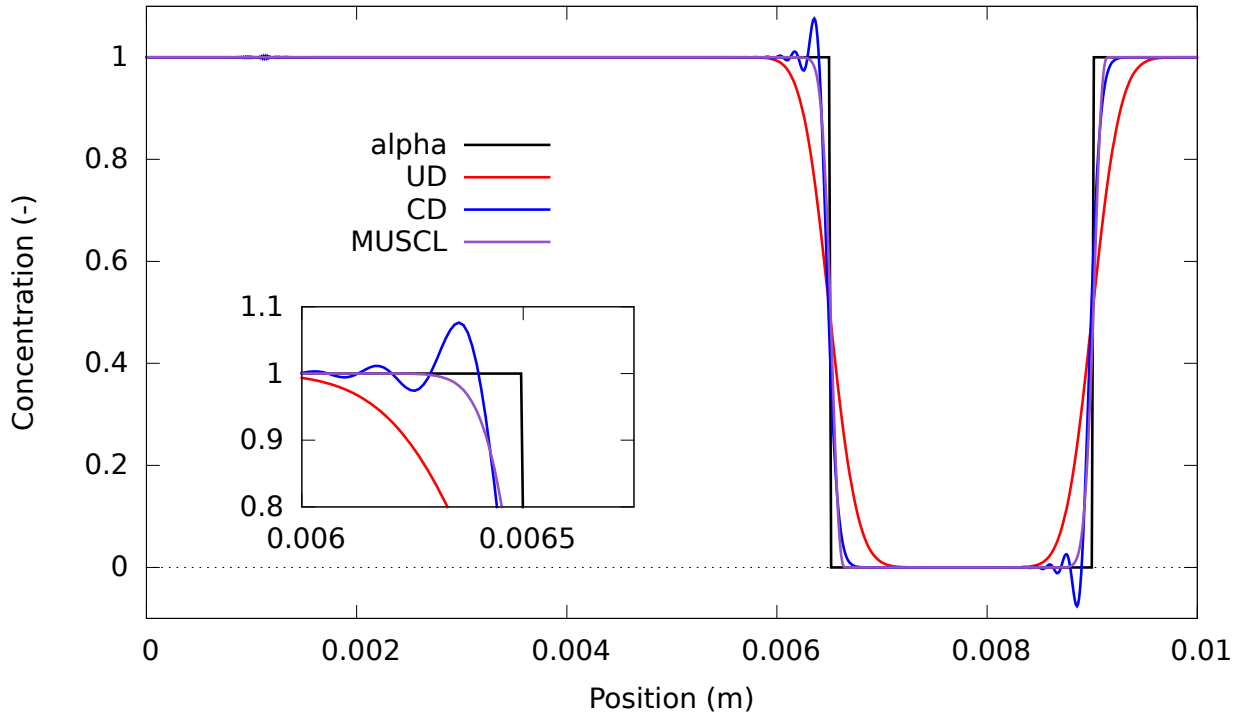

FIGURE 2.26: Comparison of the volume fraction field α and the liquid phase concentration $C_{k,1}$ obtained using different interpolation schemes

In figure 2.26, we can see that the low order UD scheme in red fails to prevent artificial mass transfer. The use of high order interpolation schemes such as CD or MUSCL cannot preserve the sharp profile either. The blue curve standing for CD scheme shows over- and under-shoots of the concentration profile and tends to be oscillatory, which is an issue for

bounded variables. The over and under-shoots result from the inaccurate face concentration prediction of the CD interpolation scheme. They are quite a problem for the simulation since they break the rules of thermodynamics for saturation or provide negative concentrations. The MUSCL scheme is interesting as it avoids over- and undershoots. Furthermore, the concentration profile obtained with a MUSCL scheme is sharper than the one obtained with the UD scheme, thus, artificial mass transfer is reduced. Nevertheless, none of these three schemes give really satisfactory results, i.e. a bounded concentration profile without artificial mass transfer. For this reason, this work has focused on developping an alternate methodology for the transport of concentration consistently with the geometric VOF method `isoAdvector`.

2.4.2 Implicit formulation attempt

The main issue is to determine $(C_{k,1})_f$ in order to respect the consistency with `isoAdvector`. Firstly, relationship (1.42) applied to the VOF equation (1.53) was used to back calculate the weights that would have produced the fluxes. w_α is the linear weight and can be computed as:

$$w_\alpha = \frac{\alpha_f - \alpha_N}{\alpha_P - \alpha_N} \tag{2.8}$$

This weight is then injected into relationship (1.42) to obtain the face value for the concentration field:

$$C_{k,f} = C_{k,N} + w_\alpha (C_{k,P} - C_{k,N}) \tag{2.9}$$

The computation of the face weights is consistent with `isoAdvector` because it will enforce proportionality between the face flux of liquid and the face flux of concentration. However, this method is not applicable to a geometric VOF method such `isoAdvector`. A simple example shown in figure 2.27 illustrates cases where the face weight w_α is not defined.

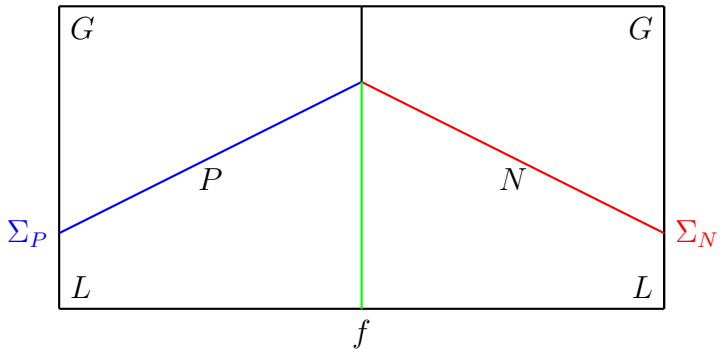

FIGURE 2.27: Schematic of two cells cut by the interface with a volume fraction of 0.5

In the idealized case depicted in figure 2.27, two neighbouring cells P and N with a volume fraction of 0.5 share a face f. A similar situation might also occur in cases with a large curvature. The portion of face f that is immersed in the liquid phase is 0.75. Therefore, α_f is not included between the values of cells P and N. For `isoAdvector`, this configuration is not an issue since α_f comes from relationship (1.65). We could have replaced the undefined weights by some calculated with an UD scheme, which is unconditionaly bounded and stable. However, during tests, too many faces with undefined weights replaced using UD were encountered. This led to an over diffused interface, with a lot of inconsistencies and artificial mass transfer. Thus, another methodology had to be developed specifically for geometric VOF methods such as `isoAdvector`.

2.4.3 Description of a geometric methodology

As `isoAdvector` calculates the amount of liquid that flows through a face, it is consistent to use the phase average concentration from relationship (1.71) to determine the amount of species k that flows through a face during a time step. The phase average is determined from the volume average that is stored at a cell centre and from relationship (1.72):

$$\langle C_{k,1} \rangle_{V_1} = \frac{\langle C_{k,1} \rangle_V}{\alpha} \tag{2.10}$$

The phase average represents the liquid (or gas) concentration. To obtain the face value we multiply it by α_f, since this formulation will return how much of species k inside phase 1 flows through face f:

$$(C_{k,1})_f = \alpha_f \frac{\langle C_{k,1} \rangle_V}{\alpha} \tag{2.11}$$

Following this, the question of which cell centre value ($\langle C_{k,1} \rangle_{V_P}$ or $\langle C_{k,1} \rangle_{V_N}$) should be used is raised. In line with the `isoAdvector` approach, the direction of the flow if followed, so that the upwind cell is used. The basic algorithm is shown below in figure 2.28.
In the algorithm in figure 2.28, `alphaPhi` is the flux returned by `isoAdvector`. The method can be applied to any solver (i.e. `interFoam`) as long as `alphaPhi` is accessible. The algorithm works in parallel and the basic communication function was modified to exchange data only when needed. In the bulk of each phase, a MUSCL scheme is applied to limit numerical diffusion, however, any higher order scheme could be used. The tolerance called `alphaTol` in figure 2.28 should be chosen accordingly to the tolerances of `isoAdvector`, which are used to determine whether the liquid volume inside a cell should be considered as meaningful or not. If the liquid volume is not meaningful, it can be considered as noise left by the advection and

```
scalar Cf = 0;
if (alphaf > alphaTol)
{
      if (alphaPhi > 0 && alphaOwn > alphaTol)
      {
        Cf = alphaf * COwn / alphaOwn;
      }
      if (alphaPhi < 0 &&  alphaNei > alphaTol)
      {
        Cf = alphaf * CNei / alphaNei;
      }
}
else
{
      Cf = 0;
}
return Cf;
```

FIGURE 2.28: Function computing the face concentration

the algorithm should not try to advect concentration in the cell. Since relationship (2.11) requires dividing by the volume fraction, the scheme could become very oscillatory, especially in cases of existing wiggles in the volume fraction field. To mitigate these issues, it was necessary to work at low CFL numbers (≤ 0.1) and use a limiter, for which the development will be presented later.

2.4.4 Parallelization of the algorithm

It is very easy to implement a new interpolation scheme in OpenFOAM® when using the existing framework. The interpolation scheme loops over all the mesh faces and it then distinguishes the case whether the face is an internal face or a boundary face. If the face is a boundary face, it can be part of a coupled patch or not. If the patch is coupled, this means that it is the interface between two processors. For coupled patches, data exchange is performed to give access to the neighbouring field of the patch. It is the field on the other side of the patch that is owned by the neighbouring processor. The interpolation weight is then computed with relationship (1.42). However, both neighbour and owner values are not used for the interpolation. The parallelization must take into account the fact that only the liquid phase concentration is used to compute the face value. Figure 2.29 shows an interface cell next to the processor boundary illustrated by the blue patch. As cell P is an interface cell, our custom scheme is applied and the face value on the patch is computed consistently with `isoAdvector`. On the other hand, cell N is not an interface cell and the face value on the patch has a default value (computed with the van Leer limiter). The boundary field on the patch will then be different for the two processors. Further, the value on the patch must be synchronized when one of the two cells is an interface cell. To do so, the classic function

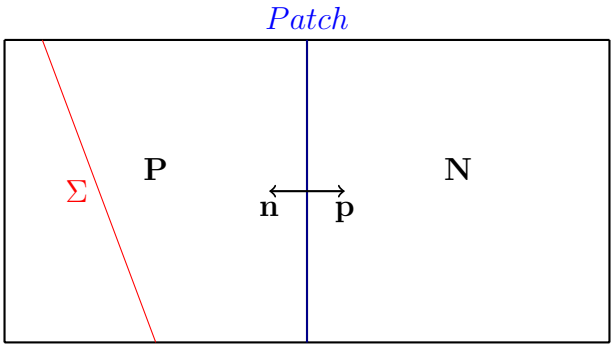

FIGURE 2.29: Representation of two neighbouring cells on two processors with the patch face in blue

that does the parallel synchronization between the cores is modified by adding a condition on the presence of the interface cell between one of the cells. If the processor has an interface cell, then it should not be synchronized with the value on the other processor. Similarly, if the neighbouring processor has an interface cell, its value should be computed with to the custom interpolation scheme.
The question is what happens when the two cells are interface cells ? Let's take a look at figure 2.30 for which the two cells are interface cells.

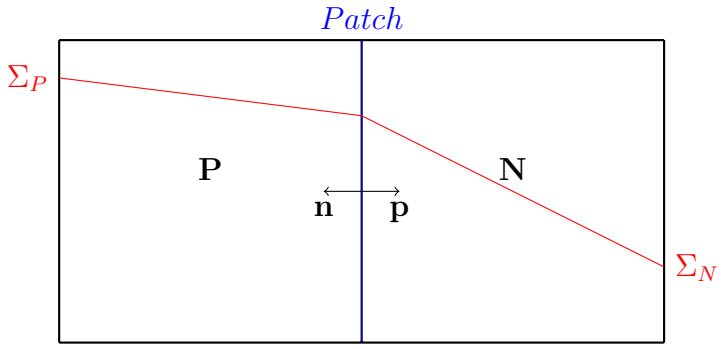

FIGURE 2.30: Representation of two neighbouring cells on two processors with the patch face in blue

The custom scheme is applied on both boundary faces of the patch face in blue. Each processor has an updated face value, however we may wonder if the computed value is the same: the owner and neighbours are swapped. The face normals are depicted by the lowercase letter p and n (they point out of the cell). This means that the flux is the same but with an opposite sign. If the reconstructed flux is positive on the face patch, it means that the local decomposed flux was positive for the left processor and negative for the right processor. Therefore, the computation will, in both cases use cell P values of concentration and volume fraction. In this case, it is not necessary to synchronize because the two processors have the

same face value on their boundary field for the blue patch.

2.5 Diffusing a species without phase change

After presenting how consistency was guaranteed after the introduction of a new interpolation scheme for the face value of the concentration, the diffusion operator present on the right-hand side of equation (1.33) must be dealt with. Indeed, there is no diffusion in the transport equation of the volume fraction field (1.53). If there is a diffusion flux from a bulk cell into an interface cell, consistency with `isoAdvector` will no longer be guaranteed. Three types of corrections for the diffusion operator were developed and will be presented in the following sections. It should also be mentioned that the chemical diffusion of species is performed implicitly in time after the advection, the mass source term and the volume change have updated the concentration field explicitly in time. We follow for that the recommendations of Fleckenstein and Bothe [90] who highlighted the importance of having the species transfer and volume change before the diffusion of species inside the phases, otherwise undershoots could occur because too much species would have diffused before the volume changes. In all the following section, simple test cases will be used to illustrate the issue and the solution proposed. In these test cases, no mass transfer occurs, and the transport of one dilute species present only in the liquid phase is followed. For the sake of clarity, we will drop subscript k for the diluted species. Furthermore, the dilute species is only soluble in the liquid phase and therefore, the gas phase will not be considered. All phase averaged concentrations implicitly refer to the liquid phase average concentrations. Averaged concentration over a control volume V_i are written $\langle C \rangle_{V_i}$ and liquid phase average concentration in this control volume $\langle C \rangle_{V_i,L}$.

2.5.1 Correction of the diffusion coefficient

The first method consists of modifying directly the diffusion coefficient to avoid diffusion. We use it only for cases where there is no phase change and only a concentration field inside a specific phase must be advected. This is physically relevant to cases where a given species is injected in a phase but will not transfer into the other phase, which can occur, depending on the temperature and pressure conditions. In this case, the easiest way to avoid inconsistencies introduced by diffusion is cutting off the diffusion coefficient on these faces. Let's consider a

1D structured stencil where the diffusion equation has been integrated as shown in figure 2.31. The sketch represents a 1D case. We remind the reader that OpenFOAM® cases are always 3D. For this 1D case, all fluxes through y and z faces are canceled as `empty` boundary conditions are applied.

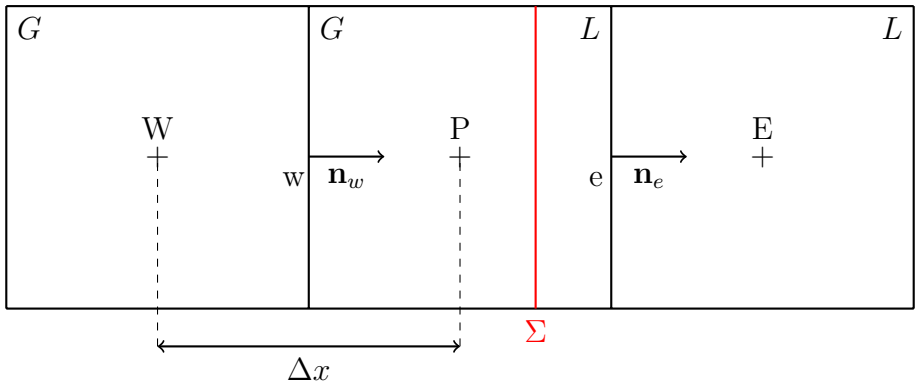

FIGURE 2.31: Simple 1D uniform structured stencil for the integration of the diffusion equation

Cell P in figure 2.31 is cut by the interface Σ. If there is a diffusion flux through face w, the volume fraction of cell E and the concentration of cell E will not change by the same amount during a time step. The idea is thus to impose $D_w = 0$. This correction is conservative and is also consistent with the two-field approach. Indeed, in the two-field approach, the diffusive fluxes inside the bulk phase and the diffusive flux at the interface between phases are separated. In a case where there is no phase change, there is no diffusion fluxes at the interface. Thus, cutting off the diffusion fluxes occurring inside an interface cell will only make a small deviation in the interface cell. This very simple correction is only valid when there is no phase change. When there is phase change, the diffusion cannot simply be cut off, since, otherwise species transferring from the other phase will not be able to flow through the accepting phase. This is because the diffusion flux at the interface is computed as a volumetric source term.

2.5.2 Correction of the diffusion fluxes

We begin with a uniformly distributed species to describe the issues and the solution. Later, another test case with a slug of uniform concentration is also used. The methodology presented here can be applied to both cases, with or without concentration gradients. The

starting point is the transport of species k described by the diffusion equation:

$$\frac{\partial C}{\partial t} = \nabla \cdot (D \nabla C) \tag{2.12}$$

and is discretised implicitly in time:

$$\langle C \rangle_{V_i}^{n+1} = \langle C \rangle_{V_i}^{n} + \frac{\Delta t}{V_i} \times \sum_f (D \ \mathbf{n} \cdot \nabla C^{n+1} A)_f \tag{2.13}$$

Figure 2.31 shows three 1D cells of a structured uniform mesh. The interface between the gas G and the liquid L is shown in red. We drop the brackets and replace the volume V_i of cell i by its corresponding letter. The concentration gradients on faces e and w are then:

$$(\nabla C)_w^{n+1} = \frac{C_P^{n+1} - C_W^{n+1}}{\Delta x} \tag{2.14}$$

$$(\nabla C)_e^{n+1} = \frac{C_E^{n+1} - C_P^{n+1}}{\Delta x} \tag{2.15}$$

The interface cell P is partially filled with liquid and therefore, $C_P^{n+1} < C_E^{n+1}$ (since there is no mass transfer). However, $C_{E,L} = C_{P,L}$ because the species is perfectly mixed in the liquid phase. There is no concentration gradient in the liquid and therefore, no chemical diffusion should happen. If the diffusion equation is solved using the volume average concentration, the difference in volume fraction will create artificial diffusion. To tackle this problem, the phase average can be used to compute the diffusive fluxes. It is consistent with the two-field approach since it is the concentration gradient inside the phase that must promote chemical diffusion. The new equation can be solved to find the phase average concentration:

$$\langle C \rangle_{V_i,L}^{n+1} = \langle C \rangle_{V_i,L}^{n} + \frac{\Delta t}{V_i} \times \sum_f (D \ \mathbf{n} \cdot \nabla C^{n+1} A)_f \tag{2.16}$$

$V_{i,1}$ corresponds to the volume of phase 1 inside cell i. The new face gradients of figure 2.31 are expressed in terms of phase average concentrations:

$$(\nabla C)_w^{n+1} = \frac{1}{\Delta x} \left(\frac{C_P^{n+1}}{\alpha_P^{n+1}} - \frac{C_W^{n+1}}{\alpha_W^{n+1}} \right) \tag{2.17}$$

$$(\nabla C)_e^{n+1} = \frac{1}{\Delta x} \left(\frac{C_E^{n+1}}{\alpha_E^{n+1}} - \frac{C_P^{n+1}}{\alpha_P^{n+1}} \right) \tag{2.18}$$

Once the diffusion equation is solved and the new time step phase average concentration is obtained, the new time step volume average concentration is computed using relationship (1.72) together with the new time step volume fraction field.

To illustrate the efficiency of this method, a new test case for which the concentration of the dilute species is not uniform is used. A 1D structured mesh is used for which the channel is $L = 0.01\,\mathrm{m}$ long refined with 1000 cells. The interface moves at $0.01\,\mathrm{m\,s^{-1}}$ and is initially located at $0.2505L$. There are three species, the liquid is water, the gas is air and there is also a species diluted only in water. The diffusion coefficient of the diluted species is set to $10^{-6}\,\mathrm{m^2\,s^{-1}}$, which is much larger than typical values for diffusion coefficients in liquids. This choice was made on purpose to amplify potential issues. The diluted species in water does not cross the interface because no mass transfer occurs. Therefore, the diluted species is confined in the liquid phase. Its saturation concentration is set arbitrarily to $1\,\mathrm{kg\,m^{-3}}$.
The concentration of the dilute species is initialized as a step profile. The concentration is at saturation between $0.1L$ and $0.2L$ and zero everywhere else. As the diffusion coefficient is large, species will rapidly diffuse in both directions, towards the interface and backwards to the channel inlet. Figure 2.32 below gathers the information of the test case:

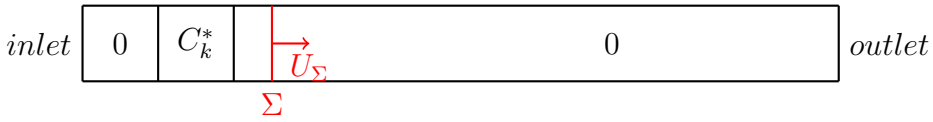

FIGURE 2.32: Schematic of the test case for the diffusion equation

As presented in the former section, in a cell cut by the interface, the phase average concentration and the volume average concentration do not coincide because the volume of liquid is smaller than the volume of the cell. The classical FVM volume average variable is used to solve the diffusion equation, we end up with the red concentration profile given on figure 2.33 which shows the volume average concentration profiles are plotted at 0.5s:
Both concentration profiles are volume average concentration profiles. In red, it is the concentration profile computed using the volume average concentration for diffusion. In blue, it is the concentration profile computed using the phase average concentration. The interface position is shown in black with the curve called "alpha". It can be seen that the global shape of the curves look very similar however, the profiles near the interface diverge. The red profile displays a decrease before showing a spike at the interface, which comes from the direction of the face gradient. As the volume fraction in the interface cell is smaller than unity, the volume average concentration of the interface cell is smaller than the one of the neighbouring cell. This is true before steady state is reached since the concentration needs time to reach the interface. At steady state, the maximum concentration is reached at the interface because the diluted species cannot transfer through the interface.
At 0.5s, the concentration profile is established such that the interface concentration is maximum. However, as the volume fraction of the interface cell is always smaller than one, a

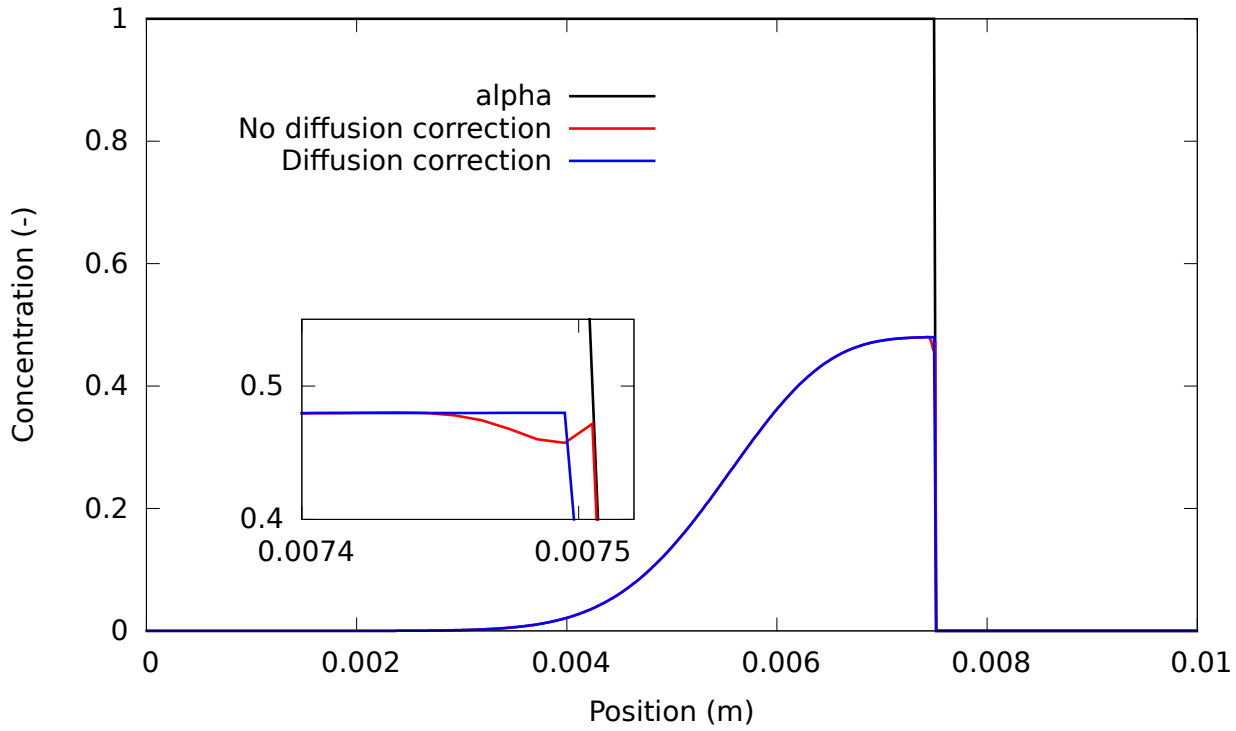

FIGURE 2.33: Non-dimensional volume average concentration profiles at $0.5s$

gradient of volume average concentration will always exist. This explains why the red concentration profile will always show a kind of wave near the interface: there is large diffusive flux resulting from the concentration gradient. This issue is illustrated well when plotting the phase average concentration instead of the volume average concentration.

The red curve displays the same kind of decrease in the interface region. The volume fraction in this zone equals one, which is why the phase average and volume average are equal. At the interface, the spike in the concentration profile is much larger than in the volume average concentration profile. This is expected because the volume fraction is smaller than one in the interface cell: the volume average is divided by a number smaller than one. Nonetheless, a spike of concentration at the interface is not physical since the diffusion is supposed to smoothen the concentration profile. In both figures 2.33 and 2.34, the blue curve entitled "diffusion correction" displays a much better profile near the interface. These blue curves were obtained when the diffusion equation is solved in terms of phase average: there is no concentration gradient of phase average on the face when steady state is reached. This basic test case shows the importance of the phase average when solving for diffusion in a two-field approach. For a single field approach, the issue is not the same since the concentration field is unique, but not necessarily continuous.

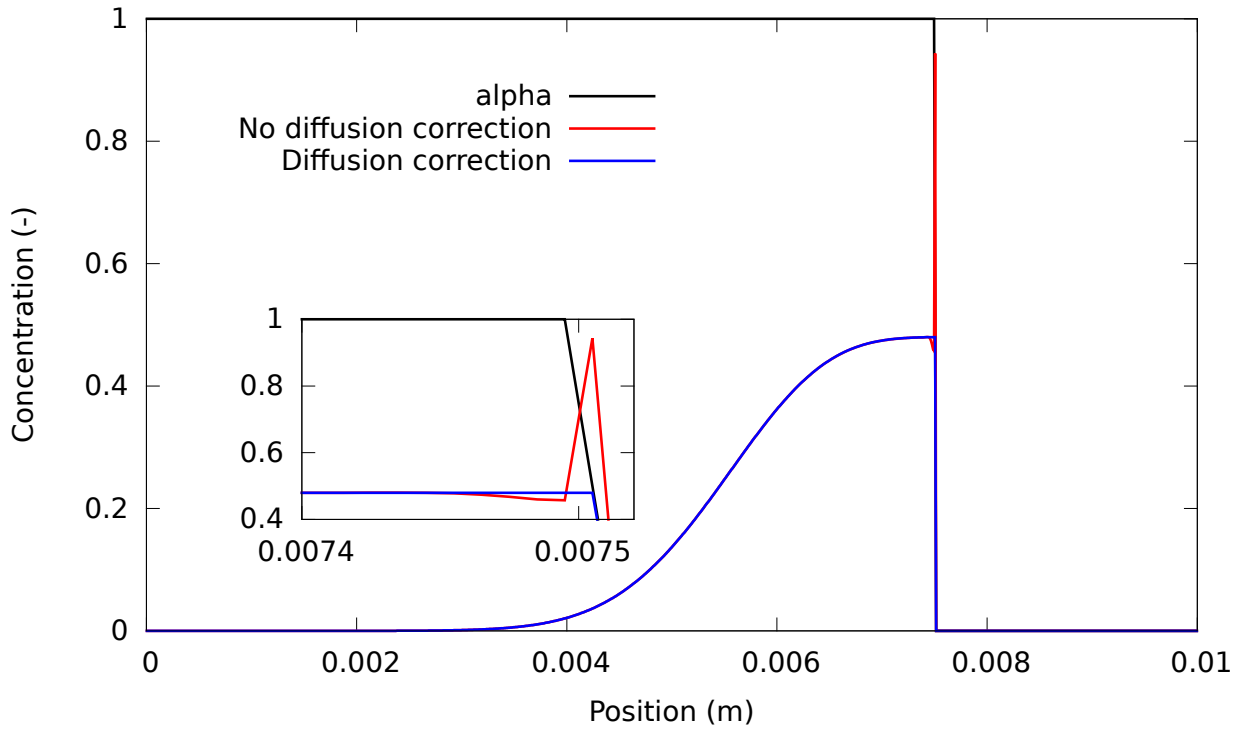

FIGURE 2.34: Non-dimensional phase average concentration profiles at $0.5s$

2.5.3 The deferred correction: an attempt to improve stability

This section aims at presenting a new idea based on an explicit correction of the diffusion matrix. Before changing a variable from volume average to phase average concentrations, the diffusive matrix is corrected directly once it is assembled (after mass transfer). However, this is very timely and also there is loss of matrix symmetry. The linear solvers had to be changed and the overall performances were far worse. To avoid the matrix manipulation, we have decided to use an additional volumetric source term that is explicit in time applied on the right-hand side of the diffusion equation. The objective of this source term is to act as a diffusion correction presented in section 2.5.2. This correction increases or decreases the face concentration gradient according to the phase average concentration. The developed form of the diffusion equation 2.13 is:

$$\left(C_P^{n+1} - C_P^n\right) \frac{V_i}{\Delta t} = D_e (\nabla C)_e^{n+1} A_e - D_w (\nabla C)_w^{n+1} A_w$$

Equation 2.14 and 2.15 can be identified within equations 2.17 and 2.18. To do so, the part that will be in the matrix is separated from the correction of the volume fraction field:

$$\Delta x(\nabla C)_w^{n+1} = \left(C_P^{n+1} - C_W^{n+1}\right) + C_P^{n+1}\left(\frac{1}{\alpha_P^{n+1}} - 1\right) - C_W^{n+1}\left(\frac{1}{\alpha_W^{n+1}} - 1\right) \tag{2.19}$$

$$\Delta x(\nabla C)_e^{n+1} = \left(C_E^{n+1} - C_P^{n+1}\right) + C_E^{n+1}\left(\frac{1}{\alpha_E^{n+1}} - 1\right) - C_P^{n+1}\left(\frac{1}{\alpha_P^{n+1}} - 1\right) \tag{2.20}$$

The trick is now to switch from the new time step value to the old time step to have a time explicit correction:

$$\Delta x(\nabla C)_w^{n+1} \approx \left(C_P^{n+1} - C_W^{n+1}\right) + C_P^{n}\left(\frac{1}{\alpha_P^{n}} - 1\right) - C_W^{n}\left(\frac{1}{\alpha_W^{n}} - 1\right) \tag{2.21}$$

$$\Delta x(\nabla C)_e^{n+1} \approx \left(C_E^{n+1} - C_P^{n+1}\right) + C_E^{n}\left(\frac{1}{\alpha_E^{n}} - 1\right) - C_P^{n}\left(\frac{1}{\alpha_P^{n}} - 1\right) \tag{2.22}$$

The deferred correction is interesting because it does not affect the matrix, it is still symmetric and diagonally dominant. The diffusive part of the equation is still performed implicitly, and only the right-hand side of the equation contains the correction. This method avoids switching from volume to phase and back to volume averages. On the other hand the correction can fail to correct "enough" the face concentration gradients. This method has been tested on other cases, we were able to reproduce a CD interpolation scheme with an implicit part using a UD interpolation scheme, plus an explicit correction, the hybrid advection equation gave almost the same results as the linear solver using directly a CD scheme. Unfortunately, the implementation of diffusion correction was more difficult, and we could not successfully use the method. That is why the correction of the diffusion fluxes is used in the remainder of the work.

2.5.4 Implementation of the transport equation

The final implementation of the new algorithm makes use of both volume average and phase average concentrations as it was presented in the previous section 2.5.2. This implementation also integrates limiters to avoid over- and under-shoots of the concentration field. The flowchart describing the algorithm is shown in figure 2.35.

The major improvement of this algorithm is the statement "bounded", which is used to verify if the advection step has produced unboundednesses in the concentration field. Limiting the face concentration is not trivial because it can take any random positive value depending on the system, the flow etc. To derive a limiter, the definition of the phase average concentration

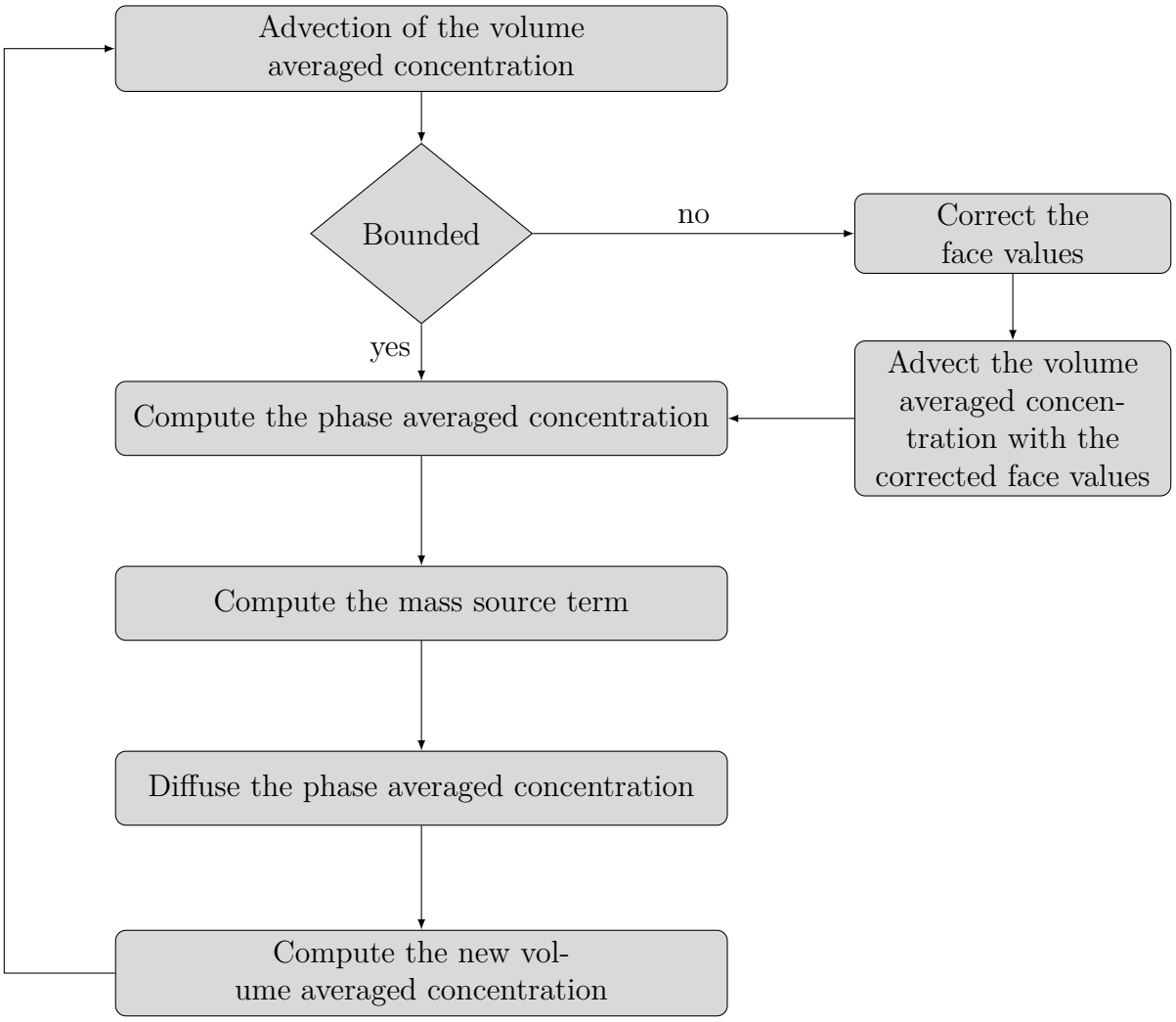

FIGURE 2.35: Flowchart of the global algorithm for the transport of concentration

and the thermodynamic value of the saturation of the liquid phase are used. The phase average represents the concentration of a given species inside the liquid or gas phase of the cell. If there is only one species, it will represent a kind of density since the species is alone in its phase. On the other hand, the saturation is the limited by thermodynamics and it imposes the maximum concentration in a mixture. It depends on the other species of the mixture, but also on temperature and pressure. If we compute the ratio between the phase average concentration and the saturation limit is computed. This degree of filling represents how much species the phase can still accept. The creation of under- or over-shoots by the advection process can be evaluated. This is useful when dealing with cells that are close to the saturation or almost empty of fluid. However, it is not possible to limit the concentration of a cell when the species is still being transferred and the phase is far from being saturated. Because there are no ways of limiting the concentration other than this physical limit. In the algorithm, the logical statement "bounded" uses the degree of filling of phase 1 to assess

the "space" left for species k:

$$\text{degree of filling} = \frac{\langle C_{k,1} \rangle_{V_1}}{C^*_{k,1}} \tag{2.23}$$

The sequence of the "bounded" statement is described with the flowchart in figure 2.36.

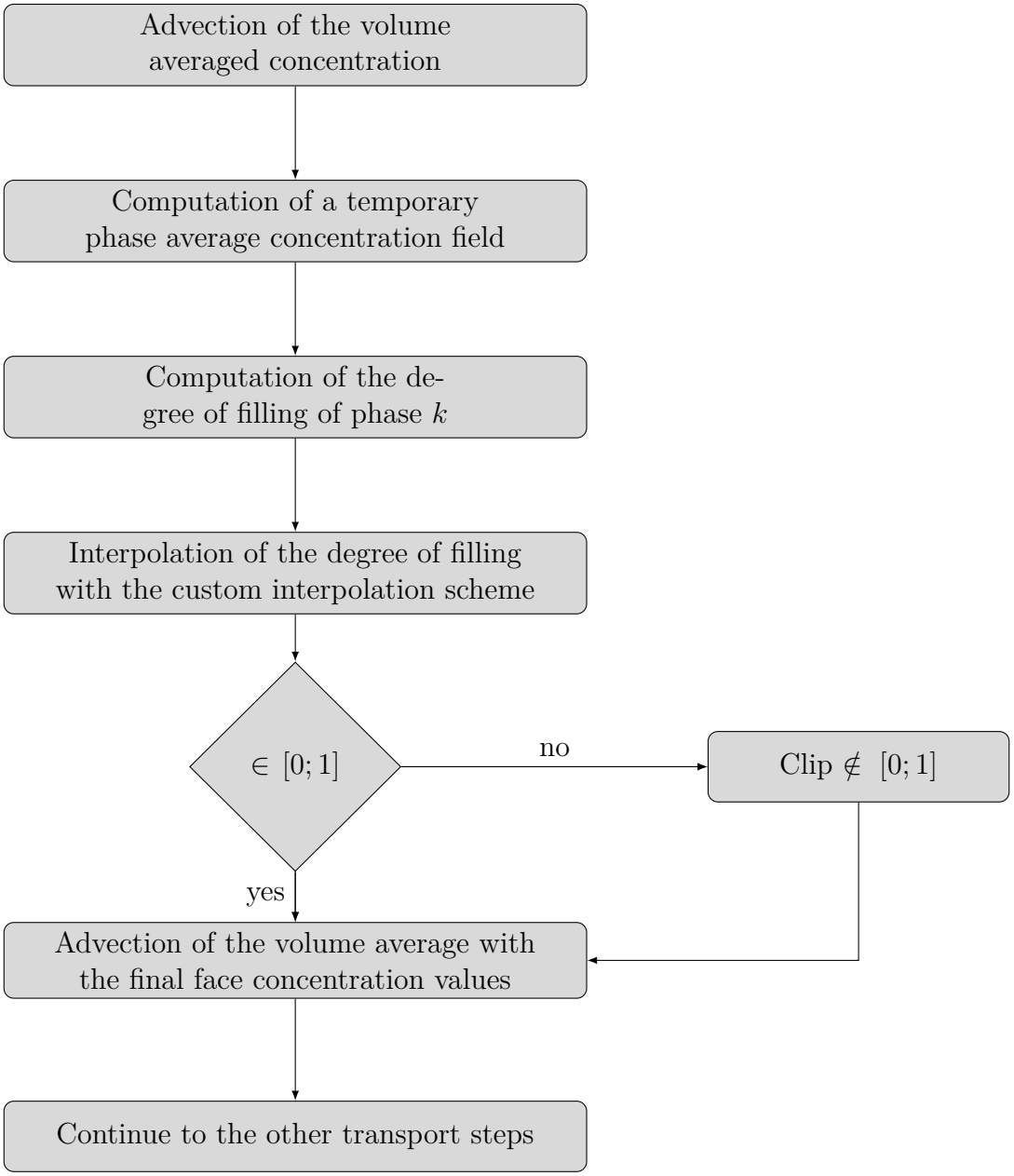

FIGURE 2.36: Flowchart for the correction of the advection process

The important part in the correction of the advection step is the evaluation of the unboundedness. The bounded nature of the "degree of filling" is used in order to verify how the interpolation scheme produces over- and under-shoots since the degree of filling comes from

the phase average concentration, the interpolation scheme is slightly modified, and the degree of filling value in the upwind cell is multiplied by the surface fraction field. The result gives information on how much the face is "saturated" by species k. The degree of filling of the face cannot be negative nor can it be greater than one. There are two options to bound the face values. The first is to clip values that are negative and greater than one; however, this may create a conservation error. The second option is to redistribute the excess of concentration (what is over the saturation concentration) in the neihgbouring cells. In the current implementation, the clipping option was chosen for two reasons. Firstly, because `isoAdvector` uses a clipping option and it is compulsory to be as consistent as possible with `isoAdvector`. The other reason comes from the origin of the unboundednesses. The error occurs because the volume average concentration is divided by the volume fraction field to obtain the phase average concentration. When the cells are almost empty and the volume fraction is close to zero, any small error on the volume fraction has a large impact on the phase average concentration. Redistributing this error does not produce a better advection because the error does not have any physical meaning in the first place. The comparison of results with and without this limiting procedure will be addressed later in simulations of T-junctions.

2.6 Validation of concentration transport without phase change

2.6.1 Generic test cases

The first case is used to test the advection implementation and is the same case introduced in figure 2.25 adapted in 2D and 3D. 1D channels give perfect results, in terms of consistency with `isoAdvector` therefore, it is necessary increasing the complexity to really assess the algorithm performances. 2D and 3D results of developed Taylor flow (without bubble generation) are presented. Two important quantities are monitored. The first one is the total deviation of the concentration from the saturation concentration:

$$L_1 : \sum_i \left| \alpha_i - \frac{\langle C_{k,1} \rangle_{V_i}}{C^*_{k,1}} \right| \tag{2.24}$$

Since there is only advection and the phase average concentration is initially equal to the saturation concentration, this norm L_1 must stay low. The other quantity is infinite norm:

$$L_\infty : \max\left(\left|\alpha - \frac{\langle C_{k,1}\rangle_V}{C^*_{k,1}}\right|\right) \tag{2.25}$$

Using two different norms is helpful to analyze where the error is located. A large L_1 norm can be explained by small errors in each cell, but on many cells. On the other hand, it can also be a large error in a unique cell.
Figure 2.37 shows the comparison of liquid concentration fields in Taylor flow forupwind differencing, MUSCL and the custom interpolation scheme.

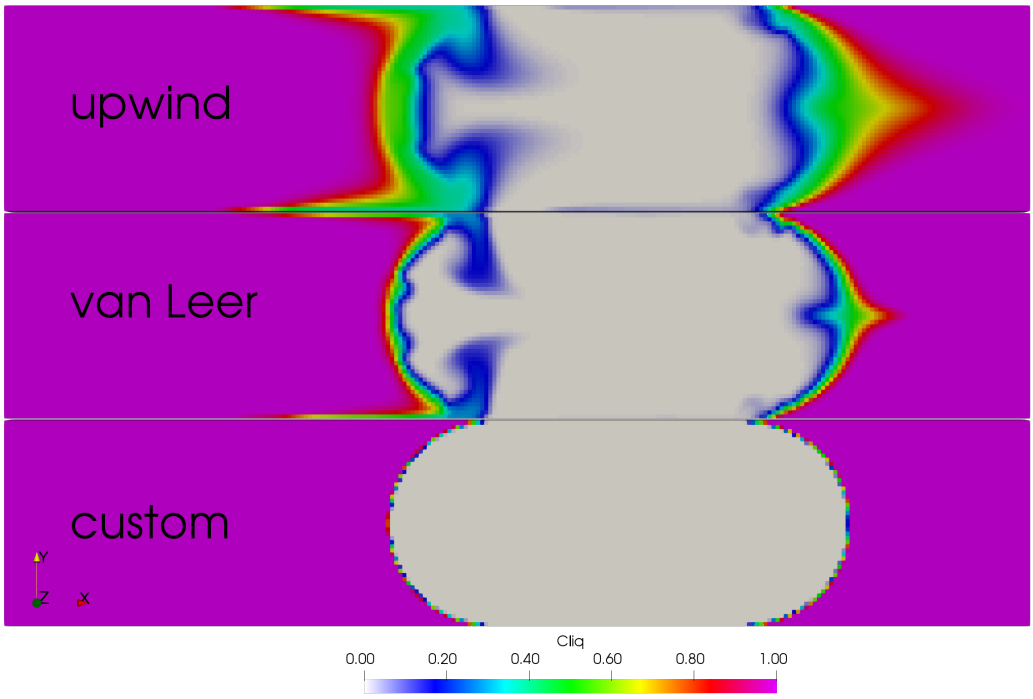

FIGURE 2.37: Liquid concentration field obtained with three different interpolation schemes for the face values

It can be seen once again that upwind differencing and MUSCL fail to provide a sharp interface for the liquid concentration. In two dimensions, the error caused by numerical diffusion is much more troublesome than in 1D. The number of cells concerned by inconsistencies is large, the liquid phase concentration field will be non-zero in many cells. On the other hand, the custom scheme allows a consistent interpolation of the concentration field with `isoAdvector`.

2.6.1.1 Mesh sensitivity analysis

To analyze the performance of the interpolation method, the errors for different cases (2D and 3D) will be compared. The first case corresponds to the channel in figure 2.25 transposed into a two dimensionnal case. Three levels of refinement are compared to evaluate the impact of spatial discretisation.

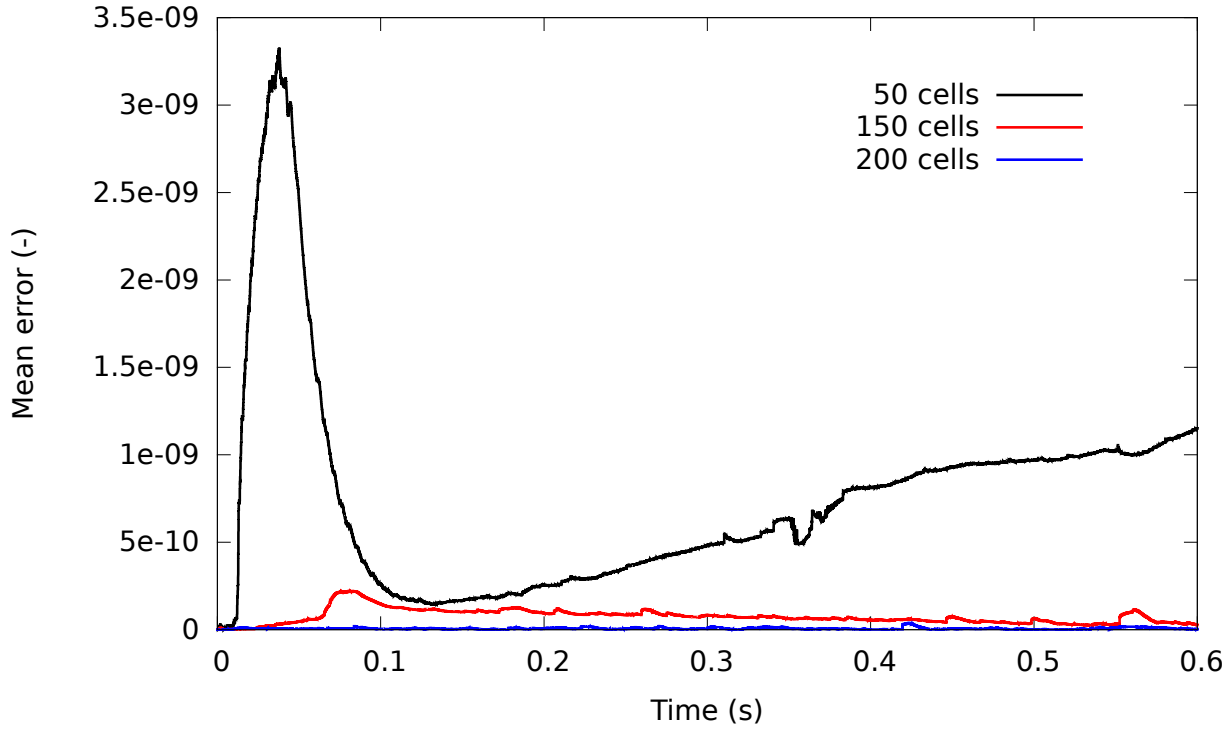

FIGURE 2.38: Comparison of the mean error value for three levels of refinement

To allow a relevant comparison between meshes, the error on the graph corresponds to the L_1 norm 2.24 divided by the total number of cells, giving the mean value of the distribution. The trend changes from the 50 cells mesh to the 200 cells per diameter mesh, shown in red. For the 50 cells mesh, a large increase of the error occurs before 0.1 s and then the error finally decreases. This large error seems to appear after the bubble has taken its final shape and starts mowing in the channel. The fact that this spike is smaller for other levels of refinement must be linked to the better performances of `isoAdvector` on a refined mesh. The error is increasing with time for the 50 cells mesh, while it decreases for the two other levels of refinement. We believe that this might be attributed to the finer mesh, which helps prevent the propagation of the error caused by the customized interpolation method. Nevertheless, the low error generated by the method justifies its use without compromising the results from mass transfer or chemical reaction.

2.6.1.2 3D simulations

Figure 2.39 shows the mean L_1 error variations with time for the test case in figure 2.25 but in three dimensions compared to the same results obtained in two dimensions.

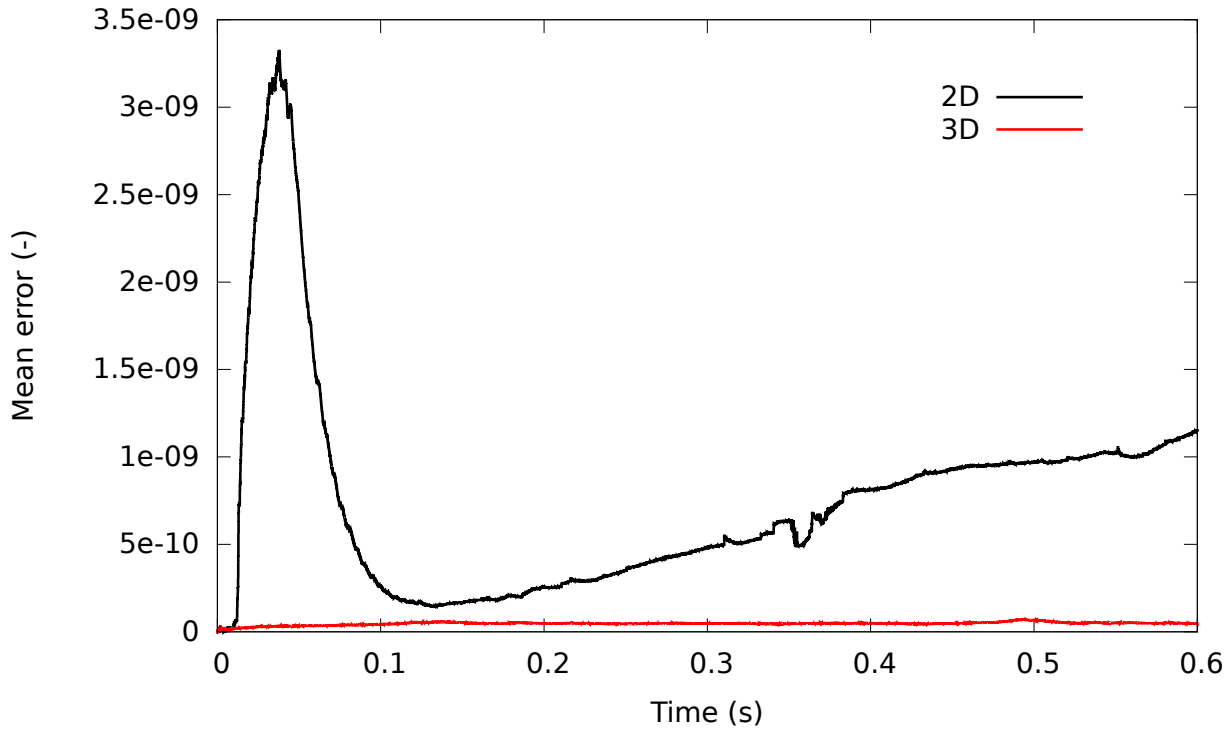

FIGURE 2.39: Comparison between 2D and 3D simulations of the mean error value

It is worth noting that the overall trend differs significantly from the 2D simulations. Apart from some sporadic peaks, the error is much more steady for the 3D model and the order of magnitude is also reduced. The results are improved by an order of magnitude for the 3D simulation, the imrovement is linked to the boundary conditions at the walls and the better results obtained with `isoAdvector`. As the interface advection is more stable, the concentration transport is also enhanced. Figure 2.40 shows the maximum error variations from 2D and 3D simulations. The order of magnitude is similar for the maximum error with more oscillations in 3D.

This is not surprising since the "empty" boundary condition for the non-significant direction was replaced by a wall boundary condition. To confirm the hypothesis of a more appropriate boundary condition, figure 2.41 shows the deviation field $\alpha_i - \frac{\langle C_{k,1} \rangle_{V_i}}{C^*_{k,1}}$ of three different cross-sections of the 3D case compared with the 2D results. The planes are defined by the normal vectors: at the top there is the plane with normal $(0, 1, 0)$, the second one $(0, 0, 1)$ and third $(0, 1, 1)$. The last case at the bottom is the 2D case.

The intriguing aspect lies in the distribution of the error inside the domain. For the 2D case,

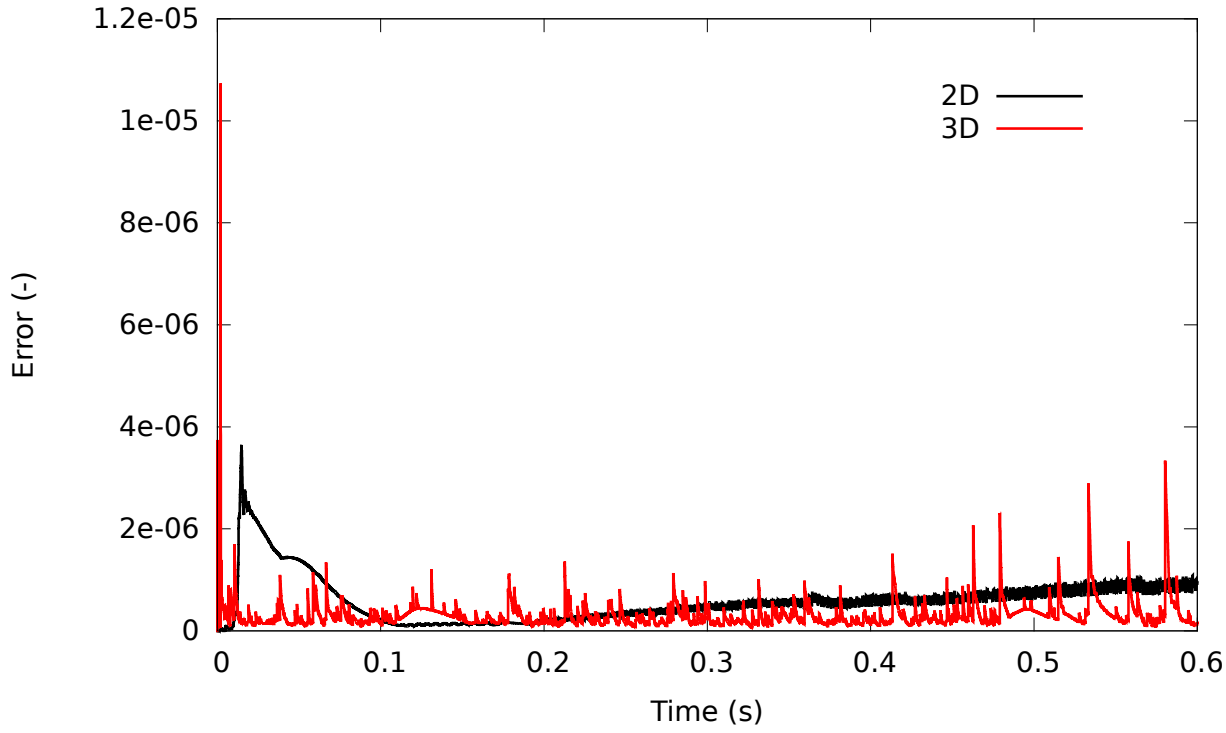

FIGURE 2.40: Comparison between 2D and 3D simulations of the maximum error value

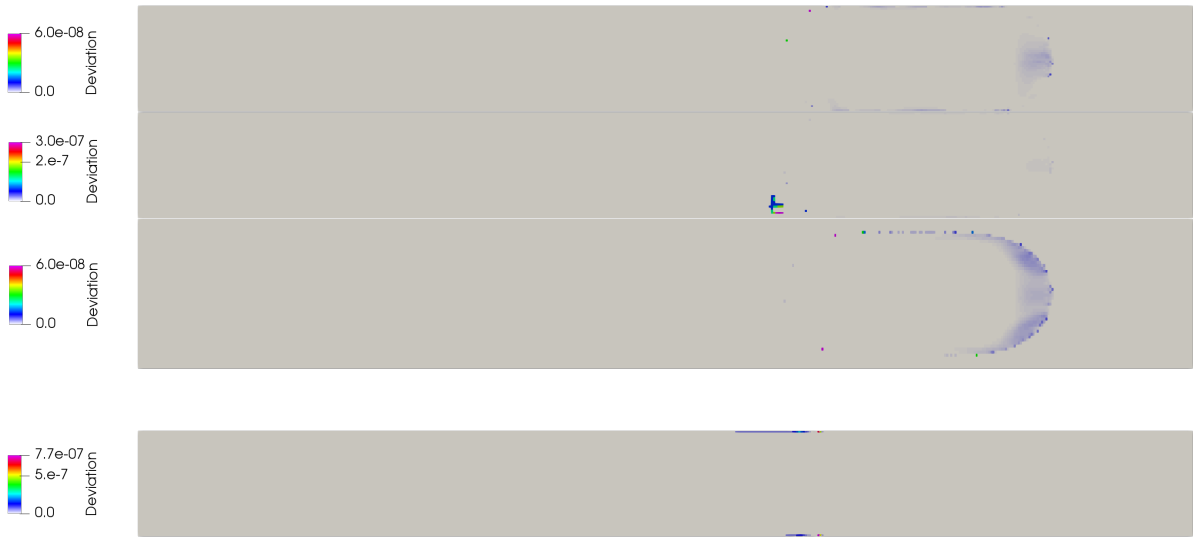

FIGURE 2.41: Comparison of the 3D (top) and the 2D (bottom) error distributions in a straight channel

the principal error occurs along the walls of the channel. For the 3D configuration, the error is dispersed more evenly inside the gas bubble which shape can be identified in the blueish region near the channel outlet. It is also worth mentioning that the volume fraction in the bubble may not be exactly zero, depending on the tolerances chosen for `isoAdvector`. Some very small volumes of liquid can remain after the interface has left the cell. Of course, these

small liquid volumes are not meaningful and represent a volume fraction smaller than the selected tolerances. In figure 2.41, the volume fraction of cells in blue inside the gas bubble in the 3D case (top three cutting planes) are very small. Therefore, the error displayed is not an issue since the limiter prevents the liquid phase concentration from becoming non-zero anywhere in the gas phase. Fortunately, the best results come from the 3D simulation.

2.6.1.3 Impact of `isoAdvector` tolerances

`isoAdvector` introduces several tolerances. The `surfCellTol` is used to find all cells cut by the interface. For these cells, the `isoFaceTol` is used to find the position of the interface inside the cell. Finally, the `snapTol` can be used to clip unboundedness of the volume fraction field. The default values of these tolerances provided by the solver are $1e-08$, $1e-08$ and 0, respectively. For our cases we have set both `surfCellTol` and `isoFaceTol` to the same value. A sensitivity analysis of these two tolerances will be presented after. The `snapTol` was set to $1e-12$. Although its default value was initially 0, it was lowered to prevent bubbles from forming near the axis in axisymmetric cases. Using the snap tolerance can have a minor impact on the mass conservation because bounding is forced, but with such a low value it can be neglected. Figure 2.42 shows error values when varying both `surfCellTol` and `isoFaceTol` tolerances.
All four levels of tolerances give relatively similar results. Increasing these tolerances will lead to more cells with a low volume of liquid when the interface has already left. A tolerance of $1e-03$ will result in a thicker interface causing numerical diffusion in the concentration transport step. The default tolerance of $1e-08$ implemented with `isoAdvector` does not necessarily need any adjustment.

2.6.1.4 Conclusions on the generic test cases

These generic test cases enabled the implementation of the method, set up the solver and to fine tune the numerical parameters. They are also faster to run than realistic geometries and have widely been used for pre-processing. However, they do have several limitations. Firstly, there is no gas injection and the size of the bubble is always determined by the initialization. Also, the liquid film between the gas bubble and the wall is more difficult to establish than in a classical T-junction. For this reason it is also necessary to test the method in more realistic geometries to validate the solver, before adding complexity such as mass transfer. In these test cases, mass conservation was not discussed since the comprehensive mass conservation

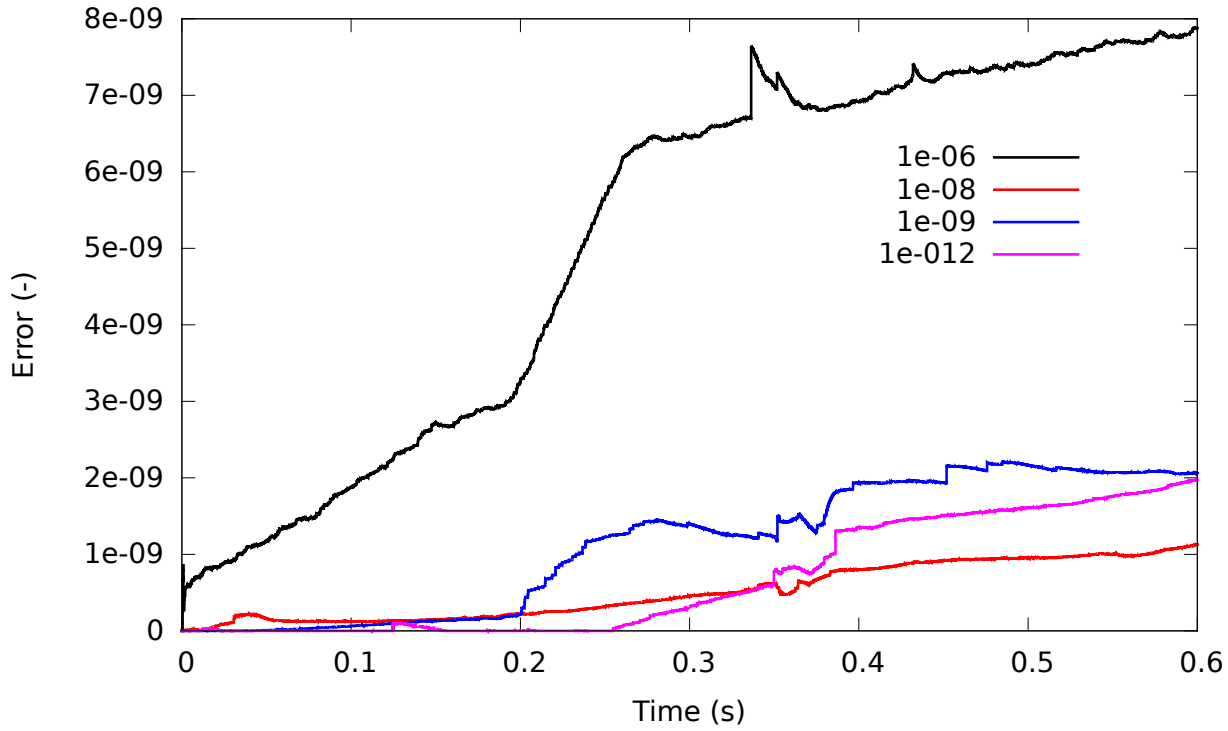

FIGURE 2.42: Mean error variations with time according to `surfCellTol` and `isoFaceTol` values

is ensured by `isoAdvector`, and concentration conservation is maintained when the errors remain minimal.

2.6.2 Simulation of Taylor flow without phase change-limits and difficulties

This section will present additional results obtained in order to validate the transport of concentration. Here, the simulations are extended to T-junctions which are used to generate Taylor flow by controlling the flowrate ratio. Compared with linear channels presented in section 2.6.1, T-junctions are more challenging to simulate because the generation of the bubble implies a complex interface motion. The T-junctions geometries are the same as those in section 2.3.3.5.

2.6.2.1 Results without face limited concentration

It is believed that the oscillations and overshoots in the concentration fields in figure 2.45 were caused by oscillations of volume fraction. For a flow that is not alligned with the uniform mesh illustrated by the cells on figure 2.43, the cell faces can be alternatively full or empty of liquid.

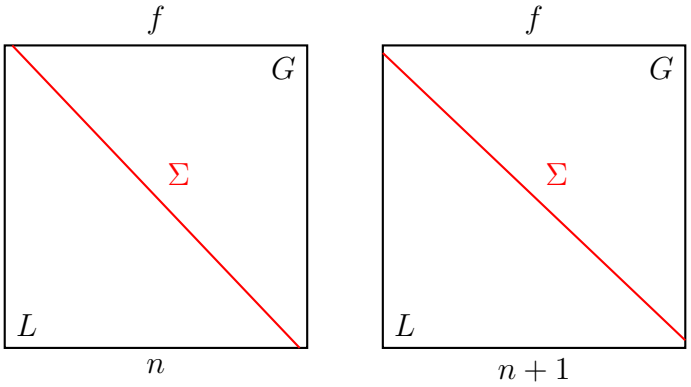

FIGURE 2.43: Schematic of an interface crossing a 2D cell diagonally

When a bubble grows in a T-junction, depending on the ratio of the superficial velocities, the interface might move diagonally as presented by the red line in figure 2.43. The issue with such orientation is the computation of α_f. In this example, we consider a face f at time n and after advection at time $n+1$. The top face f is alternatively crossed by the interface on the left, and in the gas bulk on the right. On the left, α_f can be very small whilst it is zero on the right. If the interface moves such that the roles are reverted at time $n+2$, α_f can start to oscillate. Figure 2.44 shows the time evolution of α_f on a specific face illustrating this behaviour.

`isoAdvector` does include limiters on the face value α_f and some clipping options. Therefore, the lower and upper bounds for the volume fraction are strictly respected, with a minor impact on the overall mass conservation. However, limiters where not initially included for the face concentrations. We will now see how the oscillations described on picture 2.44 can impact the concentration transport. The scaling law applied to compute the face concentration is given by relationship (2.11). When α_f starts oscillating, two methods are available to ensure boundedness. Either the fluxes are bounded and the excess of liquid can be then redistributed conservatively to accepting adjacent cells. The other option entails directly correcting α to limit it between 0 and 1. In rare instances, correcting the fluxes may not be adequate. Even though α is corrected, the fluxes responsible for generating this volume fraction field can still be incorrect. In this scenario, a corrected α and perhaps an incorrect

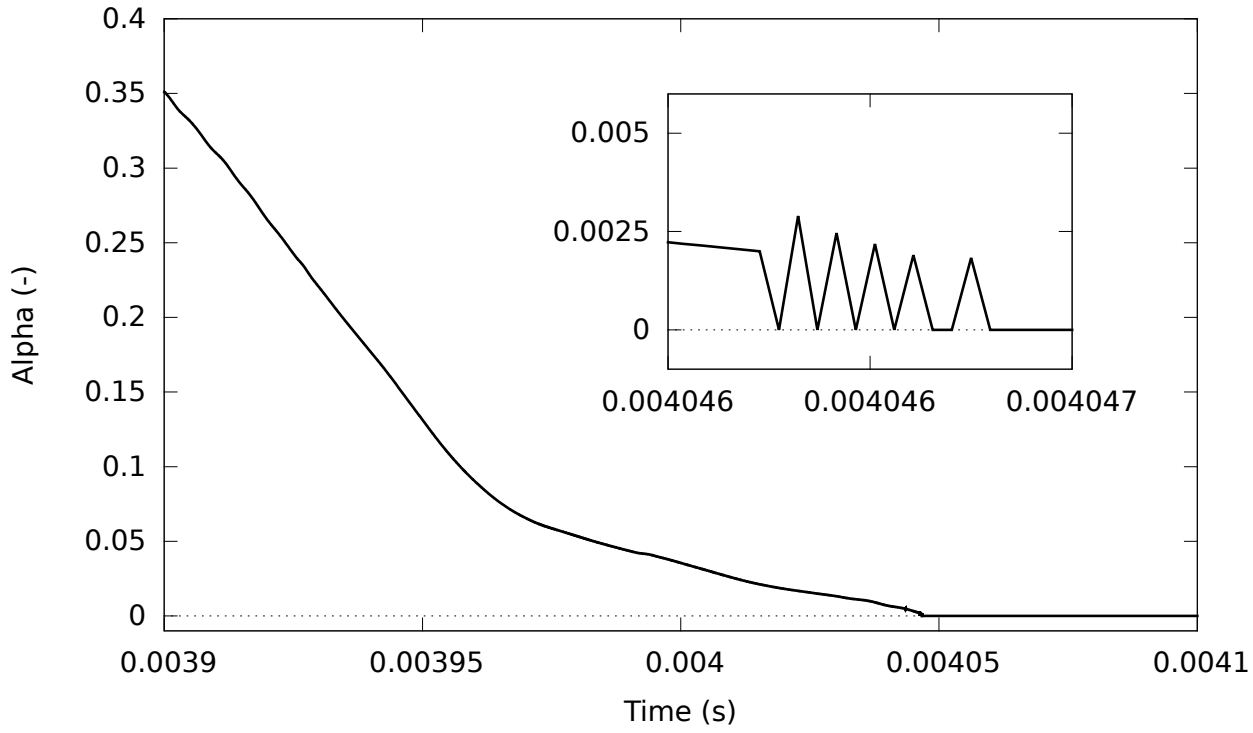

FIGURE 2.44: Time variation of the surface fraction on a face for a 2D T-junction

value of α_f are used, causing the concentration field to diverge from its expected value, $\alpha C^*_{k,1}$. To exemplify this event, a T-junction configuration with a ratio of liquid to gas superficial velocities, which exhibits a tangentially moving interface within the mixing region,is chosen. Figure 2.45 presents two snapshots captured at the same moment. In the illustration, the bubble contour is superimposed onto the background representing the volume fraction. On the left-hand side, the scale of the previous time step was kept on purpose. Thus, there is the old time step error field, mostly colored in blue, and a pink spot on the bubble contour. This pink spot is actually a set of cells where the error exceeds the maximum value on the scale of the previous time step. On the right-hand side, an adapted scale has been used to plot the same data. The error values of this spot are at least 10,000 times larger than the ones of the previous time step. Depending on the flow conditions, the error can either be mitigated by the bulk interpolation scheme or continue to be amplified. The first simulations where run without concentration face limiters and the CFL number was reduced to 0.01 help minimize the unphysical overshoot of concentration. However, excessive reduction of the time step is not viable for industrial simulations where a large CFL is required. For limiters, the question of mass conservation must be kept in mind. Indeed, if the concentration overcomes the saturation value and the excess is clipped, mass could be lost. One alternative implemented in `isoAdvector` redistributes the excess of liquid in neighbouring cells, which have some "space"

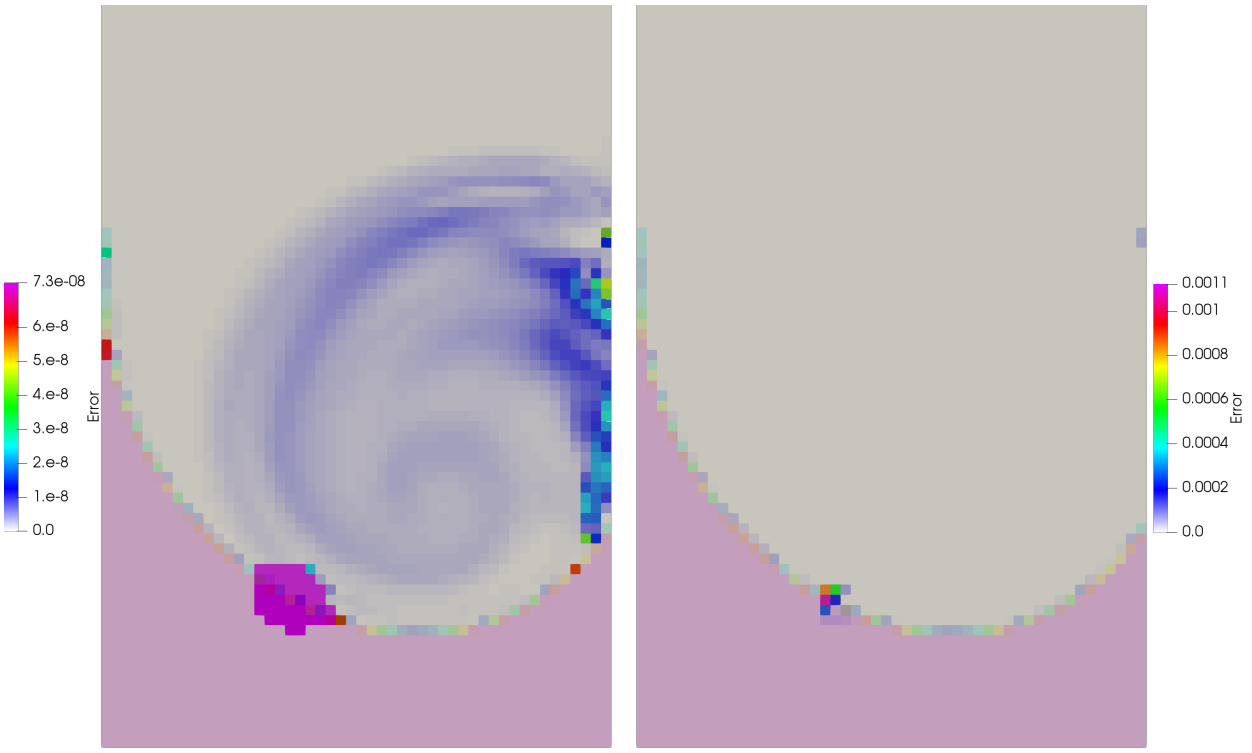

FIGURE 2.45: Visualization of the error "explosion" in the bubble growing in a T-junction

left. For concentration transport, it might not be relevant to implement such a conservative bounding. In the case of concentration, the error mainly comes from numerical errors accumulated when dividing by small volume fractions. Redistributing an error that has no physical meaning would mainly result in an accumulation of error. To overcome this, a limiter based on a physical parameter, the saturation, has been developped. This limiter avoids exceeding the saturation limit. In a multicomponent mixture, individual mass fractions can be lower than the saturation limit. If the mass fraction is at the same time lower than the saturation limit but higher than what it should be in the mixture, the limiter cannot restrain the mass fraction. Usually, for a mixture of n species, only $n-1$ equations are solved and the mass fraction of the last species is determined by taking the complementary to unity. Doing so enforces mass conservation but does not guarantee that individual mass fractions are correct. Mass conservation can again be verified by a low value of relationship (2.24). All the following results will be using the limiter presented in section 2.5.4.

2.6.2.2 2D T-junction

Section we will compare mean error results obtained for 2D T-junctions using different levels of refinement or flowrates. Figure 2.46 shows the mean error value for two mesh levels, 50 and 100 cells per diameter. It can be seen that the custom interpolation scheme allows a low

mean error value $< 1e-06$, even with 50 cells per diameter.

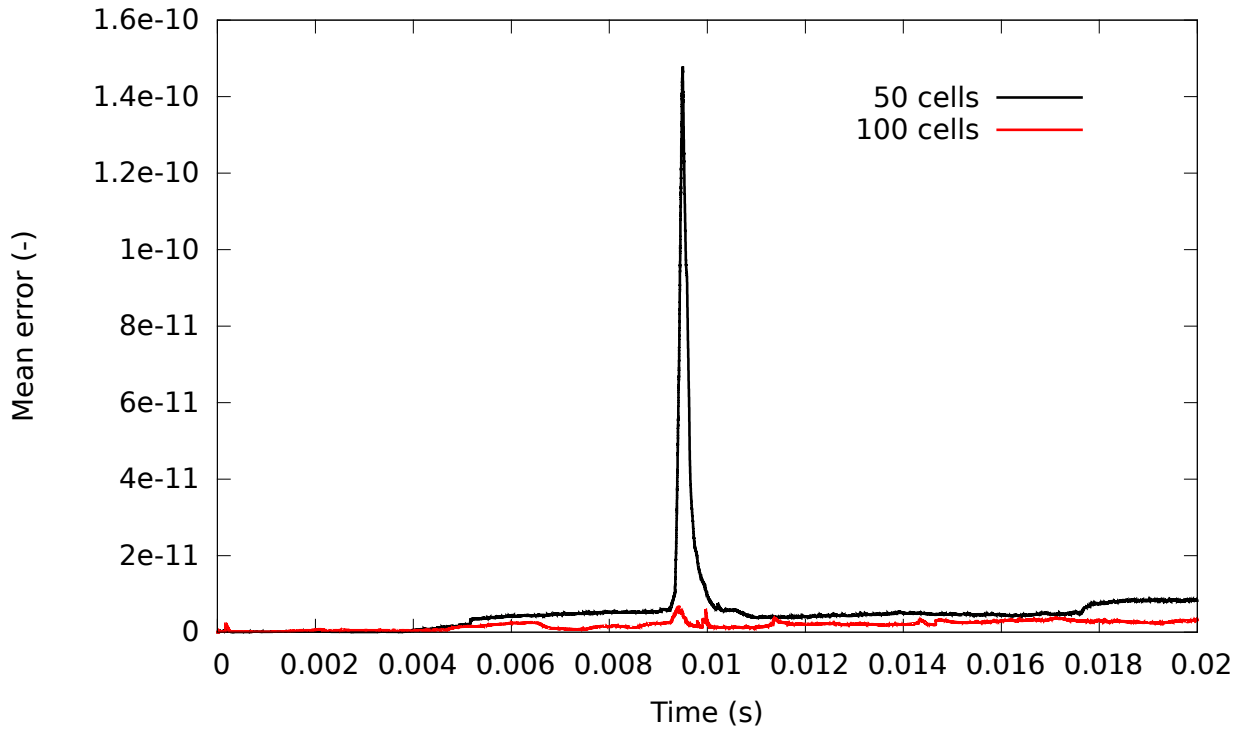

FIGURE 2.46: Mean error comparison between two refinement levels for a 2D T-junction

A 200 cells per diameter mesh was not achievable in time. However, we still observe better results with a finer mesh. Figure 2.46, shows a large spike appearing just before 0.01 s; this corresponds to the moment when the first bubble is generated. It occurs because when the interface breaks, a complex interface motion occurs, and the interpolation scheme is not in the best conditions since large concentration changes occur. The sharpness of the spike is explained by the lack of numerical diffusion. If the error was spread in the neighbouring cells, it would slowly decrease with time. The mean error decreases and this must be because the limiter clips the excess of concentration.

Figure 2.47 shows the maximum error L_∞ for two levels of refinement. The maximum of error has a global shape similar to the mean error value in figure 2.46 (black curve). The mesh with 100 cells per diameter to has larger infinite norm values. For the black curve, the same spike when the first bubble is generated is observed. This is expected because almost all the error is produced when the interface breaks. For the case with 100 cells per diameter, a small spike is observed close to 0.01 s, but the identification is more difficult. Furthermore, even though the maximum error can be larger for the case with 100 cells per diameter, it should be recalled that this is an error on the concentration. Therefore, smaller cells also represent smaller masses and smaller errors on mass conservation as well.

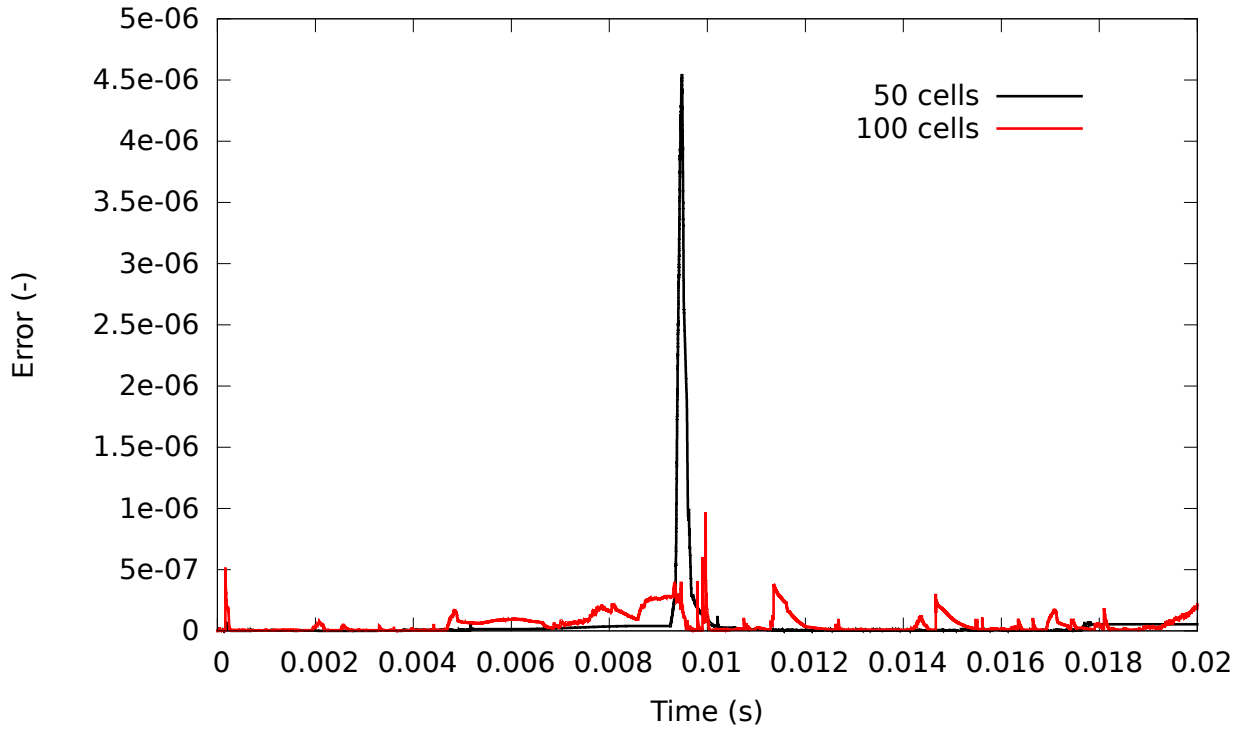

FIGURE 2.47: Maximum error comparison between two refinement levels for a 2D T-junction

2.6.2.3 Capillary number sensibility

After the difficulties faced with T-junctions and the need of limiters, the impact of capillary forces on the error generated by the transport equation is assessed. Three different Ca were tested and both gas and liquid velocities were changed. Figure 2.48 shows the time variation of mean error for the three different capillary numbers.

The largest error in blue corresponds also to the largest capillary number, hence, the smallest capillary forces. For the black and red curves, the order of magnitude of the error is quite the same. For the black curve, there is no error spike at the bubble release. Nevertheless, there is a larger amount of error that is finally diffused after 0.01 s. The large spike on the blue curve corresponds also to the generation of the bubble (the superficial velocities are larger, so the bubble is detaching faster). The error is finally diffused by the bulk interpolation scheme because it must be stuck in a low velocity zone where no recirculation occurs, for example near the walls. It is important mentioning that these results on represent a difference between the expected value from `isoAdvector` and the result of the transport equation. Therefore, if the advection algorithm gives poor results, the deviation could be low whereas the results are still wrong and nonphysical. It is not very surprising that the larger the velocity, the larger

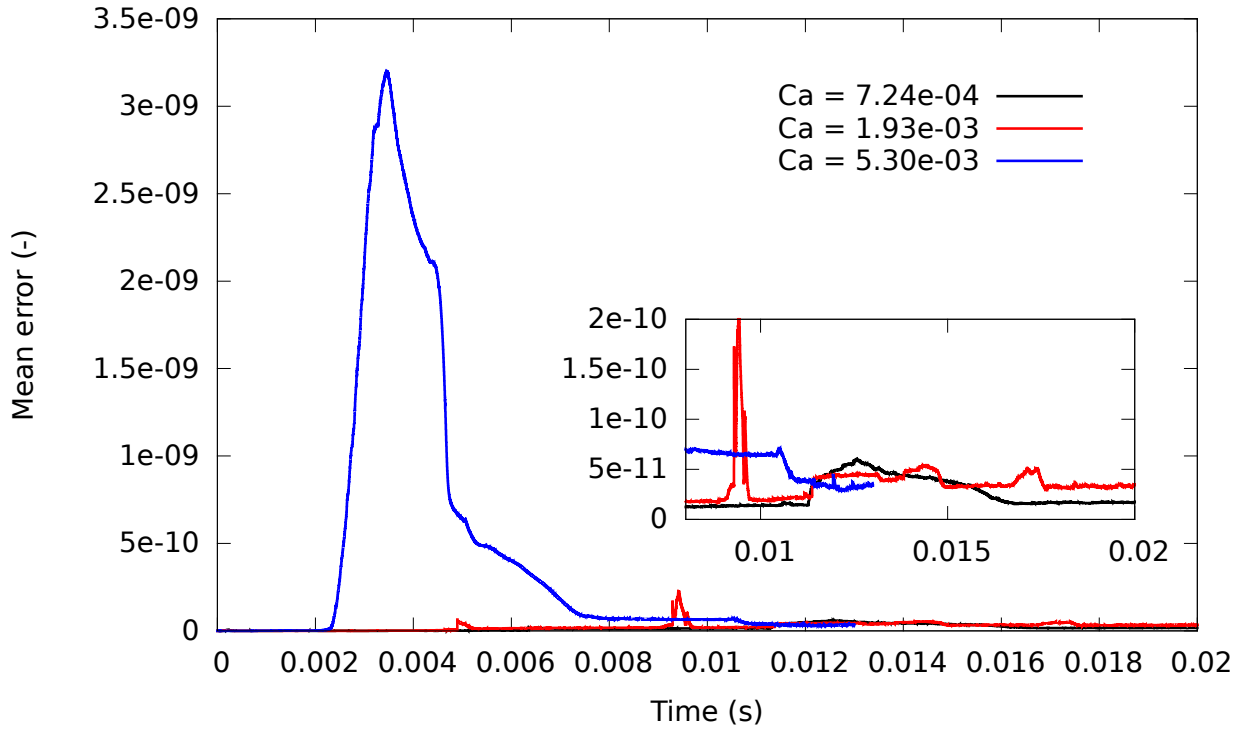

FIGURE 2.48: Comparison of the mean error values obtained for three different Ca numbers in a T-junction

the deviation. Indeed, large fluxes and quick changes in volume fraction are more difficult to follow. Reducing the CFL number can mitigate the issue but at a higher numerical cost.

2.6.2.4 3D T-junction

From previous test cases, we expect better results in 3D for the T-junction as well. However, we will see that the results are not really improved. Figure 2.49 shows the time evolution of the mean error for a 3D T-junction. The mesh is the same as in 2D. There are also 50 cells in the third direction.

The plot only shows results up to 0.002 s, the simulation was extremely computationally demanding since it represents already more than 1 500 000 s, almost 18 days of simulation time. The steady increase of the error plus the relatively large values reached do not correspond to the trends found before. This must be linked to the interface advection, leaving some small nonrelevant amounts of liquid behind.

Figure 2.50 shows the volume fraction field on the wall of the gas injector corresponding to the plane $z = 0$.

Even if the inner cross-sections of the T-junction have a well resolved interface with few issues, small liquid volumes remain within the gas bubble near the walls. They appear as

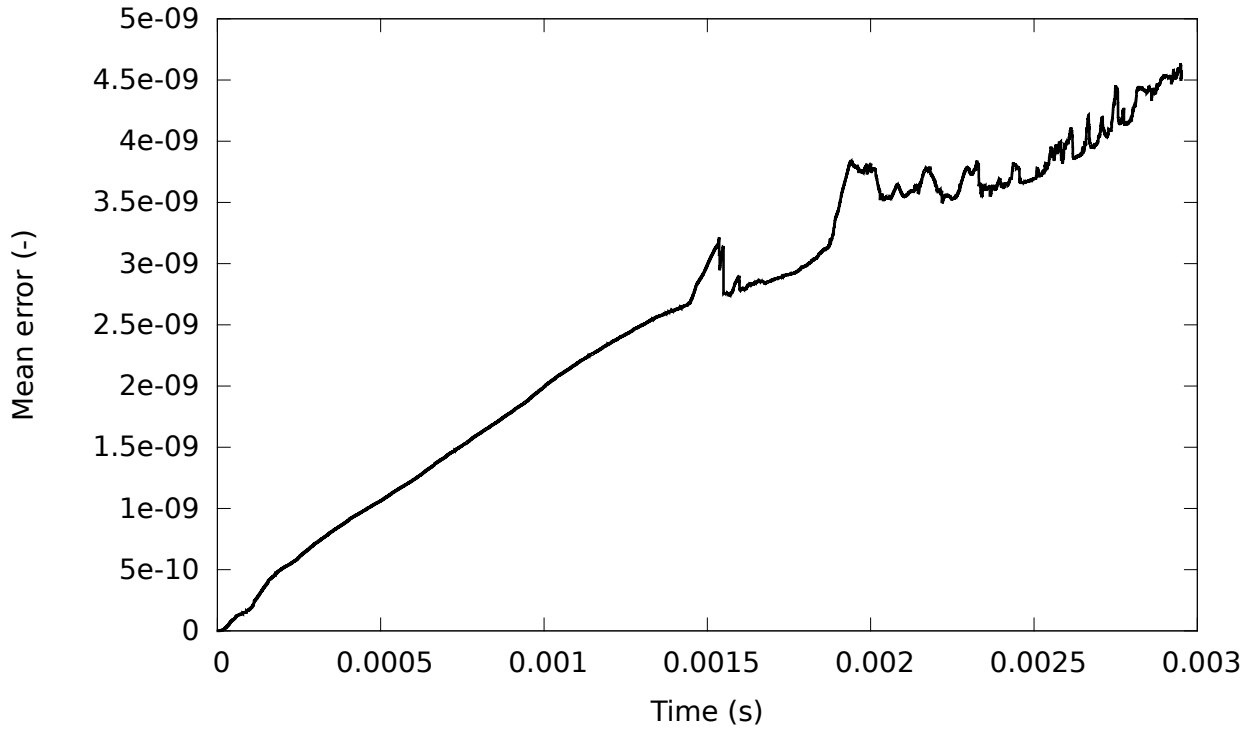

FIGURE 2.49: Time evolution of the mean error in a 3D T-junction

small blue dots on figure 2.50. At gas inlet, located at the top of figure 2.50, the circular shape of the bubble appears in the corners. As was said before, no specific treatment of the boundary condition has been implemented for the interpolation scheme. The combination of these two error sources might explain the larger error observed for the 3D T-junction. A longer gas inlet might help to overcome the boundary issue. However, even if the mean error is at least ten times larger for the 3D T-junction than the 2D T-junction, $1e-09$ of relative error compared to cells filled with a concentration of $1\,\mathrm{kg\,m^{-3}}$ is still a good precision.

2.6.2.5 Conclusions on the specific tests in T-junctions

T-junctions exhibit significantly more challenging flow conditions compared with straight channels. During the tests, it was quite difficult to make the liquid film appear around the Taylor bubble using a straight channel. This may be due to the boundary condition used for the contact angle. The global deviation of the concentration from the expected value, expressed by relations (2.24) and (2.25), is small and the method can be confidently applied to other flow conditions. It was also seen that tailoring a limiter specifically for the transport equation was compulsory to avoid difficult flow conditions. Lastly, the performances of the transport equation mostly depend on the ones of the VOF solver. Therefore, the classical guidelines of fluid dynamics apply to the transport of concentration, a good mesh with low

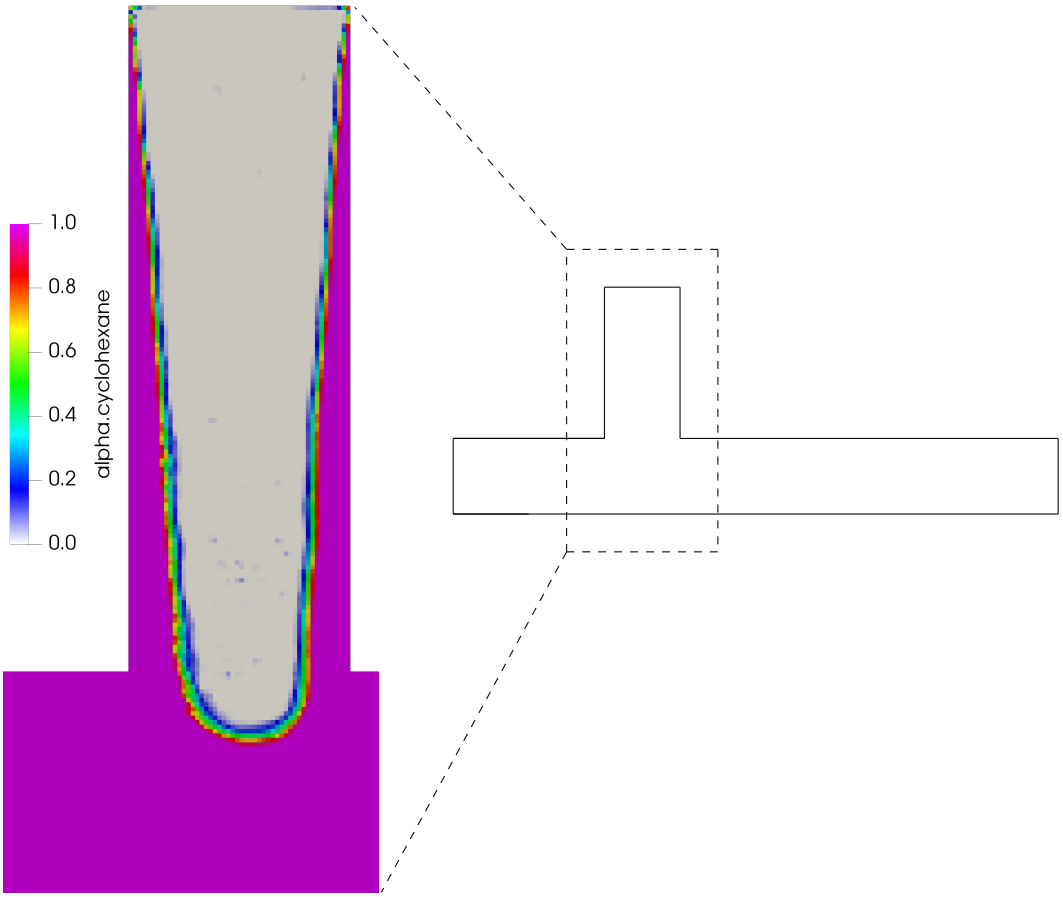

FIGURE 2.50: Gas bubble on the outer wall of the gas inlet of a 3D T-junction

non-orthogonality is preferred, the tolerances of the different solvers involved must be selected wisely. The larger contribution to overall error seems to come from the bubble generation.

2.7 Conclusion

This chapter was devoted to the bedrock of this work, the transport equation. The new methodology introduced to interpolate a passive scalar from cell centers onto cell faces is very valuable because it allows the consistent transport of a passive scalar with an interface. Designing an interpolation scheme adapted to the geometric nature of `isoAdvector` was compulsory. The adequacy of tolerances between the top layer interpolation schemes and the base algorithm `isoAdvector` was also highlighted. An innovative idea to avoid non-physical diffusion based on both volume and phase averages has been proposed. We use alternatively each averaging technique according to the moment in sequence of the algorithm. Using the phase average instead of the volume average in the diffusion fluxes computation

enables non-physical concentration gradients to be avoided. As a general conclusion on the error introduced by interpolation schemes, it should be emphasized that the significance of the error must be considered accordingly to the purpose of the simulation. In all the cases presented, the relative error compared to a cell with a concentration of $1\,\mathrm{kg\,m^{-3}}$ is totally negligible, however, without limiters, small error can be amplified and become non-negligible.

Chapter 3

Mass transfer at a gas-liquid interface in the Volume of Fluid framework

3.1 Introduction

After building a robust transport equation that guarantees no spurious mass transfer occurs, we move on to the physical transfer of species at the interface. In this chapter, we will implement mass transfer as a volumetric source term. Afterwards, test cases will be used to validate the developments. The numerical developments will then be used for practical applications. Mass transfer around Taylor bubbles in microchannels. Implementing mass transfer in a VOF context is a challenging task and as numerical issues in the transport equation must firstly be addressed before phase change. The most difficult part of species transfer is the computation of an accurate concentration gradient that will drive the species flux at the interface.

3.2 Implementing concentration driven phase change with a volumetric source term

Many analogies can be made between concentration driven and thermal driven phase change. Most of the work in the current literature has been dedicated to thermal-driven phase change [104–108]. The nuclear industry one of the main contributors to this field of study. From a physical perspective, concentration-driven mass transfer occurs when the chemical

potential of a species is different on the two sides of an interface. A flux of species will cross the interface until the chemical potentials are equal, such that equilibrium is reached. Nevertheless, equilibrium does not mean that the variables such as density, viscosity or chemical diffusion must be continuous at the interface. Most of the time they are not, because of the change of physical properties between phases. The discontinuity of a variable at the interface is known as a jump. There will be a jump condition for the main balance equations, i.e. conservation of mass, momentum, energy and entropy at the interface. The presence of a dividing surface makes the derivation of a transport surface theorem mandatory. In the case of multiphase flows, the transport theorem of a general quantity is more complex since the relative motion of phases and their boundaries must be taken into account. A rigorous derivation of a surface transport theorem (which is required for a general expression of a transport theorem in multiphase flows) can be found in the following works [109–113]. The first equation that is presented here comes from mass conservation and it expresses that mass is also conserved at the dividing surface:

$$\int_{\Sigma} \frac{d_{(s)}\rho^{(\sigma)}}{dt} + \rho^{(\sigma)}\nabla_{(\sigma)} \cdot (\mathbf{U}^{(\sigma)}) + [\![\rho(\mathbf{U} - \mathbf{U}^{(\sigma)}) \cdot \mathbf{n}_{(\sigma)}]\!]\, dA = 0 \tag{3.1}$$

This integral balance must be true everywhere on the interface. Therefore, the local balance holds:

$$\frac{d_{(s)}\rho^{(\sigma)}}{dt} + \rho^{(\sigma)}\nabla_{(\sigma)} \cdot (\mathbf{U}^{(\sigma)}) + [\![\rho(\mathbf{U} - \mathbf{U}^{(\sigma)}) \cdot \mathbf{n}_{(\sigma)}]\!] = 0 \tag{3.2}$$

Equation 3.2 is true everywhere on the interface, except on the boundary of the interface if it exists. The boundary of the interface will be a contact line between the interface and a solid. For a general quantity ϕ, $[\![\phi\mathbf{n}]\!] = \phi_1\mathbf{n}_1 + \phi_2\mathbf{n}_2$ stands for the difference of the quantity between phases 1 and 2. (σ) stands for a surface property, as well as the surface operator. $\mathbf{U}^{(\sigma)}$ is the surface velocity, and can be replaced by the surface averaged interface velocity $\mathbf{U}_\Sigma$, for simplicity. The surface velocity is the time rate of change of an interface particle; see [111] for full details. The normal component of $\mathbf{U}_\Sigma$ must be equal to the normal component of the interface. The tangential component of an interface particle is equal to the limit of the tangential component of the velocity on both sides of the interface. The basic assumption of continuity of the tangential velocity for viscous fluids through the interface justifies the use of the interface normal $\mathbf{n}_{(\sigma)}$ in the expressions of the jumps. Note that equation 3.2 also holds for the density of the mixture. If we are interested in the density of species k and we consider the surface density constant in time and in space (on the surface of course), the simplified jump condition in terms of concentration can be written as:

$$[\![C_k(\mathbf{U}_k - \mathbf{U}^{(\sigma)}) \cdot \mathbf{n}_{(\sigma)}]\!] = 0 \tag{3.3}$$

When switching from equation 3.2 to equation 3.3, the reference velocity has been changed from $\mathbf{U}$ to $\mathbf{U}_k$. It is important to note that the difference of velocity between the total mixture and species k is the diffusivity of species k inside the mixture. The velocity of species k using its diffusive flux $\mathbf{j}_k$ can be expressed as:

$$\mathbf{j}_k = C_k(\mathbf{U} - \mathbf{U}_k) \tag{3.4}$$

Rquation 3.2 is usually used with simplifying assumptions. For example, if there is no mass transfer, $\mathbf{U} \cdot \mathbf{n}_{(\sigma)} = \mathbf{U}^{(\sigma)} \cdot \mathbf{n}_{(\sigma)}$ on the interface. This means that the local phase velocity and the interface velocity are equal in the direction normal to the interface. When there is mass transfer, the mass flux $\dot{m}$ can be defined with relationship 3.3:

$$\dot{m}_k = C_{k,1}(\mathbf{U}_{k,1} - \mathbf{U}^{(\sigma)}) \cdot \mathbf{n}_{(\sigma)} = C_{k,2}(\mathbf{U}_{k,2} - \mathbf{U}^{(\sigma)}) \cdot \mathbf{n}_{(\sigma)} \tag{3.5}$$

Where 1 and 2 are the phases considered. $U_{k,1}$ is the velocity of species k inside the phase 1. It is important to note that from this jump condition, the mass flux of species k is equal in both phases:

$$\sum_{i \in 1,2} \dot{m}_i = 0 \tag{3.6}$$

Equation 3.6 implies that the interface cannot hold mass and what comes out of a phase must go into the other phase. This is a very important aspect to consider when implementing a source term; mass conservation must be respected. The jump of concentration at the interface based on the mixture velocity and the diffusive flux can finally be expressed as:

$$[\![C_k(\mathbf{U} - \mathbf{U}^{(\sigma)})]\!] \cdot \mathbf{n}_{(\sigma)} + [\![\mathbf{j}_k]\!] \cdot \mathbf{n}_{(\sigma)} = 0 \tag{3.7}$$

Equation 3.7 is interesting because it separates the jump condition between two contributions. The first term is the difference of velocity between the interface and the phase, in the direction normal to the interface. A second term is the diffusive flux of species k, which is the difference of the species own velocity and the mixture velocity, represented by the concentration gradient in dilute conditions with Fick's law. The difference of velocities expresses how the local velocity is different from the interface velocity. It means that, locally, there is a contraction or a dilatation of the phase due to mass transfer at the interface. It also means that species transfer is always accompanied by volume changes. If no volume changes can be accounted for, only dilute conditions can be simulated where the approximation $\mathbf{U} \cdot \mathbf{n}_{(\sigma)} \approx \mathbf{U}^{(\sigma)} \cdot \mathbf{n}_{(\sigma)}$ holds.

In order to define the jump condition in the momentum balance, Cauchy's stress tensor $\mathbf{T}$

is emplyed. The same considerations are then used to transform the surface integral into a differential equation:

$$\rho^{(\sigma)}\frac{d_{(s)}\mathbf{U}^{(\sigma)}}{dt} = \nabla_{(\sigma)}\cdot\mathbf{T}^{(\sigma)} + \rho^{(\sigma)}\mathbf{g}^{(\sigma)} - [\![\rho(\mathbf{U}-\mathbf{U}^{(\sigma)})(\mathbf{U}-\mathbf{U}^{(\sigma)})\cdot\mathbf{n}_{(\sigma)} - \mathbf{T}\cdot\mathbf{n}_{(\sigma)}]\!] = 0 \quad (3.8)$$

In practical applications, the body force contribution of the surface can be neglected. For a Newtonian fluid with constant surface density and after rearrangement, a simpler expression for the jump of momentum is obtained:

$$[\![\rho\mathbf{U}(\mathbf{U}-\mathbf{U}^{(\sigma)})\cdot\mathbf{n}^{(\sigma)} - \mathbf{T}\cdot\mathbf{n}^{(\sigma)}]\!] = \sigma\kappa\mathbf{n}^{(\sigma)} + \nabla_{(\sigma)}\sigma \quad (3.9)$$

In equation 3.9, σ is the surface tension force coefficient and (σ) is the superscript for surface quantities. κ is the interface curvature. $\rho\mathbf{U}(\mathbf{U}-\mathbf{U}^{(\sigma)})$ induces a jump in momentum for two reasons: (1) the two phases do not have the same density; (2) each of the phases has a different velocity than the interface and than the other phase. Similarly, there is a jump of momentum because the stress tensor is different from one phase to another in the direction normal to the interface (the hypothesis of continuity of tangential velocities through the interface still holds here). On the right-hand side, the surface tension force, that is the intrinsic force of the interface present as soon as there is curvature. If there is no mass transfer, the relationship simplifies $[\![-\mathbf{T}\cdot\mathbf{n}^{(\sigma)}]\!] = \sigma\kappa\mathbf{n}^{(\sigma)} + \nabla_{(\sigma)}\sigma$. $\nabla_{(\sigma)}$ is the surface gradient of surface tension coefficient, responsible for the so-called Marangoni effect. The other conservation equations and their underlying jump conditions will not be demonstrated here, althouhg a full derivation can be found in [111].

The above descriptions of how the mass and momentum will change after crossing the interface enable the volumetric source term to be described. The mass flux at the previous time step will be added when solving the Poisson equation for pressure. This explicit volumetric source term will create a non-divergence-free cell where the volumes of phases will be able to change due to mass transfer. The new velocity field will then be used to advect the concentration field of the previous time step. Therefore, the coupling between mass transfer and the momentum equation will be explicit in time and this will impose a restriction on the global time step to be valid. From equation 3.3, the partial mass flux can be expressed as:

$$\dot{m}_k = \frac{C_k}{\rho}\dot{m} + \mathbf{j}_k\cdot\mathbf{n}_{(\sigma)} = w_k\dot{m} + \mathbf{j}_k\cdot\mathbf{n}_{(\sigma)} \quad (3.10)$$

Note that in equation 3.10, the concentration C_k of species k is used in the definition of the mass quantity of k present in the phase mixture, ρ is the density of the phase mixture, w_k is the mass fraction of species k.

3.2.1 Computation of the advective part of the source term

In systems where the species have a high Pe number, or in advection-dominated conditions, the difference between the bulk and the interface velocity can become non-negligible. Such systems require the advective contribution to the overall mass transfer to be considered. To do so, equation 3.11 must be evaluated:

$$\mathbf{U} - \mathbf{U}_\Sigma \tag{3.11}$$

In the following text, the local interface velocity $\mathbf{U}^\sigma$ has been replaced by the average velocity of the plan in a cell $\mathbf{U}_\Sigma$, which is accessible from a computing perspective. Since the momentum and concentration transport equations are not coupled, the old time step values must be used to evaluate relationship 3.11. The velocity $\mathbf{U}$ is the $n-1$ iterative velocity. It can be non-divergence-free only in interface cells since a source term in the Poisson equation to solve for pressure is added. The interface velocity is naively computed using the successive centroid positions of the interface:

$$\mathbf{U}_\Sigma = \frac{\mathbf{x}_\Sigma^n - \mathbf{x}_\Sigma^{n-1}}{\Delta t} \tag{3.12}$$

At this point, the interface position has already been updated since the VOF equation is solved before species transport. The source term used in the VOF equation to account for the volume change is the mass source term of the old time step, which is itself based on the time step before. Therefore, the interface displacement of relationship 3.12 does not rely on the current and the $n-1$ concentration fields. Instead, it is based on the $n-1$ and $n-2$ concentration fields. This delay imposed by the global sequence of the algorithm and the explicit discretisation of the source term is then much easier to implement. The hypothesis is acceptable when the time step is low, but since `isoAdvector` imposes a limit of 0.2 on the CFL number, that is consistent. To implement the source term relationship 3.7 must be integrated on the interface surface. At this stage, several basic assumptions are made. Firstly, the interface concentration is considered constant all over the surface. The interface concentration and the cell concentration are assumed to be the same, which means that there is no concentration gradient in the interface cell. Finally, the PLIC surface is used to approximate $\int_\Omega \nabla\alpha \; dV$. These assumptions facilitate the implementation of the algorithm and enable better consistency of `isoAdvector` when advecting a plane interface in a 3D cell.

The final computation of the advective contribution is given by:

$$\dot{m}_{k,adv} = C_k^n \left(U - U_\Sigma\right) \frac{A_{PLIC}}{V} \tag{3.13}$$

3.2.2 Computation of the diffusive part of the source term

Usually, Fick's law is used to express the flux based on the concentration gradient. However, the relationship is limited to dilute cases or to the binary diffusion of one species in another one. For a more general description of the diffusive fluxes in non-dilute conditions, the Maxwell-Stefan equation should be used; see for example [114] or [11] chapter 17.9. More experimental data are required to describe the binary interactions between constituents in the mixture. The remainder of this work will be restricted to a binary mixture. This restriction is valid for the simulation of mass transfer without chemical reaction, because the diffusion of only one species in the other phase is studied. For the multicomponent mixtures, it should be kept in mind that the hypothesis is only valid in dilute conditions. Fick's law for phase 1 is given as:

$$\mathbf{j}_{k,1} = D_{k,1} \nabla C_{k,1} \tag{3.14}$$

The same can be applied to the second phase. Diffusive motion of species k in the phase and through the interface is split so that the bulk motion is accounted for implicitly in time, while the diffusive flux through the interface is added as a volumetric source term explicit in time. The explicit source term is based on relationship 3.14 applied at the interface. To determine the Fick's flux at the interface, it is important to describe how the diffusion coefficient is extended from the bulk phase properties and how the concentration gradient at the interface is computed. The next section will be dedicated to the computation of the gradient. The volume change effects will be discussed later on.

The computation of an accurate concentration gradient at the interface is very challenging. The concentration profile in the concentration boundary layer near the interface is very steep, making the value of the gradient decay very fast after the interface. Typically, in convection-dominated flows, the concentration boundary layer scales with the hydrodynamic boundary layer divided by the square root of the Schmidt number [11, 66]. The resulting concentration boundary layer can be tens of times smaller than the hydrodynamic boundary layer. It turns out that the mesh refinement needed for a precise linear approximation of the gradient is very fine. Furthermore, in a computation, the direction of the gradient at the interface hardly intersects a cell centre where the concentration is known. Multiple computations of the temperature gradient have been proposed for thermally-driven simulations [115–118]. For

concentration-driven phase change, Weiner and Bothe [68] proposed a subgrid-scale model that avoids the heavy refinement of the mesh near the interface.
Consider a cell cut by the interface as displayed on figure 3.1. It can be seen in figure 3.1

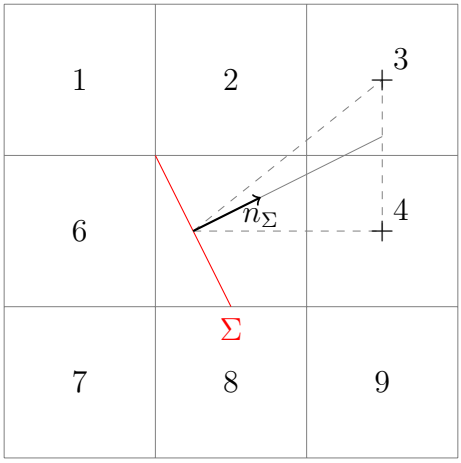

FIGURE 3.1: Stencil for the computation of an interfacial concentration gradient

that the interface normal is not necessarily aligned with a cell centre. Indeed, most of the time it is not. The easiest way of computing a gradient is with a linear approximation:

$$\nabla C|_\Sigma = \frac{C_\Sigma - C_3}{\mathbf{x}_5 - \mathbf{x}_3} \tag{3.15}$$

Here the value at the closest centroid in the interface normal direction, i.e. cell 3 is used. A more realistic approach could use the two closest centroids to compute an interpolation of a bulk concentration. Nevertheless, whatever the method chosen to compute the concentration in the bulk, it relies on the linear gradient assumption. To illustrate this issue, a simple 1D mesh example is given for which the analytical concentration profile is plotted in figure 3.2. The black curve is the theoretical concentration profile and it can be seen how fast the concentration profile decays in the first cell of this simple mesh. To determine the concentration gradient at the interface (node P), the concentration at a known node (node E) must be used. The blue curve in figure 3.2 represents the linear approximation of equation 3.15. However, this linear approximation under-estimates the real concentration gradient, which would be better estimated by the red line in figure 3.2. Another approximation is:

$$\int_\Sigma D_{eff}\, \nabla C|_\Sigma \; dA \approx A_{PLIC} D_{eff} \left\langle \nabla C \right\rangle_{A_\Sigma} \tag{3.16}$$

Equation 3.16 is not as straightforward as one can imagine. It supposes implicitly that the area of the interface inside the cell given by $A_\Sigma = \int_\Omega \nabla\alpha \; dV$ and the PLIC surface A_{PLIC}

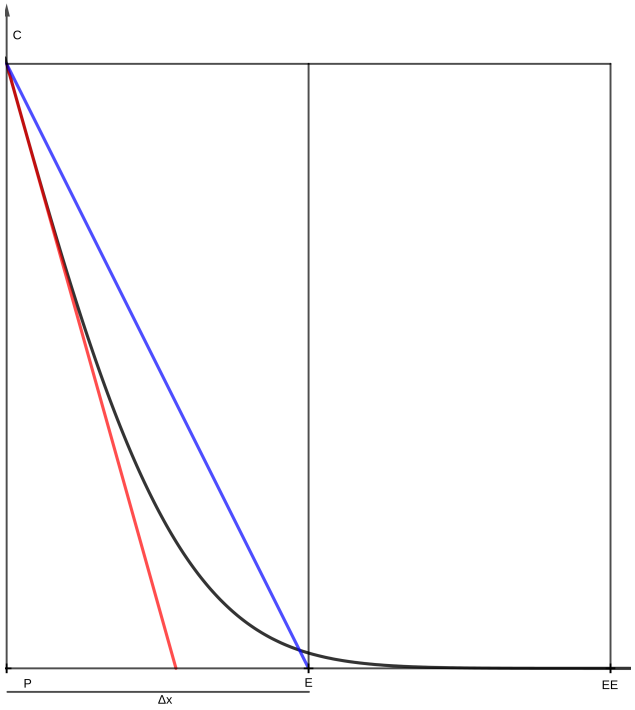

FIGURE 3.2: 1D mesh with the concentration variations in ordinate

are equal. In the first implementation of the concentration gradient computation, a switch is included in order to add the current interface cell in the choice of neighbours. The switch is illustrated by figure 3.3.

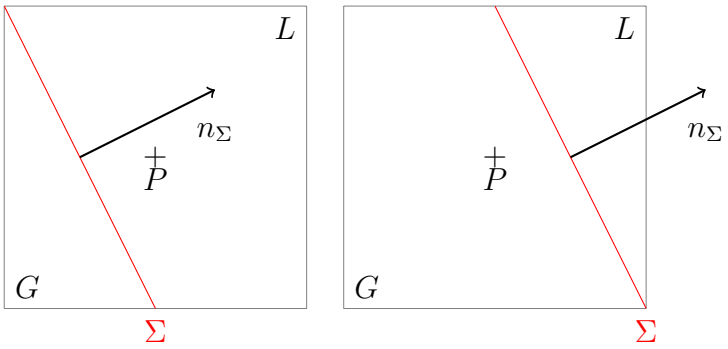

FIGURE 3.3: Two cells with a different interface position and the corresponding interface normal

These two cells have the same orientation. The centroid of cell P is inside the liquid phase for the left cell, and inside the gas phase for right cell. To compute a concentration gradient at the interface in the liquid phase, the neighbouring cell in the direction normal to the interface must be chosen. For the left cell, we propose to add the current cell P inside the list of the neighbouring cells. If the interface normal is closer to cell P's centroid, its concentration

value can be used as a second concentration to compute relationship 3.15. For the right cell on figure 3.3, cell P must not be included since the centroid is clearly in the opposite direction of the interface normal. This switch is quite easy to implement. It only requires adding the current cell in the list of neighbours. However, it is important to make sure the centroid of the interface does not coincide with the cell centroid, otherwise the gradient will be undefined.

3.2.3 Updating the concentration field

The source term is computed based on the local interface concentrations. Using Henry's constant, it is possible to assess how the concentration is far from equilibrium, and then orient the flux from liquid to gas or from gas to liquid. The evaluation of the local equilibrium allows the computation of mass transfer in both directions. The concentration is updated with the mass source term after the advection step and before the diffusion step. The diffusive component of the mass source term is calculated from the approximated relationship 3.16. In case of large Pe, only the diffusive part of the mass source term is needed to obtain precise results. However, for larger contributions of advection to the overall transfer, it is necessary to compute the advective part of the source term with relationship 3.13. Once both contributions are known, the overall mass source term simply is the sum of both. Given the sequence of the algorithm, it is not possible to compute the volume change due to the diffusive part, then to use the interface displacement to update the interface velocity. In such conditions, the interface velocity would always be underestimated. On the other hand, using the old time step values to compute the volume change will delay the effect of advection on mass transfer. Furthermore, using an explicit source term requires the addition of limiters on the mass transfer.

Let's consider a diffusive flux at the interface, that uses the concentration gradient computed from the interface concentration and the cell concentration. When the cell reaches the interface concentration, the gradient becomes zero and the mass source term vanishes. Since the gradient uses the value at the old time step, the concentration in the cell might overcome the saturation concentration in some specific cases (for example when advection occurred and increased the concentration). Thus, limiters are required to make sure the physical saturation is respected. The limiter is defined as:

$$\dot{m}_{max} = \frac{C_{\Sigma,k,1} - C_{k,1}}{\Delta t} \tag{3.17}$$

For this limiter, the concentration $C_{k,1}$ is the cell concentration in the interface cell after advection and before diffusion. If $\dot{m} > \dot{m}_{max}$, the concentration will become greater than the saturation after update. In order for the simulation to remain mass conservative, this corrected mass flux must absolutely be used in all further computations. Once the correct mass source term has been calculated and the concentration has been updated, volume can be changed using the α-field.

3.2.4 Introducing volume change in the volume fraction equation

Relationship 3.3 states that as soon as there is mass transfer there is a difference between the bulk phase velocity and the interface velocity. Since the interface position is tracked by the volume fraction field, it is necessary to update the position of the interface with respect to the amount of species that has changed phase in order to take into account volume change. To ensure mass conservation, equation 1.53 integrates a source term:

$$\frac{\partial \alpha}{\partial t} + \nabla \cdot (U\alpha) = \frac{\langle \dot{m} \rangle|_\Sigma}{\rho_L} \tag{3.18}$$

$\langle \dot{m} \rangle|_\Sigma$ is the mean volumetric mass flux (units $\mathrm{kg\,m^{-3}\,s^{-1}}$) at the interface and is divided by the liquid density because the reference phase is the liquid. $\langle \dot{m} \rangle|_\Sigma$ represents how much the liquid expands or contracts due to mass transfer.
The continuity equation also must be modified to account for the change of volume:

$$\nabla \cdot U = \langle \dot{m} \rangle|_\Sigma \left(\frac{1}{\rho_L} - \frac{1}{\rho_G} \right) \tag{3.19}$$

In OpenFOAM®, the continuity equation is implemented in the `pEqn.H` file when dealing with transient solvers using the PISO algorithm. When updating the volume fraction field, the interface is not explicitly reconstructed. This means that the volumetric source term that is added to the volume fraction only globally indicates how the volume of liquid changes during the time step and there is no coupling between the VOF equation and the transport of species. The volume fraction field is updated once mass transfer has been applied and before the diffusion part of the equation is solved.

3.2.5 Numerical implementation

This section presents the code used to compute the mass source term and the concentration update.

```
if (avgWeight != 0 && alpha[cellI] != 0)
{
    diffusiveFlux[cellI] = pos0(avgdCLVLidN) * avgdCLVLidN / avgWeight * D[cellI]
    * mag(interfaceNormals[cellI]) / mesh.V()[cellI] / alpha[cellI];
}
```

FIGURE 3.4: Parallel implementation of the mass source term

Figure 3.4 uses the average concentration of neighbouring cells `avgdCLVidN` and distances to compute the concentration gradient and multiply the gradient by a diffusion coefficient to obtain a diffusive flux. A list of neighbouring cells is created to have access to the neighbouring concentrations and their cell centres. This implementation is easy to parallelize. The diffusive flux is then divided by the product of volume fraction and cell volume, giving the liquid volume inside the cell, to obtain a volumetric source term. The concentration is updated using the phase average concentration:

```
CLVLi.oldTime()[cellI] = CLVLi.oldTime()[cellI]
+ massTransferLi[cellI] * mesh.time().deltaTValue();
```

FIGURE 3.5: Phase average concentration field update

The interest of updating the phase average concentration field instead of the volume average concentration field is to impose limiters if needed. Since the diffusion part of the equation is solved implicitly later on, the old time step value is replaced by the one after mass transfer. The volume fraction field is updated similarly:

```
volTransferi = massTransferLi / rho1;
alpha1[cellI] = alpha1[cellI]
+ volTransferi[cellI] * mesh.time().deltaTValue();
```

FIGURE 3.6: Volume fraction field update after mass transfer

3.3 The Stefan problem in 1D

Analytical solutions of mass transfer problems are quite rare. However, known solutions are useful for validating CFD models. The Stefan's case is one of the rare problems for which an analytical solution exists. The partial differential equation describing the motion of species i is written as:

$$\frac{\partial C_{k,j}}{\partial t} = \nabla \cdot (D_{k,j} \nabla C_{k,j}) \quad j = \{1, 2\} \tag{3.20}$$

3.3.1 Test case setup

The test case is very simple and one dimensional comprising a bubble of gas, which is initialized on the left-hand side of figure 3.7. The liquid on the right-hand side is free of species. The flux of species through the interface causes and increase in the concentration of the species in the liquid phase. Since there is a volumetric source term included in the continuity equation, the change of volume causes the interface to move. In the current case, the gas concentration was set to $1\,\mathrm{kg\,m^{-3}}$ and the Henry constant to 10. The concentration in the liquid is expected to increase up to $0.1\,\mathrm{kg\,m^{-3}}$.

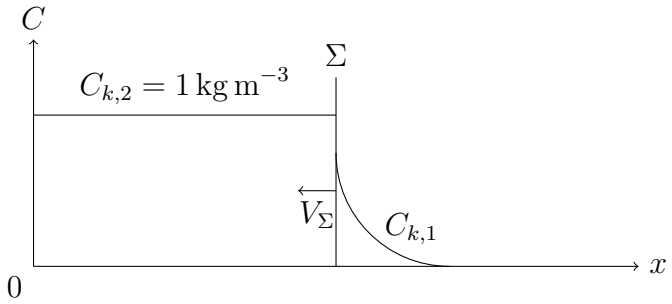

FIGURE 3.7: Numerical set up for Stefan's sucking interface test case

3.3.2 Analytical solution

The analytical solution of equation 3.20 is given by the error function:

$$C_{k,1}(x,t) = \frac{C_{k,2}}{H}\left(1 - \mathrm{erf}\left(\frac{x}{2\sqrt{t\ D_{k,1}}}\right)\right) \tag{3.21}$$

To compute the interface movement, the interface gradient is needed. From the concentration field, the interface gradient can be derived as:

$$\frac{\partial C_{k,1}}{\partial \boldsymbol{n}_\Sigma} = -\frac{C_{k,2}}{H\sqrt{\pi D_{k,1}}}\frac{1}{\sqrt{t}} \tag{3.22}$$

The interface velocity can be deduced:

$$V_\Sigma = -D_{k,1}\frac{C_{k,2}}{H\sqrt{\pi D_{k,1}}}\frac{1}{\sqrt{t}} \tag{3.23}$$

The interface position is then obtained by integrating the interface velocity:

$$x_\Sigma(t) = 2\frac{C_{k,2}}{H}\sqrt{t\ D_{k,1}/\pi} \tag{3.24}$$

Once the theoretical interface position is obtained from relationship 3.24, it can be compared with the numerically predicted interface position obtained from the interface reconstruction algorithm. An important thing to mention here is the consistency between the imposed numerical boundary conditions, and the hypothesis used to obtain 3.21. The analytical solution is derived for a concentration in the liquid phase equal to 0 at infinity. Numerically, a `zeroGradient` is imposed at the outlet to let the concentration field evolve freely. However in order to respect the analytical derivation, the outlet should be located as far as possible from the interface.

3.3.3 Results and discussion

While this test case may appear simple, the calculation of gradients can significantly impact the outcomes, as demonstrated in section 3.2.2. To evaluate the performances of the in-house developments, the Stefan case has been simulated for several uniform meshes with a constant diffusivity of $1 \times 10^{-9}\,\mathrm{m^2\,s^{-1}}$ and figure 3.8 displays the results. A low diffusion coefficient decreases the Sc number, which leads to a thinner concentration boundary layer. Therefore, a low diffusivity imposes stricter conditions on the gradient calculation. The base mesh tested comprised 250 cells. The black curve corresponds to the analytical solution. The lowest quality mesh in red gives the poorest results and refining the mesh reduces the deviation of the numerical prediction from the expected solution. It can be seen that all curves present changes in slopes at some point and this occurs when the interface changes cell. The gradient is computed with the linear approximation given in equation 3.15. When

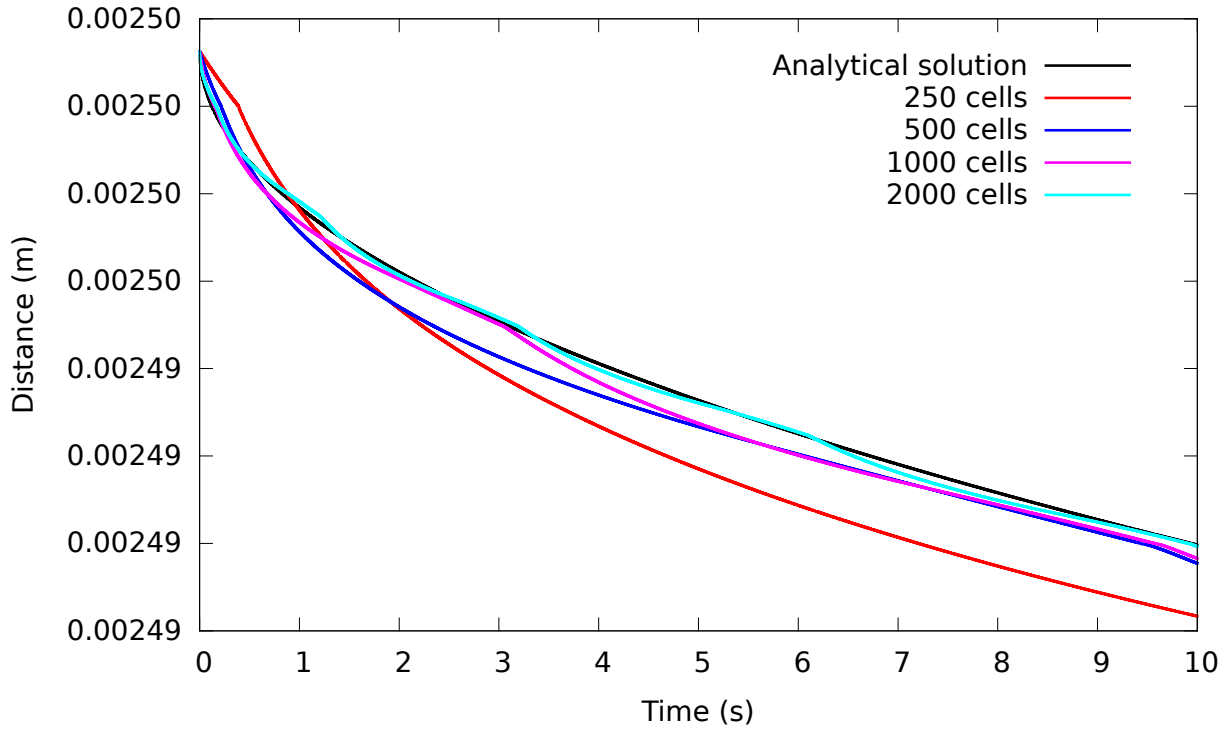

FIGURE 3.8: Time evolution of the interface position for different mesh refinements

the interface enters a new cell, the second point taken for the distance is the new neighbouring cell centre. Therefore, the distance used for the gradient is not a smooth function of time. The more refined the mesh, the better are the results but the smaller the time step. A compromise is therefore needed between compuational time and precision. Improvements of the gradient computations could also be imagined. For example, it could be possible to compute more accurate weights for the neighbouring average, which may improve the results for 2D and 3D computations.

Regarding the concentration field, good agreement is reached for all refinement levels. Figure 3.9 shows the concentration profile obtained for the base mesh of 250 cells after 10 s. The vertical black bar of the analytical solution corresponds to the concentration jump at the interface (only one field for the analytical solution). The important parameter to respect is the saturation concentration obtained with Henry constant. The maximum phase average concentration divided by the saturation concentration is indeed 0.1 in figure 3.9, which is the expected value for the maximum concentration in the liquid phase. For a larger diffusivity, the mass transfer magnitude and the diffusion velocity in the liquid phase would be much larger. A longer channel might be necessary, or a different set of boundary conditions.

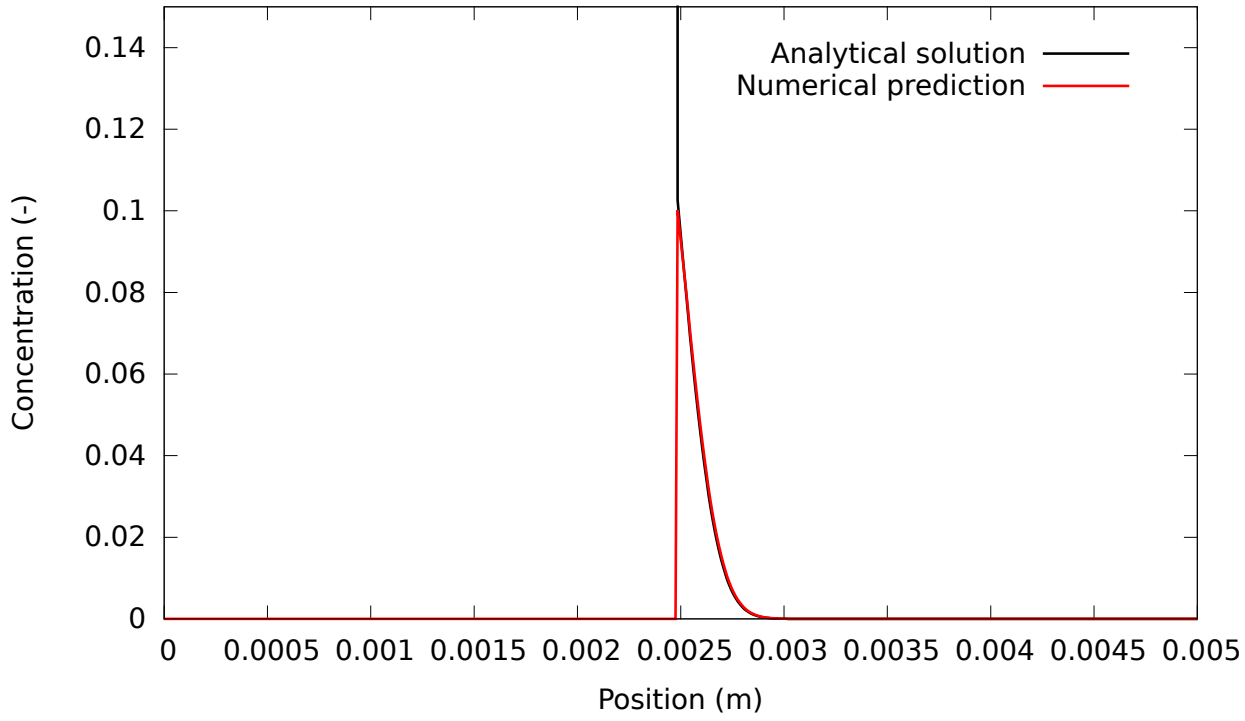

FIGURE 3.9: Comparison between the analytical concentration and its numerical counterpart with a diffusivity of $1 \times 10^{-9}\,\mathrm{m^2\,s^{-1}}$

3.3.4 Subgrid scale model

A subgrid scale model can be used to avoid the full resolution of the equations. For mass transfer, it is of interest to use such model to avoid the gradient computation, which is numerically very demanding. A subgrid scale model is adapted to a situation. In most cases, it employs hypotheses about the flow regime or its orientation that allow the simplification of the desired equation. For the example here, the objective is the enhancement of the gradient computation. To do so, an expression is required for the gradient that can be obtained either analytically, or by solving a partial differential equation simpler than the full system.
For Stefan's case in figure 3.7, the analytical expression of the gradient can be used to compute the mass source term; relationship 3.22 inside the source term given by equation 3.16. In Stefan's case, there is a large Pe number and the advective part of the mass source term becomes negligible compared with the diffusive part. This is true at least at the beginning when the interface starts moving. Obviously this is a relatively simple test case and the subgrid scale model cannot be applied to anything but Stefan's case. The numerical implementation 3.10 of this new mass source term replaces the one given in figure 3.4.
The implementation of the mass source term is straightforward. Only the source term has to been changed, updating the concentration using equation 3.6. To verify the algorithm, the

```
if (avgWeight != 0 && alpha[cellI] != 0)
{
    diffusiveFlux[cellI] = CGVGi[cellI] / (H.value()
    * Foam::sqrt(constant::mathematical::pi * D[cellI]))
    / Foam::sqrt(mesh.time().value()) * mag(interfaceNormals[cellI])
    / mesh.V()[cellI] * D[cellI] / alpha1[cellI];
}
```

FIGURE 3.10: Mass source term for the subgrid-scale model

gradient computation has been replaced by the analytical solution. The analytical position of the interface (given by a square root function) is compared with the numerical prediction after update of the volume fraction field in figure 3.11. The concentration field over the

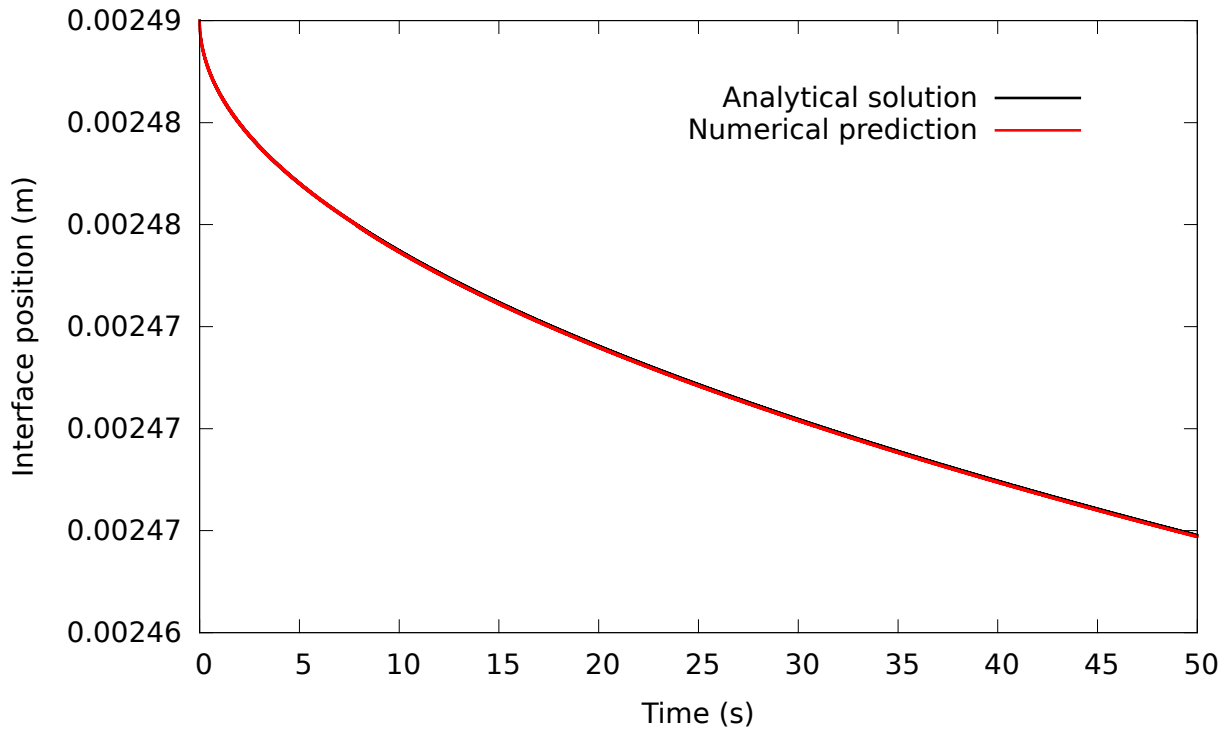

FIGURE 3.11: Comparison between the analytical solution of the interface displacement and its numerically predicted counterpart with a diffusivity of $1 \times 10^{-9}\,\mathrm{m^2\,s^{-1}}$

length of the channel at 50 s is given in figure 3.12. It can be seen how perfect the predictions are when the suitable gradient computation is employed. Capturing the diffusion profile for the concentration is not so difficult. For a stationary case without volume change, the concentration profile in the liquid phase only depends on diffusion since the interface does not move. Indeed, the main difficulties appear when the interface starts moving. For a 1D case, there is no interpolation of the cell centred values onto the cell faces, the face is either totally immersed in the liquid with $\alpha_f = 1$ or totally immersed in the gas $\alpha_f = 0$. This

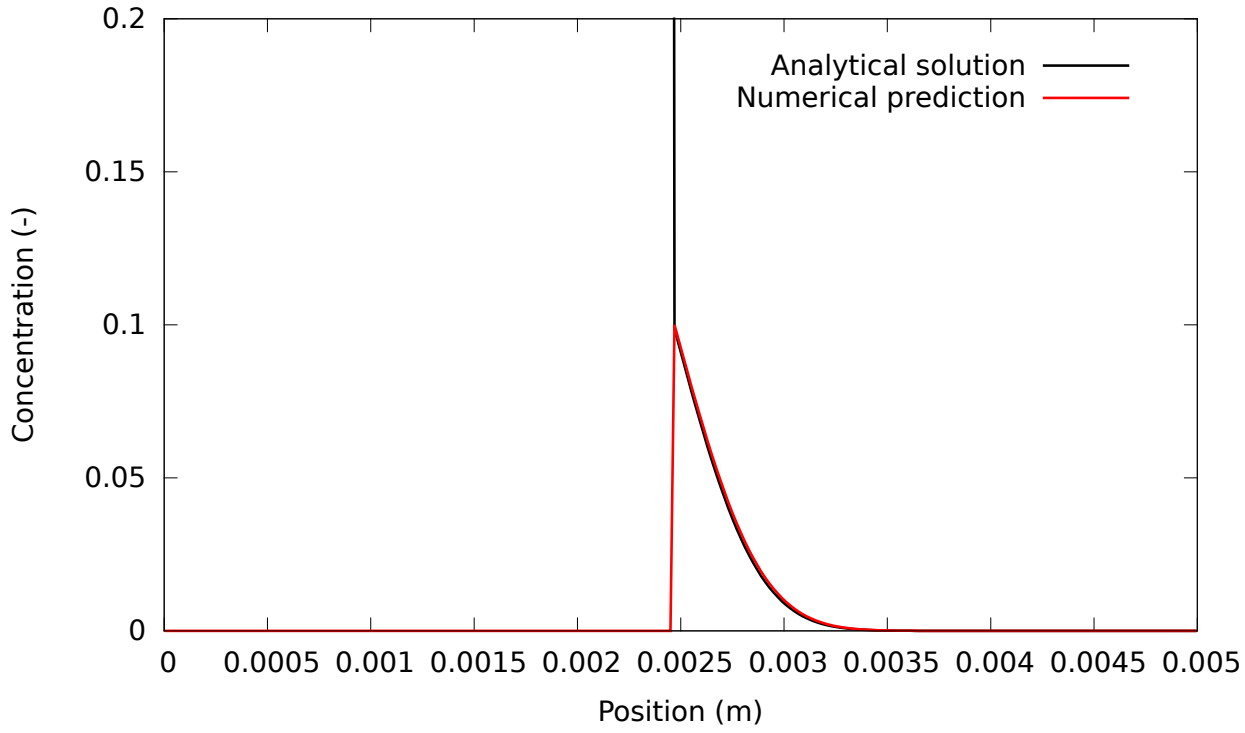

FIGURE 3.12: Comparison between the analytical concentration and its numerical counterpart with a diffusivity of $1 \times 10^{-9}\,\mathrm{m^2\,s^{-1}}$

greatly simplifies the case and explains why such accurate results are obtained. For more realistic conditions, new subgrid-scale models must be adapted to the system. In the work of Bothe & Fleckenstein [66], the authors have successfully designed a subgrid scale model for convection-dominated flows.

3.4 Other validation test cases

Many other test cases were used to validate the solver under variable conditions. Among these test cases are cases with large deformations of the interface. These cases are tricky to solve because the VOF solver can have some difficulties to advect the interface. When the deformations are too large, the interface may break up and form secondary droplets. The concentration transport should be able to capture such phenomena. Only one test is presented here: a rising bubble in a quiescent liquid with a modified gravity acceleration equal to $0.981\,\mathrm{m\,s^{-2}}$. The liquid is water and the gas air at room pressure and temperature. This test serves as a proof of concept for more real life applications.

Figure 3.13 shows the concentration of the transported species in the liquid phase around

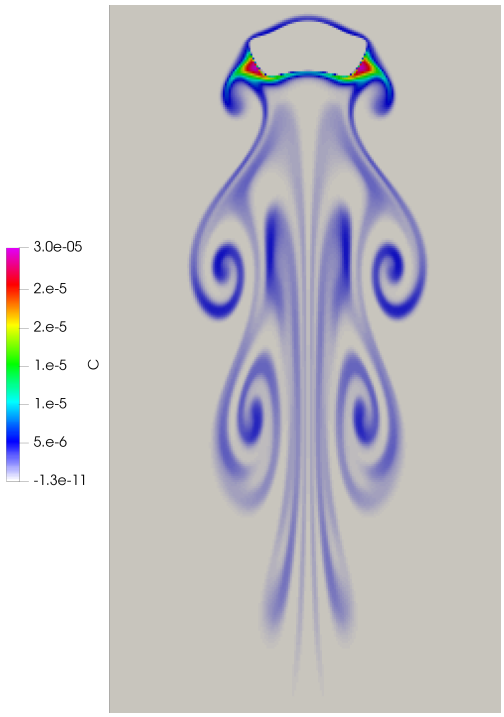

FIGURE 3.13: Liquid concentration "C" around a rising bubble in a quiescent liquid with a modified gravity acceleration

the rising bubble. The diffusivity of the dilute species was set to $1 \times 10^{-5}\,\mathrm{m^2\,s^{-1}}$ to highlight possible issues with the transport of concentration. In figure 3.13, it is important to make sure that the concentration does not display undershoots that are too large. The liquid concentration should be zero in the gas phase. The concentration profile in the liquid bulk is determined by the bulk interpolation scheme for advection (MUSCL here) and the bulk diffusion discretisation (central differencing). These are highly reliable schemes, so that there is no doubt the bulk concentration distribution is accurate. On the other hand, the concentration values may be questioned since no mesh sensitivity analysis was performed on this case.

3.5 Mass transfer around a Taylor bubble in a T-junction

In this section, the focus is on the mass transfer around the Taylor bubbles generated in a T-junction. The species to be transferred is ethylene, diffusing into cyclohexane. The global properties are those of pure ethylene for the gas phase, and of pure cyclohexane for liquid phase. The arbitrary saturation concentration is $0.1\,\mathrm{kg\,m^{-3}}$. Henry's constant is set to 10 for convenience. Figure 3.14 shows two gas channels with 50 mesh cells per diameter on the

left-hand side and 100 mesh cells per diameter on the right-hand side. The focus is put on the gas inlet when the bubble grows just before generation. At this point, the interface has a very regular shape and is pushed towards the edge where the break-up occurs.

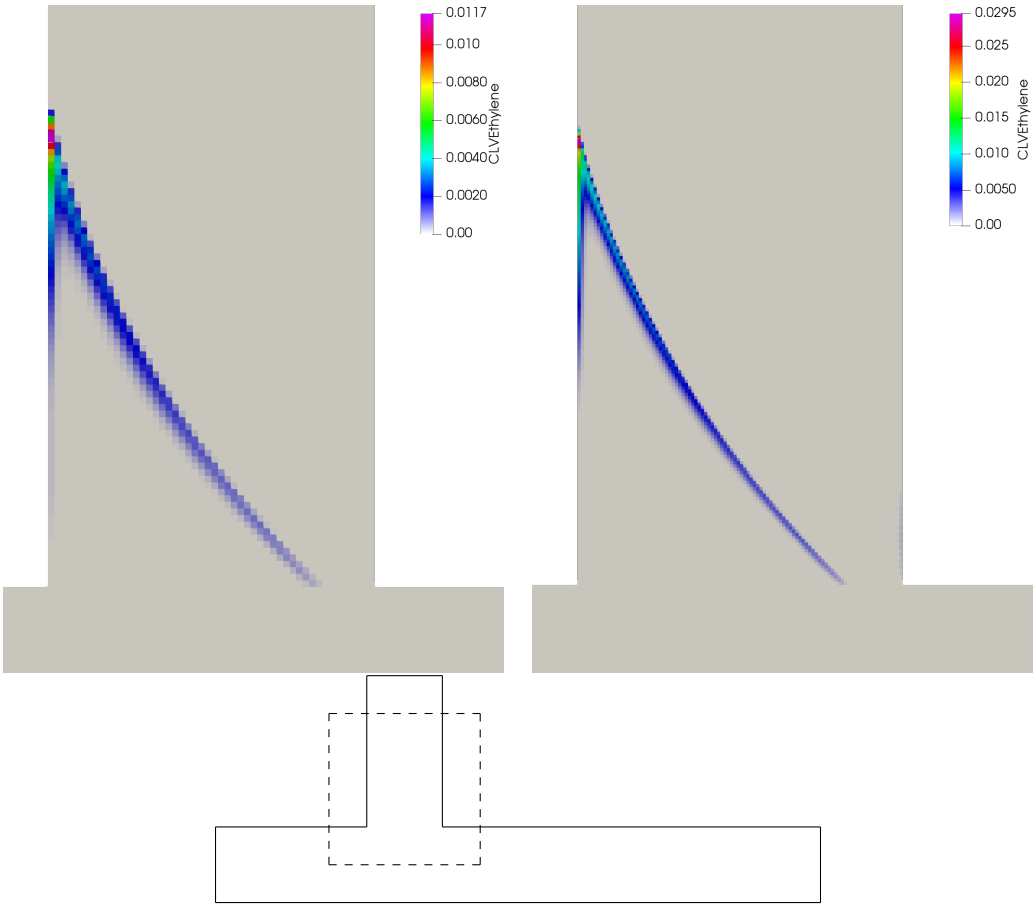

FIGURE 3.14: Liquid phase concentration field of ethyene close to the interface of a growing bubble in the gas injector of a T-junction

The first comment on figure 3.14 is the range of concentration in the liquid phase after transfer. On the coarse mesh on the right, the largest concentration is about 0.0117, while it is 0.0295 on the thinner mesh. The two different meshes do not give the same results because the gradient is smaller on the coarse mesh. The other important aspect of these simulations is the concentration boundary layer thickness. On a coarser mesh, the boundary layer is thicker, even though the number of cells in the layer is the same. This is another issue as it is known in most cases the concentration boundary layer thickness depends on the Sc number and not on the grid size. Grid independency has not been reached yet but improving mesh quality would greatly increase the simulation time.

After the first bubble is generated, the interface retracts into the gas channel. At this point, in 2D simulations (as was pointed out in section 2.3.3.5), a pouch of liquid can be trapped

in the gas channel. It is believed that it is due to the 2D simulation, which does offer more freedom to the interface. Since there is an absence of pouches in 3D simulations. The issue with this liquid retention happens when mass transfer is involved. Indeed, since there is liquid, gas and an interface, there will be mass transfer. When liquid is trapped for a long time, in proximity to a diffusive gas it will become saturated. This is physical behaviour, and the solver should be able to capture. However, it is not clear whether the liquid should remain there during the whole simulation, there are some concerns about this result. The situation is illustrated in figure 3.15.

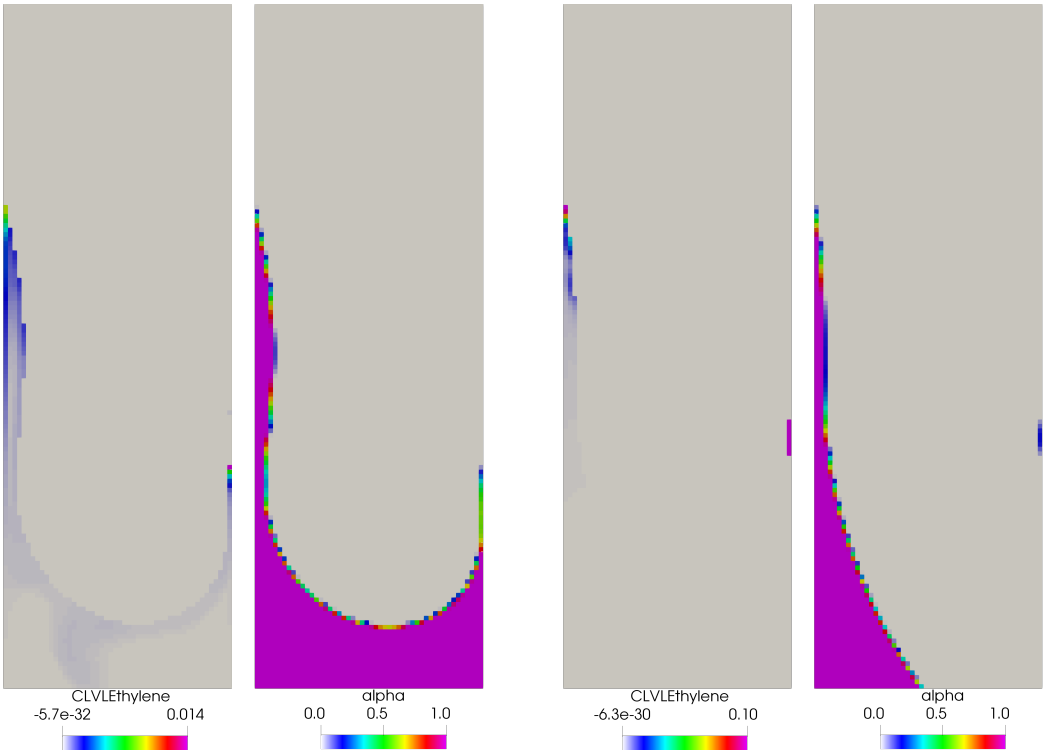

FIGURE 3.15: Mass transfer around a bubble growing downward in the gas injector of a 2D T-junction

The left-hand and right-hand sides show the phase average concentration field ('CLVLEthylene') and the volume fraction field at 0.01 s, and 0.02 s, respectively. Isolated cells near the wall that tend to accumulate the concentration due to the no slip velocity boundary condition can be seen.

Figure 3.16 shows the phase average concentration field for a fully developped Taylor bubble. The recirculations occurring in the liquid slug and carrying the dilute species can be clearly seen. However, for a small diffusivity such as $1 \times 10^{-9}\,\mathrm{m^2\,s^{-1}}$ used here, the length required to reach a good level of mixing is important and very demanding computationally. Figure 3.16 also shows a chequerboard like field near the wall in the bubble. These "wiggles"

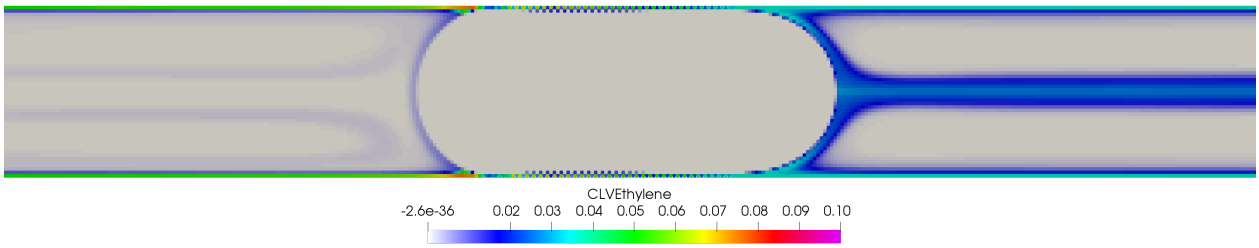

FIGURE 3.16: Mass transfer around a developped Taylor bubble flowing from left to right in the channel of a 2D T-junction

appear in the concentration field because they are present in the volume fraction in the first place. These "wiggles" represent an additional challenge for concentration transport because they require the computation of fluxes in a highly oscillating volume fraction field, which is always difficult to handle numerically. The other important result given by such results is the concentration distribution. The low concentrated zones in dark blue are mainly located in the liquid recirculation and at the caps of the bubble. On the other hand, the liquid film around the bubble is more concentrated with a turquoise colouration. The question of which of these two zones contributes most to the overall mass transfer could be answered computing the local Sh number. The concentration is indeed larger in the film, but the caps gather more cells. Furthermore, the thickness of the concentration boundary layer decreases as the mesh is refined, different results will be obtained in terms of mass transfer.
Figure 3.17 compares the liquid phase concentration field of ethylene for a two-dimensional and a three-dimensional T-junction.
In the case of the 3D simulation, only the cross-section of the central region of the channel is displayed. While the 2D and 3D fields appear quite similar, there are noteworthy distinctions that should be highlighted. The most noticeable difference is observed on the left side of the developing bubble. In the 3D T-junction, there is a recirculation pattern along the left edge of the injector, and the bubble shape also varies. These distinctions could be attributed to the transition from two to three dimensions and the change in boundary conditions. Furthermore, the order of magnitude of the liquid phase concentration also changes; this may be attributed to the increased level of freedom provided by the 3D simulation, especially for the chemical diffusion in the liquid bulk.

3.6 Conclusion

In this chapter the theoretical background behind mass transfer, from surface mass balances on the interface to the numerical implementation of a source term have been presented.

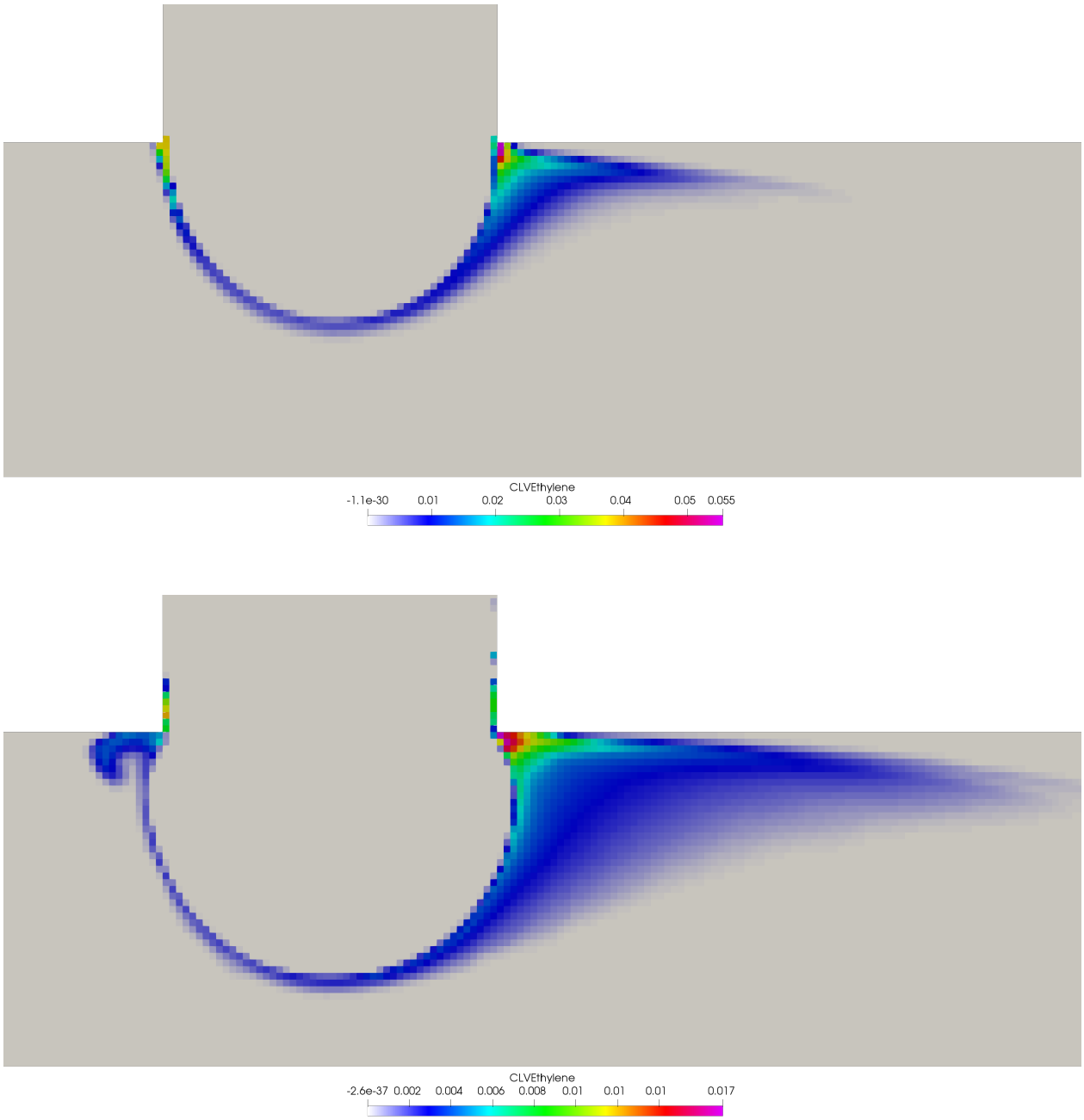

FIGURE 3.17: Liquid phase ethylene concentration comparison between 2D (top) and 3D (bottom) T-junctions

A 1D test case called the Stefan case has enabled the numerical implementation to be validated using well-known analytical results. This test case also allowed the main difficulty of the two-field approach to be illustrated, being the computation of the interface concentration gradient. The results highlighted the need to balance accuracy and feasibility of simulations. To avoid very fine meshes, an appealing solution can be found in subgrid-scale models.
The majority of the simulations on Taylor flows use periodic unit cells to avoid the full simulation of the T-junction. A sufficient mesh refinement is achievable and accurate results

can be obtained with this method. However, the question of the bubble generation to the overall mass transfer contribution cannot be addressed without simulating the full injector. With T-junctions simulations, the importance of 3D validation cases have been discussed, especially at the capillary scale where the hydrodynamics in itself is a challenging step have been discussed.

Chapter 4

Towards the simulation of reactive Taylor flows

4.1 Introduction

The numerical simulation of a 3D T-junction including mass transfer and chemical reaction is a really challenging objective. It requires several achievements such as the full description of the system used, including the properties of the involved species. Additionally, the algorithm presented in chapter 2 and 3 must be extended to include the chemical reaction as another source term producing or consuming species. Chapter 4 presents the different steps that have been covered during this project to complete the simulation of chemical reaction in microchannels. Firstly, the physical properties of all involved species are determined, then, the chemical reaction is intensively reviewed. Finally, the numerical implementation of a chemical reaction is detailed. Additional test cases used to further validate mass transfer without chemical reaction are also discussed. These preliminary steps are necessary to move towards realistic 3D simulations of reactive Taylor flows which has not been covered here.

4.2 Oligomerization of ethylene

This first section is devoted to the prediction of physical properties. The chemical reaction chosen as a test case is also presented.

4.2.1 Prediction of the physical properties

The fluid properties are a compulsory step to each numerical investigation. These properties are the input parameters that give credit to the results. For example, a direct numerical simulation of the hydrodynamics and the mass transfer at the interface of a two-phase flow requires the thermodynamic background to account for the phase equilibrium. In this section, the thermo-physical properties of the fluids are discussed and the models chosen for the prediction of these properties under the experimental conditions are presented.

4.2.1.1 Compressibility and density prediction

A first important aspect of a CFD simulation is the choice between a compressible or incompressible solver. Indeed, the conceptual approach is rather different. A compressible solver uses a variable density and computes the pressure through an equation of state. On the other hand, an incompressible solver uses a constant density and solves for the pressure resulting in a divergence free velocity field. Hence, an important step is to verify the conditions of pressure and temperature to determine the state of the fluids. The critical properties of ethylene are shown in the table 4.1 hereafter. The study of the compressibility is important,

TABLE 4.1: Critical properties of ethylene (database DIPPR)

T_c (K)	282.34
P_c (bar)	50.41
Acentric factor ω	0.086248
Critical compressibility Z_c	0.281

given the operating conditions. In a multiphase problem, the liquid phase will be considered incompressible, but the ethylene (gas phase) needs to be given attention, since the temperature is above the critical temperature. To determine the behaviour of the fluid, an equation of state approach is used to solve the compressibility factor Z. For a real fluid, the ideal gas law can be adapted as follows:

$$P\overline{V} = ZRT \tag{4.1}$$

Solving a cubic equation of state (EOS), i.e. van der Walls, Soave-Redlich-Kwong or Peng-Robinson EOS, the compressibility factor, which indicates the behaviour of the fluid can be determined. For this purpose, the Z value has been calculated for different operating conditions (T and P) using the Soave-Redlich-Kwong (SRK) and Peng-Robinson (PR) equations. These methods are relevant because of their robustness in the vicinity of the critical point,

which is the case here. More information about the methods for each EOS can be found in appendix B.

Density prediction

Using equation 4.1, the density can be modelled as:

$$\rho = \frac{P}{ZRT} M_{ethylene} \tag{4.2}$$

where ρ ($\mathrm{kg\,m^{-3}}$) is the density at (T,P) and $M_{ethylene} = 28\,\mathrm{g\,mol^{-1}}$ is the molar weight of ethylene. Table 4.2 shows predicted densities with the two equations of state:

TABLE 4.2: Prediction of ethylene density ($\mathrm{kg\,m^{-3}}$) under operating temperature and pressure. Results obtained with SRK (left) and PR (right)

	Temperature (°C)		
Pressure (bar)	30	40	50
10	11.77	11.32	10.91
20	25.13	23.98	22.96
30	40.69	38.39	36.41

	Temperature (°C)		
Pressure (bar)	30	40	50
10	11.86	11.40	10.99
20	25.52	24.34	23.28
30	41.69	39.27	37.21

As a point of comparison, the prediction of the density using the ideal gas law would be less reliable for pressure close to the critical pressure. The expression of the ideal gas law is: $\rho = \frac{P}{RT} M_{ethylene}$. The table 4.3 shows the ideal gas results for the operating conditions.

TABLE 4.3: Prediction of ethylene density ($\mathrm{kg\,m^{-3}}$) under operating temperature and pressure. Results obtained with an ideal gas assumption

	Temperature (°C)		
Pressure (bar)	30	40	50
10	11.11	10.75	10.42
20	22.22	21.51	20.84
30	33.33	32.26	31.26

These values can be compared with the values with the NIST database in table 4.4. The calculated values vary very slightly compared with the NIST database, which uses a more complex equation of state. These results exemplify how important the change of density with pressure can be. As the pressure increases, it becomes closer to the critical pressure of ethylene and as the temperature is already above its critical temperature, the gas becomes closer to the supercritical state, which is very different from the gaseous state. However,

TABLE 4.4: Density prediction from the NIST database for ethylene (left) and cyclohexane (right)

	Temperature (°C)		
Pressure (bar)	30	40	50
10	11.79	11.35	10.94
20	25.18	24.04	23.02
30	40.81	38.51	36.54

	Temperature (°C)		
Pressure (bar)	30	40	50
10	770.1	760.6	751.1
20	771.0	761.6	752.1
30	771.9	762.6	753.1

supercritical ethylene in the system will not occur under the range of operating conditions. The liquid phase density is less sensitive to changes due to temperature. On the right-hand side of table 4.4, the values of the density of pure cyclohexane are given. The density of the liquid phase should however be different from these values since it will be a mixture of cyclohexane, ethylene, products (at least butene) and perhaps the catalyst if sufficient data are available to consider it. The Peng-Robinson law is able to predict the density of the mixture using a reduced temperature and pressure of the mixture obtained from the values of the pure components.

4.2.1.2 Solubility

As a starting point, only the dissolution of ethylene in cyclohexane is considered, not the evaporation of cyclohexane in ethylene. The solubility is important because it indicates the amount of ethylene that can be dissolved in the cyclohexane. Ethylene will dissolve into the cyclohexane as long as a driving force is present. This force is the concentration gradient of ethylene. When the ethylene concentration in the liquid phase has reached the thermodynamic equilibrium, the saturation of the cyclohexane prevents any other ethylene molecule to cross the interface. Experiments conducted by Zhuze and Zhurba [1] give data on the influence of pressure and temperature on the solubility of ethylene in cyclohexane as given in figure 4.1.

The relevant data for the targeted operating conditions is given in table 4.5. The isotherm at 40 °C was not present in the original work from [1], however, the value can be interpolated between the two isotherms 30 °C and 50 °C with a simple arithmetic average. This interpolation might not be exact regarding the variations of the solubility with temperature but it provides an acceptable estimation. It can be seen that the ethylene is highly soluble in cyclohexane. Between 10 and 20 bar, the solubility is multiplied by two. In terms of thermodynamics, this means that the equilibrium concentration is also doubled and this

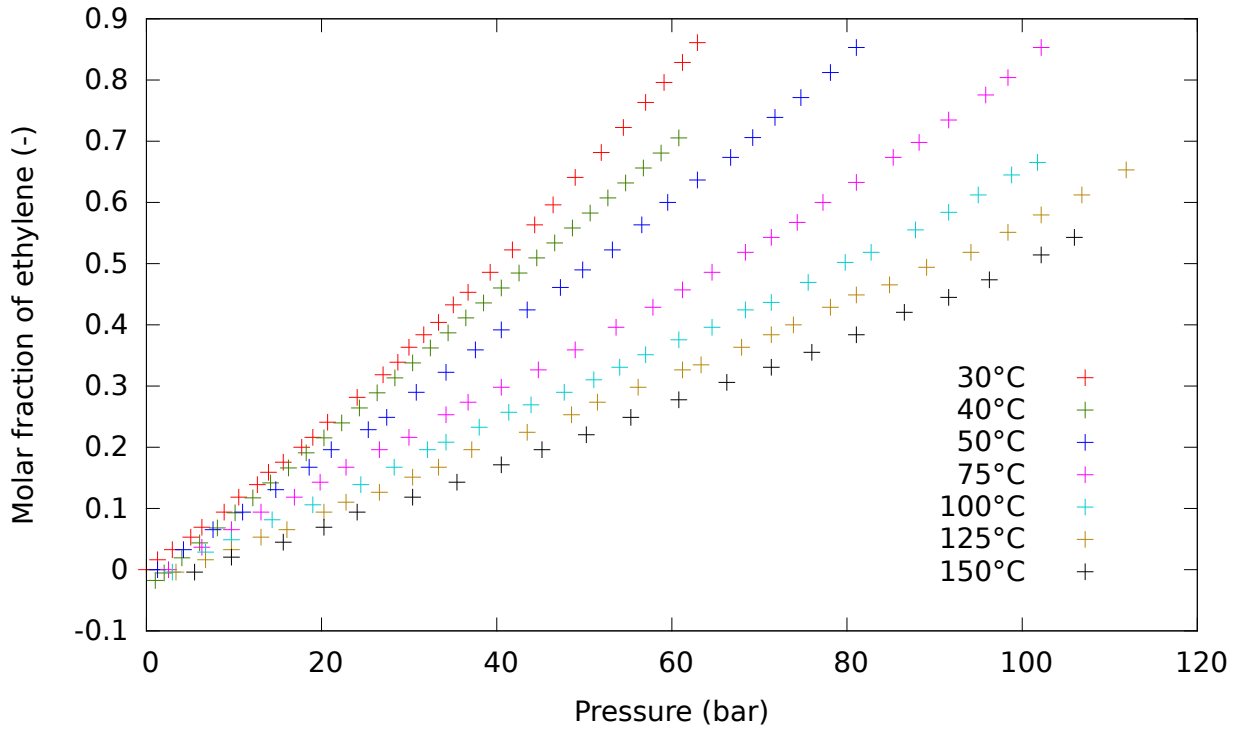

FIGURE 4.1: Isotherms of solubility of ethylene in cyclohexane with pressure from the work of Zhuze and Zhurba [1]

TABLE 4.5: Values of the molar fraction of ethylene under pressure and temperature from [1]

	Temperature (°C)		
Pressure (bar)	30	40	50
10	0.110	0.098	0.084
20	0.229	0.208	0.180
30	0.358	0.325	0.280

will influence the rate of mass transfer. It is therefore important to predict the solubility of ethylene in cyclohexane at each pressure and temperature.

4.2.1.3 Diffusivity

The diffusivity coefficient appears in Fick's law to calculate the mass flux:

$$J_A = -D_{AB} \nabla C_A \tag{4.3}$$

where J_A is the molar flux (or mass flux) in $\mathrm{mol\,m^{-2}\,s^{-1}}$, ∇C_A is the concentration gradient in $\mathrm{mol\,m^{-4}}$ and D_{AB} is the diffusivity coefficient of species A in the binary mixture AB in $\mathrm{m^2\,s^{-1}}$. This coefficient varies (at least in a first approximation) with the temperature, pressure, and the concentrations of other species in the mixture. In our situation, the diffusion of ethylene in itself for the gas side must be separated from that of the liquid phase. For the gas phase, ethylene is pure, and the reaction does not take place in the gas phase. On the other hand, the liquid phase is more complex. There are more than one species, since there is the solvent, cyclohexane, the gas, ethylene, the catalyst and also the reaction products. In a first approach, only ethylene and cyclohexane are considered; the products and catalyst will not. The difficulty of considering a mixture of the solute, the solvent and the products is taking into account the impact of the concentrations on the diffusivity coefficient.
Indeed, many derivations for diffusivity coefficients are for infinitely dilute conditions, while others focus on the self-diffusing solvent or solute. There is also uncertainty in applying a correlation for a binary mixture of two gases only to ethylene to predict self diffusion. However, it is interesting to test these correlations to appreciate the effects of temperature and pressure on the diffusion coefficient. A small impact of one parameter could be an acceptable error regarding the other sources of uncertainty such as the chemical reaction.

Gas phase

In the following text, methods to derive the different diffusion coefficients are presented. All these methods are detailed in [119], which contains the information needed to predict the thermophysical properties of the fluids.
The theory behind the diffusivity coefficient for a binary system of gases at low to moderate pressures can be attributed to Enskog and Chapman [120], who both solved the Boltzmann equation and derived the following relationship:

$$D_{AB} = \frac{3}{16}\frac{(4\pi kT/M_{AB})^{0.5}}{n\pi\sigma_{AB}^2\Omega_D} f_D \tag{4.4}$$

M_A and M_B are the molar weights of species A and B ($\mathrm{g\,mol^{-1}}$). $M_{AB} = 2[1/M_A + 1/M_B]^{-1}$. n is the number density of molecules in the mixture, k is the Boltzmann's constant ($k = 1.38 \times 10^{-23}\,\mathrm{J\,K^{-1}}$), T is the temperature (K), Ω_D is the collision integral for diffusion, which depends on temperature and the interactions forces chosen, σ_{AB} is the characteristic length of the intermolecular force law and f_D is a correction term. If M_A and M_B are of the same order of magnitude, f_D is around 1. n can be expressed with the ideal-gas law, but with higher temperature and pressure it may be less precise. Nevertheless, empirical correlations for binary gases at low pressures exist to predict the diffusion coefficient. The works of Fuller

et al. [2, 121, 122] modified a relationship from Wilke and Lee [123] to obtain the following:

$$D_{AB} = \frac{0.00143T^{1.75}}{PM_{AB}^{1/2}\left[(\Sigma_v)_A^{1/3} + (\Sigma_v)_B^{1/3}\right]^2} \tag{4.5}$$

Where P is the pressure (bar), Σ_v is the summation of the diffusion volumes for species A or B. Other terms are the same as in equation 4.4. These diffusion volumes are given in the work of Fuller et al. [2], however, the authors indicate that these values are based only on a few studies.

TABLE 4.6: Atomic diffusion volumes from [2]

Atomic diffusion volume increments ($cm^3\,mol^{-1}$)			
C	15.9	F	14.7
H	2.31	Cl	21.0
O	6.11	Br	21.9
N	4.54	I	29.8
Aromatic ring	-18.3	S	22.9
Heterocyclic ring	-18.3		

For the diffusion of ethylene in itself, $(\Sigma_v)_A = (\Sigma_v)_B = 41.04\,cm^3\,mol^{-1}$. Using relationship 4.5, the values of ethylene diffusing in itself in the gas phase have been computed. The values presented in table 4.7 were calculated at low pressures, since the relationship 4.5 has only been verified for low pressures. When the pressure increases, the product $D_{AB}\,P$ is no longer constant and this relationship does not represent the behaviour of the gas anymore. To predict the diffusivity of a gas under pressure, Takahashi [3] proposed a method to correct

TABLE 4.7: Values of ethylene diffusivity in the gas phase ($cm^2\,s^{-1}$) computed from relationship 4.5 at low pressures

	Temperature (°C)		
Pressure (bar)	30	40	50
1	0.102	0.108	0.114
2	0.051	0.054	0.057
3	0.034	0.036	0.038

the product $D_{AB}\,P$. This method is applied to the self-diffusing ethylene and the relationship is given below:

$$\frac{D_{AB}\,P}{(D_{AB}\,P)^+} = f(T_r, P_r) \tag{4.6}$$

The superscript + stands for the product at low pressure. The value of function $f(T_r, P_r)$ is obtained in the following chart published by [3]. Only the curves of low reduced temperature

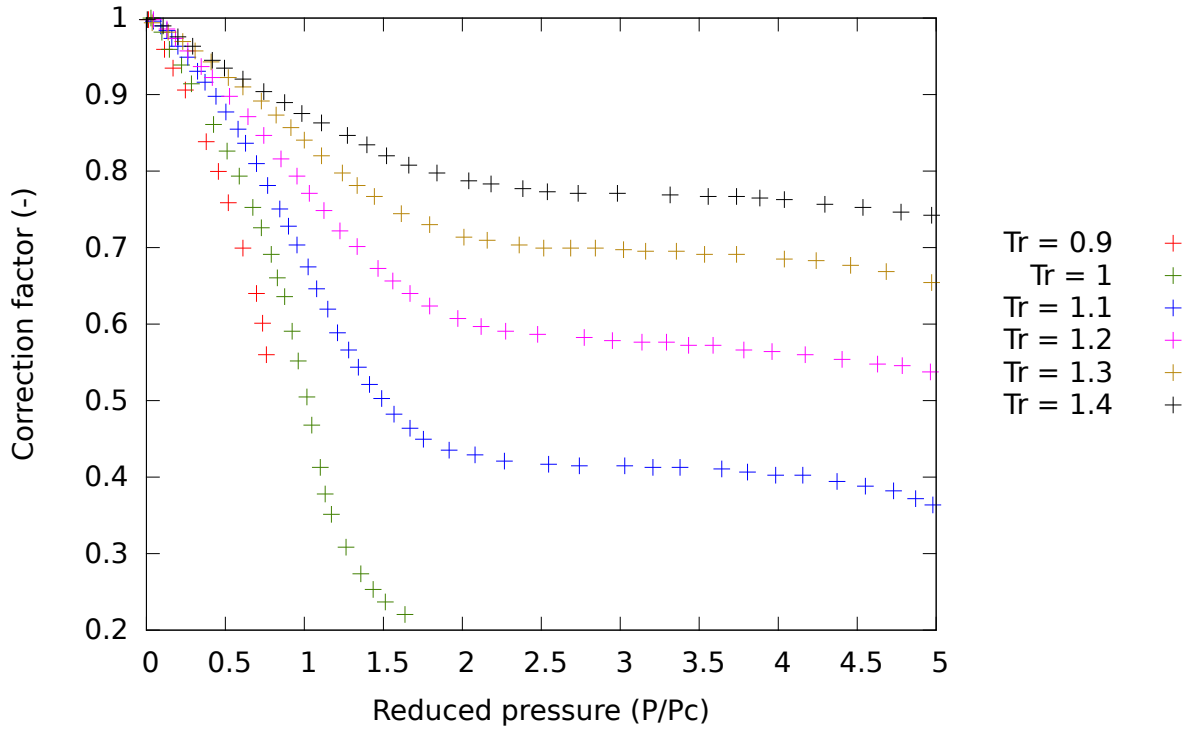

FIGURE 4.2: Takahashi's correction factor at reduced pressure and temperature for gaseous diffusion coefficient

from 0.9 to 1.1 are useful for the current case. Applying relationship 4.6, the diffusivity in the real operating conditions from the values of the table 4.7 can be deduced. The values of diffusivity for the current operating conditions are gathered in the table 4.8 below. The

TABLE 4.8: Values of ethylene diffusivity in the gas phase ($cm^2\,s^{-1}$) computed from the relationship of Takahashi [3] at operating pressures

	Temperature (°C)		
Pressure (bar)	30	40	50
10	0.0098	0.0104	0.0110
20	0.0047	0.0049	0.0052
30	0.0029	0.0030	0.0032

influence of pressure in relationship 4.5 can be observed. When the pressure increases from 1 bar to 2 bar, the diffusion coefficient is divided by two. This means the variation of the coefficient is strongly influenced by pressure. The same conclusion from the data corrected with Takahashi's method can be drawn. However, before considering a pressure dependent

diffusion coefficient, it should be verified that pressure variations in the different cases require a prediction of a pressure-dependent diffusion coefficient.

Liquid phase

The density of liquids, in comparison with gases, implies that diffusion coefficients in liquids are smaller than in gases. The Stokes-Einstein equation has been used as a starting point to derive empirical models. It can be written as follows:

$$D_{AB} = \frac{RT}{6\pi\,\eta_B\,r_A} \tag{4.7}$$

η_B is the viscosity of the solvent and r_A is the radius of the spherical solute. The literature is more detailed about the influence of temperature on the diffusivity of ethylene in cyclohexane than it is for the impact of pressure. A study of the impact of temperature for the mixture ethylene-cyclohexane, and another one for the impact of pressure on the self-diffusion of cyclohexane in itself is therefore presented. Even though these equations may not apply to the ethylene-cyclohexane mixture, the impact of temperature and pressure on the self-diffusion of cyclohexane is of interest. That is the change of the diffusivity coefficient that is important: if it varies only slightly with temperature or pressure, then a simplifying assumption can be made and constant data at a reference state can be used. Ethylene might be very soluble in cyclohexane, however its molar fraction will not exceed 36% (see table 4.5). Determining the self-diffusity of cyclohexane is a good starting point to predict the diffusion coefficient of the mixture.

Influence of temperature

Chen et al. [124] investigated the influence of temperature on the diffusivity coefficient of several gases in solvents, including cyclohexane, although they do not evaluate the impact of pressure. Their results are given in the table below. The current operating conditions

Temperature (K)	Diffusivity coefficient ($10^9 D_{EC}$ in $\mathrm{m^2\,s^{-1}}$)
280.6	2.35
298.2	3.20
323.2	4.67
343.2	6.08
363.2	7.89

TABLE 4.9: Impact of temperature on the diffusivity coefficient of ethylene in cyclohexane

range between 303.15 K and 323.15 K. According to their results, the diffusivity coefficient should vary from 3.2×10^{-9} to $4.67 \times 10^{-9} \mathrm{m^2\,s^{-1}}$, which is less than one order of magnitude. However, these results might have been obtained under a different pressure than the current

operating conditions. No detail about the pressure was given, so it was assumed as atmospheric pressure. Another way to predict the diffusion coefficient is the Wilke and Chang relationship [125]:

$$D^{\circ}_{AB} = 7.4 \times 10^{-8} \frac{(\phi_B M_B)^{0.5} T}{\eta_B V_A^{0.6}} \tag{4.8}$$

Where A is the solute and B the solvent, D° is in $\mathrm{cm^2\,s^{-1}}$ and represents the diffusion coefficient of solute A in solvent B at infinite dilution, M_B is the solvent molecular weight in $\mathrm{g\,mol^{-1}}$, ϕ_B is a dimensionless association factor (2.6 for water, 1.9 for methanol, 1.5 for ethanol and 1 for a nonassociated solvent), η_B is the viscosity of the solvent (in cP), V_A is the molar volume of the spherical solute in $\mathrm{cm^3\,mol^{-1}}$.

Influence of pressure

Relationship 4.8 is not suitable for prediction of the impact of pressure. However, the use of the viscosity at high pressure could be an option to determine the diffusion coefficient at high pressure from the relationship $D^{\circ}_{AB}\,\eta_{AB} = constant$. Dymond and Woolf [126] showed that this relationship should be satisfactory for large solute molecules. Using the values of viscosity at high pressure, the following values for the infinite dilute diffusion coefficient of ethylene in cyclohexane were computed:

TABLE 4.10: Infinite dilute diffusivity of ethylene in cyclohexane calculated with the Wilke-Chang relationship $\times 10^{-5}\,\mathrm{cm^2\,s^{-1}}$

	Temperature (°C)		
Pressure (bar)	30	40	50
10	2.395	2.883	3.432
20	2.362	2.843	3.384
30	2.331	2.804	3.337

The impact of pressure is low (as it is on viscosity). On the other hand, the impact of temperature is not negligible. An increase of 10 °C leads to a change of around 20% of the diffusion coefficient. In a first approximation, constant values of infinite dilute diffusivity are considered at each operating condition. However, if the heat released by the reaction is too high, the energy conservation equation must be solved to determine the temperature field and recalculate the value of the diffusion coefficient at local temperatures. The difficulty of finding information about the pressure dependency of the diffusivity coefficient led us to consider the variation of the self-diffusion coefficient only. As discussed in the solubility section 4.2.1.2, ethylene is highly soluble in cyclohexane. When considering a one-fluid approach, the diffusivity coefficient of this new fluid has to be introduced, using those of each species of the mixture. Several options are available to define the diffusivity in each

computational cell of the domain. One way is to define a mean diffusivity coefficient as presented by Haroun [64]. In this case, an arithmetic mean over the volume fraction of the fluids in the cell can be used. Another common formulation consists in using a harmonic mean, as presented in the work from Deising [67]. In all cases, the diffusivity coefficient of a cell will depend on the volume fraction of the compounds. As the solubility increases, the contribution of the ethylene diffusivity in the averaged diffusivity increases. If the change of both ethylene and cyclohexane diffusivity with pressure cannot be considered negligible, then it must be predicted.

The changes in cyclohexane self-diffusion as a function of pressure will now be discussed. Jonas [4] conducted experiments to determine the "self-diffusion" of cyclohexane under pressure and temperature for 313 K and 333 K. . This approximation seems accurate at low

TABLE 4.11: Values of self-diffusion of cyclohexane ($\times 10^{-5}\,cm^2\,s^{-1}$) under pressure and temperature from Jonas [4]

	Temperature (°C)		
Pressure (bar)	30	40	50
10		1.97	2.47
20		1.94	2.44
30		1.91	2.41

pressures but not at high pressures where the linear dependence of the diffusion with pressure is no longer valid.

4.2.1.4 Viscosity

Gas phase

For gases, the impact of pressure on the viscosity depends on the reduced pressure and temperature.

The effect of temperature has less impact on the gas phase. Since the reaction occurs in the liquid phase, it can be supposed that the temperature will not vary that much in the gas phase. As seen from the table 4.12, a change of 10 °C leads to a variation of 3% of the viscosity. It is therefore appropriate to start with a constant viscosity for ethylene in the gas phase. For the pressure, an increase of 10 bar will also induce a change of around 3% of the viscosity. Hence, the simulation can be set to incompressible regarding the pressure drop in the reactor. It is once again relevant to use a constant viscosity regarding the influence of

TABLE 4.12: Values of dynamic viscosity ($\times 10^{-5}$ Pa s) under pressure and temperature for ethylene from NIST

	Temperature (°C)		
Pressure (bar)	30	40	50
10	1.07	1.10	1.13
20	1.10	1.13	1.16
30	1.15	1.18	1.20

pressure.

Liquid phase

The viscosity of liquids decreases with temperature and it increases with pressure.

TABLE 4.13: Values of dynamic viscosity (mPa s) under pressure and temperature for cyclohexane from NIST

	Temperature (°C)		
Pressure (bar)	30	40	50
10	0.829	0.711	0.616
20	0.840	0.721	0.625
30	0.852	0.731	0.634

From the values of viscosity in table 4.13, it can be seen how small the impact of pressure is. At a given temperature, an increase of 10 bar results in a variation of around 1.4% the viscosity. On the other hand, the impact of temperature is important. At a given pressure, the change from 30 °C to 50 °C results in a 25% variation of the viscosity. The effect of temperature is thus important, especially in the case of an exothermic reaction. A high local reaction rate will increase the temperature and may modify the viscosity in non-negligible proportions. Furthermore, the change of pressure in the reactor due to head losses is small as was noted during experiments [41]. Hence, it is a valid assumption to consider a constant value of viscosity for each pressure and only predict a change with temperature.

4.2.1.5 Thermal conductivity

Gas phase

The thermal conductivity of gases increases with pressure. However, this effect is limited as long as a moderate pressure is reached.

TABLE 4.14: Values of thermal conductivity ($W\,m^{-1}\,K^{-1}$) versus pressure and temperature for ethylene from NIST

	Temperature (°C)		
Pressure (bar)	30	40	50
10	0.022	0.023	0.024
20	0.023	0.024	0.025
30	0.024	0.025	0.027

An increase of 10 bar will change the thermal conductivity by around 5%. The same order of change is observed for an increase of 10 °C. As already mentioned, the pressure drop is low in a micro tube reactor. A prediction of the thermal conductivity variation versus pressure is thus not needed and the assumption of a constant value for each pressure is valid. In the case of the gas, the same conclusion applies to the temperature change since the temperature gradients will mostly be located in the liquid phase. In conclusion, the assumption of a constant value for thermal conductivity is sufficient for each operating condition.

Liquid phase

Generally, the thermal conductivity decreases when increasing the temperature. The conductivity of liquids is larger than that of gases at low pressure. At moderate pressure, under 50 bar, the effect of pressure on the conductivity is often neglected. The data for the thermal conductivity are more easily accessible compared with diffusivity data.

TABLE 4.15: Values of thermal conductivity ($W\,m^{-1}\,K^{-1}$) versus pressure and temperature for cyclohexane from NIST

	Temperature (°C)		
Pressure (bar)	30	40	50
10	0.1232	0.1209	0.1187
20	0.1236	0.1214	0.1191
30	0.1240	0.1218	0.1195

The effect of temperature and pressure is quite small, as shown in table 4.15. An increase of 10 bar changes the conductivity by around 3% and an increase of 10 °C induces a change of around 2%. Some experiments report values of pressure drop of up to 3 bar over the length of the reactor. Thus, the local change in pressure is small and its influence on the prediction of the thermal conductivity can be neglected. A pressure drop of 3 bar induces a change of less than 1% of the thermal conductivity, which is small enough to assume a constant value.

4.2.1.6 Surface tension

A linear relationship between temperature and surface tension is widely used. It is an important property at the microscale as the capillary force becomes dominant. The surface tension is used to calculate the surface tension force, which defines the shape of the interface. For VOF simulations, the computation of the surface tension force is a major issue. Small errors in the computation of this force will create a source term in the momentum conservation which in the end produces spurious currents.
Table 4.16 shows the variations of surface tension coefficient with temperature and it can be concluded that the influence of temperature (in the range of interest) on surface tension is of the order of 10%.

TABLE 4.16: Values of surface tension coefficients for cyclohexane from NIST

Temperature (K)	Surface tension ($\mathrm{N\,m^{-1}}$)
303	0.0241
313	0.0229
323	0.0217

Surface tension coefficients are measured at the saturation temperature of the compound. The values correspond to the temperature dependence of the surface tension coefficient of cyclohexane in equilibrium with its own vapour phase. No pressure dependence was found in the literature. As the measure is done at the saturation temperature, the pressure is also fixed. Phase composition affects the surface tension coefficient, however, data found in the literature only presented the surface tension coefficient of a pure component. We have provided results as meaningful as possible but finding experimental data for very specific mixture is sometimes complicated.

4.2.2 Description of the chemical reaction

The reaction studied is the oligomerization of ethylene. The catalyst considered for this reaction is the Nickel(II) 2-ethylhexanoate. It is activated in situ using ethylaluminium dichloride.

$$2\mathrm{C_2H_4} \xrightarrow[\mathrm{EtAlCl_2}]{\mathrm{Ni(2\text{-}EH)_2}} C_4H_8 \tag{4.9}$$

In the following text, the complex will simply be noted Ni-H for convenience. We also adopt a classification of the products by size of the olefin. Butene C_4H_8 is present as three isomers:

1-butene, 2-butene(cis) and 2-butene(trans). The name C_4 stands for these three isomers. Before the $\beta - H$ elimination, another ethylene coordination and insertion can occur. In this case, the product formed is hexene. Depending on where ethylene is inserted, the product can be either a linear hexene or one of its branched isomers. In some cases, the dimerization of butene can also happen. Longer chains can be obtained. However, the selectivity decreases as the length of the chain increases. Table 4.17 summarizes the distribution of the products:

TABLE 4.17: Products distribution (w%) reported by Mahmoud Kamaleddine

Isomere	Relative weight
C_4	70-80
C_6	20-30
C_8, C_{10}, C_{12+}	5-10

Considering all the reactions for the heavier olefins, such as C8+, is not very relevant because the mass fraction of these alkenes is smaller than 10%. However, their inclusion will introduce a lot of secondary reactions and make the simulation much more complex. There are everal possibilities to model the reaction depending on how many products are considered. The easiest kinetic scheme is to only consider the butene dimerization, even though at least 20% of the products are neglected. Nonetheless, this assumption makes the model of the chemical reaction much simpler. The definition of the reaction is then:

$$Ni - H + 2C_2 \longrightarrow Ni - H + C_4 \tag{4.10}$$

Since there is only one reaction, the rate of reaction can be written as:

$$r = k[Ni - H][C_2] \tag{4.11}$$

A more complete kinetic model would account for the produced isomers of hexene. The model of this reaction consists of two steps. It starts with a growth phase where a free molecule of ethylene reacts with a complex of nickel and ethylene. A chain termination step then occurs: an oligomer is formed while the catalyst is freed for the insertion of a new ethylene molecule. This reaction model will be described using a general form. Where two indices, one for the degree of polymerization (m) and one for the counting (j) with $m \geq 1$ and $j \geq 1$ are used. The growth reactions (step A) involving the lighter olefins are given below:

$$Ni(C_2)_{m-j} + (C_2)_j \longrightarrow Ni(C_2)_m \tag{4.12}$$

In the case where $m = j$, the initiation step occurs and $Ni - H$ can be written instead of $Ni(C_2)_0$.
The second step (B) of chain termination can be represented as follows:

$$Ni(C_2)_{m-j} + (C_2)_j \longrightarrow Ni - H + (C_2)_m \tag{4.13}$$

In this definition of the mechanism, the isomers are gathered under a mass category. This description is interesting because it is general and can describe the longer isomers as well. In the current case, $m = 3$ correspondig to hexene.
We will now discuss the reactions involved in this description to better understand how many species are being dealt with. For the first stage, the growth reactions are obtained when equation 4.12 takes the values of $j \in [1:3]$ and $m \in [1:3] \,|\, m \geq j$. For clarity $(C_2)_j$ is written as C_{2j}. The first reactions are the initiations that can occur for $j = 1$, $j = 2$ and $j = 3$ depending on the molecule linked to the catalyst. All the combinations of m and j can then be written respecting the constraints:

$$\begin{aligned}
Ni - H + C_2 &\longrightarrow Ni - C_2 \\
Ni - H + C_4 &\longrightarrow Ni - C_4 \\
Ni - H + C_6 &\longrightarrow Ni - C_6 \\
Ni - C_2 + C_2 &\longrightarrow Ni - C_4 \\
Ni - C_4 + C_2 &\longrightarrow Ni - C_6 \\
Ni - C_2 + C_4 &\longrightarrow Ni - C_6
\end{aligned} \tag{4.14}$$

For the chain termination step, the same method is applied to derive the following equations, except that in this case: $m \geq j + 1$.

$$\begin{aligned}
Ni - C_2 + C_2 &\longrightarrow Ni - H + C_4 \\
Ni - C_2 + C_4 &\longrightarrow Ni - H + C_6 \\
Ni - C_4 + C_2 &\longrightarrow Ni - H + C_6
\end{aligned} \tag{4.15}$$

Each of these reactions can be associated with a reaction rate; the reaction orders are usually taken as one. More details about the catalytic system can be found in [127]. These reaction rates only consider the chain becoming heavier each time an ethylene is inserted and all the mechanisms leading to this result are "hidden" in the kinetic constant. A reaction rate can be associated with each reaction listed in 4.14. In a first approximation, it is assumed that

all reactions are of second order:

$$\begin{aligned} r_1 &= k_1[C_2][Ni-H] \\ r_2 &= k_2[C_4][Ni-H] \\ r_3 &= k_3[C_6][Ni-H] \\ r_4 &= k_4[C_2][Ni-C_2] \\ r_5 &= k_5[C_2][Ni-C_4] \\ r_6 &= k_6[C_4][Ni-C_2] \end{aligned} \tag{4.16}$$

Similarly, the rates of the termination steps can be written as:

$$\begin{aligned} r_7 &= k_7[C_2][Ni-C_2] \\ r_8 &= k_8[C_4][Ni-C_2] \\ r_9 &= k_9[C_2][Ni-C_4] \end{aligned} \tag{4.17}$$

The constants $k_i \mid i \in [1:9]$ can be described by an Arrhenius law and are related to the temperature as follows:

$$k_i = k_{ref,i} \times \exp\left[\frac{-E_{a,i}}{R} \times \left(\frac{1}{T} - \frac{1}{T_{ref,i}}\right)\right] \tag{4.18}$$

$E_{a,i}$ is the activation energy ($\mathrm{J\,mol^{-1}}$), $k_{ref,i}$ is the pre-exponential factor which depends on the chemical reaction ($\mathrm{m^3\,mol^{-1}\,s^{-1}}$) at $T_{ref,i}$ (°C).

As said before, the partial orders in equations 4.16 and 4.17 are taken to have a value of one. During the catalyst screening tests, the experiments were in agreement with one for each partial order. The experiments also indicated that the reaction takes place in the liquid bulk. In the case of microreactors, recirculations occur in the liquid bulk. Therefore, as a starting point it is considered that the liquid bulk is perfectly mixed, which means that the ethylene is diluted homogeneously in the liquid phase as soon as it transfers from the gas phase. This perfectly mixed liquid phase is an assumption that is not verified. To check if this hypothesis is relevant, the characteristic time of mixing in the liquid bulk can be compared with the characteristic time of the reaction. If the mixing is much slower than the reaction, the reaction will occur near the interface as soon as the ethylene enters the liquid phase. It will lead to a high concentration gradient and reaction rate at the interface, in addition to the high density gradient of the interface itself. In this case, the simulation will be more complex. However, it seems reasonable to start with a homogeneous concentration of both ethylene and catalyst in the liquid phase, meaning that in each cell the reaction rate

would be the same as a mean value calculated on the whole liquid slug.

4.3 Implementing a chemical reaction through a volumetric source term

Many different types of chemical reactions exist, therefore a one-fits-all description would not be realistic. Hence, the implementation details of the developed methods will be tailored to the specific needs of ethylene oligomerization. All theoretical details about the chemical reaction will be presented later in section 4.2.2. The focus will be on second order power law kinetics, although it should be transposable to any kind of power law order. Chemical reaction is essentially another source term that must update a given field based on local conditions. In light of this, chemical reactions can then be modelled either as a surface reaction or a volumetric reaction. For surface reactions, the reaction rate will depend on the surface concentration and the contact area. Such reactions occur at the interface because the reaction rate is so large that the reagent is totally consumed as soon as it crosses the interface. On the other hand, a volumetric reaction is considered when the rate of reaction is not limited by previous transport steps. Volumetric reactions occur in the bulk and are not localised at the interface. Under these conditions, the reagents are transported away from the interface and can be consumed on the way. Heterogeneous catalysis reactions are often considered as surface reactions. Their reaction rate depends on surface-active sites and the adsorption of reagents onto the active sites. For homogeneous catalysis, the reaction occurs when the compound is diluted is the same phase as the catalyst. Nevertheless, a homogeneous catalysis reaction could be a surface reaction if the reaction rate is very large compared with the characteristic time of transfer from the gas to the liquid. Experimental data are necessary to substantiate the preference for one formulation over another. Kamaleddine and coworkers [26] reported Ha numbers between 0.13 and 0.5 in a study of mass transfer in microfluidic devices in the case of oligomerization of ethylene. The parameters giving these values were typical concentrations for catalyst screening in stirred tanks. The authors concluded the oligomerization reaction was not mass transfer limited in their operating conditions.
In these conditions, a volumetric source term accounting for the chemical reaction is developed. The reaction rate constant is firstly determined and can be written for the general reaction:

$$\nu_A \mathrm{C_A} \longrightarrow \nu_B C_B \tag{4.19}$$

As:

$$r = k\, C_A^{\nu_A}\, C_B^{\nu_B} \tag{4.20}$$

A mass balance over each species must take into account the stoechiometry, if $i \in A, B$:

$$R_i = \nu_i r \tag{4.21}$$

Note that the balance must be a mass balance or a molar balance since volume is not necessarily conserved during the reaction. Furthermore, equation 4.21 only considers one reaction. If the species is involved in multiple reactions, the expression must include all the reactions rates and the respective stoechiometric coefficients of the species in the reaction. The definitions of the reaction rate given by equation 4.20 are adapted to sequential solving. Coupling all individual mass balances of species involved in multiple reactions is quite difficult. Indeed, as will be seen, the reaction systems can be very large and even include chain reactions. Consistently with the mass transport and mass transfer, the reaction rate is dealt with explicitly in time. The reaction rate is computed after advection and mass transfer but at the same time as diffusion, as recommended by Fleckenstein and Bothe [90]. The concentrations used to compute the reaction rate are not updated at the same moment for each species. The only way to compute multispecies transport is to create a list of species and then loop over this list. Therefore, if the first species has already been updated for advection and mass transfer, it may not be the case for the second species which comes after in the species' list. Once the reaction rate is determined, it is used on the right-hand side of the diffusion equation solved implicitly in time. Issues might appear if the concentration of a species ever becomes negative.

In order to implement this, all of the involved species are defined in a sub-dictionary inside the `constant/transportProperties` file. For each species, several properties must be declared. An example is given below:

```
Ethylene
{
        DL              1e-09;
        DG              0;
        H               10;
        CLsat           0.1;
        CGsat           1;
        Mw              0.2805;
        coeff           -2;
        kArrhenius      0;
}
```

FIGURE 4.3: Definition of the species Ethylene inside the `constant/transportProperties` dictionary

The properties defined in this sub-dictionary are read at the beginning of the simulation. If one value is missing, a default value is assigned instead (1 for H for example). D_L and D_G are the species diffusion coefficients in the liquid and gas phases, respectively. H is Henry's constant for the considered species. $C_{L,sat}$ and $C_{G,sat}$ are the saturation concentrations of the species in liquid and gas phase. In case of a pure component, these saturation concentrations correspond to the density of the phases to match the hydrodynamics solver. M_W is the molar weight, `coeff` is the power ν in relationship 4.20. Finally, $k_{Arrhenius}$ is the rate constant, which depends on temperature, involved in relationship 4.20. Since this is an isothermal solver, the user should compute the rate constant at the operating temperature, prior to the simulation. All the previously mentioned properties have SI units. The order of the chemical reaction will indicate the units of the rate constant.

For chemical systems with multiple reactions, the solver can be extended to create a list of reactions that the user would supply as an input dictionary like `transportProperties`. A possible implementation may include a base dictionary, called for example `reactionProperties`. The main dictionary may be composed of sub-dictionnaries, one per chemical reaction. In these sub-dictionnaries, the reagents and products can be specified, their stoechiometric coefficients, the rate constant and so on. To compute the final reaction source term, the algorithm loops over all chemical reactions present in the `reactionProperties`. The final computation is then the product of the concentration of all the involved reagents at their respective power times the rate constant. In the equation, the stoechiometric coefficient multiplies the reaction rate to make it a source or a sink term. The current version of the code for a single chemical reaction is given in figure 4.4.

```
forAll(species, i)
{
        ...
        forAll(species, j)
        {
                reactionRatei *= pow(CLVLj, coeffj);
        }
        ...
        CLVLi.correctBoundaryConditions();
        fvScalarMatrix CLVEqni
        (
                fvm::ddt(CLVLi)
              - fvm::laplacian(DLeffi, CLVLi)
              - coeffi * reactionRatei
        );
        CLVEqni.relax();
        CLVEqni.solve();
}
```

FIGURE 4.4: Source code of the chemical reaction source term and equation solving

In figure 4.4, `CLVL` is for the phase average concentration (concentration in the liquid averaged over the volume of liquid). `fvm::ddt` is the time variation operator, `fvm::laplacian`

is the diffusive part and `reactionRatei` is the source term standing for the chemical reaction for species i. It is very convenient working with chemical reactions following a power law because programming reduces to a simple loop over all species and to multiplying by the concentration to obtain the final reaction rate. Another option would be to place the computation of the reaction rate before the first `forAll`. In this sequence a small loop will allow the computation of the reaction rate once and for all species, the transport equations would then be included in another `forAll` loop over all species that would take most of the computational effort. Finally, the reaction is either a source or a sink term depending on the sign of `coeffi`, the stoechiometric coefficient of species i in the reaction considered. It is easier to start with only one reaction and increase the system complexity after validation. Figure 4.5 shows the flowshart of the complete algorithm that inlcudes the partial implementation of a chemical reaction source term.

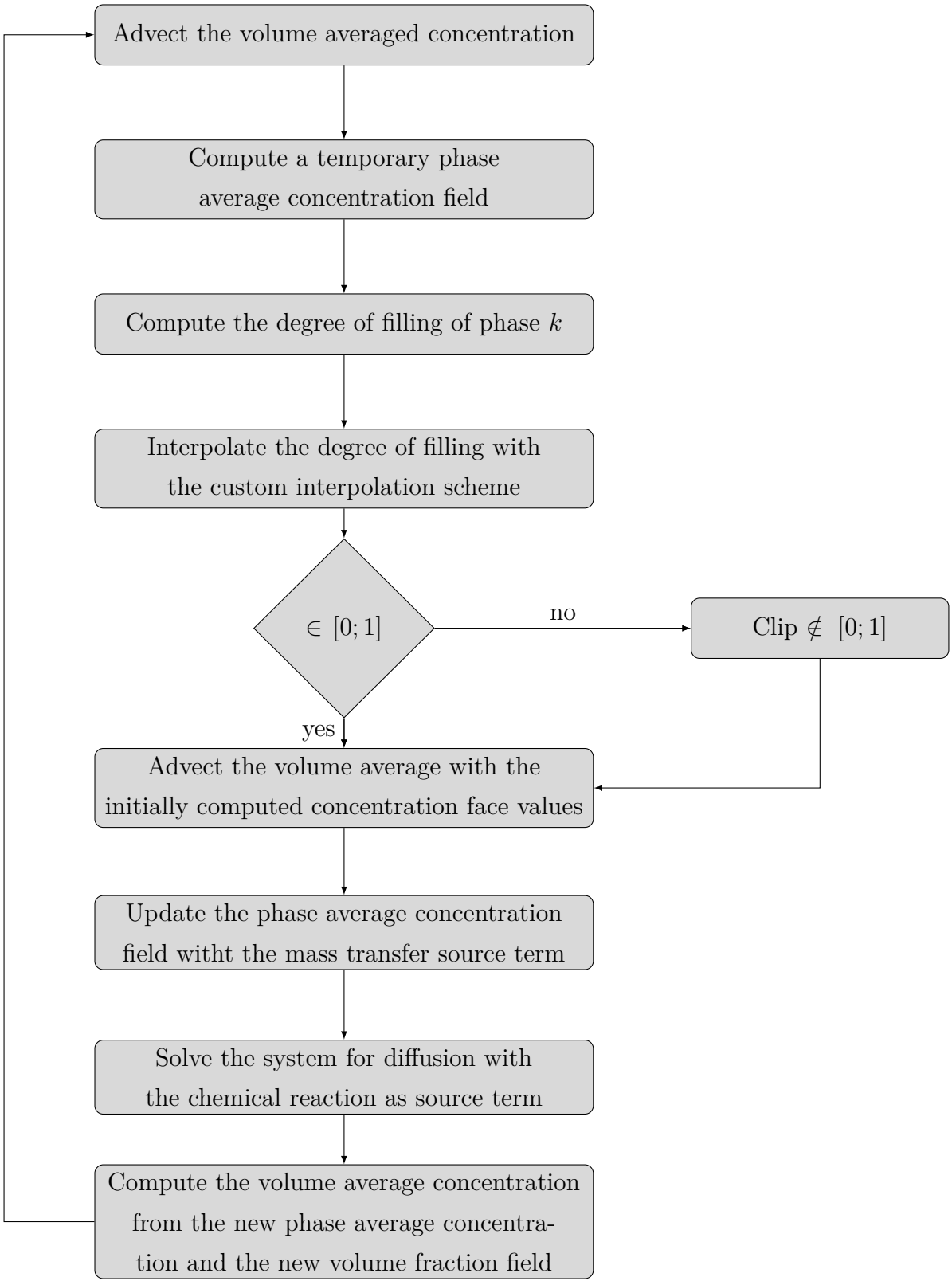

FIGURE 4.5: Flowchart of the algorithm sequence for one species

4.4 Preliminary test cases

4.4.1 Motivation for additional test cases

Recreating numerically the entire experimental configuration poses several issues. Firstly, the size of the mesh required would be substantial. Indeed, the size of the cells should allow the liquid film to be captured, which is typically of the order of magnitude of the micron, see table 1.1 for more details. Then, the other issue is the physical calculation time required to observe steady state Taylor flow. Since cells are very small, the CFL number imposes a huge restriction on the time step, and the numerical time required to reach steady state is not achievable in practice. The following of the text will showcase initial findings obtained for a system involving ethylene and the catalyst without chemical reaction. These test cases aim at verying the performances of the solver handling an additional species, the catalyst, and are also required to validate the geometry in real conditions.

4.4.2 Reactors description

Experimentally, the catalyst is injected in presence of diluted ethylene to promote the reaction. To do this a second mixing cross is added after the T-junction for contacting. The reactor used to conduct the experiment was 1 m long. A small tube of 8 cm was used to allow a Taylor flow to establish before injecting the catalyst. At the end of the reactor, an inhibitor is injected to stop further chain reactions. Temperature and pressure operating conditions are $30\,°\text{C} < T < 50\,°\text{C}$ and $10\,\text{bar} < P < 30\,\text{bar}$. The fluid properties are detailed in the section 4.2.1. Considering a mean temperature and pressure of 40 °C and 20 bar, the values of Re, We and Ca are given in the table 4.18 below for the different superficial velocities. To simulate a 8 cm spacing between the gas inlet and the catalyst inlet, 1,000,000 cells of 4

Table 4.18: Values of the dimensionless numbers for the minimum and maximum superficial velocities

Gas superficial velocity ($\text{mm}\,\text{s}^{-1}$)	Liquid superficial velocity ($\text{mm}\,\text{s}^{-1}$)	Re_G	Re_L	We_G	We_L	Ca	Bo
3.4	0.6	3.62	0.32	6.00e-06	6.10e-06	1.26e-04	0.08
21.0	2.1	22.34	1.11	2.31e-04	7.33e-05	7.27e-04	0.08

microns squared (2D) cells are needed. The physical time required for the liquid to travel

through the 8 cm tube at $0.1\,\mathrm{m\,s^{-1}}$ is almost 1 s. The typical time step observed during the 2D simulations was around 2×10^{-7} s and the cumulated time spent to simulate 0.1 s was approximately 175.000 s, more than 48 h. It is too numerically demanding to simulate a reactor of 1 m, that is why the geometry of the reactor has been adapted.

Experimentally, the activator does not participate in the reaction, that is why its injection was not studied at first. However, the addition of another inlet on the channel has undoubtly an impact on the flow and the generation of bubbles. All the alternative geometries integrate an additional inlet for the catalyst. Several configurations were tested, with an inlet of catalyst before and after the gas inlet, a mixing cross for the catalyst was also tested to replicate the injection of activator. The injection of the inhibitor was not simulated here. The concentration of catalyst in the liquid phase was set to $0.01\,\mathrm{kg\,m^{-3}}$, consistently with the concentration of catalyst around 10 ppm reported in [26].

The three configuration tested are plane 2D geometries with different position for the catalyst inlet and the same diameter value of 0.2 mm. The objective of these test cases is to compare the mixing and the distribution of the liquid phase ethylene concentration. Figure 4.6 shows the first configuration where the catalyst is injected before the gas inlet.



FIGURE 4.6: T-junction where the catalyst inlet is on the side of the gas inlet

Figure 4.7 shows a configuration where the catalyst injector is on the other side of the gas inlet. This new configuration is used to test whether the injection of catalyst improves the mixing in the liquid slugs compared to 4.6.

Figure 4.8 shows the last configuration tested, which is closer to the experimental set-up with a mixing cross after the gas inlet. For this specific test, the catalyst is injected at each inlet with the same flow-rate as the previous cases.

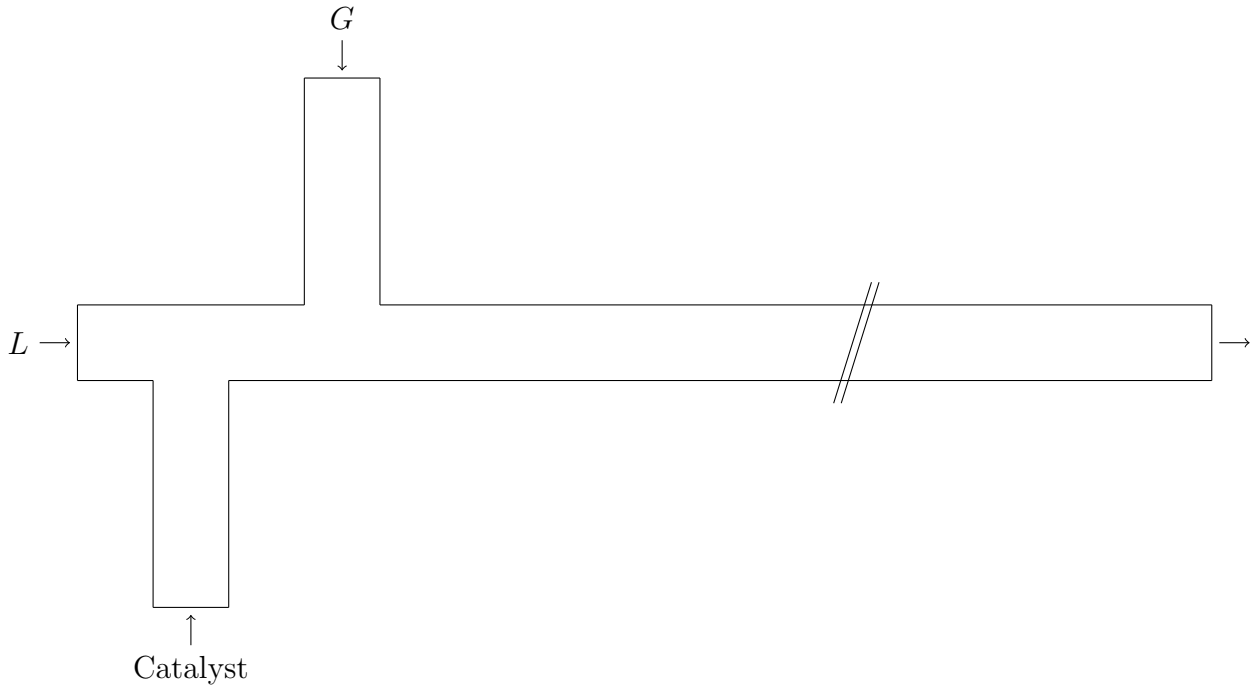

FIGURE 4.7: T-junction where the catalyst inlet is on the opposite side of the gas inlet

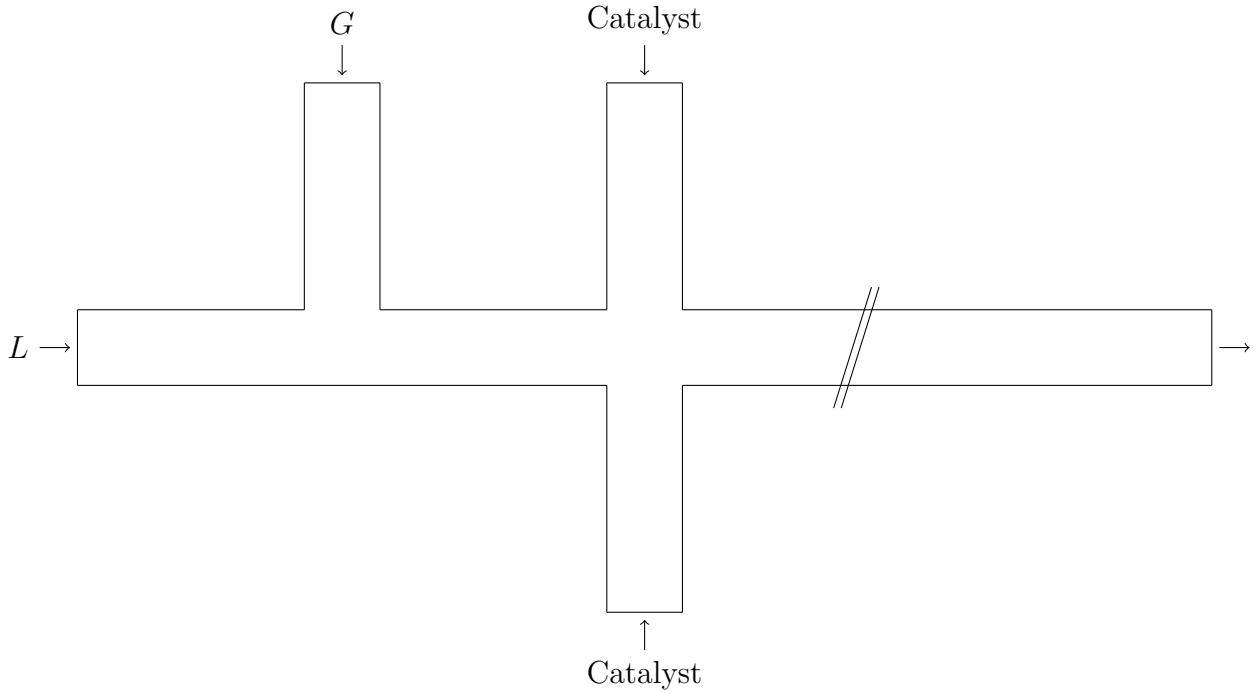

FIGURE 4.8: T-junction where the catalyst is injected in a mixing cross after the gas inlet

4.4.3 The catalyst inlet is on the side of the gas inlet

Figure 4.9, shows the liquid phase ethylene concentration and catalyst concentration during the early stage of bubble growth.

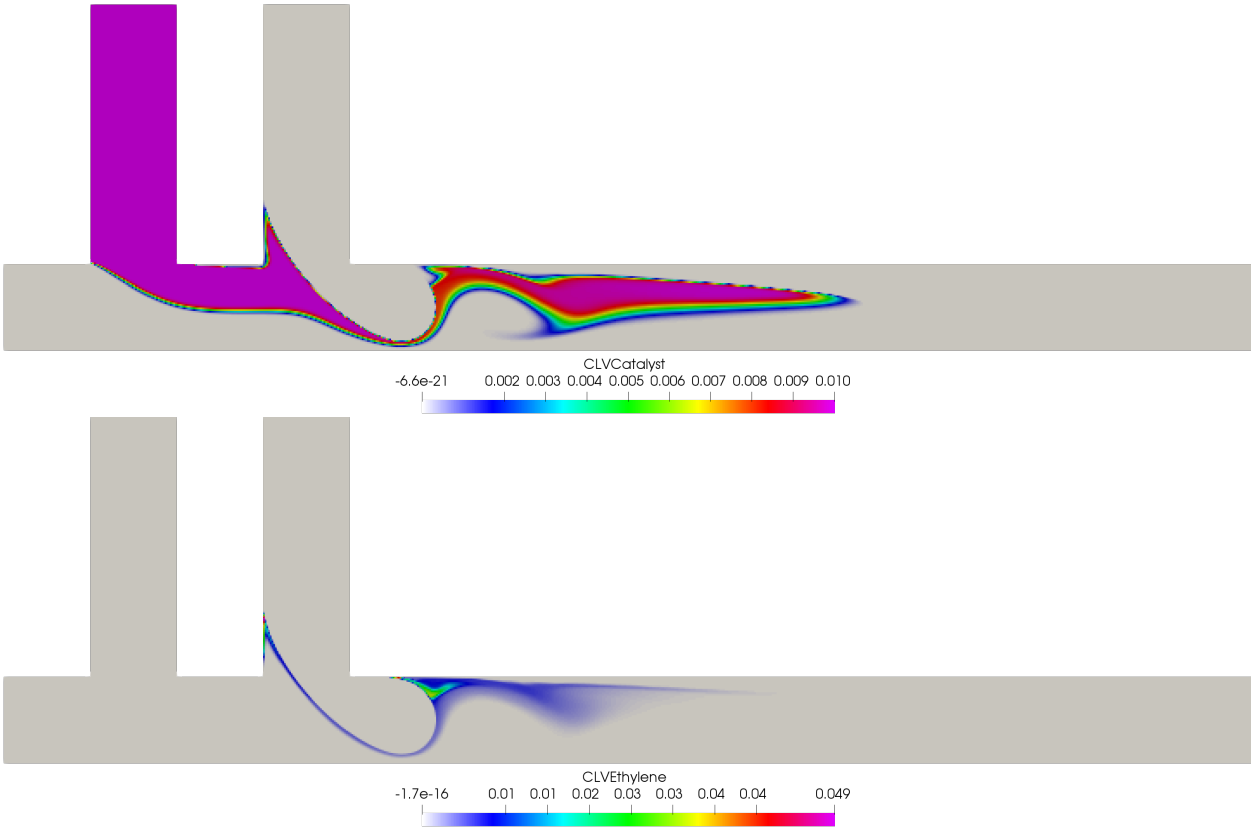

FIGURE 4.9: Catalyst (top) and ethylene (bottom) fields in a 2D T-junction with injectors at 0.005 s

The way the concentration of catalyst is distributed inside the mixing region highlights how the growing bubble modifies the flow field in this area. Since the flow-rate of both liquid inlet and catalyst are the same, the catalyst is confined in the upper half of the channel. In concentration field of ethylene, the larger values of concentration at the tip of the bubble in green indicate a stagnation point. At the cap of the forming bubble, the velocity is smaller in the confined area between the gas and the wall. Which is why the concentration increases and species accumulate there. For the catalyst, the concentration spreads from the inlet towards the bubble and even follows the interface inside the gas injector. This behaviour was expected since the catalyst does not transfer into the gas, so it is trapped in the liquid phase and is carried by the velocity field. This also allows to verify that the diffusion correction also works for the catalyst. The diffusivity of the catalyst is assumed as $1 \times 10^{-9}\,\mathrm{m^2\,s^{-1}}$.
Figure 4.10 displays the same fields after 0.05 s of physical time. Several bubbles have been

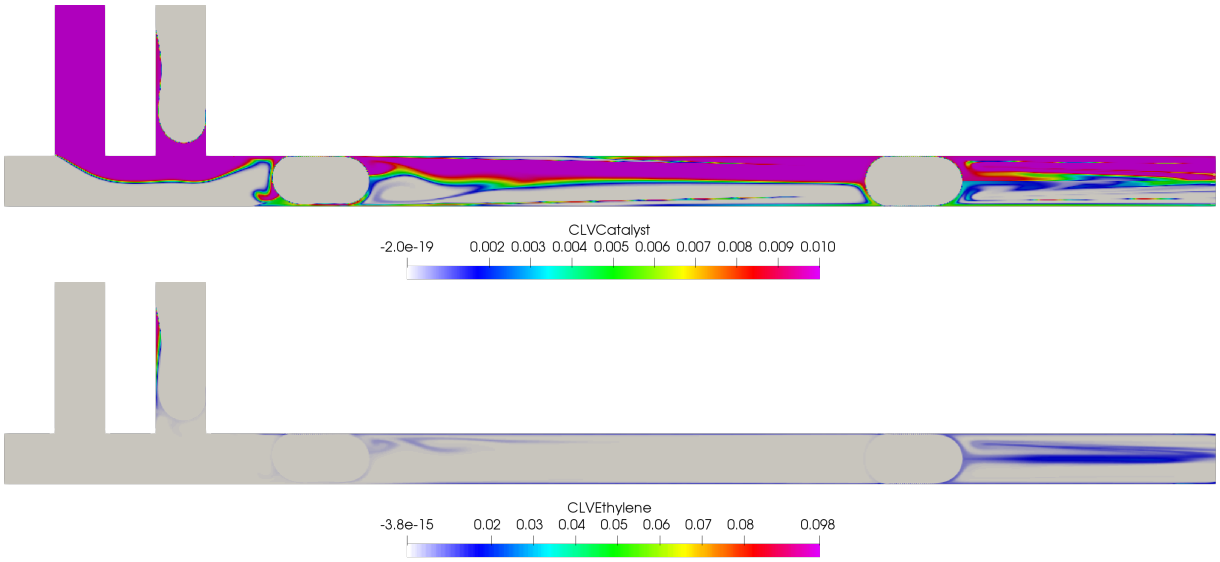

FIGURE 4.10: Catalyst (top) and ethylene (bottom) fields in a 2D T-junction with injectors at 0.05 s

simulated, and the classical features of a Taylor flow are now visible. In the slug on the left-hand side, the mixing of the catalyst is low since the bubble has just been generated. However, in the slug on the righ-hand side, the mixing is improving. More distance from the generator are required to reach the same level of mixing for such conditions of superficial velocities compared with cases with smaller slugs.
Regarding the concentration of ethyelene, the rear of the bubble does not seem to contribute much to mass transfer. Larger dissolved ethylene concentrations are also located at the walls of the channel, where the velocity is zero. This observation is in line with the idea of large liquid film contribution to the overall mass transfer.

4.4.4 The catalyst inlet is on the opposite side of the gas inlet

Figure 4.11 shows the liquid ethylene concentration and the catalyst concentration for a T-junction with an additional catalyst inlet.
Figure 4.11 shows a significant segregation of the catalyst. It tends to remain on the side of its injector. The flow conditions create slugs too long for a good recirculation. Puting the catalyst inlet on the other side of the gas inlet does not improve the mixing significantly.

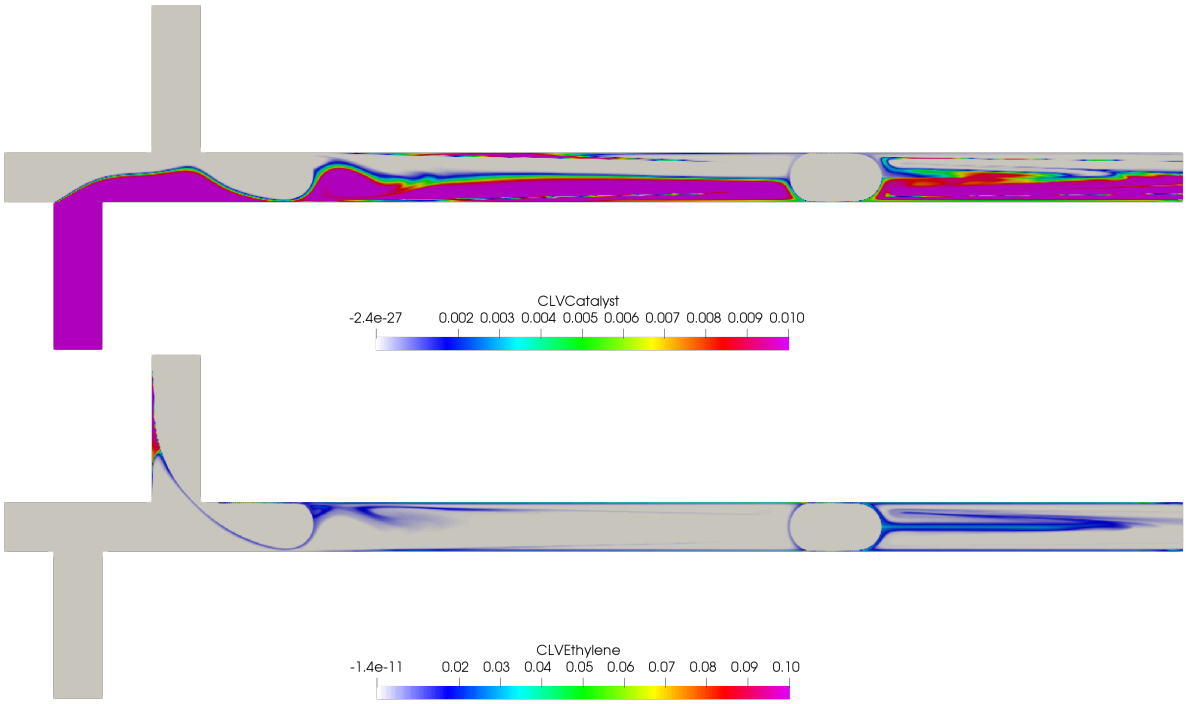

FIGURE 4.11: Catalyst (top) and ethylene (bottom) fields in a 2D T-junction with injectors at 0.1 s

4.4.5 The catalyst is injected in a mixing cross after the gas inlet

The third test case uses a cross juction for the mixing of the catalyst. For the two previous geometries, the injection of catalyst did not modify the flow very much. This third geometry is used to simulate systems where an additional species must be used to activate the catalyst e.g. an activator. For the previous geometries the flow was not excessively modified, but this new geometry might have a significant impact on the generation of bubbles. Figure 4.12 shows the catalyst and ethylene concentration fields after 0.02 s.

The flow in the cross junction is modified as it can be seen on the ethylene concentration field. More ethylene is dispersed at the center of the channel as it can be seen at the center of the mixing cross. Also, the cross junction further promotes even the recirculation in the liquid slugs. Nevertheless, there is actually a significant segregation between the upper and lower part of the channel. Looking at the catalyst field in top of figure 4.12, it looks like the catalyst from the upper inlet will never be in contact with the one from the lower inlet. This is important when considering experimental set-up, whereby the catalyst is injected at one inlet and the activator is injected at another inlet. Consequently, if the catalyst does not come into contact with the activator, the reaction may not occur. Therefore, with these flow conditions, a longer channel must be used to allow the liquid slugs to be perfectly mixed. For

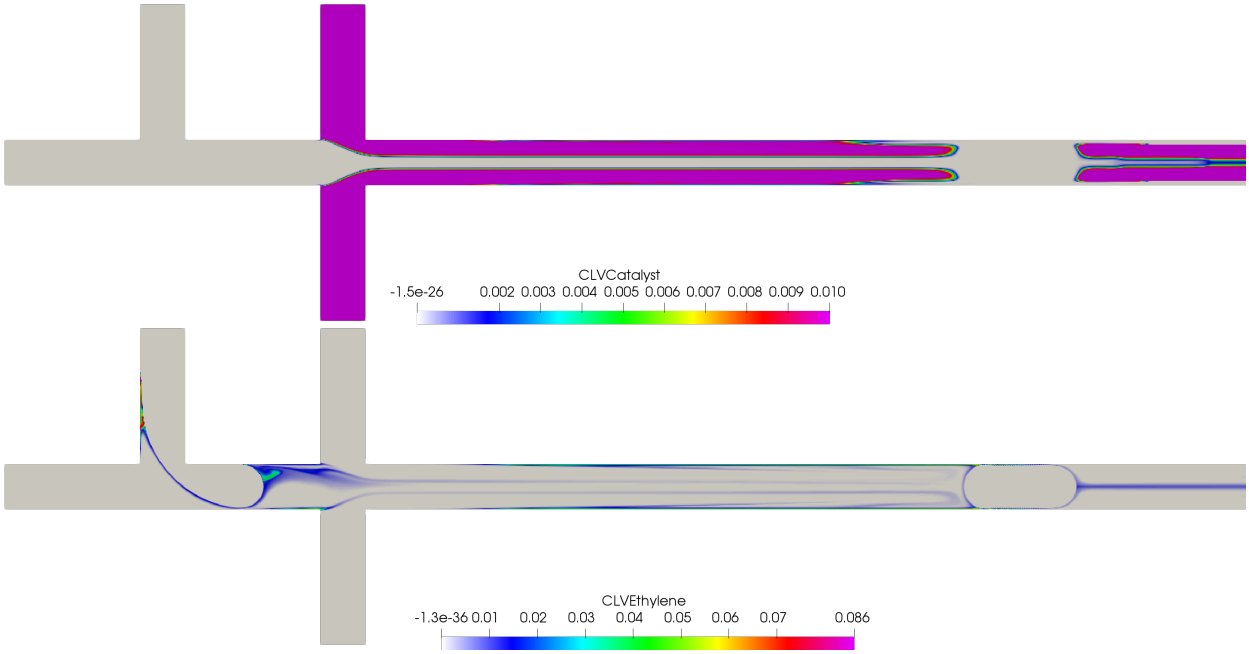

FIGURE 4.12: Catalyst (top) and ethylene (bottom) fields in a 2D T-junction with injectors after 0.02 s

this simulation it is not as important as it would be to simulate chemical reaction between ethylene and the catalyst.

4.5 Conclusion

In this chapter the partial implementation of a power law chemical reaction has been presented. A lot of effort has been put into the rigorous description of the physical properties of the mixture components. Test cases were used to demonstrate the capability of the solver to handle multicomponent systems. The difficulties linked to the simulation time required to reach steady state and the length of the channel needed were also highlighted. To promote mixing in the liquid slugs, other flow conditions with larger gas superficial velocities could be used. Otherwise, a longer distance must be simulated to obtain satisfactory results in terms of mixing. More advanced simulations, particularly in 3D, as well as additional developments would be required to run the full simulations of oligomerization reaction in microchannels. Adaptative mesh refinement might be a solution to reach a good level of refinement, allowing the capture of the liquid film near the wall, without the necessity of a very fine mesh where it is not needed.

Conclusions

This work has been dedicated to the numerical simulations of reactive Taylor flows. It is focused on the comparison of existing VOF solvers, the implementation of a transport equation for the concentration of a chemical species, the validation of the solver and the prediction of the physical properties.

The performances of the available VOF solvers in OpenFOAM® were compared in order to choose the most suitable option to simulate the highly capillary flows. It was found that `interFlow` gives better results when simulating capillary flows because it includes a reconstruction of the interface. Regarding Taylor flows, `interFlow` was also the solver allowing the better prediction of the bubbles lengths.

The implementation of a transport equation for concentration has been detailed. The novelty of this work is the usage of a two-field approach combined to the geometric VOF method `isoAdvector`. To avoid the so-called artificial mass transfer, a new methodology to interpolate the concentration from cell centers onto cell faces was proposed. This new methodology is very innovative since it makes use of both phase average and volume average concentrations to avoid nonphysical fluxes. A new method used to correct diffusive fluxes was presented, allowing the correct computation of concentration gradients on cell faces. The implementation of concentration-driven mass transfer has been detailed. The performances of the algorithm have been tested intensively. Finally, fluid properties were investigated in order to provide as much physical data to future simulations as possible.

Several challenges encountered during this project were familiar hurdles extensively documented in the existing literature. It came as no surprise that accurately modelling the liquid film between a Taylor bubble and the channel proved to be a complex endeavor. In most numerical simulations, the capture of the liquid film was not possible since the meshes were not refined enough. Additionally, achieving a precise calculation of the interfacial concentration gradient necessitated an extensively refined mesh, which inevitably extended simulation times. Dealing with the unbounded nature of the concentration variable presented its own set of numerical challenges. The development of a limiter to avoid over- and under-shoots

was compulsory for simulation of bubble growth in T-junctions. Among all the constraining factors, the actual time required to achieve a steady state in a simulation of the complete T-junction geometry could be the most significant.
The chemical reaction remains the most substantial unachieved segment of the work. While the solver is usable in its current form, further developments are essential to fully incorporate the reactive part in the framework. Concerning the temperature-dependent behaviour of fluid properties, an in-depth review and prediction was carried but was not used yet. The time invested in the prediction was not in vain, as it provided valuable insights into the system and aided in determining the appropriate numerical models to extend `interFlow` towards chemically driven mass transfer.

Perspectives

The solver was inteded to deal with non-dilute species. However, the difficulty to properly model diffusion in non-dilute multispecies conditions was one of the reason why it is not fully adapted to work in such conditions. The other reason being the need of updating the density of the phase with respect to the proportions of each species in the cell. A better option to work in such non-dilute conditions could be the use of mass fractions instead of concentrations in the transport equations. The use of mass fractions is interesting because it could reduce the number of equations to be solved by one. Expressing mixing properties such as density is also more straightforward with mass fractions.

Integrating energy conservation with the chemical reaction presents a complex challenge due to the temperature-dependent nature of fluid properties, resulting in intricate equation coupling. Rather than attempting to simultaneously solve the entire system, a more streamlined approach involves employing a passive scalar, representing temperature. Fluid properties could be updated at each time step with the new temperature.

Further validation experiments are essential to evaluate the performance of the solver, particularly in both 2D and 3D scenarios. It's important to note that the analytical Stefan case used to verify the volume change resulting from mass transfer offers an analytical solution exclusively in 1D.

An appealing strategy for addressing the demands of mesh refinement is the use of subgrid-scale models. In the context of mass transfer, these models can effectively calculate precise interfacial concentration gradients, avoiding the necessity for highly refined meshes. Developing such models would really enhance the results, but they would have to be designed specifically for a given purpose.

The application of the solver to address remaining questions about Taylor flows and T-junctions will have to be covered in future research. Quantitative Sherwood numbers to quantify mass transfer in T-junctions were not studied here. Additionally, the role of bubble generation in overall mass transfer and the contribution of the liquid film will be explored in distinct investigations.

Appendix A

Hydrodynamics study

The flow rates and the corresponding velocities and bubbles lengths used for the hydrodynamics study of the T-junction provided by Guo and coworkers [5] are gathered in table A.1.

Table A.1: Operating conditions and results from the work of Guo et al. [5]

$Q_G(\mathrm{mL\,h^{-1}})$	$Q_L(\mathrm{mL\,h^{-1}})$	$U_G(\mathrm{m\,s^{-1}})$	$U_L(\mathrm{m\,s^{-1}})$	$L_{exp}(\mathrm{mm})$	$L_{sim}(\mathrm{mm})$	Re_G	Re_L
1	0.5	0.0347	0.0174	1.10-1.17	1.20-1.23	0.58	3.48
1	1	0.0347	0.0347	0.66-0.72	0.71-0.73	0.58	6.94
1	2	0.0347	0.0694	0.47-0.49	0.51-0.54	0.58	13.9
1	3	0.0347	0.1042	0.38-0.40	0.39-0.41	0.58	20.8
1	5	0.0347	0.1736	0.35-0.39	0.34-0.36	0.58	34.7
1	10	0.0347	0.3472	0.20-0.23	0.21-0.22	0.58	69.4
2	0.8	0.0694	0.0278	1.02-1.12	1.19-1.21	1.16	5.56
2	2.2	0.0694	0.0764	0.73-0.76	0.70-0.72	1.16	15.3
2	4.1	0.0694	0.1424	0.38-0.45	0.47-0.49	1.16	28.5
2	5.0	0.0694	0.1736	0.36-0.40	0.39-0.41	1.16	34.7
2	10.0	0.0694	0.3472	0.21-0.22	0.22-0.23	1.16	69.4

Appendix B

Fluid properties

B.1 Compressibility and density prediction

B.1.1 Soave-Redlich-Kwong

The first EOS presented is a modification of the previous work from Redlich and Kwong. Soave [128] used the acentric factor as a third parameter to obtain the SRK EOS, which is widely used now. The formulation is given below:

$$P = \frac{R\,T}{\overline{V} - b} - \frac{\alpha\, a}{\overline{V}(\overline{V} + b)} \tag{B.1}$$

Where P the pressure (Pa), $\overline{V}$ the molar volume ($\mathrm{m^3\,mol^{-1}}$), T the temperature (K) and R the ideal gas constant ($8.3145\,\mathrm{J\,mol^{-1}\,K^{-1}}$). a, b and α are functions of T or P, and are defined for this EOS in terms of the acentric factor ω as follows:

$$\alpha = \left[1 + \left(0.48508 + 1.5517\omega - 0.15613\omega^2\right)\left(1 - \sqrt{\frac{T}{T_c}}\right)\right]^2 \tag{B.2}$$

$$a = 0.42747\,\frac{R^2 T_c^2}{P_c} \tag{B.3}$$

$$b = 0.08664\,\frac{R T_c}{P_c} \tag{B.4}$$

After introducing $Z = P\overline{V}/(RT)$ from equation 4.1 into B.1, and after introducing the two coefficients $A = \frac{\alpha a P}{R^2 T^2}$ and $B = \frac{bP}{RT}$, equation B.1 can then be written as follows:

$$Z^3 - Z^2 + (A - B - B^2)Z - AB = 0 \tag{B.5}$$

The SRK EOS thus reduces to a third order polynomial.

B.1.2 Peng-Robinson

The formulation of the PR equation is quite close to the one from SRK. Peng and Robinson [129] proposed this formulation to overcome the poor prediction of the liquid phase at low reduced temperature (not the case in this work) from the SRK EOS.

$$P = \frac{RT}{\overline{V} - b} - \frac{\alpha a}{\overline{V}^2 + 2b\overline{V} - b^2} \tag{B.6}$$

The coefficients change from the formulation of SRK:

$$\alpha = \left(1 + m\left(1 - \sqrt{\frac{T}{Tc}}\right)\right)^2 \tag{B.7}$$

$$m = 0.37464 + 1.54226\omega - 0.26992\omega^2 \tag{B.8}$$

The formulation of m was modified in 1978 to better predict the behaviour of heavy compounds:

$$m = 0.37464 + 1.54226\omega - 0.26992\omega^2$$

if $\omega < 0.491$, which is the case here, otherwise:

$$m = 0.379642 + 1.487503\omega - 0.164423\omega^2 - 0.0016666\omega^3$$

$$a = 0.5724\,\frac{R^2 T_c^2}{P_c} \tag{B.9}$$

$$b = 0.007780\,\frac{RT_c}{P_c} \tag{B.10}$$

Similarly to the SRK EOS, after introducing Z in equation B.6, a third order polynomial equation for Z is obtained:

$$Z^3 - (1 - B)Z^2 + (A - 3B^2 - 2B)Z - (AB - B^2 - B^3) = 0 \tag{B.11}$$

B.1.3 Compressibility factor prediction

A third order polynomial has no more than three roots and the values can be either real or complex, depending on the coefficients. When three real roots are present, the smaller one stands for the liquid phase, the middle one has no thermodynamical meaning and the largest one represents the gas phase. The discriminant indicates the nature of the roots. To understand the physical meaning of the roots, one should calculate the discriminant. Given the third order polynomial equation:

$$x^3 + bx^2 + cx + d = 0 \tag{B.12}$$

The study of the sign of the discriminant indicates the nature of the roots. The discriminant can be determined as follows:

$$\Delta = 4c^3 + 27d^2 + 4db^3 - b^2c^2 - 18bcd \tag{B.13}$$

1. if $\Delta > 0$, there is one real root and two complex conjugate roots
2. if $\Delta < 0$, there are three distinct real roots
3. if $\Delta = 0$, there are three real roots, with a multiple root

For the different operating conditions from 30 to 50 °C and from 10 to 30 bar, the discriminant and the value of the compressibility factor for each EOS are derived. The discriminants were all positive for both SRK and PR (the two EOS give close results), meaning that there is only one real root, which represents the state of the fluid. When Z is close to 0, the fluid acts like a liquid, whereas for higher values near 1, it behaves like an ideal gas. The difference in prediction between SRK and PR is low, which gives confidence about the results. Furthermore, each method shows a good prediction of the critical compressibility factor, the factor calculated for the critical pressure and temperature: $Z_{C,SRK} = 0.3467$ and $Z_{C,PR} = 0.3214$. From these values of Z, it can be concluded that ethylene acts more like a gas than a liquid under operating conditions below 30 bar. It is therefore acceptable to consider the ethylene phase as compressible. The equation of state approach allows the calculation of the density of the gas in the real fluid conditions, which is necessary in order

TABLE B.1: Values of the compressibility factor Z for different temperatures and pressure using the SRK equation

	Temperature (°C)		
Pressure (bar)	30	40	50
10	0.9440	0.9498	0.9549
20	0.8841	0.8968	0.9078
30	0.8190	0.8404	0.8586

TABLE B.2: Values of the compressibility factor Z for different temperatures and pressure using the PR equation

	Temperature (°C)		
Pressure (bar)	30	40	50
10	0.9370	0.9430	0.9483
20	0.8705	0.8837	0.8951
30	0.7995	0.8215	0.8402

to obtain relevant results. Indeed, since the reaction is exothermic, high temperatures may occur and it is important to predict the density with fidelity.

Bibliography

[1] T. P. Zhuze and A. S. Zhurba. Solubilities of ethylene in hexane, cyclohexane, and benzene under pressure. *Bulletin of the Academy of Sciences of the USSR, Division of chemical science*, 9(2):335–337, 1960. doi: 10.1007/BF00942915. URL `https://doi.org/10.1007/BF00942915`.

[2] Edward N. Fuller, Keith Ensley, and J. Calvin Giddings. Diffusion of halogenated hydrocarbons in helium. the effect of structure on collision cross sections. *The Journal of Physical Chemistry*, 73(11):3679–3685, 1969. doi: 10.1021/j100845a020. URL `https://doi.org/10.1021/j100845a020`.

[3] Shinji Takahashi. Preparation of a generalizes chart for the diffusion coefficients of gases at high pressures. *Journal of Chemical Engineering of Japan*, 7(6):417–420, 1975. doi: 10.1252/jcej.7.417.

[4] J. Jonas, D. Hasha, and S. G. Huang. Density effects of transport properties in liquid cyclohexane. *The Journal of Physical Chemistry*, 84(1):109–112, 1980. doi: 10.1021/j100438a024. URL `https://doi.org/10.1021/j100438a024`.

[5] Fang Guo and Bin Chen. Numerical study on taylor bubble formation in a microchannel t-junction using vof method. *Microgravity Science and Technology*, 21(1): 51–58, 2009.

[6] Laurent Lebreton and Anthony Andrady. Future scenarios of global plastic waste generation and disposal. *Palgrave Communications*, 5(1):1–11, 2019.

[7] Michiel T. Kreutzer, Freek Kapteijn, Jacob A. Moulijn, and Johan J. Heiszwolf. Multiphase monolith reactors: Chemical reaction engineering of segmented flow in microchannels. *Chemical Engineering Science*, 60(22):5895 – 5916, 2005. ISSN 0009-2509. doi: https://doi.org/10.1016/j.ces.2005.03.022. URL `http://www.sciencedirect.com/science/article/pii/S0009250905002526`. 7th International Conference on Gas-Liquid and Gas-Liquid-Solid Reactor Engineering.

[8] Axel Günther, Saif A. Khan, Martina Thalmann, Franz Trachsel, and Klavs F. Jensen. Transport and reaction in microscale segmented gas–liquid flow. *Lab Chip*, 4:278–286, 2004. doi: 10.1039/B403982C. URL http://dx.doi.org/10.1039/B403982C.

[9] Axel Günther, Manish Jhunjhunwala, Martina Thalmann, Martin A. Schmidt, and Klavs F. Jensen. Micromixing of miscible liquids in segmented gas-liquid flow. *Langmuir*, 21(4):1547–1555, 2005. doi: 10.1021/la0482406. URL https://doi.org/10.1021/la0482406.

[10] Said Irandoust, Sylvie Ertlé, and Bengt Andersson. Gas-liquid mass transfer in taylor flow through a capillary. *The Canadian Journal of Chemical Engineering*, 70(1):115–119, 1992. doi: https://doi.org/10.1002/cjce.5450700116. URL https://onlinelibrary.wiley.com/doi/abs/10.1002/cjce.5450700116.

[11] R.B. Bird, W.E. Stewart, and E.N. Lightfoot. *Transport Phenomena*. Number vol. 1 in Transport Phenomena. Wiley, 2006. ISBN 9780470115398. URL https://books.google.fr/books?id=L5FnNlIaGfcC.

[12] Fred Fairbrother and Alfred E. Stubbs. 119. studies in electro-endosmosis. part vi. the "bubble-tube" method of measurement. *J. Chem. Soc.*, pages 527–529, 1935. doi: 10.1039/JR9350000527. URL http://dx.doi.org/10.1039/JR9350000527.

[13] G. I. Taylor. Deposition of a viscous fluid on the wall of a tube. *Journal of Fluid Mechanics*, 10(2):161–165, 1961. doi: 10.1017/S0022112061000159.

[14] F. P. Bretherton. The motion of long bubbles in tubes. *Journal of Fluid Mechanics*, 10(2):166–188, 1961. doi: 10.1017/S0022112061000160.

[15] Pascale Aussillous and David Quéré. Quick deposition of a fluid on the wall of a tube. *Physics of Fluids*, 12(10):2367–2371, 2000. doi: 10.1063/1.1289396. URL https://aip.scitation.org/doi/abs/10.1063/1.1289396.

[16] Piotr Garstecki, Michael J. Fuerstman, Howard A. Stone, and George M. Whitesides. Formation of droplets and bubbles in a microfluidic t-junction—scaling and mechanism of break-up. *Lab Chip*, 6:437–446, 2006. doi: 10.1039/B510841A. URL http://dx.doi.org/10.1039/B510841A.

[17] V van Steijn, MT Kreutzer, and CR Kleijn. micro-piv study of the formation of segmented flow in microfluidic t-junctions. *Chemical Engineering Science*, 62:7505–7514, 2007. ISSN 0009-2509.

[18] W.Blake Kolb and Ramon L. Cerro. Coating the inside of a capillary of square cross section. *Chemical Engineering Science*, 46(9):2181–2195, 1991. ISSN 0009-2509. doi: https://doi.org/10.1016/0009-2509(91)85119-I. URL https://www.sciencedirect.com/science/article/pii/000925099185119I.

[19] Chaoqun Yao, Zhengya Dong, Yuchao Zhao, and Guangwen Chen. The effect of system pressure on gas-liquid slug flow in a microchannel. *AIChE Journal*, 60(3):1132–1142, 2014. doi: https://doi.org/10.1002/aic.14306. URL https://aiche.onlinelibrary.wiley.com/doi/abs/10.1002/aic.14306.

[20] Lixia Yang, Nicolas Dietrich, Karine Loubière, Christophe Gourdon, and Gilles Hébrard. Visualization and characterization of gas–liquid mass transfer around a taylor bubble right after the formation stage in microreactors. *Chemical Engineering Science*, 143:364 – 368, 2016. ISSN 0009-2509. doi: https://doi.org/10.1016/j.ces.2016.01.013. URL http://www.sciencedirect.com/science/article/pii/S0009250916000221.

[21] T. Deleau, M.H.H. Fechter, J-J. Letourneau, S. Camy, J. Aubin, A.S. Braeuer, and F. Espitalier. Determination of mass transfer coefficients in high-pressure two-phase flows in capillaries using raman spectroscopy. *Chemical Engineering Science*, 228: 115960, 2020. ISSN 0009-2509. doi: https://doi.org/10.1016/j.ces.2020.115960. URL http://www.sciencedirect.com/science/article/pii/S0009250920304929.

[22] Piotr Garstecki, Howard A. Stone, and George M. Whitesides. Mechanism for flow-rate controlled breakup in confined geometries: A route to monodisperse emulsions. *Phys. Rev. Lett.*, 94:164501, Apr 2005. doi: 10.1103/PhysRevLett.94.164501. URL https://link.aps.org/doi/10.1103/PhysRevLett.94.164501.

[23] Norbert Völkel. *Design and characterization of gas-liquid microreactors*. PhD thesis, INPT, December 2009. URL https://oatao.univ-toulouse.fr/7168/.

[24] Thomas Abadie. *Hydrodynamics of gas-liquid Taylor flow in microchannels*. PhD thesis, INPT, November 2013.

[25] Alexandre Martin, Séverine Camy, and Joëlle Aubin. Hydrodynamics of co2-ethanol flow in a microchannel under elevated pressure. *Chemical Engineering Science*, 178: 297–311, 2018. ISSN 0009-2509. doi: https://doi.org/10.1016/j.ces.2017.12.046. URL https://www.sciencedirect.com/science/article/pii/S0009250917307832.

[26] Mahmoud Kamaleddine, Charles Bonnin, Typhène Michel, Léna Brunet-Errard, Joëlle Aubin, and Laurent Prat. Gas-liquid flow characterization and mass transfer study in a

microreactor for oligomerization catalyst testing. *Chemical Engineering and Processing - Process Intensification*, 166:108476, 2021. ISSN 0255-2701. doi: https://doi.org/10.1016/j.cep.2021.108476. URL https://www.sciencedirect.com/science/article/pii/S025527012100177X.

[27] Chaoqun Yao, Zhengya Dong, Yuchao Zhao, and Guangwen Chen. An online method to measure mass transfer of slug flow in a microchannel. *Chemical Engineering Science*, 112:15 – 24, 2014. ISSN 0009-2509. doi: https://doi.org/10.1016/j.ces.2014.03.016. URL http://www.sciencedirect.com/science/article/pii/S0009250914001274.

[28] S. Irandoust and B. Andersson. Mass transfer and liquid-phase reactions in a segmented two-phase flow monolithic catalyst reactor. *Chemical Engineering Science*, 43:1983–1988, 1988.

[29] Said Irandoust and Bengt Andersson. Liquid film in taylor flow through a capillary. *Industrial & Engineering Chemistry Research*, 28(11):1684–1688, 1989. doi: 10.1021/ie00095a018. URL https://doi.org/10.1021/ie00095a018.

[30] Gorazd Berčič and Albin Pintar. The role of gas bubbles and liquid slug lengths on mass transport in the taylor flow through capillaries. *Chemical Engineering Science*, 52(21):3709 – 3719, 1997. ISSN 0009-2509. doi: https://doi.org/10.1016/S0009-2509(97)00217-0. URL http://www.sciencedirect.com/science/article/pii/S0009250997002170.

[31] Juan G Santiago, Steve T Wereley, Carl D Meinhart, DJ Beebe, and Ronald J Adrian. A particle image velocimetry system for microfluidics. *Experiments in fluids*, 25(4):316–319, 1998.

[32] Mohammadreza Haghnegahdar, Stephan Boden, and Uwe Hampel. Investigation of mass transfer in milli-channels using high-resolution microfocus x-ray imaging. *International Journal of Heat and Mass Transfer*, 93:653–664, 2016. ISSN 0017-9310. doi: https://doi.org/10.1016/j.ijheatmasstransfer.2015.10.033. URL https://www.sciencedirect.com/science/article/pii/S0017931015010364.

[33] Adil Dani, Pascal Guiraud, and Arnaud Cockx. Local measurement of oxygen transfer around a single bubble by planar laser-induced fluorescence. *Chemical Engineering Science*, 62(24):7245–7252, 2007. ISSN 0009-2509. doi: https://doi.org/10.1016/j.ces.2007.08.047. URL https://www.sciencedirect.com/science/article/pii/S0009250907006914. 8th International Conference on Gas-Liquid and Gas-Liquid-Solid Reactor Engineering.

[34] Pierre Valiorgue, Nicolas Souzy, Mahmoud El Hajem, Hamda Ben Hadid, and Serge Simoëns. Concentration measurement in the wake of a free rising bubble using planar laser-induced fluorescence (plif) with a calibration taking into account fluorescence extinction variations. *Experiments in fluids*, 54(4):1–10, 2013.

[35] M. Jimenez, N. Dietrich, and G. Hébrard. Mass transfer in the wake of non-spherical air bubbles quantified by quenching of fluorescence. *Chemical Engineering Science*, 100:160–171, 2013. ISSN 0009-2509. doi: https://doi.org/10.1016/j.ces.2013.01.036. URL https://www.sciencedirect.com/science/article/pii/S0009250913000493. 11th International Conference on Gas-Liquid and Gas-Liquid-Solid Reactor Engineering.

[36] Thomas Häber, Mulubrhan Gebretsadik, Henning Bockhorn, and Nikolaos Zarzalis. The effect of total reflection in plif imaging of annular thin films. *International Journal of Multiphase Flow*, 76:64–72, 2015. ISSN 0301-9322. doi: https://doi.org/10.1016/j.ijmultiphaseflow.2015.06.009. URL https://www.sciencedirect.com/science/article/pii/S0301932215001482.

[37] C. Butler, E. Cid, and A.-M. Billet. Modelling of mass transfer in taylor flow: Investigation with the plif-i technique. *Chemical Engineering Research and Design*, 115:292 – 302, 2016. ISSN 0263-8762. doi: https://doi.org/10.1016/j.cherd.2016.09.001. URL http://www.sciencedirect.com/science/article/pii/S0263876216302866. 10th European Congress of Chemical Engineering.

[38] J.M. van Baten and R. Krishna. Cfd simulations of mass transfer from taylor bubbles rising in circular capillaries. *Chemical Engineering Science*, 59(12):2535 – 2545, 2004. ISSN 0009-2509. doi: https://doi.org/10.1016/j.ces.2004.03.010. URL http://www.sciencedirect.com/science/article/pii/S0009250904001861.

[39] R. Higbie. The rate of absorption of a pure gas into a still liquid during short periods of exposure. *Trans. AIChE*, 31:365–389, 1935. URL https://ci.nii.ac.jp/naid/10003391803/en/.

[40] Jun Yue, Lingai Luo, Yves Gonthier, Guangwen Chen, and Quan Yuan. An experimental study of air–water taylor flow and mass transfer inside square microchannels. *Chemical Engineering Science*, 64(16):3697–3708, 2009. ISSN 0009-2509. doi: https://doi.org/10.1016/j.ces.2009.05.026. URL https://www.sciencedirect.com/science/article/pii/S0009250909003388.

[41] Mahmoud Kamaleddine. *Transposition de tests de catalyse homogène en microréacteur*. PhD thesis, INPT, December 2020. URL https://www.theses.fr/2020INPT0130.

[42] Vania Santos-Moreau, José Carlos B. Lopes, and Cláudio P. Fonte. Estimation of kla values in bench-scale stirred tank reactors with self-inducing impeller by multiphase cfd simulations. *Chemical Engineering & Technology*, 42(8):1545–1554, 2019. doi: https://doi.org/10.1002/ceat.201900162. URL https://onlinelibrary.wiley.com/doi/abs/10.1002/ceat.201900162.

[43] J.U Brackbill, D.B Kothe, and C Zemach. A continuum method for modeling surface tension. *Journal of Computational Physics*, 100(2):335–354, 1992. ISSN 0021-9991. doi: https://doi.org/10.1016/0021-9991(92)90240-Y. URL https://www.sciencedirect.com/science/article/pii/002199919290240Y.

[44] Lev Davidovich Landau and Evgeny Mikhailovich Lifshitz. *Theoretical Physics, Vol. 5: Statistical Physics*. Nauka, Moscow, 1976.

[45] J.H. Ferziger and M. Peric. *Computational Methods for Fluid Dynamics*. Springer Berlin Heidelberg, 2012. ISBN 9783642976513. URL https://books.google.fr/books?id=mbd3NAEACAAJ.

[46] Hrvoje Jasak, Aleksandar Jemcov, Zeljko Tukovic, et al. Openfoam: A c++ library for complex physics simulations. In *International workshop on coupled methods in numerical dynamics*, volume 1000, pages 1–20, 2007.

[47] Michele Benzi. Preconditioning techniques for large linear systems: A survey. *Journal of Computational Physics*, 182(2):418–477, 2002. ISSN 0021-9991. doi: https://doi.org/10.1006/jcph.2002.7176. URL https://www.sciencedirect.com/science/article/pii/S0021999102971767.

[48] S. Patankar. *Numerical Heat Transfer and Fluid Flow*. Series in computational methods in mechanics and thermal sciences. Taylor & Francis, 1980. ISBN 9780891165224. URL https://books.google.fr/books?id=5JMYZMX3OVcC.

[49] R.I Issa. Solution of the implicitly discretised fluid flow equations by operator-splitting. *Journal of Computational Physics*, 62(1):40–65, 1986. ISSN 0021-9991. doi: https://doi.org/10.1016/0021-9991(86)90099-9. URL https://www.sciencedirect.com/science/article/pii/0021999186900999.

[50] Johannes G. Khinast. Impact of 2-d bubble dynamics on the selectivity of fast gas–liquid reactions. *AIChE Journal*, 47(10):2304–2319, 2001. doi: https://doi.org/10.

1002/aic.690471015. URL https://aiche.onlinelibrary.wiley.com/doi/abs/10.1002/aic.690471015.

[51] B. Aboulhasanzadeh, S. Thomas, M. Taeibi-Rahni, and G. Tryggvason. Multiscale computations of mass transfer from buoyant bubbles. *Chemical Engineering Science*, 75: 456–467, 2012. ISSN 0009-2509. doi: https://doi.org/10.1016/j.ces.2012.04.005. URL https://www.sciencedirect.com/science/article/pii/S000925091200231X.

[52] Johannes G. Khinast, Athanas A. Koynov, and Tiberiu M. Leib. Reactive mass transfer at gas–liquid interfaces: impact of micro-scale fluid dynamics on yield and selectivity of liquid-phase cyclohexane oxidation. *Chemical Engineering Science*, 58(17):3961–3971, 2003. ISSN 0009-2509. doi: https://doi.org/10.1016/S0009-2509(03)00311-7. URL https://www.sciencedirect.com/science/article/pii/S0009250903003117.

[53] Stefan Radl, Athanas Koynov, Grétar Tryggvason, and Johannes G. Khinast. Dns-based prediction of the selectivity of fast multiphase reactions: Hydrogenation of nitroarenes. *Chemical Engineering Science*, 63(12):3279–3291, 2008. ISSN 0009-2509. doi: https://doi.org/10.1016/j.ces.2008.03.025. URL https://www.sciencedirect.com/science/article/pii/S0009250908001462.

[54] Zeljko Tukovic and Hrvoje Jasak. Simulation of free-rising bubble with soluble surfactant using moving mesh finite volume/area method. In *Proceedings of 6th International Conference on CFD in Oil & Gas, Metallurgical and Process Industries, no. CFD08-072*, 2008.

[55] Kathrin Bäumler. *Simulation of single drops with variable interfacial tension*. PhD thesis, Friedrich-Alexander-Universität Erlangen-Nürnberg (FAU), 2014.

[56] Christoph Lehrenfeld. *On a space-time extended finite element method for the solution of a class of two-phase mass transport problems*. PhD thesis, Universitätsbibliothek der RWTH Aachen, 2015.

[57] Paul S. Weber, Holger Marschall, and Dieter Bothe. Highly accurate two-phase species transfer based on ale interface tracking. *International Journal of Heat and Mass Transfer*, 104:759–773, 2017. ISSN 0017-9310. doi: https://doi.org/10.1016/j.ijheatmasstransfer.2016.08.072. URL https://www.sciencedirect.com/science/article/pii/S0017931015316744.

[58] Chao Yang and Zai-Sha Mao. Numerical simulation of interphase mass transfer with the level set approach. *Chemical Engineering Science*, 60(10):2643–2660, 2005.

ISSN 0009-2509. doi: https://doi.org/10.1016/j.ces.2004.11.054. URL https://www.sciencedirect.com/science/article/pii/S0009250904009601.

[59] Kiran B. Deshpande and William B. Zimmerman. Simulations of mass transfer limited reaction in a moving droplet to study transport limited characteristics. *Chemical Engineering Science*, 61(19):6424–6441, 2006. ISSN 0009-2509. doi: https://doi.org/10.1016/j.ces.2006.06.013. URL https://www.sciencedirect.com/science/article/pii/S0009250906003873.

[60] Xuan Cai, Holger Marschall, Martin Wörner, and Olaf Deutschmann. Numerical simulation of wetting phenomena with a phase-field method using OpenFOAM®. *Chemical Engineering & Technology*, 38(11):1985–1992, 2015. doi: 10.1002/ceat.201500089.

[61] F. Jamshidi, H. Heimel, M. Hasert, X. Cai, O. Deutschmann, H. Marschall, and M. Wörner. On suitability of phase-field and algebraic volume-of-fluid OpenFOAM® solvers for gas-liquid microfluidic applications. *Computer Physics Communications*, 236:72–85, 2019.

[62] *VOF-Simulations of Mass Transfer From Single Bubbles and Bubble Chains Rising in Aqueous Solutions*, volume Volume 2: Symposia, Parts A, B, and C of *Fluids Engineering Division Summer Meeting*, 07 2003.

[63] D. Bothe, M. Koebe, K. Wielage, J. Prüss, and H.-J. Warnecke. *Direct numerical simulation of mass transfer between rising gas bubbles and water*, pages 159–174. Springer Berlin Heidelberg, Berlin, Heidelberg, 2004. ISBN 978-3-642-18540-3. doi: 10.1007/978-3-642-18540-3_13. URL https://doi.org/10.1007/978-3-642-18540-3_13.

[64] Y. Haroun, D. Legendre, and L. Raynal. Volume of fluid method for interfacial reactive mass transfer: application to stable liquid film. *Chemical Engineering Science*, 65(10):2896 – 2909, 2010. ISSN 0009-2509. doi: https://doi.org/10.1016/j.ces.2010.01.012. URL http://www.sciencedirect.com/science/article/pii/S0009250910000291.

[65] Holger Marschall, Korbinian Hinterberger, Christian Schüler, Florian Habla, and Olaf Hinrichsen. Numerical simulation of species transfer across fluid interfaces in free-surface flows using openfoam. *Chemical Engineering Science*, 78:111–127, 2012. ISSN 0009-2509. doi: https://doi.org/10.1016/j.ces.2012.02.034. URL https://www.sciencedirect.com/science/article/pii/S0009250912001303.

[66] Dieter Bothe and Stefan Fleckenstein. A volume-of-fluid-based method for mass transfer processes at fluid particles. *Chemical Engineering Science*, 101:283 – 302,

2013. ISSN 0009-2509. doi: https://doi.org/10.1016/j.ces.2013.05.029. URL http://www.sciencedirect.com/science/article/pii/S0009250913003606.

[67] Daniel Deising, Holger Marschall, and Dieter Bothe. A unified single-field model framework for volume-of-fluid simulations of interfacial species transfer applied to bubbly flows. *Chemical Engineering Science*, 139:173 – 195, 2016. ISSN 0009-2509. doi: https://doi.org/10.1016/j.ces.2015.06.021. URL http://www.sciencedirect.com/science/article/pii/S0009250915004297.

[68] Andre Weiner and Dieter Bothe. Advanced subgrid-scale modeling for convection-dominated species transport at fluid interfaces with application to mass transfer from rising bubbles. *Journal of Computational Physics*, 347:261–289, 2017. ISSN 0021-9991. doi: https://doi.org/10.1016/j.jcp.2017.06.040. URL https://www.sciencedirect.com/science/article/pii/S0021999117304941.

[69] C.W Hirt and B.D Nichols. Volume of fluid (vof) method for the dynamics of free boundaries. *Journal of Computational Physics*, 39(1):201–225, 1981. ISSN 0021-9991. doi: https://doi.org/10.1016/0021-9991(81)90145-5. URL https://www.sciencedirect.com/science/article/pii/0021999181901455.

[70] Tomislav Maric, Holger Marschall, and Dieter Bothe. vofoam - a geometrical volume of fluid algorithm on arbitrary unstructured meshes with local dynamic adaptive mesh refinement using openfoam, 2013.

[71] Mark Owkes and Olivier Desjardins. A computational framework for conservative, three-dimensional, unsplit, geometric transport with application to the volume-of-fluid (vof) method. *Journal of Computational Physics*, 270:587–612, 2014. ISSN 0021-9991. doi: https://doi.org/10.1016/j.jcp.2014.04.022. URL https://www.sciencedirect.com/science/article/pii/S002199911400285X.

[72] Johan Roenby, Henrik Bredmose, and Hrvoje Jasak. A computational method for sharp interface advection. *Royal Society open science*, 3(11):160405, 2016.

[73] Johan Rønby Pedersen, Bjarke Eltard Larsen, Henrik Bredmose, and Hrvoje Jasak. A new volume-of-fluid method in openfoam. In Michel Visonneau, Patrick Queutey, and David Le Touzé, editors, *MARINE 2017 Computational Methods in Marine Engineering VII*, pages 266–278. International Center for Numerical Methods in Engineering, 2017. 7th International Conference on Computational Methods in Marine Engineering, MARINE 2017 ; Conference date: 15-05-2017 Through 17-05-2017.

[74] Suraj S Deshpande, Lakshman Anumolu, and Mario F Trujillo. Evaluating the performance of the two-phase flow solver interFoam. *Computational science & discovery*, 5 (1):014016, 2012.

[75] Ruben Scardovelli and Stéphane Zaleski. Direct numerical simulation of free-surface and interfacial flow. *Annual Review of Fluid Mechanics*, 31(1):567–603, 1999. doi: 10.1146/annurev.fluid.31.1.567. URL https://doi.org/10.1146/annurev.fluid.31.1.567.

[76] N Ashgriz and J.Y Poo. Flair: Flux line-segment model for advection and interface reconstruction. *Journal of Computational Physics*, 93(2):449–468, 1991. ISSN 0021-9991. doi: https://doi.org/10.1016/0021-9991(91)90194-P. URL https://www.sciencedirect.com/science/article/pii/002199919190194P.

[77] BJ Parker and DL Youngs. *Two and three dimensional Eulerian simulation of fluid flow with material interfaces*. Atomic Weapons Establishment, 1992.

[78] Murray Rudman. Volume-tracking methods for interfacial flow calculations. *International Journal for Numerical Methods in Fluids*, 24(7):671–691, 1997. doi: https://doi.org/10.1002/(SICI)1097-0363(19970415)24:7<671::AID-FLD508>3.0.CO;2-9. URL https://onlinelibrary.wiley.com/doi/abs/10.1002/%28SICI%291097-0363%2819970415%2924%3A7%3C671%3A%3AAID-FLD508%3E3.0.CO%3B2-9.

[79] William J. Rider and Douglas B. Kothe. Reconstructing volume tracking. *Journal of Computational Physics*, 141(2):112–152, 1998. ISSN 0021-9991. doi: https://doi.org/10.1006/jcph.1998.5906. URL https://www.sciencedirect.com/science/article/pii/S002199919895906X.

[80] Denis Gueyffier, Jie Li, Ali Nadim, Ruben Scardovelli, and Stéphane Zaleski. Volume-of-fluid interface tracking with smoothed surface stress methods for three-dimensional flows. *Journal of Computational Physics*, 152(2):423–456, 1999. ISSN 0021-9991. doi: https://doi.org/10.1006/jcph.1998.6168. URL https://www.sciencedirect.com/science/article/pii/S002199919896168X.

[81] James Edward Pilliod and Elbridge Gerry Puckett. Second-order accurate volume-of-fluid algorithms for tracking material interfaces. *Journal of Computational Physics*, 199(2):465–502, 2004. ISSN 0021-9991. doi: https://doi.org/10.1016/j.jcp.2003.12.023. URL https://www.sciencedirect.com/science/article/pii/S0021999104000920.

[82] Henning Scheufler and Johan Roenby. Accurate and efficient surface reconstruction from volume fraction data on general meshes. *Journal of Computational Physics*, 383: 1–23, 2019. ISSN 0021-9991. doi: https://doi.org/10.1016/j.jcp.2019.01.009. URL https://www.sciencedirect.com/science/article/pii/S0021999119300269.

[83] Lionel Gamet, Marco Scala, Johan Roenby, Henning Scheufler, and Jean-Lou Pierson. Validation of volume-of-fluid openfoam® isoadvector solvers using single bubble benchmarks. *Computers & Fluids*, 213:104722, 2020. ISSN 0045-7930. doi: https://doi.org/10.1016/j.compfluid.2020.104722. URL https://www.sciencedirect.com/science/article/pii/S0045793020302929.

[84] Athanas Koynov, Johannes G. Khinast, and Grétar Tryggvason. Mass transfer and chemical reactions in bubble swarms with dynamic interfaces. *AIChE Journal*, 51 (10):2786–2800, 2005. doi: https://doi.org/10.1002/aic.10529. URL https://aiche.onlinelibrary.wiley.com/doi/abs/10.1002/aic.10529.

[85] B. Aboulhasanzadeh and G. Tryggvason. Effect of bubble interactions on mass transfer in bubbly flow. *International Journal of Heat and Mass Transfer*, 79:390–396, 2014. ISSN 0017-9310. doi: https://doi.org/10.1016/j.ijheatmasstransfer.2014.08.027. URL https://www.sciencedirect.com/science/article/pii/S0017931014007145.

[86] Julien Maes and Cyprien Soulaine. A unified single-field volume-of-fluid-based formulation for multi-component interfacial transfer with local volume changes. *Journal of Computational Physics*, 402:109024, 2020. ISSN 0021-9991. doi: https://doi.org/10.1016/j.jcp.2019.109024. URL http://www.sciencedirect.com/science/article/pii/S0021999119307302.

[87] Colin Butler, Emmanuel Cid, Anne-Marie Billet, and Benjamin Lalanne. Numerical simulation of mass transfer dynamics in taylor flows. *International Journal of Heat and Mass Transfer*, 179:121670, 2021. ISSN 0017-9310. doi: https://doi.org/10.1016/j.ijheatmasstransfer.2021.121670. URL https://www.sciencedirect.com/science/article/pii/S0017931021007730.

[88] Palas Kumar Farsoiya, Stéphane Popinet, and Luc Deike. Bubble-mediated transfer of dilute gas in turbulence. *Journal of Fluid Mechanics*, 920:A34, 2021. doi: 10.1017/jfm.2021.447.

[89] Kalyani Kentheswaran, Nicolas Dietrich, Sébastien Tanguy, and Benjamin Lalanne. Direct numerical simulation of gas-liquid mass transfer around a spherical contaminated bubble in the stagnant-cap regime. *International Journal of Heat and*

Mass Transfer, 198:123325, 2022. ISSN 0017-9310. doi: https://doi.org/10.1016/j.ijheatmasstransfer.2022.123325. URL https://www.sciencedirect.com/science/article/pii/S0017931022007955.

[90] Stefan Fleckenstein and Dieter Bothe. A volume-of-fluid-based numerical method for multi-component mass transfer with local volume changes. *Journal of Computational Physics*, 301:35–58, 2015. ISSN 0021-9991. doi: https://doi.org/10.1016/j.jcp.2015.08.011. URL https://www.sciencedirect.com/science/article/pii/S0021999115005306.

[91] Freddy L. Durán Martínez, Carine Julcour, Anne-Marie Billet, and Faïçal Larachi. Modelling and simulations of a monolith reactor for three-phase hydrogenation reactions — rules and recommendations for mass transfer analysis. *Catalysis Today*, 273: 121 – 130, 2016. ISSN 0920-5861. doi: https://doi.org/10.1016/j.cattod.2016.04.009. URL http://www.sciencedirect.com/science/article/pii/S0920586116302620. 5th International Conference on Structured Catalysts and Reactors, ICOSCAR-5, Donostia-San Sebastián, Spain, 22-24 June, 2016.

[92] Mino Woo, Steffen Tischer, Olaf Deutschmann, and Martin Wörner. A step toward the numerical simulation of catalytic hydrogenation of nitrobenzene in taylor flow at practical conditions. *Chemical Engineering Science*, 230:116132, 2021. ISSN 0009-2509. doi: https://doi.org/10.1016/j.ces.2020.116132. URL https://www.sciencedirect.com/science/article/pii/S0009250920306643.

[93] Raghvendra Gupta, David F. Fletcher, and Brian S. Haynes. On the cfd modelling of taylor flow in microchannels. *Chemical Engineering Science*, 64(12):2941 – 2950, 2009. ISSN 0009-2509. doi: https://doi.org/10.1016/j.ces.2009.03.018. URL http://www.sciencedirect.com/science/article/pii/S0009250909001766.

[94] Stéphane Popinet and Stéphane Zaleski. A front-tracking algorithm for accurate representation of surface tension. *International Journal for Numerical Methods in Fluids*, 30(6):775–793, 1999. doi: https://doi.org/10.1002/(SICI)1097-0363(19990730)30:6<775::AID-FLD864>3.0.CO;2-\#. URL https://onlinelibrary.wiley.com/doi/abs/10.1002/%28SICI%291097-0363%2819990730%2930%3A6%3C775%3A%3AAID-FLD864%3E3.0.CO%3B2-%23.

[95] J. Tan, Y.C. Lu, J.H. Xu, and G.S. Luo. Mass transfer characteristic in the formation stage of gas–liquid segmented flow in microchannel. *Chemical Engineering Journal*, 185-186:314–320, 2012. ISSN 1385-8947. doi: https://doi.org/10.1016/

j.cej.2012.01.054. URL https://www.sciencedirect.com/science/article/pii/S1385894712000575.

[96] R. G. Cox. Inertial and viscous effects on dynamic contact angles. *J. Fluid Mech.*, 357: 249–278, 1998.

[97] S. F. Kistler. Hydrodynamics of wetting. *J.C. Berg (Ed), Wettability, Surfactant Science Series*, pages 251–309, 1993.

[98] Bram Van Leer. Towards the ultimate conservative difference scheme i. the quest of monotonicity. In *Proceedings of the Third International Conference on Numerical Methods in Fluid Mechanics: Vol. I General Lectures. Fundamental Numerical Techniques July 3–7, 1972 Universities of Paris VI and XI*, pages 163–168. Springer, 1972.

[99] Bram van Leer. Towards the ultimate conservative difference scheme. ii. monotonicity and conservation combined in a second-order scheme. *Journal of Computational Physics*, 14(4):361–370, 1974. doi: https://doi.org/10.1016/0021-9991(74)90019-9. URL https://www.sciencedirect.com/science/article/pii/0021999174900199.

[100] Bram Van Leer. Towards the ultimate conservative difference scheme iii. upstream-centered finite-difference schemes for ideal compressible flow. *Journal of Computational Physics*, 23(3):263–275, 1977. ISSN 0021-9991. doi: https://doi.org/10.1016/0021-9991(77)90094-8. URL https://www.sciencedirect.com/science/article/pii/0021999177900948.

[101] Bram Van Leer. Towards the ultimate conservative difference scheme. iv. a new approach to numerical convection. *Journal of Computational Physics*, 23(3):276–299, 1977. ISSN 0021-9991. doi: https://doi.org/10.1016/0021-9991(77)90095-X. URL https://www.sciencedirect.com/science/article/pii/002199917790095X.

[102] Bram van Leer. Towards the ultimate conservative difference scheme. v. a second-order sequel to godunov's method. *Journal of Computational Physics*, 32(1):101–136, 1979. ISSN 0021-9991. doi: https://doi.org/10.1016/0021-9991(79)90145-1. URL https://www.sciencedirect.com/science/article/pii/0021999179901451.

[103] Ami Harten. High resolution schemes for hyperbolic conservation laws. *Journal of Computational Physics*, 49(3):357–393, 1983. ISSN 0021-9991. doi: https://doi.org/10.1016/0021-9991(83)90136-5. URL https://www.sciencedirect.com/science/article/pii/0021999183901365.

[104] M. Magnini, B. Pulvirenti, and J.R. Thome. Numerical investigation of hydrodynamics and heat transfer of elongated bubbles during flow boiling in a microchannel. *International Journal of Heat and Mass Transfer*, 59:451–471, 2013. ISSN 0017-9310. doi: https://doi.org/10.1016/j.ijheatmasstransfer.2012.12.010. URL `https://www.sciencedirect.com/science/article/pii/S0017931012009556`.

[105] S. Bortolin, E. Da Riva, and D. Del Col. Condensation in a square minichannel: Application of the vof method. *Heat Transfer Engineering*, 35(2):193–203, 2014. doi: 10.1080/01457632.2013.812493. URL `https://doi.org/10.1080/01457632.2013.812493`.

[106] Sihan Chen, Zhen Yang, Yuanyuan Duan, Ying Chen, and Di Wu. Simulation of condensation flow in a rectangular microchannel. *Chemical Engineering and Processing: Process Intensification*, 76:60–69, 2014. ISSN 0255-2701. doi: https://doi.org/10.1016/j.cep.2013.12.004. URL `https://www.sciencedirect.com/science/article/pii/S0255270113002808`.

[107] S.Q. Li, P. Wang, and T. Lu. Numerical simulation of direct contact condensation of subsonic steam injected in a water pool using vof method and les turbulence model. *Progress in Nuclear Energy*, 78:201–215, 2015. ISSN 0149-1970. doi: https://doi.org/10.1016/j.pnucene.2014.10.002. URL `https://www.sciencedirect.com/science/article/pii/S0149197014002662`.

[108] N. Samkhaniani and M.R. Ansari. Numerical simulation of bubble condensation using cf-vof. *Progress in Nuclear Energy*, 89:120–131, 2016. ISSN 0149-1970. doi: https://doi.org/10.1016/j.pnucene.2016.02.004. URL `https://www.sciencedirect.com/science/article/pii/S0149197016300269`.

[109] Clifford Truesdell and Richard Toupin. *The classical field theories*. Springer, 1960.

[110] John C Slattery. *Advanced transport phenomena*. Cambridge University Press, 1999.

[111] John C Slattery, Leonard Sagis, and Eun-Suok Oh. *Interfacial transport phenomena*. Springer Science & Business Media, 2007.

[112] Mamoru Ishii and Takashi Hibiki. *Thermo-fluid dynamics of two-phase flow*. Springer Science & Business Media, 2010.

[113] Christophe Morel. Mathematical modeling of disperse two-phase flows. 2015.

[114] Ross Taylor and Rajamani Krishna. *Multicomponent mass transfer*, volume 2. John Wiley & Sons, 1993.

[115] H.S. Udaykumar and W. Shyy. Simulation of interfacial instabilities during solidification—i. conduction and capillarity effects. *International Journal of Heat and Mass Transfer*, 38(11):2057–2073, 1995. ISSN 0017-9310. doi: https://doi.org/10.1016/0017-9310(94)00315-M. URL https://www.sciencedirect.com/science/article/pii/001793109400315M.

[116] Yohei Sato and Bojan Ničeno. A sharp-interface phase change model for a mass-conservative interface tracking method. *Journal of Computational Physics*, 249:127–161, 2013. ISSN 0021-9991. doi: https://doi.org/10.1016/j.jcp.2013.04.035. URL https://www.sciencedirect.com/science/article/pii/S0021999113003197.

[117] Kong Ling, Zeng-Yao Li, and Wen-Quan Tao. A direct numerical simulation for nucleate boiling by the voset method. *Numerical Heat Transfer, Part A: Applications*, 65(10):949–971, 2014. doi: 10.1080/10407782.2013.850971. URL https://doi.org/10.1080/10407782.2013.850971.

[118] Isaac Perez-Raya and Satish G. Kandlikar. Discretization and implementation of a sharp interface model for interfacial heat and mass transfer during bubble growth. *International Journal of Heat and Mass Transfer*, 116:30–49, 2018. ISSN 0017-9310. doi: https://doi.org/10.1016/j.ijheatmasstransfer.2017.08.106. URL https://www.sciencedirect.com/science/article/pii/S0017931017322408.

[119] Bruce E. Poling, J. M. Prausnitz, and John P. O'Connell. *The properties of gases and liquids*. McGraw-Hill, New York, 5th ed edition, 2001. ISBN 978-0-07-011682-5.

[120] Kenneth R. Cox and Walter G. Chapman. The properties of gases and liquids, 5th edition by bruce e. poling (university of toledo), john m. prausnitz (university of california at berkeley), and john p. o'connell (university of virginia). mcgraw-hill: New york. 2001. 768 pp. $115.00. isbn 0-07-011682-2. *Journal of the American Chemical Society*, 123(27):6745–6745, 2001. doi: 10.1021/ja0048634. URL https://doi.org/10.1021/ja0048634.

[121] E. N. Fuller and J. C. Giddings. A Comparison of Methods for Predicting Gaseous Diffusion Coefficients. *Journal of Chromatographic Science*, 3(7):222–227, 1965. ISSN 0021-9665. doi: 10.1093/chromsci/3.7.222. URL https://doi.org/10.1093/chromsci/3.7.222. _eprint: https://academic.oup.com/chromsci/article-pdf/3/7/222/885636/3-7-222.pdf.

[122] Edward N. Fuller, Paul D. Schettler, and J. Calvin. Giddings. New method for prediction of binary gas-phase diffusion coefficients. *Industrial & Engineering Chemistry*, 58(5):18–27, 1966. doi: 10.1021/ie50677a007. URL https://doi.org/10.1021/ie50677a007.

[123] C. R. Wilke and C. Y. Lee. Estimation of diffusion coefficients for gases and vapors. *Industrial & Engineering Chemistry*, 47(6):1253–1257, 1955. doi: 10.1021/ie50546a056. URL https://doi.org/10.1021/ie50546a056.

[124] Bobby H.C. Chen and S.H. Chen. Diffusion of slightly soluble gases in liquids: Measurement and correlation with implications on liquid structures. *Chemical Engineering Science*, 40(9):1735 – 1741, 1985. ISSN 0009-2509. doi: https://doi.org/10.1016/0009-2509(85)80035-X. URL http://www.sciencedirect.com/science/article/pii/000925098580035X.

[125] C. R. Wilke and Pin Chang. Correlation of diffusion coefficients in dilute solutions. *AIChE Journal*, 1(2):264–270, 1955. doi: https://doi.org/10.1002/aic.690010222. URL https://aiche.onlinelibrary.wiley.com/doi/abs/10.1002/aic.690010222.

[126] John H. Dymond and Lawrie A. Woolf. Tracer diffusion of organic solutes in n-hexane at pressures up to 400 mpa. *J. Chem. Soc., Faraday Trans. 1*, 78:991–1000, 1982. doi: 10.1039/F19827800991. URL http://dx.doi.org/10.1039/F19827800991.

[127] Pierre-Alain R Breuil, Lionel Magna, and Helene Olivier-Bourbigou. Role of homogeneous catalysis in oligomerization of olefins: Focus on selected examples based on group 4 to group 10 transition metal complexes. *Catalysis Letters*, 145(1):173–192, 2015.

[128] Giorgio Soave. Equilibrium constants from a modified redlich-kwong equation of state. *Chemical Engineering Science*, 27(6):1197 – 1203, 1972. ISSN 0009-2509. doi: https://doi.org/10.1016/0009-2509(72)80096-4. URL http://www.sciencedirect.com/science/article/pii/0009250972800964.

[129] Ding-Yu Peng and Donald B. Robinson. A new two-constant equation of state. *Industrial & Engineering Chemistry Fundamentals*, 15(1):59–64, 1976. doi: 10.1021/i160057a011. URL https://doi.org/10.1021/i160057a011.